



HAL
open science

Electrolyte Engineering via Novel Salts and Additives for Aqueous Energy Storage Solutions

John Brown

► **To cite this version:**

John Brown. Electrolyte Engineering via Novel Salts and Additives for Aqueous Energy Storage Solutions. Analytical chemistry. Sorbonne Université, 2024. English. NNT: 2024SORUS235 . tel-04794011

HAL Id: tel-04794011

<https://theses.hal.science/tel-04794011v1>

Submitted on 20 Nov 2024

HAL is a multi-disciplinary open access archive for the deposit and dissemination of scientific research documents, whether they are published or not. The documents may come from teaching and research institutions in France or abroad, or from public or private research centers.

L'archive ouverte pluridisciplinaire **HAL**, est destinée au dépôt et à la diffusion de documents scientifiques de niveau recherche, publiés ou non, émanant des établissements d'enseignement et de recherche français ou étrangers, des laboratoires publics ou privés.

Sorbonne Université

Ecole doctorale - ED 397 - Physique et Chimie des Matériaux

Collège de France

Laboratoire – Chaire de Chimie du Solide et de l'Energie

Electrolyte Engineering via Novel Salts and Additives for Aqueous Energy Storage Solutions

John Brown

Doctoral thesis in Materials Science / Physics and Chemistry

Supervised by Alexis Grimaud

Presented and defended publicly on September 27th 2024, in front of the jury:

Dr. Alexandre Ponrouch	Tenure scientist, ICMAB, Spain	President
Prof. Erik Berg	Professor, Uppsala University, Sweden	Referee
Dr. Frédéric Favier	Research Director, Université Montpellier, France	Referee
Dr. Natacha Krins	A. Professor, Sorbonne University, France	Examiner
Dr. Phillipe Stevens	Senior Researcher, EDF, France	Examiner
Prof. Jean-Marie Tarascon	Professor, Collège de France, France	Invited
Prof. Patrik Johansson	Professor, Chalmers University of Technology, Sweden	Invited
Dr. Alexis Grimaud	A. Professor, Boston College, USA	Thesis Director



Except where otherwise noted, this work is licensed under
<http://creativecommons.org/licenses/by-nc-nd/3.0/>

Sorbonne Université

Ecole doctorale - ED 397 - Physique et Chimie des Matériaux

Collège de France

Laboratoire – Chaire de Chimie du Solide et de l'Energie

Ingénierie des Électrolytes via de Nouveaux Sels et Additifs pour les Solutions Aqueuses de Stockage d'Énergie

John Brown

Thèse de doctorat en Physique et Chimie des Matériaux

Dirigée par Alexis Grimaud

Présenté et soutenu publiquement le 27 septembre 2024, devant le jury:

Dr. Alexandre Ponrouch	Chercheur, ICMAB, Espagne	Président
Prof. Erik Berg	Professeur, Uppsala University, Suède	Rapporteur
Dr. Frédéric Favier	Directeur de recherche, Université Montpellier, France	Rapporteur
Dr. Natacha Krins	Maitre de Conférence, Sorbonne Université, France	Examineur
Dr. Phillipe Stevens	Chercheur Principal, EDF, France	Examineur
Prof. Jean-Marie Tarascon	Professeur, Collège de France, France	Membre Invité
Prof. Patrik Johansson	Professeur, Chalmers University of Technology, Suède	Membre Invité
Dr. Alexis Grimaud	A. Professeur, Boston College, Etats-Unis	Directeur

Acknowledgments

Firstly, my deepest thanks to Alexis Grimaud for his supervision throughout these three years. It was a great pleasure to work alongside you, and I learned a great deal both scientifically and professionally. Your work ethic, knowledge, and passion for science were a great inspiration, and I am incredibly grateful to have had the opportunity to learn from you. You were the perfect supervisor, giving me the freedom to explore my ideas and pursue the things I enjoyed while perfectly guiding me through the different topics. I am also incredibly grateful to have had the opportunity to spend time at Boston College. The whole PhD experience was just very enjoyable so thank you very much for that.

I would also like to thank Patrik Johansson. It was a pleasure to work alongside you, and your insights during my PhD were invaluable. Spending three very productive months with you in Sweden, where I learned many new skills, was a fantastic experience and I am very grateful. Again, the whole experience of working with you was fun and enjoyable.

I also want to acknowledge Jean-Marie Tarascon. The resources we have at the CSE lab, thanks to you, made anything feel possible and was the perfect platform for science. I loved the environment, which is at the pinnacle of research. Your passion for your work is completely unrivalled and was inspiring to be around. I am eternally grateful to have had the chance to work alongside you.

A very special thanks to Juan, who was a great mentor and taught me a lot during my time at the lab. Many of the projects would not have been possible without you. Your kindness and knowledge were such great support during my PhD. I am happy to have shared that time with you and I'm sure you will certainly go on to do great things.

Ezzoubair, you made the experience of working at the lab incredibly fun. We had so many laughs, and I have many fond memories from our time at the lab from football to ping pong to EQCM.

Ivette, who was a great help when it came to zinc batteries. It wouldn't have been possible to carry out that work without you, and I hope our work leads to something greater.

My officemates, Juan, Ronan, Zhenying, Xu and Tatjana who made coming to work every day a fun time. We had many interesting discussions and gossip about the lab, the CCP and of course science, which always made me smile.

The CSE lab as a whole, both current and former members, made the experience truly special. It really felt like a big family, and I cherish my time around all of you. There was always someone who could help with any situation. Particular thanks to Florian and Damian who helped a lot with the French admin and helped me get settled in at the lab. Also, the labs at Chalmers and Boston College, who were all very welcoming during my stays and assisted with many different experiments.

My family from Scotland, Germany, France and Australia, who were always a huge support. Finally, Alice. without you, this would not have been possible. You really are my number one fan and my biggest inspiration.

Contents

Global context	1
Outline of thesis	4
Chapter 1: Introduction to Electrolyte Engineering for Aqueous Batteries	6
1.1 Origins of Aqueous Electrolytes and Batteries	6
1.2 Origins of Li-ion Batteries (LIBs)	8
1.3 Aqueous Li-ion Batteries (ALIBs)	10
1.4 Super-Concentrated Electrolytes	12
1.4.1 <i>The Dawn of Super-concentration</i>	12
1.4.2 <i>“Solvent-in-salt”</i>	13
1.4.3 <i>Water-in-Salt Electrolytes (WISE)</i>	13
1.4.4 <i>The Problem with WISE</i>	17
1.5 Electrolyte Engineering for WISE	19
1.5.1 <i>“Molecular Crowding”</i>	19
1.5.2 <i>Solvation Structure Adaptation</i>	21
1.5.3 <i>Chaotropicity</i>	23
1.5.4 <i>How Aqueous are These Electrolytes?</i>	26
1.6 Redox-Active Organic Materials (ROMs) for ALIBs	27
1.6.1 <i>Polyimides</i>	28
1.7 Aqueous Zn-Metal Batteries	32
1.7.1 <i>Mechanisms of Zn Electrodeposition and MnO₂</i>	32
1.7.2 <i>Dendrites</i>	34
1.7.3 <i>Electrolyte Engineering for Dendrites</i>	36
Conclusions to Chapter 1	39
Chapter 2: Acid/Base Dynamics of Amino Acids in Aqueous Electrolytes	40
2.1 Prelude to the Chapter: Citrulline in WISE	40
2.2 An Introduction to the Fundamentals of the HER	44
2.2.1 <i>The Mechanism and Catalyst of Choice</i>	44
2.2.2 <i>pH Dependency of the HER</i>	44
2.2.3 <i>Playing on the Acid/Base Dynamics of the HER</i>	46
2.2.4 <i>Amino Acids as Buffers?</i>	47
2.3 Acid/Base Chemistry of Asp/Glu	47
2.4 Electrochemistry of Asp/Glu Solutions	49
2.5 The Electrochemistry of SER/HIS	54
Conclusions to Chapter 2	56
Chapter 3: A Guanidium Salt as a Chaotropic Agent for Aqueous Battery Electrolytes	57
3.1 Introduction	57
3.2 Guanidium bis(trifluoromethanesulfonyl)imide (GdmTFSI)	57
3.3 Synthesis and Material Characterisation	58

3.4 GdmTFSI in Aqueous Solutions.....	62
3.5 Chaotropic Nature of Gdm ⁺	65
3.6 Binary Mixture of GdmTFSI + LiTFSI.....	66
Conclusions to Chapter 3.....	67
Chapter 4: Zinc-Oligoether Salts as Electrolyte Additives for Aqueous Zn-Metal Batteries.....	69
4.1 Introduction.....	69
4.2 Zinc Oligoethers.....	70
4.3 Use of Zn(MEC) ₂ , Zn(MEA) ₂ and Zn(MEEA) ₂ as Additives.....	76
4.4 SEI Formation.....	82
4.5 Full Cell – Zn MnO ₂	85
4.6 LiMEEA + LiTFSI in Water.....	89
Conclusions to Chapter 4.....	91
Chapter 5: Exploring the Electrochemistry of PTCDI for Aqueous Lithium-ion Batteries.....	93
5.1 Introduction.....	93
5.2 Reversibility with Aqueous Electrolytes.....	94
5.3 Active Charge Carrier(s).....	98
5.4 Electrochemical Performance.....	105
Conclusions to Chapter 5.....	109
Conclusion and Perspectives.....	110
ANNEX.....	114
Chapter 2.....	114
<i>Materials and Methods</i>	114
<i>Supplementary Figures</i>	116
Chapter 3.....	118
<i>Materials and Methods</i>	118
Chapter 4.....	121
<i>Materials and Methods</i>	121
<i>Supplementary Figures</i>	126
Chapter 5.....	129
<i>Materials and Methods</i>	129
<i>Supplementary Figures</i>	133
References.....	135
List of Abbreviations.....	150
Résumé en Français.....	152
Abstract.....	157
Résumé.....	157

Global context

Fuelled by population growth, global energy consumption has soared since the 19th century. In recent decades, this growth has been primarily driven by economic and population expansion in emerging markets, particularly countries in Asia and Africa. To meet these growing demands, our society has largely relied on fossil fuels, natural gas, and coal, which have emitted large amounts of greenhouse gases, specifically CO₂. This rise in CO₂ is causing an increase in the Earth's temperature, projected to rise by 1.1°C by 2030. [1] The Paris Agreement aims to limit global warming to below 1.5°C, which requires keeping CO₂ concentrations below 450 ppm by 2100. However, at current emission rates, CO₂ levels are projected to reach this threshold by 2045. [2] Thus, there is an urgent need to reduce the carbon intensity of our energy supply. It is expected that renewables such as wind and solar will become key sources of electricity generation worldwide as we move towards 2050 and beyond, while coal and gas will stagnate (Fig. 0.1a-c). Currently, solar accounts for 3% of global electricity generation, a figure projected to rise to 20% by 2050 (Fig. 0.1d). Meanwhile, wind, which currently produces 6%, is expected to increase to 14% by 2050 (Fig. 0.1e). [3] Although this is promising statistic, there are hurdles to overcome for renewable energy to be fully harnessed. The issue with renewable energy sources is their intermittent nature, which renders the utilization of this energy inefficient without adequate means for storage. Implementing energy storage mechanisms would enable us to utilize renewable energy based on supply and demand. Furthermore, the transportation sector is responsible for a significant portion of greenhouse gas emissions, making its electrification a top priority for mitigating environmental impact. [3] Achieving these transitions requires the widespread adoption of cost-effective energy storage technologies. [1], [2]

Global Context

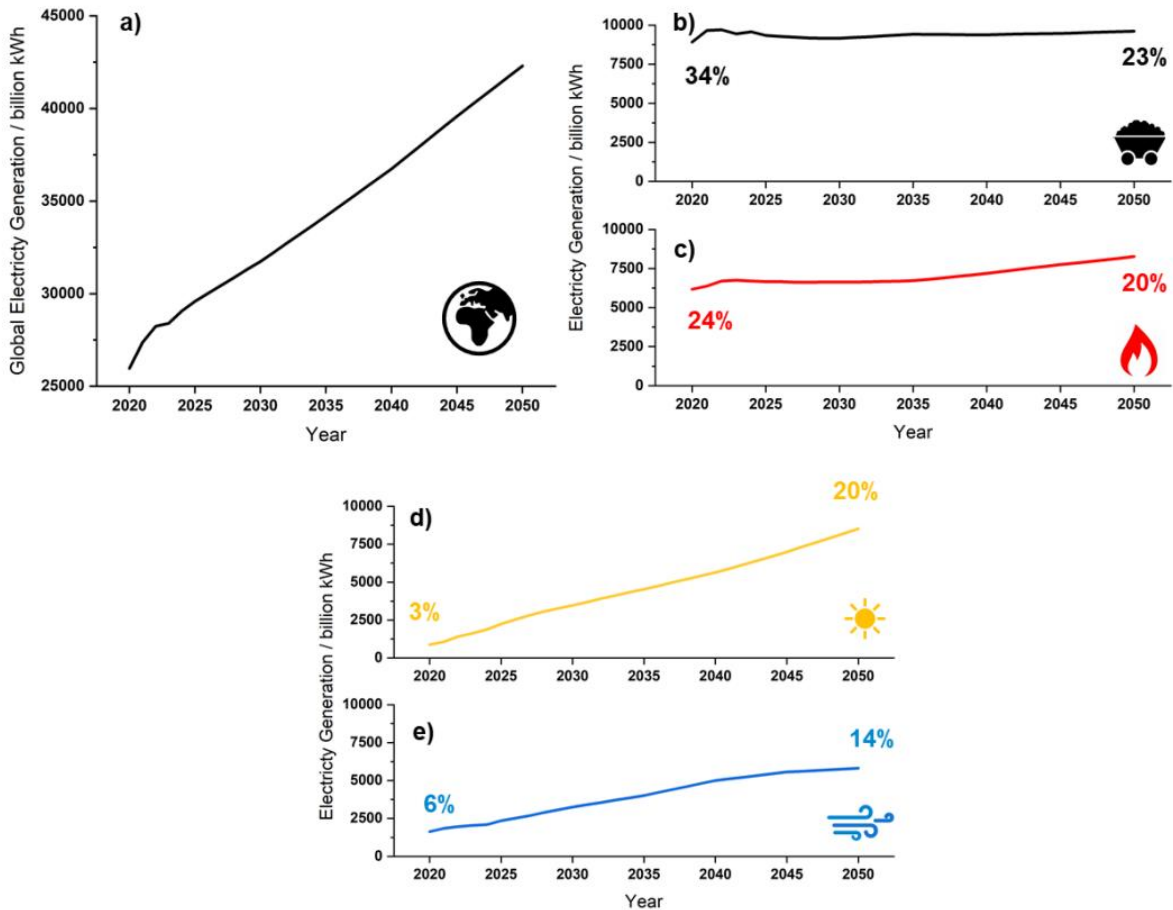


Fig. 0.1 – a) Global electricity generation, b) coal, c) gas, d) solar and e) wind, data obtained from International Energy Outlook 2023 (IEO2023). [1]

Secondary (rechargeable) batteries, which store electrical energy through chemical reactions, could certainly meet these demands. There are many different forms of rechargeable batteries, with lithium-ion (Li-ion) technology utilizing organic solvents being the most widespread today. However, there are safety and sustainability concerns with the use of such batteries. Thermal runaway can occur, posing significant safety risks, and the high production costs raise economic concerns. Hence, alternative safer and sustainable chemistries should be targeted. Besides, an overreliance on a single technology has contributed to our current challenges, so diversifying battery chemistries would be advantageous. [4], [5]

Aqueous alkaline-metal batteries and aqueous zinc-ion batteries are emerging forms of secondary batteries that emphasize safety and sustainability. Water offers advantages such as being non-flammable and cost-effective compared to their organic counterparts. However, the reactive nature of water presents a major challenge, particularly a narrow electrochemical stability window (ESW) of just 1.23 V.[6] To improve and enhance this ESW, electrolyte engineering has played a crucial role, employing various tactics such as super-concentration, dilution with organic solvents, and additives. Despite these efforts, water reactivity remains an issue, and novel solutions will always be required to push the boundaries further and address task-specific challenges. The thesis aims to further develop these technologies through electrolyte engineering, specifically novel salt design and smart electrolyte/electrode pairing while also touching on the fundamentals of water splitting through acid/base dynamics.

Outline of thesis

The first chapter introduces the key themes of the thesis: aqueous electrolytes, the reactivity of water, the origins of Li-ion technology, and the development of aqueous Li-ion batteries (ALIBs). It outlines the journey to using super-concentrated electrolytes, highlighting the challenges encountered. We discuss how electrolyte engineering has been employed to address these challenges and advance ALIBs, though with some sustainability concerns. Additionally, we explore more sustainable technologies, such as those utilising redox-active organic materials as electrodes and zinc-ion technology, which also face challenges that electrolyte engineering has and will continue to address.

The second chapter investigates the use of amino acids as additives to influence the hydrogen bonding network of water and modulate the kinetics of water splitting. Although some interesting electrolytes were developed, testing in full Li-ion cells revealed poor cycling performance. It was discovered that certain amino acids' buffering effects could be utilised to probe the acid/base dynamics of the hydrogen evolution reaction (HER). Our findings demonstrate that aspartic acid (Asp) and glutamic acid (Glu) not only act as proton donors but also provide sufficient buffering capacity to sustain H_3O^+ reduction at high current densities. By comparing these results with histidine (His) and serine (Ser), we show that the buffering capacity of amino acids is influenced by their isoelectric point (pI) and buffering pKa. This study highlights the interplay between pH, pKa, and HER kinetics, showcasing the potential of amino acids for exploring these relationships.

The third chapter presents a novel approach to designing salts for aqueous battery electrolytes. This strategy involves combining chaotropic ions, specifically guanidinium cations (Gdm^+), with bis(trifluoromethanesulfonyl)imide anions (TFSI⁻), resulting in the formation of GdmTFSI. We characterise this salt and its aqueous solutions, demonstrating that GdmTFSI disrupts the hydrogen bonding network of water, thereby influencing the reactivity of water at electrochemical interfaces. We show that Gdm^+ is more chaotropic compared to Li^+ , which allows it to expand the electrochemical stability window (ESW) by mitigating the hydrogen evolution reaction

(HER) and the oxygen evolution reaction (OER). Finally, we briefly showcase the implications of these findings when applied to a Zn || MnO₂ battery.

The fourth chapter delves deeper into novel salts by revisiting and expanding upon a family of oligoether salts. These salts feature long glyme-like ether chains, with one terminal containing a carboxyl group that forms a salt with a cation. We propose a novel series of Zn-based salts: Zinc 2-methoxyethyl carbonate (Zn(MEC)₂), Zinc 2-(2-methoxyethoxy)acetate (Zn(MEA)₂), and Zinc 2-[2-(2-methoxyethoxy)ethoxy]acetate (Zn(MEEA)₂). These salts can be used as additives in zinc-metal batteries to prevent dendrite formation. All three salts significantly increase the cycle life of AZMBs when added at just 5 wt% to a base electrolyte, which we attribute to the formation of a solid electrolyte interphase (SEI) facilitated by the salts. We also demonstrate a practical application by incorporating these salts into a urea-based electrolyte previously designed by our lab for a Zn || MnO₂ cell, resulting in significantly extended cycling performance under our testing conditions.

The fifth chapter examines the electrochemical properties of perylene-3,4,9,10-tetracarboxylic acid diimide (PTCDI) and assesses its viability as an organic anode material for ALIBs. Despite its high conductivity and low water solubility, PTCDI had not previously been used in an aqueous Li-ion electrolyte. We employ various techniques, including ex-situ IR, ex-situ XRD, and EQCM, to investigate the charge compensation mechanism. Furthermore, we demonstrate that electrolyte design plays a crucial role in performance, with salt concentration and anion choice being critical parameters that significantly impact long-term stability.

Altogether, this thesis highlights the role of electrolyte engineering for solving the various issues encountered by aqueous energy storage solutions. We build on a fundamental understanding of electrolyte concepts while demonstrating the real-world applicability of our novel electrolytes.

Chapter 1: Introduction to Electrolyte Engineering for Aqueous Batteries

This chapter is partially based on the following publications:

- **J. Brown**, A. Grimaud, 'With only a grain of salt.' *Nat Energy* vol. 7, pp. 126–127, Feb. 2021
doi: 10.1038/s41560-022-00981-3
- **J. Brown**, A. Grimaud, 'Super-concentrated Electrolytes: a WISE Choice?' – 2024 Roadmap on Sustainable Batteries: M. Titirici et al. *J. Phys. Energy* vol. 6, no. 6, Sep. 2024 - DOI: 10.1088/2515-7655/ad6bc0

1.1 Origins of Aqueous Electrolytes and Batteries

The inception of aqueous batteries dates back to Volta's creation of the voltaic pile in 1801 and was further advanced by Daniell's pile in 1836. In Daniell's configuration, brine (saltwater) served as the electrolyte, facilitating charge transfer between zinc and copper, which functioned as the anode and cathode, respectively. These electrodes underwent redox reactions, converting chemical energy into electrical energy. The zinc anode oxidises, while the copper cathode undergoes reduction (Fig. 1.1). These simultaneous reactions, occurring in the presence of an external circuit, produced a cell potential of 1.1 V. When these cells were arranged in series, they formed the first-ever primary battery. [7]

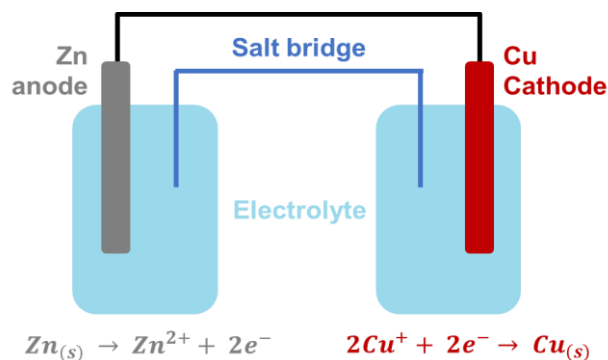
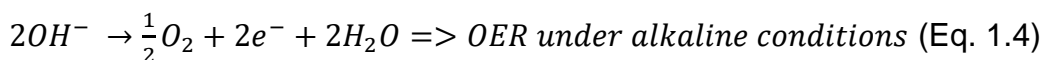


Fig. 1.1 – Schematic of Daniell's Zn Cu battery.

Batteries quickly evolved, and by 1859, Gaston Planté introduced the first rechargeable battery—the lead-acid battery—using lead as the anode, PbO_2 as the cathode, and H_2SO_4 as the electrolyte. Its affordability and reliability made it popular for uninterruptible power supplies (UPS), vehicle starting, lighting, and ignition (SLI), with an energy density of 60 Wh.kg^{-1} . [8] Sixty years later, the nickel-cadmium (Ni-Cd) battery emerged, featuring cadmium as the anode, NiOOH as the cathode, and 30% potassium hydroxide (KOH) as the electrolyte. Known for affordability and high performance, Ni-Cd batteries were ideal for power tools and early mobile phones but suffered from the "memory effect," cadmium toxicity, and limited energy density. By the mid-1980s, nickel-metal hydride (Ni-MH) batteries, which improved upon Ni-Cd technology, offered higher energy density ($70 - 110 \text{ Wh.kg}^{-1}$) and a reduced "memory effect." These batteries became popular for AA and AAA cells in portable devices and hybrid-electric vehicles like the Toyota Prius. [7], [9]

These technologies dominated the commercial battery market until 2015 and still occupy a large share today. [10] Their prevalence is due to their low cost and, in the case of lead-acid batteries, high recyclability. However, these technologies either operate within the thermodynamically stable potential window of water, or have incredibly slow kinetics for water splitting, in both cases restricting battery voltage and specific energy. [11] Indeed, the electrochemical stability window (ESW) of water is just 1.23 V, where exceeding these limits causes water splitting (Fig. 1.2). This process includes the hydrogen evolution reaction (HER) and oxygen evolution reaction (OER), producing $\text{H}_{2(g)}$ and $\text{O}_{2(g)}$, respectively. [12] The above technologies leverage the acidity or basicity of the electrolyte to maximise battery performance, however shifting pH to extend the potential limits of one reaction will in turn reduce the limits of the other. Interestingly, the HER and OER differ when under acidic or alkaline conditions as demonstrated via Eq. 1.1 – 1.4. [12]



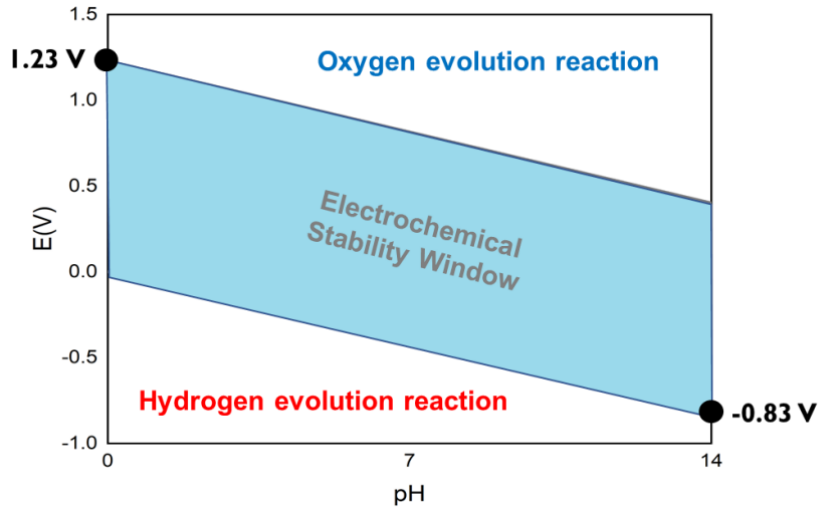
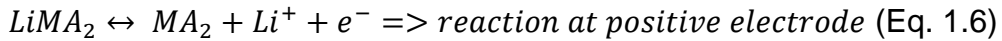
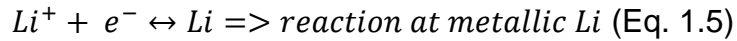


Fig. 1.2 – Electrochemical stability window of water as a function of pH.

1.2 Origins of Li-ion Batteries (LIBs)

To push past the limited energy density of the aforementioned aqueous battery technologies in section 1.1, alkali-metal based batteries based on organic electrolytes were proposed. The journey began in the 1970s with Stanley Whittingham's pioneering work. He used metallic lithium as the negative electrode and an intercalation chalcogenide-based material as the positive electrode, separated by a separator soaked in an aprotic organic liquid electrolyte containing a Li-based salt. This breakthrough utilised the reversible insertion of Li^+ cations from the Li metal into TiS_2 or MoS_2 (Eq. 1.5 & 1.6). [13], [14], [15] Lithium was chosen for its low molar mass (6.94 g.mol^{-1}), low redox potential ($\text{Li}^+/\text{Li} = -3.04 \text{ V vs SHE}$), and high theoretical capacity (3862 mAh.g^{-1}). Despite early commercialization by Exxon and Moli Energy, safety challenges arose, notably dendrite growth during charging on the Li metal, which posed short-circuiting and ignition risks (Fig. 1.3). [16]



M = transition metal and A = sulphur or oxide

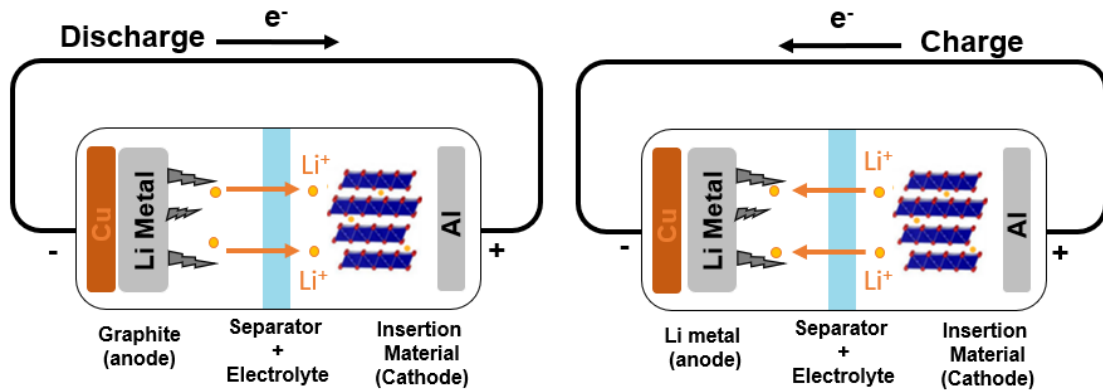


Fig. 1.3 – Schematic for Li metal battery, in discharge (left) and in charge leading to dendrites (right).

In the 1980s, John Goodenough and colleagues revolutionized battery technology by replacing sulfur-based materials with LiCoO₂ (LCO) for the positive electrode. With a redox potential of 3.7 – 3.9 V vs Li⁺/Li, this advancement paved the way for the use of non-lithiated intercalation materials as negative electrodes. [17], [18] This led to the work of Akira Yoshino, who used carbonaceous petroleum coke as the negative electrode against LCO, resulting in the first commercial Li-ion battery from Sony in 1991. [19] The collective research earned Whittingham, Goodenough, and Yoshino the Nobel Prize in Chemistry in 2019. [20] Li-ion batteries would grow substantially since, and now is the go-to battery technology with graphite (0 - 0.25 V vs Li⁺/Li) the most commonly used negative electrode (Eq. 1.7). Graphite became viable for use after the discovery of a solid electrolyte interphase (SEI). This SEI layer protects the graphite surface, allowing for stable and highly reversible cycling. [21] Lithium-based transitional metal oxides such as LiNi_xMn_yCo_{1-x-y}O₂ - NMC (3.8 – 4.3 V vs Li⁺/Li) and LiFePO₄ - LFP (3.6 V vs Li⁺/Li) are popular positive electrodes (Fig. 1.4). Such batteries have an energy density double that of Ni-MH reaching up to 220 Wh.kg⁻¹ for graphite-NMC and are used to power our electric vehicles (EVs), portable electronics and many more different technologies. [22], [23]

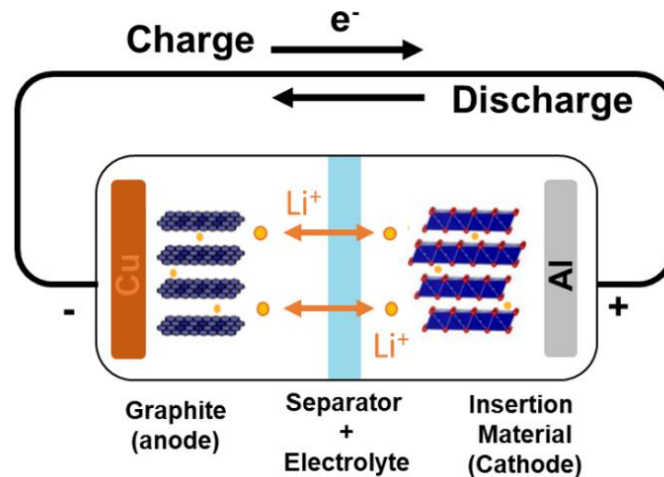


Fig. 1.4 – Schematic for Li-ion battery with graphite as the negative electrode.

Despite the widespread adoption of Li-ion batteries, the use of organic solvents remains a sustainability stumbling block where flammability and processability remains a great concern. Indeed, the ester-based solvents used such as ethylene carbonate (EC) and dimethyl carbonate (DMC) are not only highly flammable but also react with charged electrodes leading to thermal runaway. [24], [25] Furthermore, these electrolytes and thus the whole manufacturing process need to be completely moisture-free, which significantly drives up production costs. [26], [27]

1.3 Aqueous Li-ion Batteries (ALIBs)

Aqueous Li-ion batteries (ALIBs) on paper could solve these issues as the manufacturing process could be cheaper due to removing the need for a moisture free environment. Meanwhile, water is non-flammable and non-toxic. However, ALIBs are limited by the narrow ESW of water. While pure water has an ESW of 1.23 V, this can be kinetically expanded to ~2 V using saturated salt solutions and the sluggish reactivity of water splitting at interfaces. [28] On the positive electrode side, materials commonly used in organic electrolytes, like LFP, LCO, LiMn₂O₄ (LMO) can be used as the OER limit is beyond the redox potentials of these materials. The negative electrode is where we encounter the primary issue as the HER limit ($E_{HER} = -0.06 \text{ pH V vs ESH}$, 2.62 V vs Li⁺/Li at pH = 7) is drastically higher than organic solvents used in LIBs. The absence of SEI formation in organic-based electrolytes hinders the use of low-potential

negative electrodes such as graphite or metallic lithium, creating what is known as the “cathodic challenge” (Fig. 1.5). The materials that have been used are vanadium-based (LiV_3O_8 , VO_2 , V_2O_5) or NASICON polyanionic compounds $\text{LiTi}_2(\text{PO}_4)_3$ (LTP). [29] In 1994, Dahn and co-workers reported the first ALIB, utilizing VO_2 and LiMn_2O_4 with a saturated LiNO_3 electrolyte. This configuration resulted in an average cell voltage of 1.5 V and a projected energy density of 75 Wh/kg. [30] While this demonstration showed promise, it was never able to escape the confines of the laboratory. To progress aqueous electrolytes from an energy density perspective, the narrow stability window has to be extended to allow for the use of more powerful materials. Inspiration can be taken from the work carried out by Dahn, where saturated electrolytes were utilised. At higher salt concentrations, the kinetics of water splitting can be reduced, the dissolution of materials can be mitigated, and diverse physicochemical properties can be achieved. Further influence must be drawn from the critical developments of non-aqueous batteries, particularly the discovery of the SEI. Finding ways to form an effective SEI could be the key to utilising more energy-dense materials.

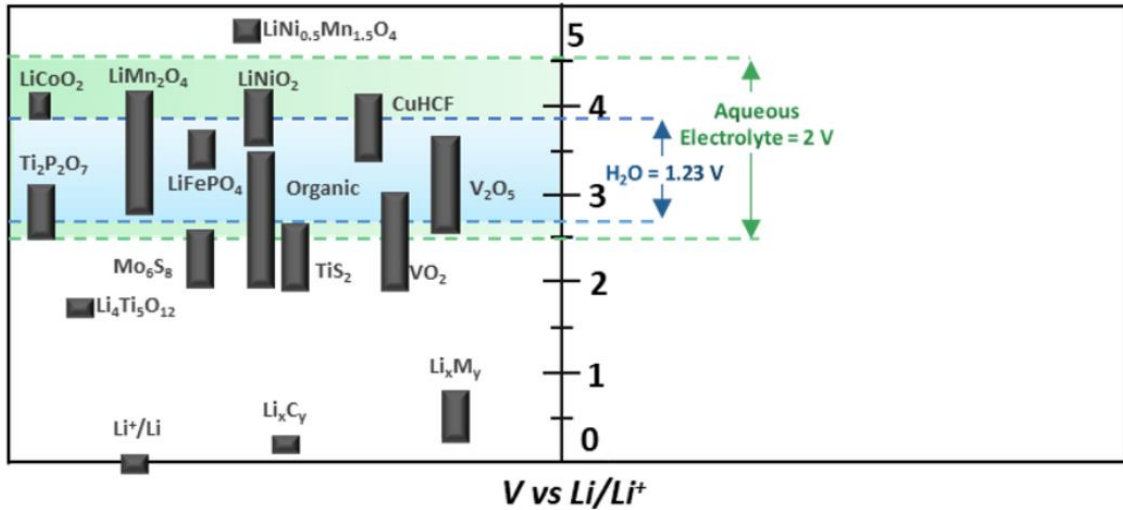


Fig. 1.5 - Intercalation potential of typically used electrodes in LIBs. Adapted from [31].

1.4 Super-Concentrated Electrolytes

1.4.1 The Dawn of Super-concentration

The initial logic of 1 mol.L^{-1} as the standard for battery electrolytes stems from the notion that peak ionic conductivity is typically achieved at this concentration. This peak results from a balance between two key factors influencing transport properties: (1) the number of ionic carriers (n), which depends on the salt's dissolution and dissociation, and (2) ionic mobility (m), which is affected by the electrolyte's viscosity (h) (Fig. 1.6). This drop-in conductivity discouraged the exploration of pushing too high in concentrations. [32] Nevertheless, work outside of aqueous electrolytes, highlighted the potential benefits of pushing in concentration. Watanabe and co-workers showcased the interesting characteristics of highly concentrated glyme-based electrolytes such as the improved thermal and electrochemical stability of the electrolytes compared to standard ones. This is attributed to the high ionic populations which are impossible at “conventional” concentrations. Most of the effects here were attributed to the solvent, whereby the glyme molecules strongly chelated the Li^+ , creating a unique solvation. [32], [33]

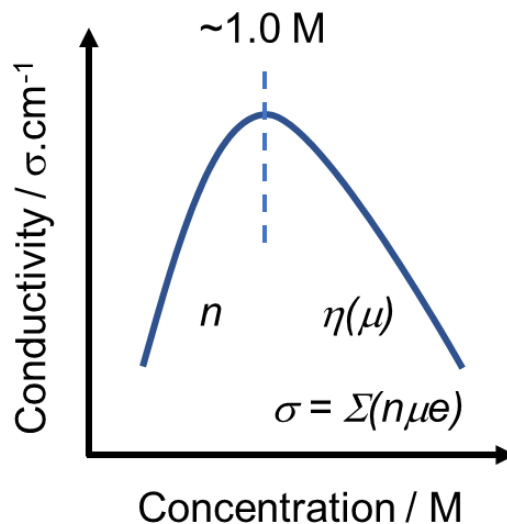


Fig. 1.6 - The interplay between ionic carrier number (n), ionic mobility (m), and solution viscosity (h) which creates a peak in ionic conductivity, typically observed around 1.0 M for most non-aqueous electrolytes. Adapted from [32].

1.4.2 “Solvent-in-salt”

It was discovered that another way to achieve these effects could be through using salts that have high solubility and dissociation in polar solvents such as the imide-based salts (Lithium bis(trifluoromethanesulfonyl)imide (LiTFSI), or its homologs: lithium bis(pentafluoroethanesulfonyl)imide (LiBETI) and lithium bis(fluorosulfonyl)imide (LiFSI). [34], [35] These salts all demonstrated high solubility in non-aqueous solvents, reaching up-to 7 mol.L^{-1} achieving a so-called “solvent-in-salt” regime, where the salt outweighs the solvent molecules in both mass and volume. At these super-concentrations, the ionic association switches from solvent-separated ion pairs (SSIP) in diluted electrolytes to the formation of contact-ion pairs (CIP) or ionic aggregates (AGG) in super-concentrated regimes (Fig. 1.7). This results in new characteristics at both the molecular and long-range scales, impacting various properties, including transport, thermal, mechanical, electrochemical, interfacial, and inter-phasic characteristics. [32], [36], [37], [38]

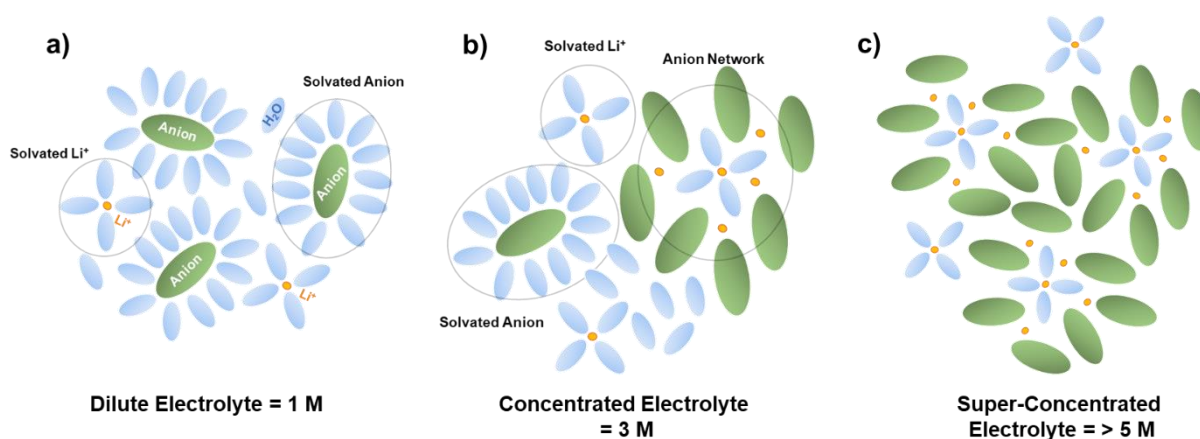


Fig. 1.7 - Scheme of solvation structure of the electrolyte in, a) diluted electrolyte, b) concentrated electrolyte and c) super-concentrated electrolyte.

1.4.3 Water-in-Salt Electrolytes (WISE)

Suo and co-workers would take these principles and apply them to aqueous electrolytes, with the so-called “water-in-salt” electrolyte (WISE). They demonstrated that LiTFSI could achieve concentrations above 5 mol.L^{-1} in water, equivalent to 21 mol.kg^{-1} , resulting in many unique properties that fundamentally transformed the paradigm of ALIBs. Indeed, when moving to these high concentrations they discovered that TFSI⁻ was directly coordinated with Li^+ , with AGG formations occurring. [39] This

can be evidenced by the Raman data seen in Fig. 1.8a where the intensities associated with the H-bond network (HBN) of water, indicated by OH stretching at 3255.5 cm^{-1} and 3403 cm^{-1} , decrease as the concentration increases from 0 to 5 M (0 to 20 m). [40] This reduction coincides with the emergence of a distinct peak at 3565 cm^{-1} , indicating disruption of the HBN of water and the reduction of free-water (Fig. 1.8a). Additionally, analysis using ^7Li and ^{19}F nuclear magnetic resonance spectroscopy (NMR) as seen in Fig. 1.8b & 1.8c, reveals changes in ionic structure. The decrease in ^7Li chemical shift with increasing salt concentration suggests an increase in electronic density around Li^+ , indicative of greater interactions between Li^+ and anions. Similarly, a shift in the ^{19}F signal suggests increased interactions between anions themselves. [39], [41] The result is a drastic change to the solvation structure compared to dilute concentrations, whereby the typical $[\text{Li}(\text{H}_2\text{O})_4]^+$ solvation sheath at dilute concentrations becomes $[\text{Li}(\text{H}_2\text{O})_{2.5}]^+[\text{TFSI}]^-$ (Fig. 1.8d). [39]

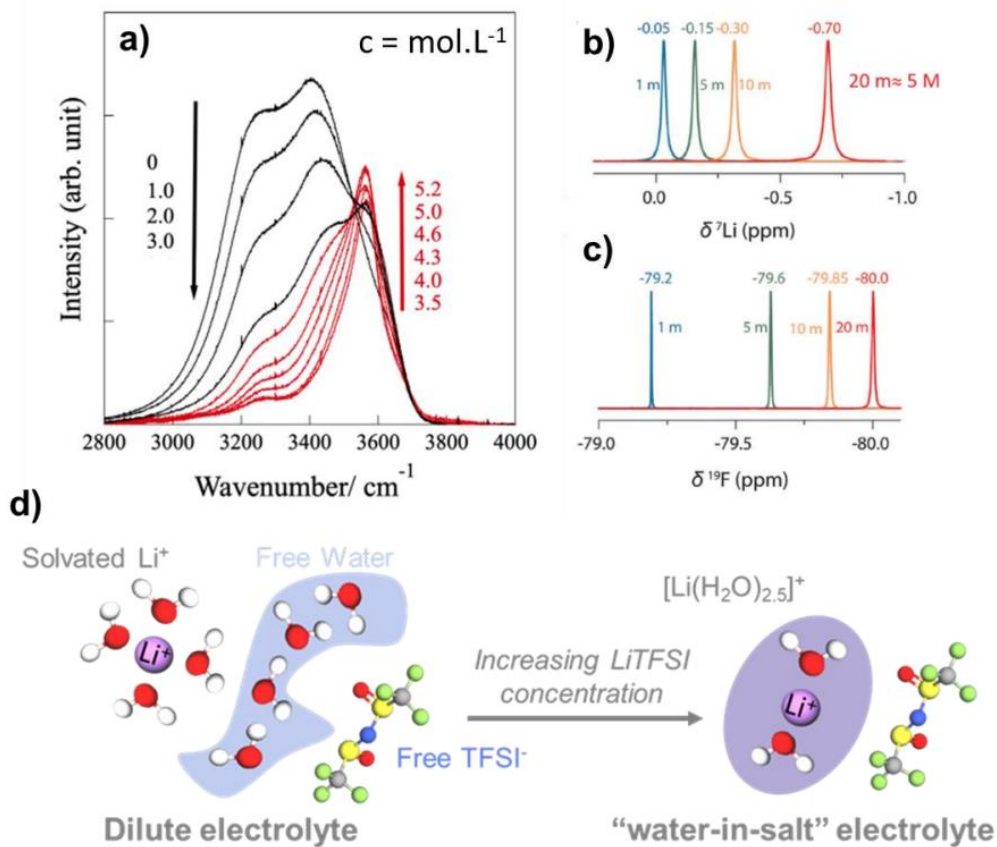


Fig. 1.8 - a) Raman spectra ($2800\text{-}4000\text{ cm}^{-1}$) for LiTFSI aqueous solutions, showing O-H stretching vibrations. Adapted from [40]. Normalised NMR spectra displaying water chemical shifts in LiTFSI solutions at various molalities (1 m blue, 5 m green, 10 m orange, 20 m red), b) ^7Li , c) ^{19}F . Adapted from [41] and d) change in solvation structure when moving from dilute to WISE.

The presence of TFSI within the solvation sheath allows for the decomposition of the anion which forms an SEI composed of LiF and CF_x . The composition and mechanism of any SEI has been contentious and this is no different with WISE. Our group has previously proposed a HER mediated mechanism whereby the generation of gaseous H_2 and the subsequent release of OH^- following Eq. 1.2 from Section 1.2, reacts with Li^+ to form LiOH depositing on the surface. The LiOH and/or the OH^- ions react with the electrophilic sulphur of the TFSI $^-$ via a nucleophilic attack producing F^- that precipitate with Li^+ due to the common ion effect. Consequently, a fluorinated SEI is formed (Fig. 1.9). [41] Recent research has proposed that while the reduction of TFSI $^-$ anion does contribute to the SEI, the precipitation of the LiTFSI salt itself is another primary contributor to the SEI. Work from Fontaine et al. showcased that HER consumes water, increasing the salt concentration at the interface beyond the saturation limit and triggering the precipitation of LiTFSI on the surface. [42] A key takeaway from the work on the SEI formation is that HER is what triggers to the formation of the SEI, not the reduction of TFSI directly. Once the SEI is formed, this is what mitigates the HER and hence extends the ESW.

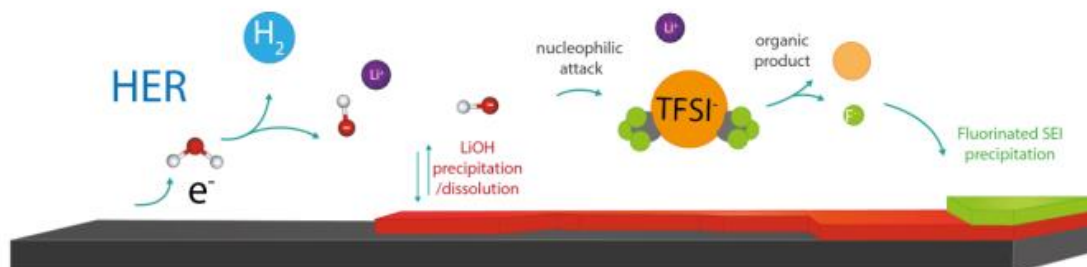


Fig. 1.9 - Formation of the SEI via HER mediated mechanism in 20 m LiTFSI (WiSE). Adapted from [42].

The formation of this SEI, followed by the creation of a hydrophobic double layer at the positive electrode that mitigates the oxygen evolution reaction (OER), extended the ESW to ~ 3 V (Fig. 1.10a-c), allowing for the utilisation of electrode materials previously deemed inaccessible (Fig. 1.10d). [43] As a proof-of-concept a 2.3 V ALIBs using Mo_6S_8 || LiMn_2O_4 was developed to showcase the potential of a WISE. This work sparked significant interest in super-concentrated aqueous electrolytes. In 2016, Yamada et al. proposed the water-in-bisalt electrolyte (WiBS), which increased the salt concentration to 28 m by adding 7 m LiBETI to 21 m LiTFSI, thereby raising the

operating potential to 3.1 V, enabling a $\text{Li}_4\text{Ti}_5\text{O}_{12} \parallel \text{Li}_{0.5}\text{Ni}_{0.5}\text{Mn}_{1.5}\text{O}_4$ battery. [44] Since, the solubility limits have been extended further, up to 63 m with a 42 m LiTFSI : 21 m $\text{Me}_3\text{EtN.TFSI}$ mixture. [45]

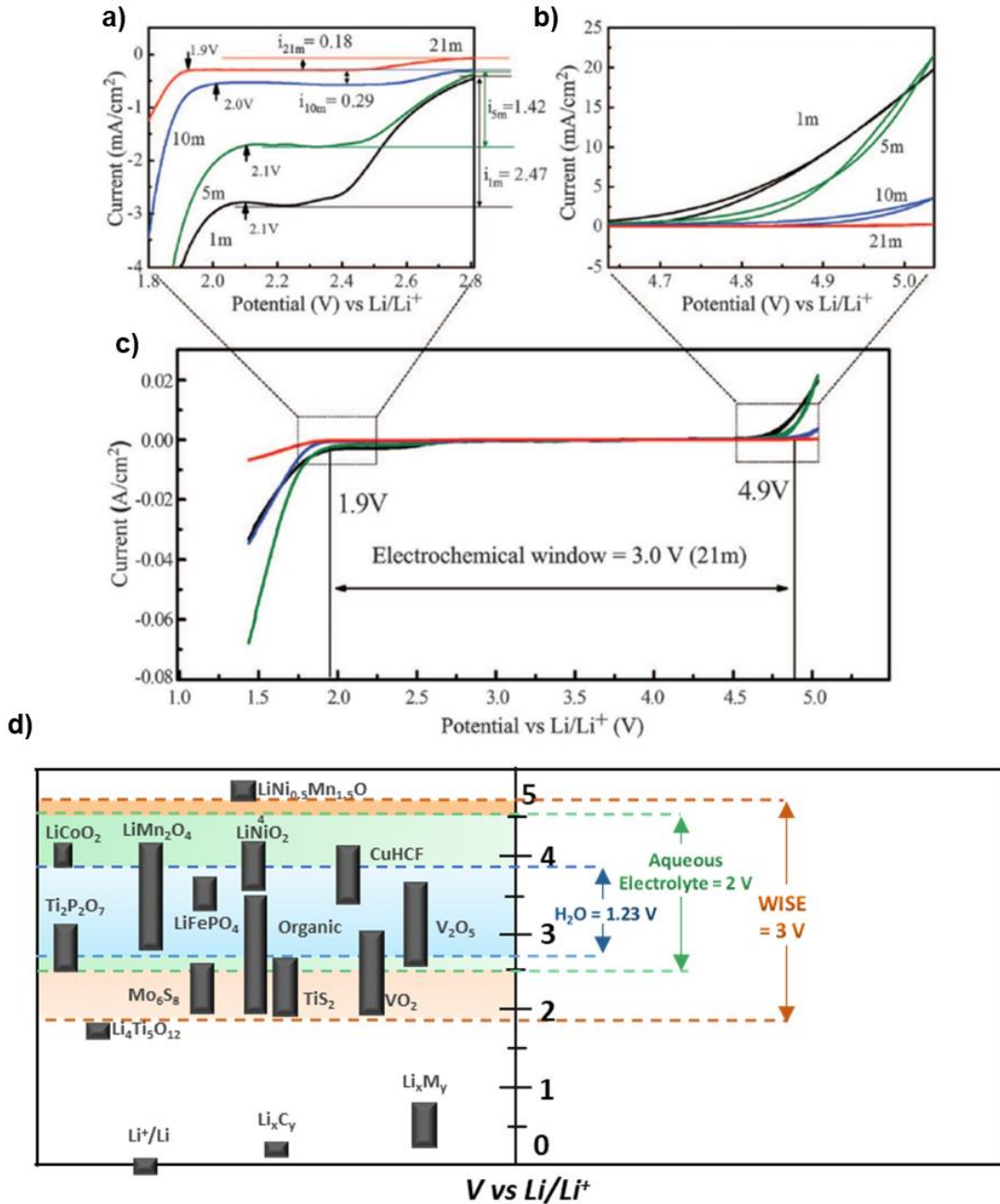


Fig. 1.10 - Electrochemical stability window (ESW) reported by Suo et al. in 2015 for various electrolytes ranging from 1 m to 21 m LiTFSI on stainless steel, a) Cathodic stability at the negative electrode, b) Anodic stability at the positive electrode, c) Overall ESW, adapted from [46] and d) Intercalation potential of typically used electrodes in LIB including WISE. Adapted from [31].

1.4.4 The Problem with WISE

While WISE are game changing for aqueous batteries, they have issues. Previous work from our group indicated that the SEI is in-fact unstable. Cyclic Voltammetry (CV) measurements on glassy carbon showcase this loss in passivation, where an initial large peak, attributed to the HER and thus SEI formation, gradually decreases and disappears after 15 cycles, in-line with the formation of a passivating layer i.e. SEI (Fig. 1.11a). However, after a 1-hour rest, this passivation is lost as the peak intensity returns to its initial level. [11] This loss of passivation can also be seen with $\text{Mo}_6\text{S}_8 \parallel \text{LFP}$ full cells as self-discharge experiments show a significant capacity drop after a 20-hour resting period (Fig. 1.11b). Furthermore, during standard galvanostatic cycling, H_2 gas concentration increases specifically during Li^+ insertion into Mo_6S_8 , potentials at which HER is likely to occur (Fig. 1.11c). All of these issues point towards the loss of passivation through SEI dissolution (Fig. 1.11d). These issues are intensified at elevated temperatures, hindering the practicality of WISE (21 m LiTFSI). In fact, when considering the aforementioned frailties, conventional WiSE-ALIBs (i.e. 21 m LiTFSI or 21 m LiTFSI + 7 m LiBETI) struggle to compete with current commercial battery technology and are unable to outperform Ni-MH batteries with regards to rate capability, self-discharge and range of operating conditions. [11]

Besides the inherent challenges for real-world applications, there are sustainability concerns associated with using such concentrated salt solutions. For instance, in terms of molarity, WISE (21 m or 5 M LiTFSI) requires five times more lithium compared to a conventional $1 \text{ mol}\cdot\text{L}^{-1}$ organic electrolyte. Additionally, the widespread use of fluorinated salts like LiTFSI in most WISEs raises environmental and safety issues due to their toxicity and corrosiveness, contradicting the initial eco-friendly premise of using an aqueous electrolyte. Furthermore, from a performance perspective, despite achieving low water content and thus altering the solvation structure of the electrolyte, water reactivity remains prevalent. To address these issues, electrolyte engineering for WISE has focused on: 1) reducing water reactivity through methods such as electrolyte crowding, solvation adaptation, and the formation of a stable SEI, and 2) reducing salt concentration.

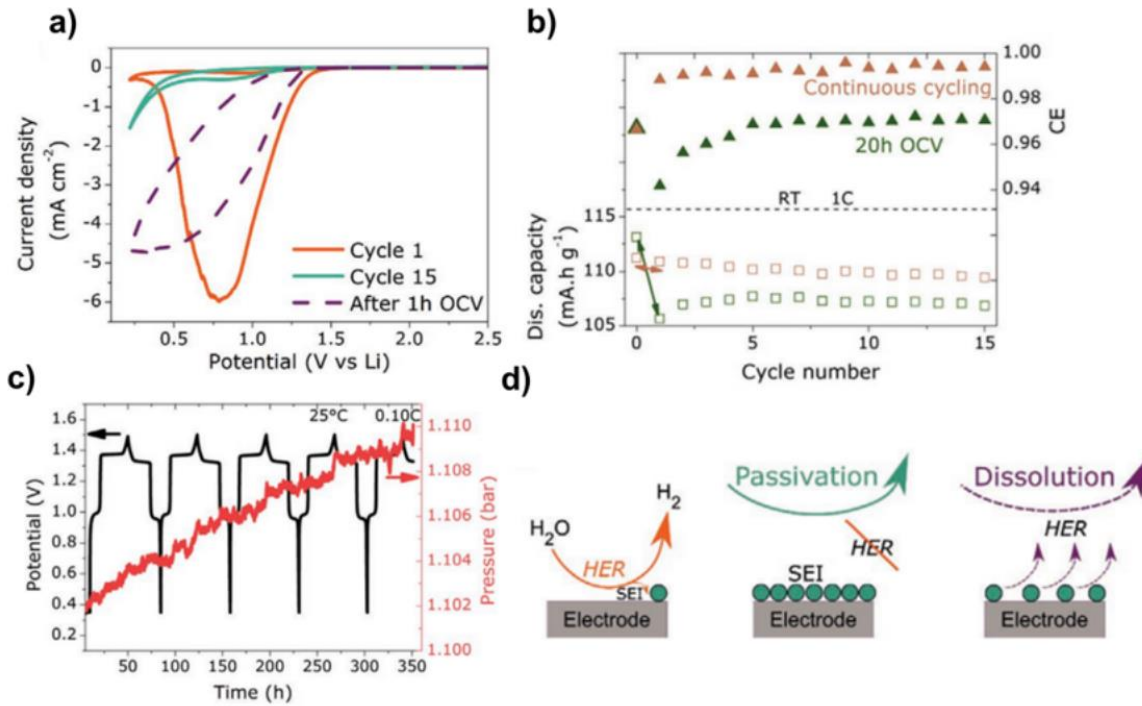


Fig. 1.11 – a) Cyclic voltammetry at 50 mV s^{-1} was performed in a three-electrode cell with a glassy carbon working electrode, Pt wire counter electrode, and silver wire pseudo-reference. The 1st (orange), 15th (green), and post 1-hour OCV (purple), b) Coulombic efficiency and discharge capacity as function of cycle number for a $\text{Mo}_6\text{S}_8/\text{LFP}$ battery using 20 m LiTFSI undergoing 20hr OCV procedure (green) and continuous cycling (brown) at 1C, c) Gas monitoring of a $\text{Mo}_6\text{S}_8/\text{LFP}$ battery using 20 m LiTFSI with potential and pressure as a function of time at 0.10C, monitored using a pressure cell and d) Schematic of SEI formation and its partial dissolution after a 1-hour resting period. Adapted from [11].

1.5 Electrolyte Engineering for WISE

1.5.1 “Molecular Crowding”

Molecular crowding is a common occurrence within living cells, where the characteristics of solution molecules significantly change when macromolecules (such as proteins, complex sugars, and polysaccharides) or small hydrophilic molecules (including metabolites and osmolytes) exceed concentrations of $80 \text{ mg}\cdot\text{ml}^{-1}$. [47] This crowded environment results in a reduction of water solvent activity due to alterations in the HBN of water. [48] Regarding battery electrolytes, a crowding agent can be added to reduce the water content via a water-miscible compound that alters the HBN of water. Lu and co-workers used poly(ethylene) glycol (PEG) as a crowding agent to reduce water activity as showcased via Fourier-transform infrared spectroscopy (FT-IR) (Fig. 1.12a & 1.12b), thereby extending the ESW to 3.2 V (Fig. 1.12c). The electrolyte, 2m LiTFSI-94% PEG-4% H₂O, is able to suppress HER to beyond 1.55 V, as demonstrated via Online Electrochemical Mass Spectrometry (OEMS) data, allowing for the use of LTO as an anode material with stable cycling up to 300 cycles (Fig. 1.12d-e). [31] There are other examples of this technique with other compounds such as 1,5-pentanediol and polyethylene glycol dimethyl ether, both of which extend the ESW further than conventional WISE. [49], [50]

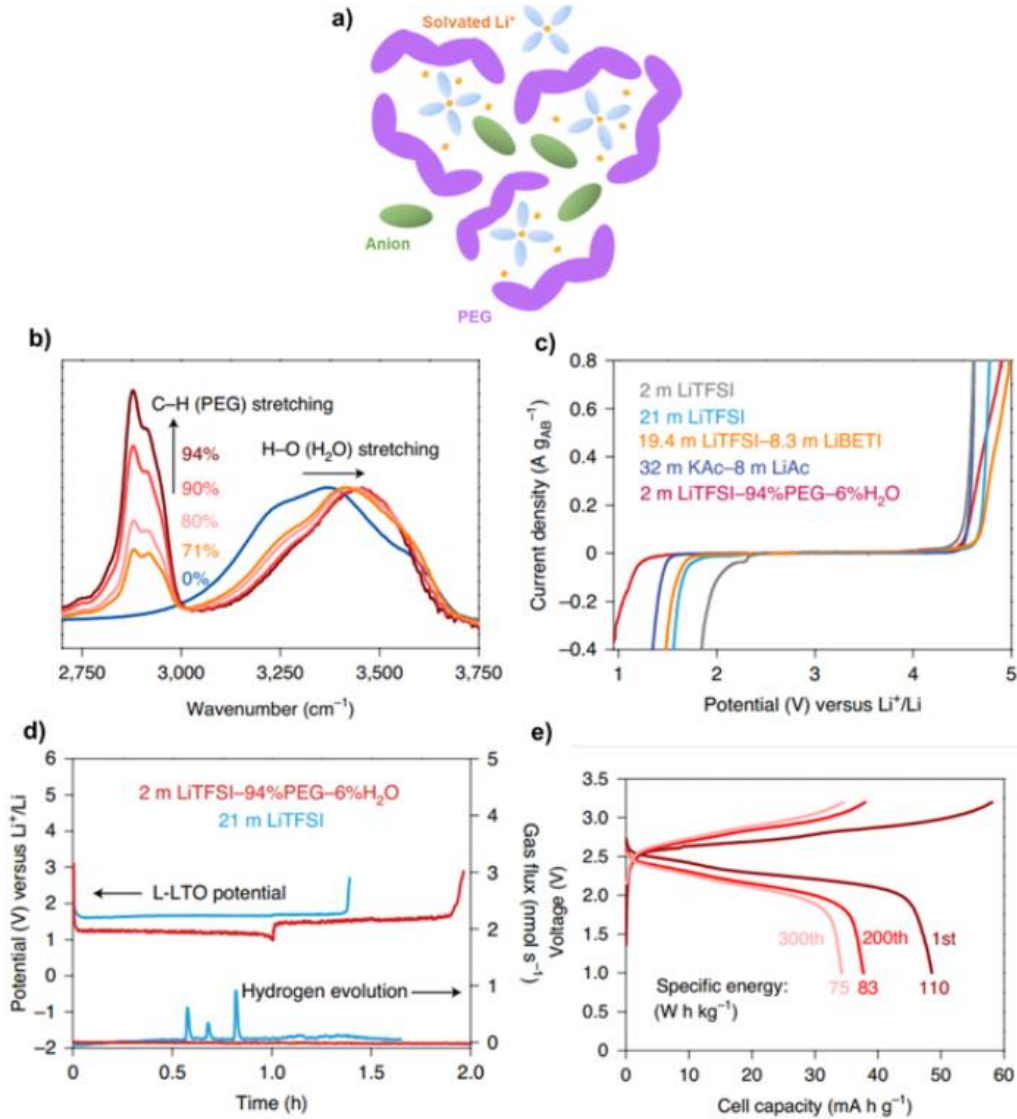


Fig. 1.12 - a) Molecular crowding effect within battery electrolytes, b) IR spectra (region 2750 – 3750) with 2 m LiTFSI with increasing wt% of PEG, c) ESW of 2m LiTFSI-94%PEG-4% H_2O , d) OEMS of 2m LiTFSI-94%PEG-4% H_2O vs 21 m LiTFSI with potential hold and H_2 gas production and e) cycling curves for LTO || LMO with 2m LiTFSI-94%PEG-4% H_2O . Adapted from [31].

1.5.2 Solvation Structure Adaptation

As mentioned in the previous section on WISE, the main chemistry at play to extend the ESW was the adaptation to the solvation structure to include TFSI⁻, reducing the number of water molecules. However, the solvation still contains water molecules which no doubt contributes to the continuous HER during cycling. Hence, strategies were developed where co-solvents are used which can preferentially solvate Li⁺ over water which would reduce the reactivity of water at the electrode interface as well as potentially contribute to the formation of an SEI. Sulfolane is confirmed to have displaced water from the solvation shell through ⁷Li NMR which showcases a blueshift in the Li peak (Fig. 1.13a & 1.13b). [51] The presence of sulfolane within the solvation allows for the decomposition of the molecule to further enhance the SEI with SO₃⁻-based compounds. The use of sulfolane also builds on the aforementioned “molecular crowding” as it is a hydrogen-bond acceptor, which breaks the HBN of water hence reducing water reactivity. Their 3.6 m LiTFSI/sulfolane-H₂O (8:8) electrolyte is able to extend the ESW to 3.4 V again, allowing for the use of LTO as an anode with LiNi_{0.5}Mn_{1.5}O₄ (LNMO) as the cathode (Fig. 1.13c & 1.13d). They demonstrate that their electrolyte has no H₂ production during cycling, resulting in reduced self-discharge compared to WISE. [51] Unfortunately, sulfolane is a rather “unfriendly” solvent with a high toxicity which somewhat defeats the purpose and principles of an aqueous electrolyte. [52]

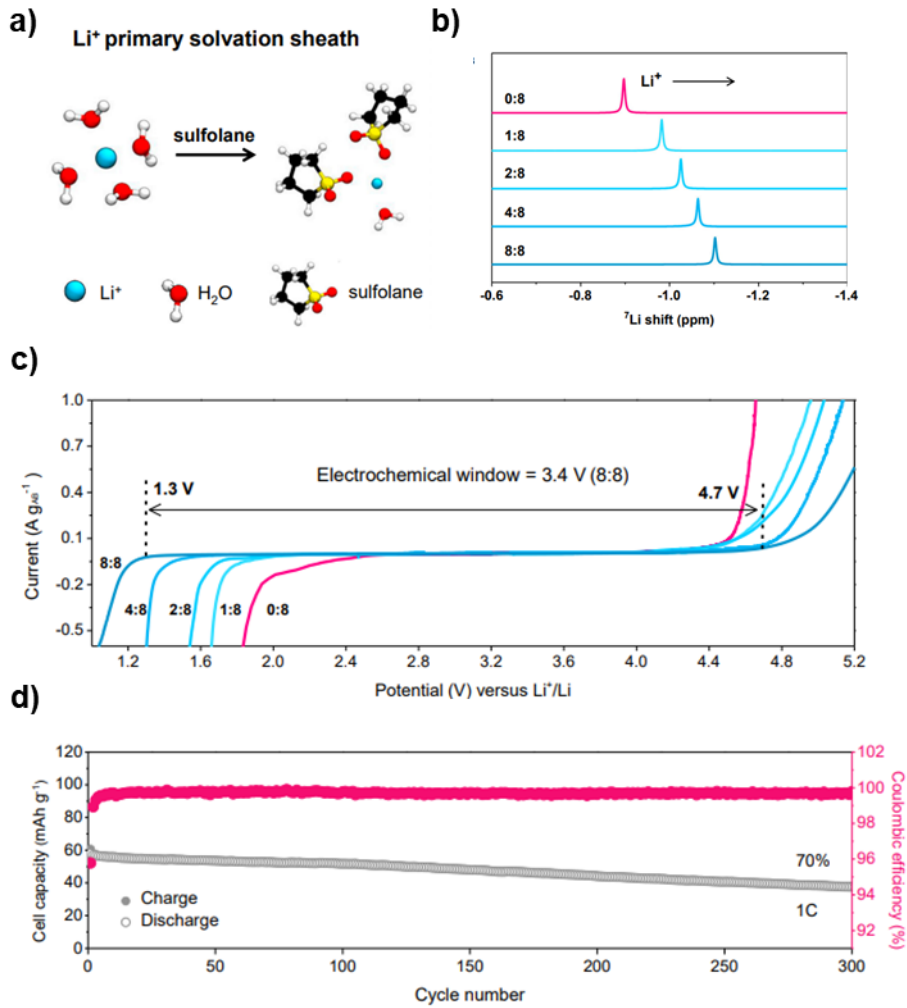


Fig. 1.13 - a) Adapted solvation obtained with sulfolane. b) ⁷Li NMR of 3.6 m of LiTFSI with increasing sulfolane content (where 8:8 is equal molar ratio of sulfolane to water) c) 3.6 m of LiTFSI with increasing sulfolane content (where 8:8 is equal molar ratio of sulfolane to water) and d) long term cycling of 3.6 m of LiTFSI 8:8 electrolyte using LTO || LNMO at 1C. Adapted from [51].

1.5.3 Chaotropicity

Wang and co-workers, would propose urea, which is more sustainable option compared to sulfolane, that can form strong interactions with Li^+ and water to alter the solvation sheath and bulk properties of the electrolyte. [53], [54] They probe different concentrations with 4.1, 4.5 and 5.1 m 4.5 m LiTFSI-urea-KOH- H_2O . The drastic change to the water structuring imposed by urea can be observed via infrared spectroscopy, where the typically broad band of water at $2,900\text{--}3,700\text{ cm}^{-1}$ is not present, only a small band at 3600 cm^{-1} . Rather the strong NH_2 stretching vibrations corresponding to urea molecule seen at $3,348$ and $3,445\text{ cm}^{-1}$ dominate the spectra with a slight shift compared to pure urea, a clear indicator to the strong hydrogen bonding between urea and water (Fig. 1.14a). This is further confirmed via ^{17}O NMR where the bulk H_2O peak undergoes a downfield shift upon the increasing addition of urea (Fig. 1.14b). Their best performing composition is 4.5 m LiTFSI-urea-KOH- H_2O , which manages to extend the ESW to 3.3 V, which is due in part to the drastic change to the HBN, but also the change in the solvation which becomes urea dominated: $\text{Li}(\text{CO}(\text{NH}_2)_2)_{2.5}(\text{H}_2\text{O})_{0.7}(\text{TFSI})_{0.8}$ (Fig. 1.14c & 1.14d). This solvation sheath enables urea to form a polymerisation product on the negative electrode, providing a passivating organic layer in addition to the inorganic SEI. The formation of the latter is catalysed by the use of KOH, which provides the OH^- required to react with TFSI $^-$ to form the LiF-based SEI. The strategy enables the use of an LTO || LMO cell with a voltage of 2.5 V, exhibiting 99.9% Coulombic efficiency in both coin and pouch cell formats, as well as a lower self-discharge rate compared to WISE (Fig. 1.14e). [54]

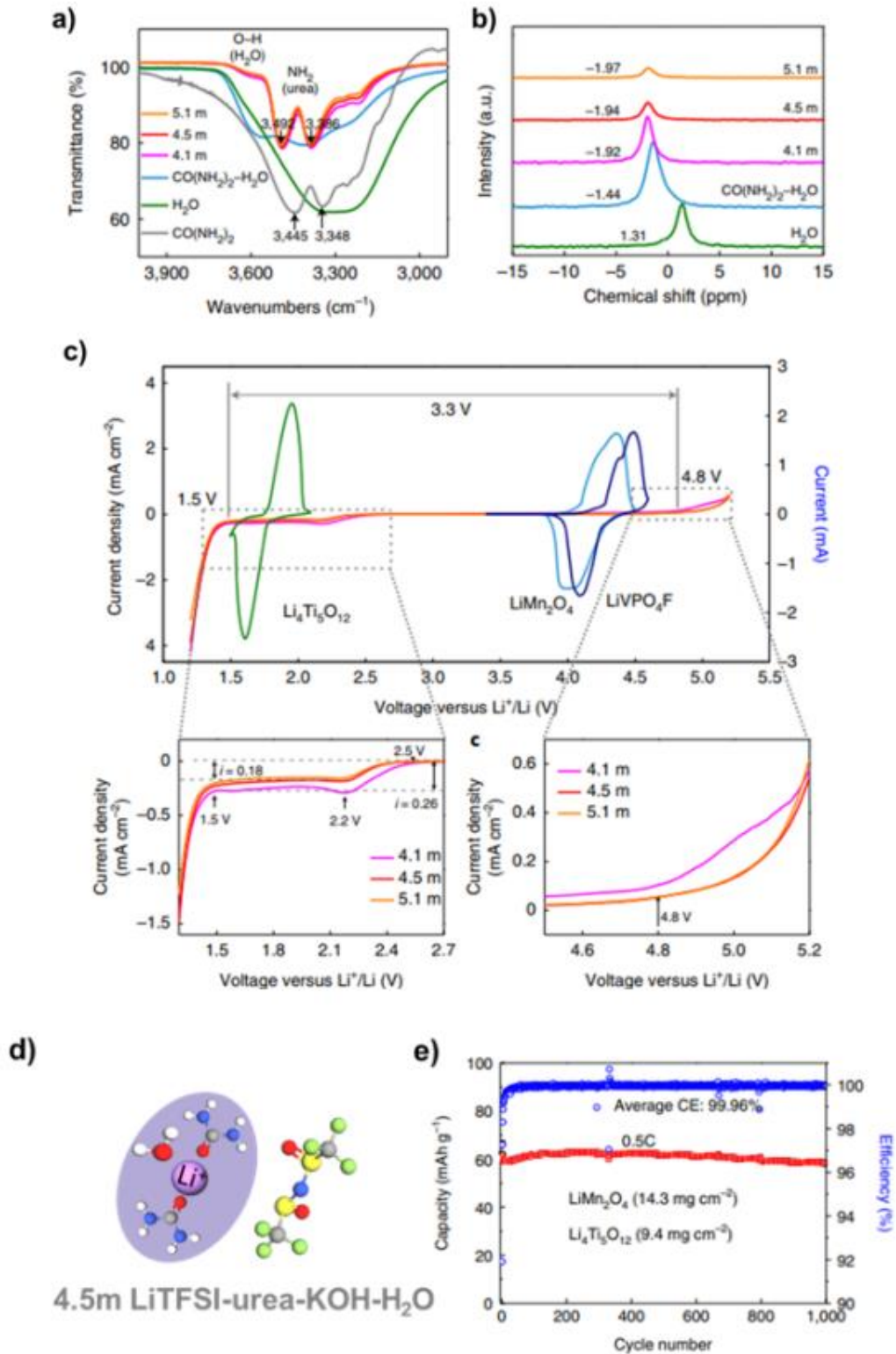


Fig. 1.14 – a) FTIR spectra of the $\text{CO}(\text{NH}_2)_2$ i.e. Urea, H_2O , $\text{CO}(\text{NH}_2)_2\text{-H}_2\text{O}$, 4.1 m, 4.5 m and 5.1 m $\text{LiTFSI-urea-KOH-H}_2\text{O}$ electrolytes, b) The chemical shift of ^{17}O NMR in water, urea-water and 4.1 m, 4.5 m and 5.1 m $\text{LiTFSI-urea-KOH-H}_2\text{O}$ electrolytes, c) ESW of 4.5 m electrolyte with LTO and LMO redox potentials and two inserts which show the reductive and oxidative limits, d) the solvation sheath of 4.5 m $\text{LiTFSI-urea-KOH-H}_2\text{O}$ electrolyte and e) long term cycling of LTO || LMO. Adapted from [54].

Compounds like urea, which are able to disrupt the HBN of water are denoted as a “chaotropic” or a “hydrotropic” agent. [54], [55], [56] These terms are usually used interchangeably within our field; however, the principles have its origin in macromolecular science. Indeed, ions can significantly influence the behaviour of aqueous solutions, a fact recognized by Franz Hofmeister. He studied salts by determining the minimum concentration required to precipitate proteins from the solution. Certain ions enhance the solubility of solutes and proteins (“salting-in”), while others reduce it (“salting-out”). The Hofmeister series organises these ions from the most effective at salting out on the left to the most effective at salting in on the right (Fig. 1.15). [57] Building on this work, ions were later grouped into kosmotropic structure makers, and chaotropic structure breakers. Kosmotropes organise the HBN of water, while chaotropes disorganise the HBN of water. Kosmotropes, with their high charge density, are more hydrated than chaotropes, leading to protein salting-out and a stronger hydrogen bonding network due to ion pairing. [58], [59], [60] Regarding battery electrolytes, the focus has been on the effect of anions, where groups have shown the beneficial effects of using chaotropic anions in solution. One example is the use of ClO_4^- which has been used in a study to reduce water reactivity through breaking the HBN of water, while also shifting the freezing point to enable cycling at as low as -50°C . [61] Another example of this principle is CF_3SO_3^- which is able to drastically reduce the freezing point of water, enabling cycling at -30°C . [62] Playing on the kosmo/chaotropic effects of the cation with respect to the HBN of water has not been widely probed electrochemically. We do need to acknowledge that the Hofmeister series itself is empirical in nature, it depends on the experimental parameters and criteria used to define it and therefore the order can vary study to study, but nevertheless it can be a useful tool when probing the effect of different ions in aqueous electrolytes.

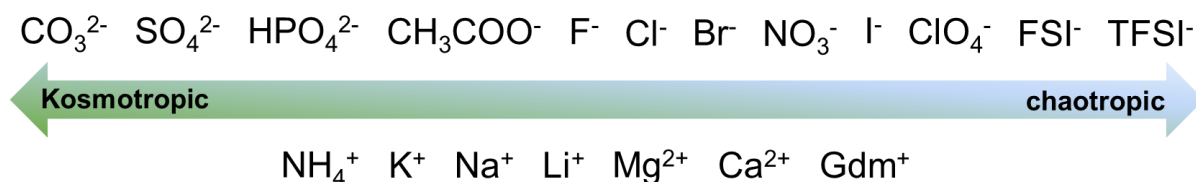


Fig. 1.15 – Hofmeister series of selected ions.

1.5.4 How Aqueous are These Electrolytes?

Interestingly, the aforementioned PEG, sulfolane and urea electrolytes are also diluents, reducing the salt concentration of the electrolyte. [31], [51], [54] Indeed, salt concentrations in these electrolytes are described as being < 5 m, drastically lower than the 21 m LiTFSI in WISE. However, an important question is how much water is actually left in these electrolytes? Fig. 1.16 showcases the mass of each component required to make 1 kg of different electrolytes: WISE [39], urea-based [54], PEG-based [31] and sulfolane-based [51]. The amount of Li salt is reduced by approximately 30%, 40%, and 50% for urea, sulfolane, and PEG-based electrolytes, respectively, compared to WISE. However, this reduction comes at the expense of water content, which is less than 5% for all three electrolytes. Based on this simple back-of-the-envelope calculation, the best way to address the issues faced by ALIBs seems to be maximizing the salt-to-water concentration. These calculations raise an important question: should we still classify these electrolytes as aqueous?

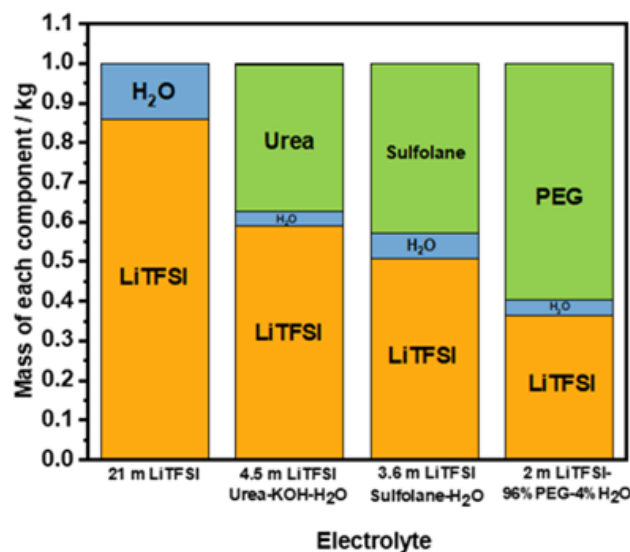


Fig. 1.16 - Mass of each component of a WISE and urea, sulfolane and PEG-based electrolytes.

Furthermore, even though these electrolytes have managed to boost the performance of ALIBs, their performance still pales in comparison to conventional organic electrolytes, which funnily enough, uses less salt. This doesn't mean we should abandon the work on super-concentration altogether; rather, we should be mindful of

the high amount of salt used. Therefore, while continuing to explore super-concentrated electrolytes, we should also consider the initial principles of ALIBs and aqueous batteries in general: safety and sustainability. Looking ahead, a primary objective for aqueous batteries should be to prioritise sustainability by seeking green, eco-friendly materials capable of operating in non-WISE conditions.

1.6 Redox-Active Organic Materials (ROMs) for ALIBs

Redox-active organic materials (ROMs) used in tandem with aqueous electrolytes is an attractive proposition from a sustainability standpoint. ROMs, composed mainly of elements abundant in the biosphere, offer the promise of renewability and environmental friendliness, matching the green ethos of aqueous electrolytes. ROMs can be broken down into three different categories, n-type, p-type and bipolar. [63] N-type ROMs undergo an initial reduction from its neutral-state which enables them to readily accept a metal counterion i.e. Li^+ , Na^+ , or Mg^{2+} and electrons, through a reversible enolization reaction with the carbonyl groups. [63], [64], [65] P-type ROMs undergo an initial oxidation from its neutral state to release an electron and thus accept the corresponding number of anions from the electrolyte. Finally, there are some materials which are able to exhibit both n/p-type characteristics and are known as bipolar ROMs (Fig. 1.17a & 1.17b). [66] The focus of this thesis will be on n-type ROMs as they function similarly to conventional cationic insertion materials. Indeed, n-type ROMs can function as either negative or positive electrodes and can be paired with any Li-containing electrode materials.

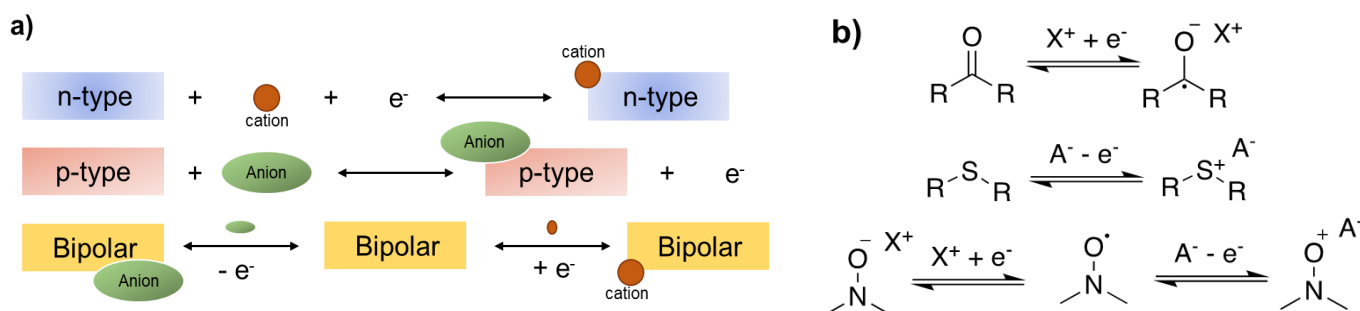


Fig. 1.17 – a) Schematic showcasing the reactions of the n-type (top), p-type (middle) and bipolar ROMs (bottom) and b) Chemical mechanism of ion uptake for n-type (top) p-type (middle) and bipolar (bottom).

Armand et al. pioneered the use of n-type ROMs, proposing quinones, with benzoquinone (BQ) being the simplest form. BQ exhibits a theoretical capacity of 496 mAh.g⁻¹ and a redox potential of approximately 2.8 V vs. Li/Li⁺ (Fig. 1.18). [67], [68] Building on this work, a wide range of carbonyl compounds, such as carboxylates, anhydrides, imides, and ketones, with redox potentials between 0.5 and 3 V vs. Li/Li⁺, have been proposed. [69] - [78] The redox potential and specific capacity of these compounds can be adjusted by incorporating electron-donating and electron-withdrawing groups or by fine-tuning the relative positions of the carbonyl groups. Given the inherent lack of anode materials functional within the ESW of aqueous electrolytes, attention has been focused on using these n-type ROMs as negative electrodes. [79]

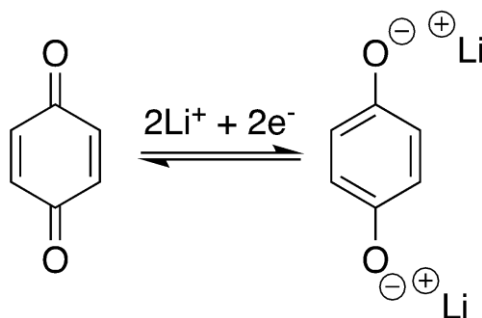


Fig. 1.18 – uptake of Li into BQ via decarboxylation mechanism.

1.6.1 Polyimides

Polyimides (PIs) have been a popular choice of ROMs for use as anode material owing to its redox potential (~2.5 V vs Li/Li⁺). PIs follow the general formula seen in Fig. 1.19, however, aromatic derivatives are the most common, due to the thermal and chemical stability.

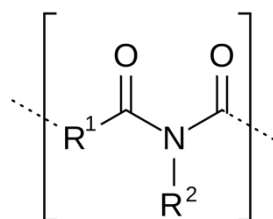


Fig. 1.19 – Chemical formula for polyimides.

A polyimide derived 1,4,5,8-naphthalenetetracarboxylic dianhydride (NTCDA) was proposed by Qin et al. paired with LiCoO_2 using a saturated 5 M LiNO_3 aqueous electrolyte. [80] Both materials lie within the ESW of the sat. $\text{LiNO}_3(\text{aq})$ electrolyte hence avoiding the HER and OER, allowing for the uptake of 2Li^+ on the NTCDA (Fig. 1.20a) and Li (de)insertion in the LCO (Fig. 1.20b). The full cell demonstrated stable cycling over 200 cycles and strong rate performance with a full cell capacity of $\sim 50 \text{ mAh}\cdot\text{g}^{-1}$ (Fig. 1.20c). [80]

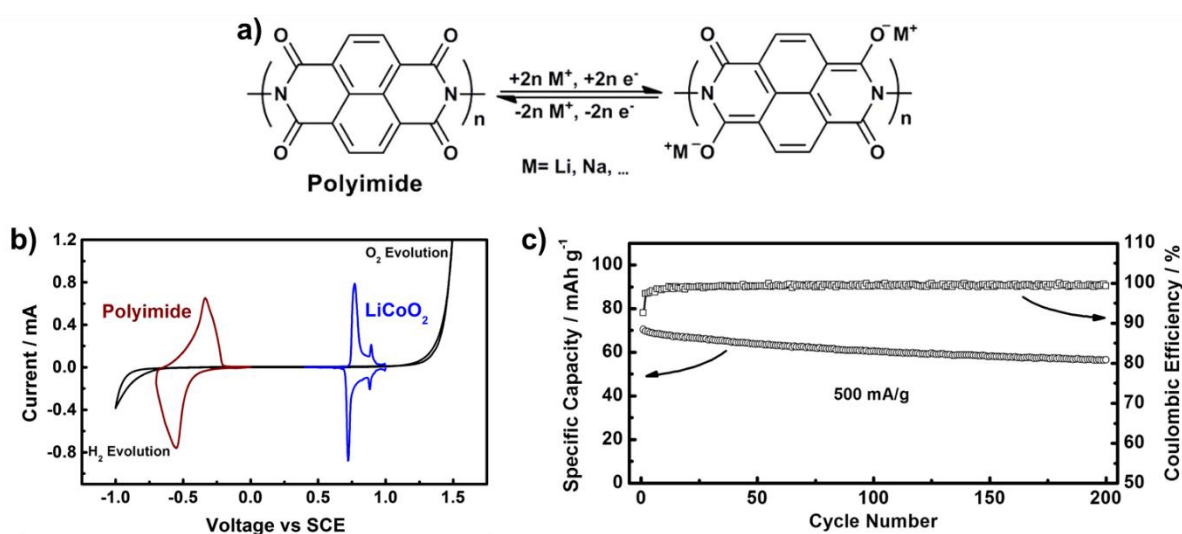


Fig. 1.20 – a) Chemical structure of NTCDA, b) ESW of sat. $\text{LiNO}_3(\text{aq})$ electrolyte with redox potentials of NTCDA and LCO and c) galvanostatic cycling of NTCDA || LCO full cell at $\sim 3\text{C}$. Adapted from [80].

Polyimide-derived NTCDA (PNTCDA) builds on previous work with NTCDA, demonstrating gradual performance improvements through the development of composites with carbon nanotubes and activated carbon, resulting in stable cycling with LMO for 1000 cycles at 2C with sat. $\text{LiNO}_3(\text{aq})$ (Fig 1.21). [72] However, PNTCDA and PIs in general have a number of different issues which have to be addressed. First, ROMs are typically insulating, requiring a significant amount of activated carbon—often around 30 wt% of the electrode—which reduces specific capacity. [70] - [73], [80] Additionally, most studies using ROMs report C-rates $>2\text{C}$. While this showcases strong rate performance, it also means that common issues like dissolution, which is prevalent for ROMs, may be obscured. However, as mentioned the tunability of carbonyl compounds is fairly high and adaptations to the organic structures can help to mitigate some of the issues.

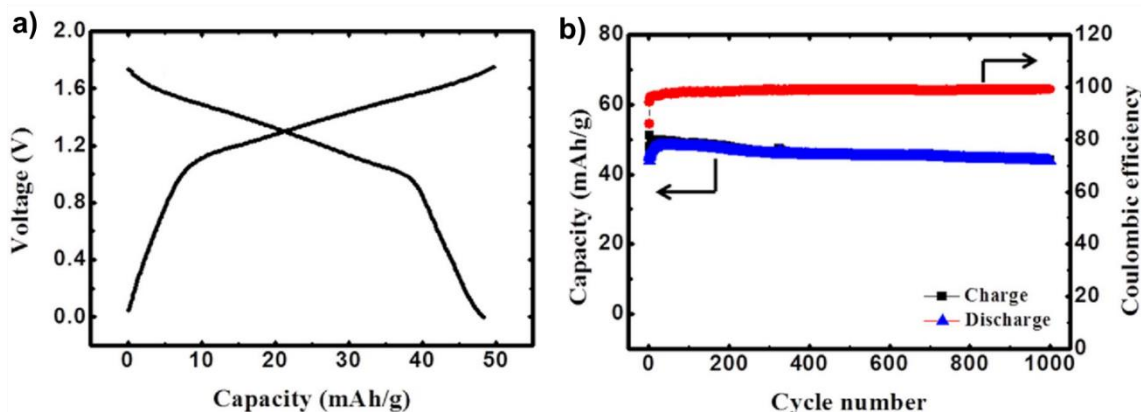


Fig. 1.21 – a) Cycling curve of PNTCDA || LMO full cell at cycle 1 and b) Galvanostatic cycling of PNTCDA || LMO full cell at 2C in sat. LiNO_{3(aq)}. Adapted from [72].

This brings us onto perylene-type molecules which display excellent charge transport properties and cycling stability with both non-aqueous and aqueous electrolytes. [81], [82] Perylene-3,4,9,10-tetracarboxylic acid diimide (PTCDI), a commercially available pigment, contains the same functional group as the polyimide-derived NTCDA, except with a larger conjugated system (Fig. 1.22a). Jiang *et al* demonstrated PTCDI to cycle well as a negative electrode for an aqueous K-ion battery (AKIB) (Fig. 1.22b) with Prussian blue $K_xFe_yMn_{1-y}[Fe(CN)_6]_w \cdot zH_2O$ as a positive electrode. They used a WISE, 22 mol/L (M) KCF₃SO₃ electrolyte, which minimised the dissolution of both active materials, to enable long term cycling albeit at a very high C-rate of 20 C (Fig. 1.22c). [83] Despite PTCDI's previous successful implementation in aqueous Na-ion, K-ion, and Mg-ion batteries (ASIBs, AKIBs, AMIBs, respectively) [84], [85], [86], its use in ALIBs remains unexplored. It would be curious to see if super concentration is required for PTCDI when used for ALIBs.

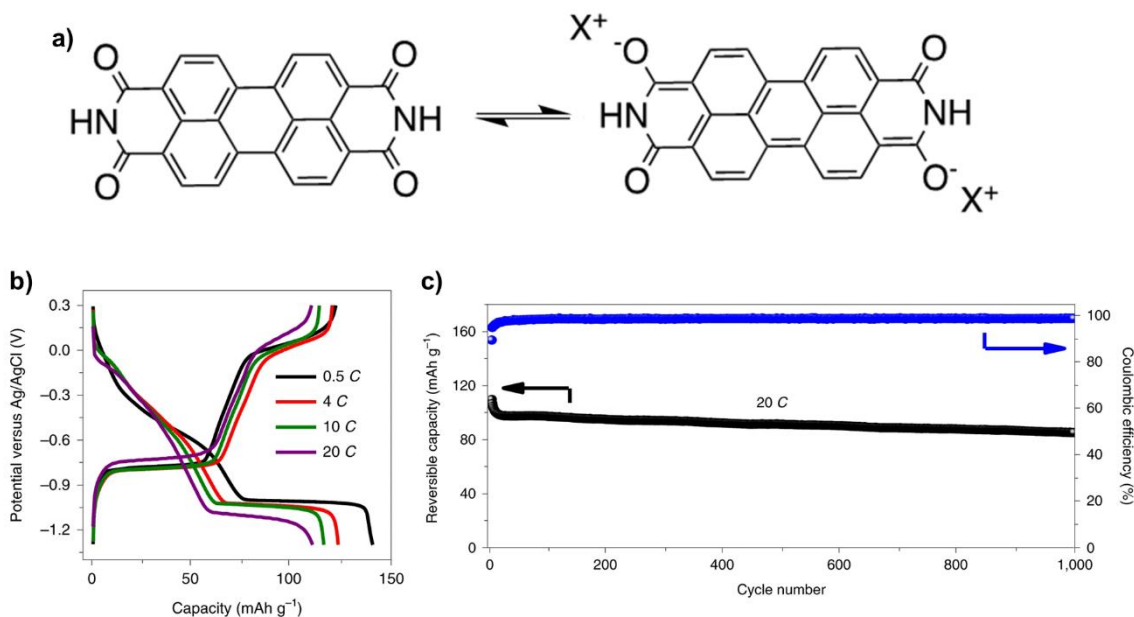


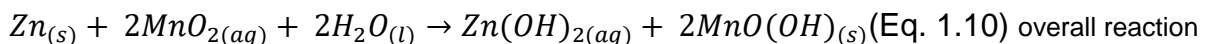
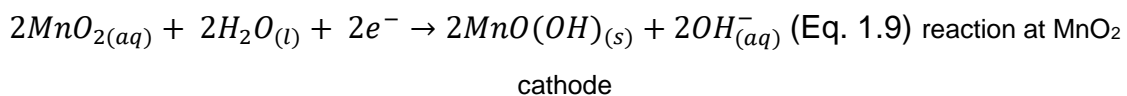
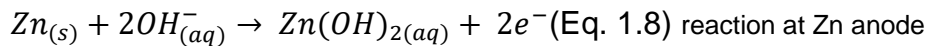
Fig. 1.22 – a) Chemical structure of PTCDI and cation uptake mechanism, b) cycling curve for PTCDI at of 0.5 C, 4 C, 10 C and 20 C in 22 M $\text{KCF}_3\text{SO}_3(\text{aq})$ electrolyte and c) Long-term cycling performance of the PTCDI anode at 20C from -1.3 to 0.3 V vs Ag/AgCl in 22 M $\text{KCF}_3\text{SO}_3(\text{aq})$ electrolyte. Adapted from [83].

The use of aqueous electrolytes alongside alternative, more sustainable chemistries, such as AKIBs, offers significant advantages in terms of cost and eco-friendliness. ROMs enable the utilisation of these chemistries due to their chemical flexibility, which allows for a wide range of redox potentials and the incorporation of different cations into the material. The combination of aqueous electrolytes with sustainable chemistries beyond lithium provides a promising pathway toward developing truly sustainable batteries, especially for large-scale stationary applications. Indeed, while lithium remains prominent in battery technology for its energy density, its sustainability is compromised by the element's low abundance and geographical mining constraints. [87], [88]

1.7 Aqueous Zn-Metal Batteries

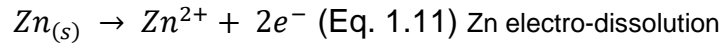
1.7.1 Mechanisms of Zn Electrodeposition and MnO₂

When considering other battery technologies beside aqueous li-ion, zinc-ion springs to mind. Zinc (Zn) exhibits approximately twice the abundance of lithium within the earth's crust and currently costs only a fraction, roughly 1/10, of the price. [89], [90] Additionally, the supply of zinc is more geographically diverse compared to lithium. [90] Zn-metal boasts impressive gravimetric (820 mAh.g⁻¹) and volumetric (5,855 mAh.cm⁻²) capacities, along with a high electrode potential of (-0.76 V vs. SHE) compared to other elements. [91] This high potential, combined with the water stability of Zn, enables the use of Zn metal anodes in aqueous environments, as demonstrated in the early work of Volta and then later Daniel with copper-zinc batteries. By 1868 Leclanche pioneered the first Zn || MnO₂ battery utilising a saline electrolyte. After nearly 100 years of development, this technology would result in the alkaline Zn || MnO₂ primary battery, simply known as an alkaline battery, used for decades to power toys, flashlights, home electronic devices and medical units to name only a few applications. The battery uses highly alkaline KOH-based electrolyte and the reaction mechanism follows Eq. 1.8 – 1.10. [7], [92]



Efforts were directed towards utilising Zn || MnO₂ as a secondary battery. However, challenges arose from irreversible transformations of manganese oxide (MnO_x) and the inherent instability of Zn in highly alkaline environments (9 M KOH). [92], [93] To solve this issue, Yamamoto in 1986 would propose a mildly acidic ZnSO₄-based electrolyte, unlocking the reversibility of the Zn || MnO₂ system. [94] Utilising acidic conditions can take advantage of a narrow pH range where Zn can successfully undergo a reversible electrodeposition process following Eq. 1.11. Theoretically speaking, the redox potential of Zn²⁺/Zn is below that of HER, suggesting that HER is completely unavoidable during Zn stripping/plating. However, HER has kinetic

limitations owing to the weak interaction between H^+ and the Zn metal surface, leading to a high overpotential for HER on Zn. [95], [96]



However, if the pH is too acidic, severe corrosion is encountered, whereas moving to higher pH results in passivation through the eventual formation of ZnO (Fig. 1.23a). Meanwhile, on the cathode side, MnO_2 has many different transformations as seen in (Fig. 1.23b).

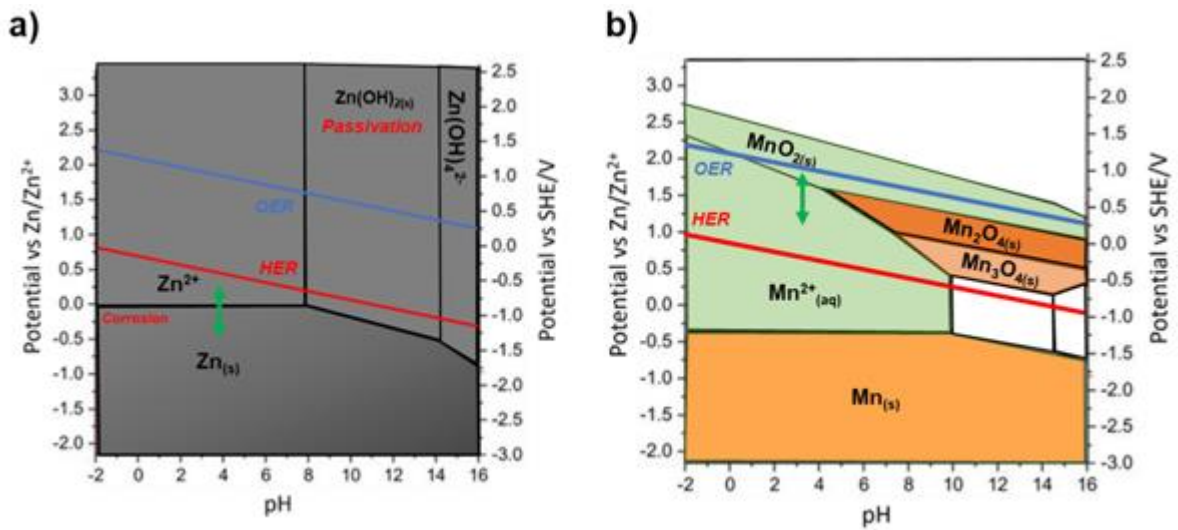
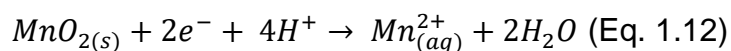
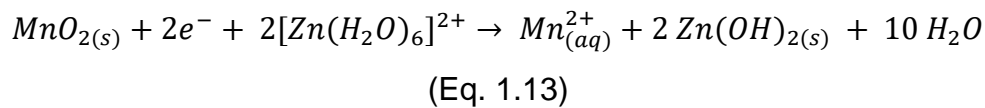


Fig. 1.23 – a) Pourbaix diagram of Zn at a concentration of 0.2 M Zn^{2+} with green arrow highlighting the mechanism at mildly acidic conditions and b) Pourbaix diagram of MnO_2 at a concentration of 0.2 M Mn^{2+} with green arrow highlighting the mechanism at mildly acidic conditions.

The exact mechanism taking place for MnO_2 within the secondary Zn || MnO_2 battery has been hotly studied and contested. The debate falls into four different reaction mechanisms: (1) Insertion reaction [97], [98], [99], similar to what has been described previously for Li-ion to form $ZnMnO_2$; (2) The reversible conversion of $MnOOH$ [100], [101], facilitated by protons; (3) The co-insertion of H^+ and Zn^{2+} into the MnO_2 [102], [103] and (4) reversible proton-coupled electrodis-solution-electrodeposition of MnO_2 . [104] - [107] Work previously carried out within the group points towards (4) as the mechanism of choice following Eq. 1.12. [93]



Irreversible MnO_2 electro-dissolution results in the loss of active material, leading to capacity fade and eventual cell death. pH and solvation structure, key concepts for aqueous electrolytes that have already been addressed, play a role in MnO_2 electro-dissolution. Indeed, the use of ZnSO_4 leads to the formation of $\text{Zn}_4\text{SO}_4(\text{OH})_6 \cdot 5\text{H}_2\text{O}$ (or ZHS), a crystalline insoluble product forms and passivates the surface of MnO_2 , somewhat acting as an SEI layer to prevent the electro-dissolution. The formation of ZHS starts with the deprotonation of solvated Zn^{2+} to form hydroxide species (Eq. 1.13) which has a low solubility within aqueous solutions, and in the presence of co-precipitated SO_4^{2-} forms ZHS. [93]



Despite the mildly acidic ZnSO_4 electrolyte exhibiting the perfect pH range for both Zn and MnO_2 , hence enabling the reversible cycling of a Zn- MnO_2 battery, technological challenges persist. The complex interactions on the cathode side, including the formation of ZHS, MnO_2 electro-dissolution, and changes in interfacial pH, are not well understood. More research is needed to stabilise the MnO_2 electrodeposition process. While this thesis uses MnO_2 as an active material, developing a deeper understanding and further stabilising MnO_2 through electrolyte engineering is beyond the scope of the thesis. However, we felt it was important to address chemistries of the full Zn || MnO_2 secondary battery. The main focus of the thesis is on stabilising the Zn surface which is dependent on factors beyond pH alone.

1.7.2 Dendrites

One of the major issues of aqueous Zn-metal batteries (AZMBs), is the same issue that stopped metallic lithium in its tracks at the birth of alkali-metal batteries, dendrites. Dendrites occur during the electrodeposition process which starts with the diffusion and then desolvation of Zn^{2+} ions from the bulk which are reduced on the electrode surface resulting in the formation and growth of nuclei that lead to Zn crystals (Fig. 1.24). Both the formation of Zn nuclei and Zn crystal growth must overcome an energy barrier, which is influenced by various conditions such as substrate flatness, electric field distribution over the substrate–electrolyte interface, and the substrate’s

affinity for Zn. [108], [109] To achieve uniform and dendrite-free Zn stripping/plating process, maintaining this energy barrier at a low, uniform, and stable level throughout the Zn deposition is required. [110], [111] Unfortunately, there is somewhat of an inevitability of inhomogeneity. Indeed, any defects to the pristine surface can lead to “nucleation seeds” which promote initial protrusions leading to the formation of dendrites (Fig. 1.24). [112] Furthermore, the Zn^{2+} concentration and electrical field distribution can fluctuate due to cell polarisation. For example, a slight overpotential can cause changes to the electric field leading to Zn^{2+} accumulation at the anode–electrolyte interface, which could lead to dendrites. [113], [114] While Zn has a rather low affinity for the HER, the Zn surface is not protected by an SEI and thus remains an aspect which can further complicate the reversible stripping/plating process on the zinc surface. If the HER does occur, some electrons intended for Zn electrodeposition are instead used for proton reduction, reducing the efficiency of the stripping/plating process. Furthermore, HER can cause corrosion on the Zn metal surface which results in the formation of “dead” zinc which also lowers efficiency (Fig. 1.24). [115], [116]

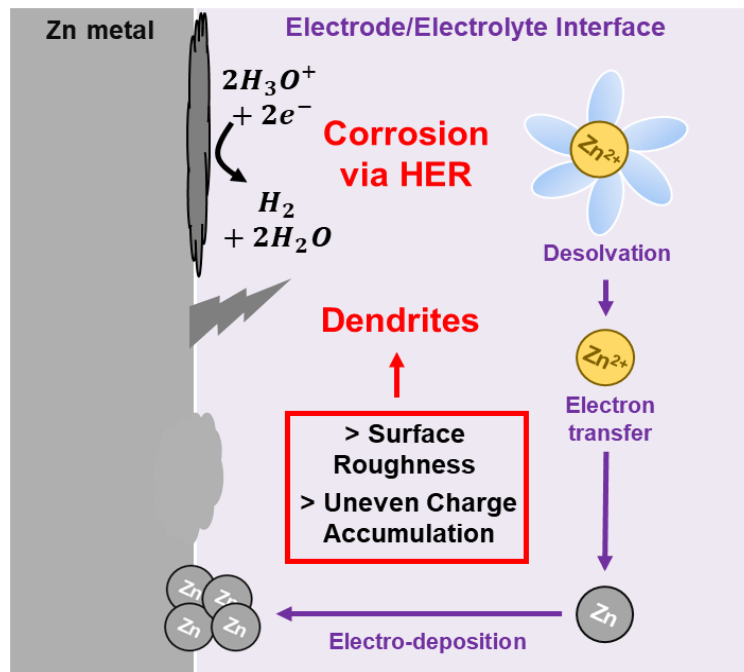


Fig. 1.24 – Schematic for electrodeposition of zinc

1.7.3 Electrolyte Engineering for Dendrites

There are many strategies to mitigate dendrite growth, with anode and separator design being popular choices. [117] - [122] However, as with ALIBs, electrolyte engineering has emerged as a particularly popular strategy, in particular electrolyte additives. These additives need to be water soluble, compatible with primary electrolyte salts, be cost-effective, and have a low toxicity. To stay in line with the green, sustainable and low-cost principles of AZMBs, the additive should ideally be compatible with the cheapest Zn salts, i.e. ZnSO_4 and ZnAc and these additives should be used sparingly, which rules out the use of super-concentrated electrolytes. [123], [124] This field is rich, with many different claims including but not limited to: (1) the additive aids in the desolvation of Zn^{2+} through solvation adaptation, (2) the additive aids in the nucleation on Zn, the additive protects and stabilises the electrolyte/electrode interface either via (3) electrostatic layer or (4) SEI formation. [124]

There are many examples of additives which are capable of following the above claims, however the general trend of additives used in tactics (1) to (4) can be determined from a few articles. For example, utilising tactic (1) of aiding in the desolvation of Zn^{2+} , solvents are often the go-to choice, following similar principles to chemistry described in section 1.5, even using some of the same chemicals such as sulfolane [125], trimethylurea (urea derivative) [126] and many more examples such as acetonitrile (ACN) [127] and tetrahydrofuran (THF) [128]. However, these solvents even though utilised in small quantities < 5 wt% are not the greenest or safest of choices. The tactic of facilitating Zn nucleation (2) can be achieved with carbon-dots which can have a large amount of different organic functionalities that preferentially bind to the Zn surface, providing a “homogenous” platform for the Zn electrodeposition. [129] Similar effects have also been achieved with functionalised organic compounds such as vanillin and arginine. [130], [131] Tactic (3) of the electrostatic layer is often achieved with polymers, preferably with long-chain polymers such as polyethylene oxide (PEO) [132], [133] and polyvinylpyrrolidone (PVP) [134]. For instance, PEO with a molecular weight of $100,000 \text{ g}\cdot\text{mol}^{-1}$ stabilises Zn anodes by promoting homogeneous Zn^{2+} distribution and forming an inert protection layer, resulting in dendrite-free Zn deposition.[133] Outside of polymers, ammonium acetate has been

shown to achieve a similar result.[135] Tactic (4) of SEI formation is typically achieved via certain organic compounds with either amide or carboxyl functionalities, such as L-cysteine [136], succinonitrile [137] and saccharin. [138] Their functionalities can be reactive at the Zn surface, enabling the construction of SEI layers on zinc surfaces. Another method is using an additive which can trigger the formation of salt decomposition, such as HTFSI which has been shown to trigger the decomposition of ZnSO₄. [139] The various examples listed above with claimed effects and performance are described in Table 1. From the many examples, it would seem that functionalised organic molecules have characteristics which can be harnessed to prevent Zn dendrites.

Electrolyte Additive	Primary Salt	Claimed effect	Performance
0.05 M Sulfolane[125]	2 M ZnSO ₄	(1) Regulate Solvation Structure	Symmetric cell: 4300 h at 2 mA cm ⁻² , 0.5 mA h cm ⁻²
0.25 M Trimethylurea[126]	2 M ZnSO ₄	(1) Regulate Solvation Structure	Symmetric cell: 1500 h at 5 mA cm ⁻² , 2.5 mA h cm ⁻²
5 vol% Tetrahydrofuran[128]	2 M ZnSO ₄	(1) Regulate Solvation Structure	Symmetric cell: 600 h at 5 mA cm ⁻² , 1 mA h cm ⁻²
10 vol% Acetonitrile[127]	1 M ZnSO ₄	(1) Regulate Solvation Structure	Cu Zn cell CE > 99.6% 1000 cycles at 2 mA cm ⁻² , 2 mA h cm ⁻²
0.1 mg/mL Functionalised Carbon-dots[129]	2 M ZnSO ₄	(2) Aid in Zn nucleation	Symmetric cell: 4000 h at 0.5 mA cm ⁻² , 0.25 mA h cm ⁻²
5mM Vanillin[130]	2 M ZnSO ₄	(2) Aid in Zn nucleation	Symmetric cell: 1000 h at 1 mA cm ⁻² , 1 mA h cm ⁻²
0.01 M Arginine[131]	1 M ZnSO ₄	(2) Aid in Zn nucleation	Symmetric cell: 500 h at 0.5 mA cm ⁻² , 0.5 mA h cm ⁻²
0.2 wt% Polyethylene oxide[132]	1 M ZnSO ₄	(3) Electrostatic Shielding Layer	Cu Zn cell CE > 99.5% over 1200 h at 1 mA cm ⁻² , 1 mA h cm ⁻²
0.5 wt% Polyethylene oxide (100,000 g.mol ⁻¹)[132]	1 M ZnSO ₄	(3) Electrostatic Shielding Layer	Cu Zn cell CE > 99.5% after 3000 h at 1 mA cm ⁻² , 1 mA h cm ⁻²
300ppm Polyvinylpyrrolidone (58,000 g.mol ⁻¹)[133]	2 M ZnSO ₄	(3) Electrostatic Shielding Layer	Symmetric cell: 1000 h at 0.5 mA cm ⁻² , 0.1 mA h cm ⁻²
0.025M Ammonium Acetate[135]	2 M ZnSO ₄	(3) Electrostatic Shielding Layer	Symmetric cell: 3500 h at 1 mA cm ⁻² , 1 mA h cm ⁻²
0.1 g/L L-cysteine [136]	2 M ZnSO ₄	(4) SEI formation	Symmetric cell:1600 h at 2 mA cm ⁻² , 2 mA h cm ⁻²
0.5 g/L Succinonitrile[137]	2 M ZnSO ₄	(4) SEI formation	Symmetric cell: 700 h at 1 mA cm ⁻² , 2 mA h cm ⁻²
0.5 g/L Saccharin[138]	2 M ZnSO ₄	(4) SEI formation	Symmetric cell over 550 h at 10 mA cm ⁻² , 10 mA h cm ⁻²
0.1M HTFSI[139]	2 M ZnSO ₄	(4) SEI formation	Symmetric cell: 2000 h at 4 mA cm ⁻² , 4 mA h cm ⁻²

Table 1 – List of different additives for Zn dendrites utilising ZnSO₄ electrolyte

The performance of an additive is typically assessed using Zn || Zn, Zn || Cu and Zn || Ti cells, with long-term galvanostatic cycling and coulombic efficiency (CE%) serving as key indicators. [140] Achieving over 1,000 hours of cycling in Zn || Zn cells with a coulombic efficiency (CE) greater than 99%, obtained through specific procedures using Zn || Cu and Zn || Ti cells are generally considered a strong indicator of stability. However, performance metrics can vary significantly due to the wide range of cycling parameters used. It is important to note the presence of “soft shorts” which can happen during cycling and give the mirage of long-term stability. Indeed, the potential curves for cells cycling normally and soft shorted cells are fairly similar and thus caution must be taken when examining the cycling curves (Fig. 1.25). [140], [141]

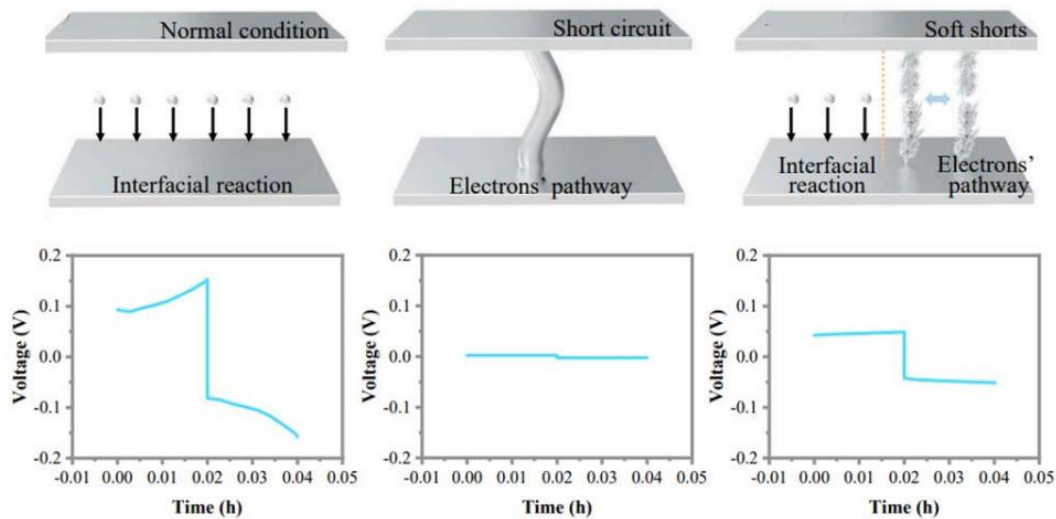


Fig. 1.25 – Schematic of normal cycling, short circuit and soft shorts along with the accompanying cycling curve. Adapted from [141].

The field of Zn dendrites is complex, with numerous articles detailing various methods to mitigate dendrite formation. Clearly, there are multiple approaches to achieve this goal. However, many examples seem to take a 'pick a chemical off the shelf' approach. A more targeted strategy for electrolyte additive design is needed. Based on the studies mentioned, this could focus on polymer-like structures, preferably ether-based with some kind of organic functionalities that can result in tactics (1) to (4) being achieved.

Conclusions to Chapter 1

The development of aqueous electrolytes has always depended on electrolyte engineering, starting with early aqueous batteries that utilised acid/base properties in technologies like lead-acid and Ni-MH. To push past the narrow ESW of water and construct more energy-dense aqueous batteries, WISE was proposed, which brought ALIBs to the forefront. WISE extended the ESW beyond 3 V through the formation of an SEI, mitigating the so-called “cathodic challenge”. The breakthrough of WISE enhanced our understanding of various electrolyte concepts, such as super-concentration and solvation properties. Despite the progress made at a fundamental level, WISE itself, in the end, was not able to fully solve the ESW issues and thus various strategies such as molecular crowding, further solvation adaptation and chaotropic effects were employed. These interesting concepts are worth exploring and developing further. However, these diluent strategies reduce the aqueous nature of the electrolyte, making it almost organic. Additionally, the use of super-concentrated electrolytes is problematic due to their high cost and the necessity of corrosive and toxic salts, which contradict the green principles of an aqueous battery. Merging ROMs with aqueous electrolytes is logical given their shared sustainable ethos. However, these materials face challenges such as low conductivity and high dissolution. Although the use of ROMs in ALIBs is not new, it is worth revisiting. Exploring alternative technologies with a long history, such as Zn-ion batteries, could be a valuable next step. AZMBs are still at the cutting edge of battery research due to their complex chemistry, which requires ongoing attention—especially concerning dendrite growth, a major barrier to widespread adoption.

Chapter 2: Acid/Base Dynamics of Amino Acids in Aqueous Electrolytes

This chapter is primarily based on the following publication:

- **J.Brown**, A.Grimaud, 'Proton-donating and chemistry-dependent buffering capability of amino acids for the hydrogen evolution reaction' *Phys. Chem. Chem. Phys.*, vol. 25, pp. 8005-8012, Feb. 2023. DOI: 10.1039/D3CP00552F

2.1 Prelude to the Chapter: Citrulline in WISE

Building on from the work carried in section 1.5.2, finding ways to further modulate solvation structure to improve the performance of ALIBs, was the initial target of the PhD. Amino acids, the building block of proteins, represented an interesting group of chemicals to achieve this. The acidic α -carboxyl (-COOH), a basic α -amine (-NH₂) groups (Fig. 2.1) could affect the hydrogen bonding network (HBN) of water through HB donor and acceptor groups, decompose to form an SEI or even affect solvation.

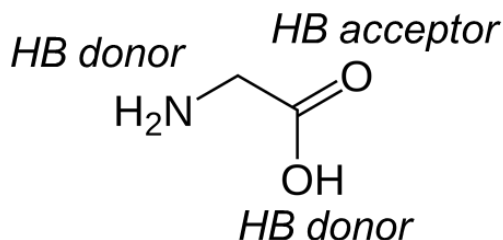


Fig. 2.1 – Structure of glycine, the simplest of amino acids with the amide (HB donor) and carboxylic acid (HB donor & acceptor).

We initially started to probe commercially available amino acids with glycine, however, we found that the solubility was limited, only enabling 4 mol.kg⁻¹ dissolved into the WISE. A common trend amongst most of the “essential” amino acids is the relatively low solubility, with glycine having the highest reported solubility at 4.9 mol.kg⁻¹_(water) ranging down to solubilities 0.2 mol.kg⁻¹_(water) for aspartic and glutamic acid. [142], [143] Beyond essential amino acids, there is a vast array of additional functional groups (-R) that lead to a wide variety of functionalities. One particularly interesting amino acid

is citrulline (CIT) (Fig. 2.2), which contains a urea functionality. As described in Section 1.5.3, this functionality has been successfully used as a diluent for WISE. [54]

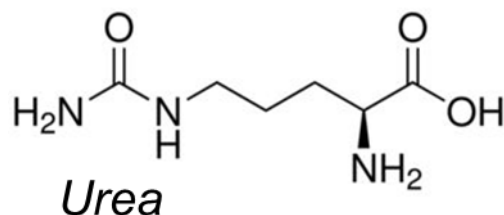


Fig. 2.2 – Structure of citrulline (CIT).

To determine if CIT has any beneficial effects akin to urea, CIT was added to aqueous solutions utilising LiTFSI salt. Interestingly, the ternary mixtures of LiTFSI, citrulline and water enables an increase in solubility of CIT, which otherwise has a moderate solubility in pure aqueous solutions $< 1 \text{ Mol.L}^{-1}$ to $> 5 \text{ mol.L}^{-1}$ (Fig. 2.3a). Indeed, concentrations of 5, 10 and 20 m CIT + 20 m LiTFSI could be achieved. This would indicate that LiTFSI has a “salting-in” effect on the CIT, potentially through the TFSI⁻, whose chaotropic nature would facilitate this. [144], [145] This can be probed via FT-IR spectroscopy where Fig. 2.3b displays the region between $700 - 850 \text{ cm}^{-1}$, which correspond to the symmetric and asymmetric C-S and SNS stretching vibrations (denoted $\nu_s\text{C-S}$ and $\nu_a\text{SNS}$) of the TFSI⁻, respectively. A redshift of these bands is observed, indicating that the TFSI⁻ is more loosely bound to Li⁺ as the concentration of CIT is increased from 0 to 20 m. This potentially indicates that TFSI⁻ is interacting with the CIT, through the protonated amino group or the amino group of the urea functionality. Fig. 2.3c showcases the FT-IR region at $2600-4000 \text{ cm}^{-1}$, which includes the -OH stretching vibration modes of water as well as the -NH stretching from the CIT. The distinct water region for WISE between $3400-3700 \text{ cm}^{-1}$ reduces in intensity as the concentration of CIT increases, indicating a change to HBN of water. This reduction in water bands gives way to the presence of -NH stretching frequencies between $2800 - 3300 \text{ cm}^{-1}$ associated with CIT, further implicating a change to the HBN of water. When probing the ionic conductivity (Fig. 2.3d) we see that upon the addition of CIT at 5, 10 and 20 m to WISE, the conductivity drastically decreases, to a very low value (*for a liquid electrolyte*) of 0.1 mS.cm^{-1} for 20 m LiTFSI + 20 m CIT. 20 m LiTFSI + 10 m CIT has a low, but slightly more manageable conductivity of 0.4 mS.cm^{-1} and was thus tested as the electrolyte for Mo₆S₈ || LiFePO₄ full cell. The cycling curves (Fig. 2.3e) display high polarisation, even at C/4, likely due to the low conductivity and high

irreversibility. The high irreversibility can be the result of electrolyte decomposition, which becomes more visible on the second cycle with notable features observed during oxidation. As mentioned in section 1.4.3, the HER catalyses the decomposition of TFSI⁻ due to the formation of OH⁻, which leads to the formation of the SEI, enabling stable cycling of Mo₆S₈. Cyclic voltammetry (CV) of 20 m LiTFSI + 10 m CIT on glassy carbon (Fig. 2.3f) revealed that the typical reduction wave for WISE with a large passivation peak is not present, instead, the HER is the main contributor to the reduction wave. The absence of this passivation peak and hence an SEI explains the poor cycling performance of the full cell as a result of continuous HER. So, while these mixtures have interesting chemical properties as showcased by the ternary plot and FT-IR, they are not suited as battery electrolytes. However, amino acids clearly have an influence on the electrochemistry of aqueous electrolytes and this result piqued our interest. Can they somehow further influence and potentially modulate the HER and other similar reactions?

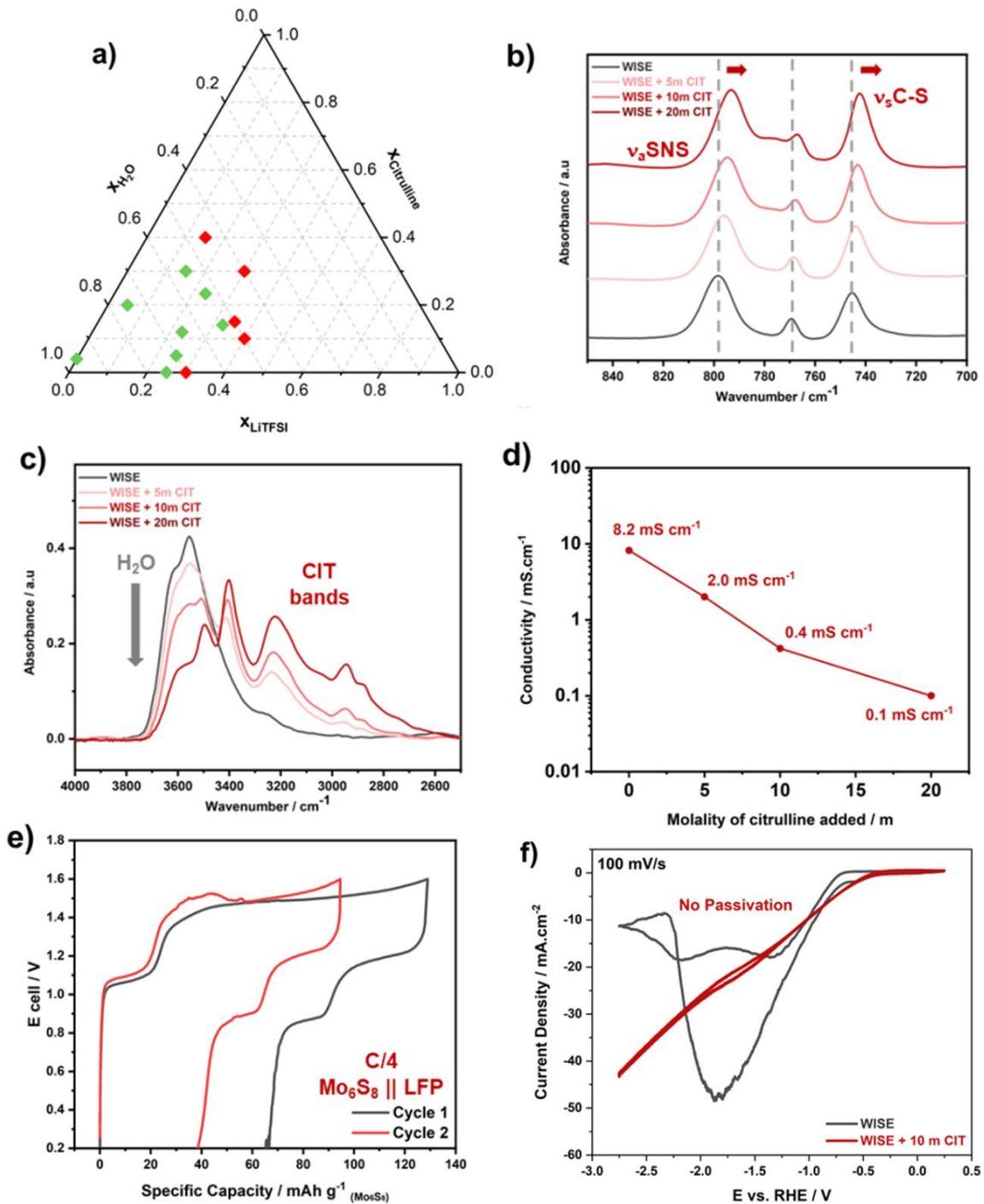


Fig. 2.3 - a) Ternary diagram for LiTFSI, CIT and water (green denotes liquid & red denotes solid), b) 700-850 cm^{-1} FTIR region of electrolytes, c) 2800-4000 cm^{-1} FTIR region of electrolytes, d) ionic conductivity of electrolytes, e) galvanostatic cycling of $\text{Mo}_6\text{S}_8 \parallel \text{LFP}$ full cell at C/4 and f) cyclic voltammety of 20 m LiTFSI and 20 m LiTFSI + 10 m CIT at 100 mV/s on glassy carbon (WE), Pt wire (CE) and standard calomel electrode (SCE).

2.2 An Introduction to the Fundamentals of the HER

2.2.1 The Mechanism and Catalyst of Choice

Before we tackle the effects of amino acids on the HER, it is worth introducing the fundamentals of the reaction. The HER involves two simultaneous proton-coupled electron transfer reactions (PCET), which happen in a sequential manner. [146], [147] The initial step is adsorption of hydrogen atoms onto the electrode surface, known as the Volmer step, $H^+ + e^- \rightarrow H^*$ where the as formed reaction intermediate (H^*) can react with another H^* to evolve $H_{2(g)}$ known as the Tafel step $2H^* \rightarrow H_2$ or undergo electrochemical recombination with protons to evolve $H_{2(g)}$ known as the Heyrovsky step $H^* + H^+ + e^- \rightarrow H_2$. [148], [149] The specific mechanism of HER greatly depends on experimental conditions such as the electrode material, typically a metal, and the electrolyte composition. [150], [151], [152] Platinum (Pt) is widely regarded as the state-of-the-art electrocatalyst for the HER due to its high exchange current density, low Tafel slope and high reversibility for the HER process. [153] - [156] These characteristics make Pt the go-to catalyst for the HER, not only for fundamental understanding but also for industrial applications. Most of the fundamental studies on the HER with Pt metal focus on acidic media.

2.2.2 pH Dependency of the HER

An important aspect of the HER is its pH dependence, as highlighted in Chapter 1.2, but the sensitivity goes deeper, where the reaction kinetics vary significantly between acidic and alkaline environments. [149], [155] Even a shift from strongly acidic (pH 0) to weakly acidic conditions (pH < 3) results a drastic change to the HER mechanism. This is due to the proton source for the reaction; where in strongly acidic conditions, H_3O^+ (H^+) is the primary reactant and follows the aforementioned PCET steps, starting with the Volmer step and proceeding with either the Tafel or Heyrovsky. Meanwhile, when moving to pH equal or superior to 3, the proton source shifts from H_3O^+ to H_2O . With H_2O as the proton source, the Volmer step, now $H_2O + e^- \rightarrow H^* + OH^-$, involves a sluggish water dissociation step (cleavage of an O-H bond) thus modifying the reduction kinetics at the catalyst/electrolyte interface. Now the RDS becomes the Heyrovsky step. Additionally, the generation of OH^- creates a concentration gradient on the electrode surface, augmenting surface alkalinity. [148],

[155], [156], [157] Furthermore, in a H^+ depleted environment, polarised water molecules preferentially interact through hydrogen bonding. This, coupled with a more rigid double layer in alkaline conditions—due to the greater disparity between the applied potential and the potential of zero charge of Pt—results in the formation of a thicker diffuse layer. This layer restricts access to the inner Helmholtz plane (IHP) at the catalyst/electrolyte interface, further impeding reaction kinetics. [149], [153], [157] The shift between the two different proton sources is clear when utilising a $pH > 2$ but < 4 . Here, there will be a certain concentration of H^+ that will act as the initial proton source for the HER, however, once these H^+ are depleted, water becomes the proton source. [149], [157] Fig. 2.4 showcases the shift whereby two reduction waves are present. The first reduction wave is attributed to proton reduction; once the protons are consumed, a plateau is reached where reaction becomes diffusion limited. This is followed by the second reduction wave corresponding to water reduction, which requires a much greater overpotential.

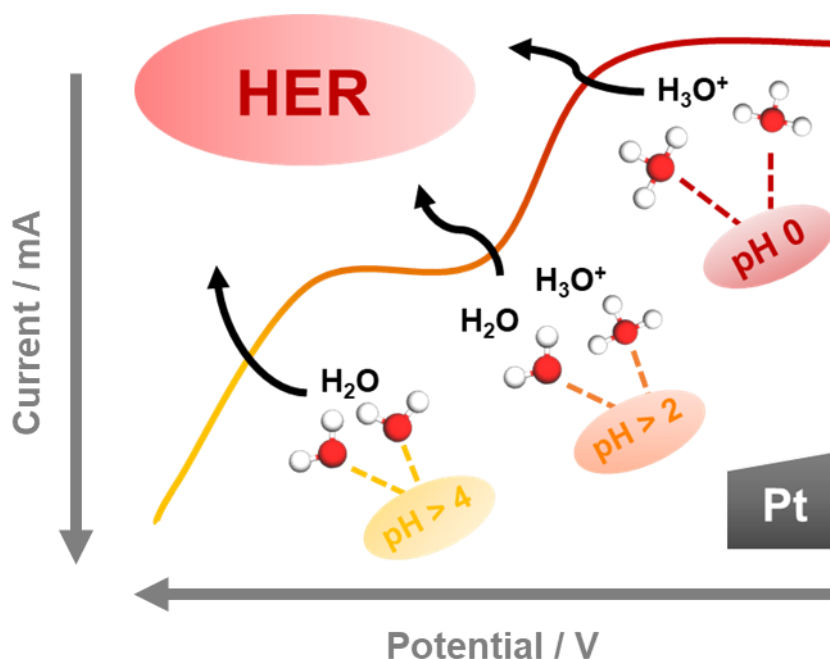


Fig. 2.4 – Switch in reactant from H_3O^+ to H_2O as pH changes and the subsequent polarisation curve. Adapted from [157].

2.2.3 Playing on the Acid/Base Dynamics of the HER

This switch in reactant was studied by Auguier et al., who demonstrated that acetate buffers, which operate around pH 4, can maintain the surface pH near the buffer pKa. [158] This sustains the concentration of H_3O^+ at the interface, delaying the point at which the reactant switches to H_2O . However, this effect is limited by the concentration of the buffer, as its buffering activity eventually becomes depleted. Nevertheless, the discovery that buffers can serve as proton donors/carriers, mitigating the acid/alkaline-shift at the surface and preventing the formation of concentration gradients, is relevant for understanding the acid/base dynamics of the HER. [158], [159], [160] To further develop the principle, Jackson et al. demonstrated that a phosphate buffer can catalyse the HER, through outcompeting H_2O as the proton donor on gold surfaces, allowing the HER rate of the buffer to match that of pH 1 while the solution pH is > 7 . Although, their work also highlights that not all buffers work, as the same effect cannot be achieved with borate buffers. They show that the mechanism of the phosphate buffer does not follow the traditional bimolecular reaction between the donor and a surface site, but instead requires the formation of an intermediate complex embedded in the double layer (Fig. 2.5). [161]

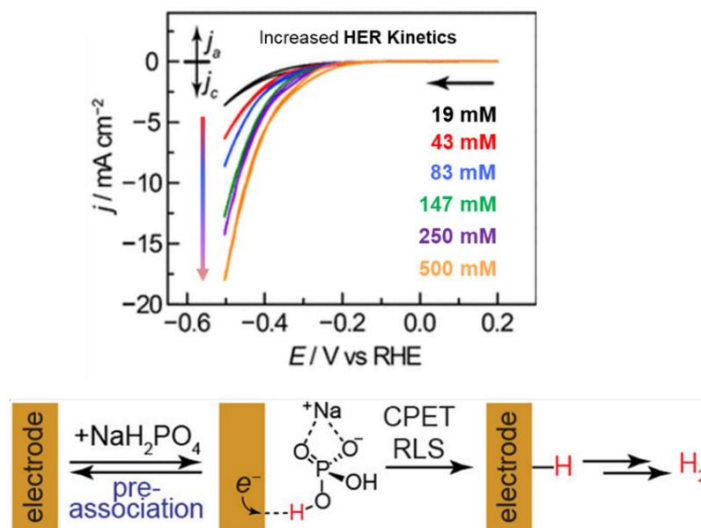
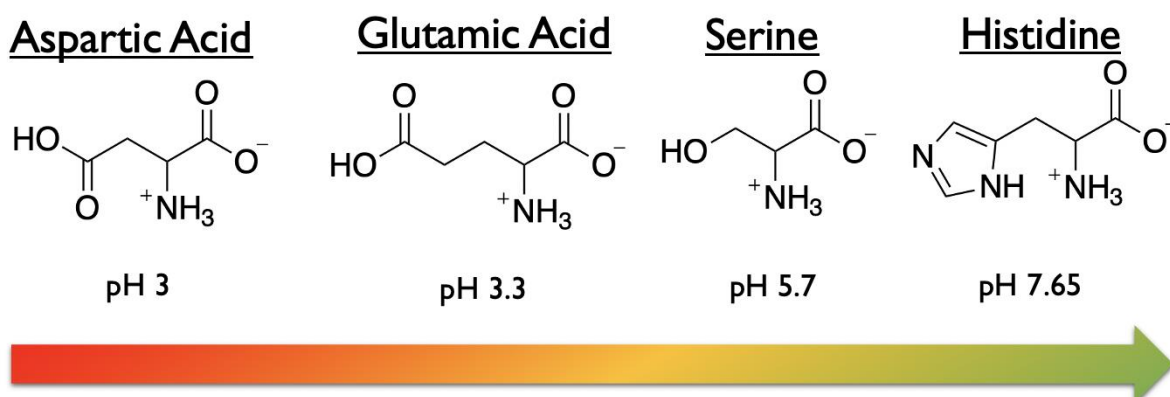


Fig. 2.5 – polarisation curves for phosphate buffer on Au surface which showcases an increase in HER kinetics with increasing phosphate buffer concentration (top) mechanism of buffer activity to facilitate HER. Adapted from [161].

2.2.4 Amino Acids as Buffers?

While buffers have seen attention within literature, amino acids have yet to be explored for proton-dependent electrochemical reduction reactions despite exhibiting buffering and proton donating/carrying capabilities, often exploited in biological systems. [162] - [165] While buffering requirements within biological systems differ greatly from electrochemical systems, many factors make amino acids intriguing for influencing the acid/base chemistry of HER. Indeed, the aforementioned acidic α -carboxyl (-COOH), basic α -amine (-NH₂) and side chains (-R), could all act as proton donors/acceptors. Furthermore, each group has a different pK_a value, meaning they can act as a buffer in three different pH ranges. To probe how these different groups could influence the HER, four different amino acids are targeted: Aspartic Acid (Asp), Glutamic Acid (Glu), Serine (Ser) and Histidine (His) which all have varying functional groups with groups at different pK_a values and different isoelectric points (pI) (Scheme. 2.1).



Scheme. 2.1 - Zwitterion structure and pH of Aspartic Acid (Asp), Glutamic Acid (Glu), Serine (Ser) and Histidine (His).

2.3 Acid/Base Chemistry of Asp/Glu

In aqueous solutions lacking proton or hydroxide sources, the predominant amino acid species in solution is the zwitterionic form, and the pH of the solution is determined by the isoelectric point (pI). The pI is governed by the dissociation constants of the most relevant ionisable groups, specifically the two carboxyl groups in the cases of Asp and Glu, where the average of their pK_a values defines the pI value. The formation of the zwitterion involves the dissociation of one of the carboxyl

groups, thereby generating H_3O^+ . Titrations depicted in Fig. 2.6a and Fig. 2.6b shows that the pI values are 3 for Asp and 3.3 for Glu. The pI remains constant regardless of amino acid concentration because of the ratio of conjugate base to acid of the ionisable groups, which can be calculated using the Henderson-Hasselbalch equation (Eq. 2.1), remains unchanged. The proton concentration at each pI can be determined using Eq. 2.2. The complete dissociation process for Asp is detailed in Scheme 2.2.

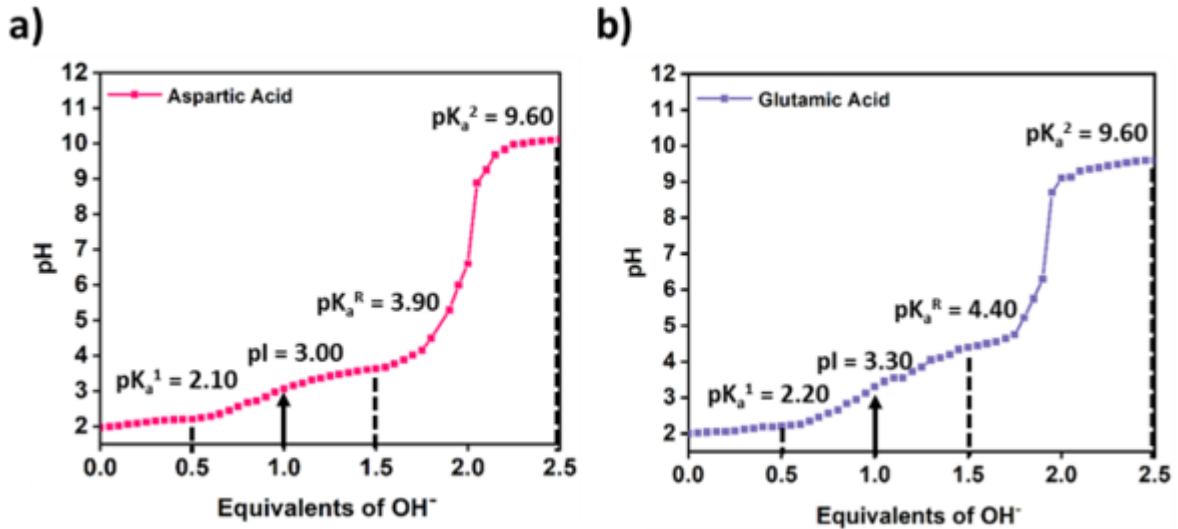
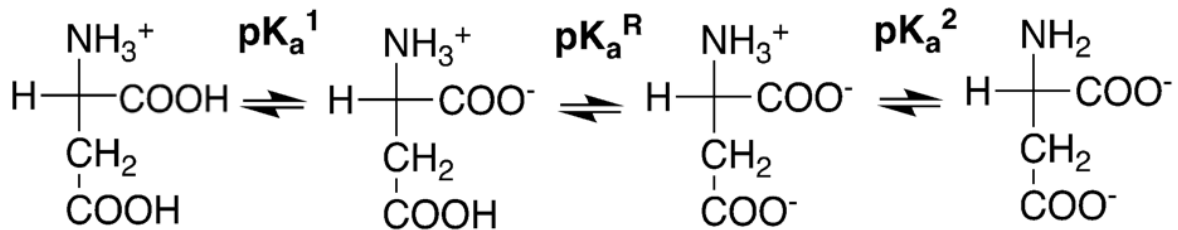


Fig. 2.6 - a) Titration of Aspartic Acid (Asp) and b) titration of Glutamic Acid (Glu), carried out using 30 mM AA and titrated with 60 mM HCl and 50 mM NaOH solutions.

$$pI = pK_a + \log \log \frac{[z-AA^-]}{[z-AA]} \quad (\text{Eq. 2.1})$$

$$= 10^{-pI} \quad (\text{Eq. 2.2})$$



Scheme 2.2 Full dissociation process for Aspartic Acid.

Amino acids are often described as buffers, which is not strictly true at their zwitterionic pH since this value lies outside the pKa range of their ionisable groups. However, the pKaR (pKa for the side chain) for both Asp and Glu is 3.9 and 4.3, respectively. Therefore, if there is a shift in solution pH both Asp and Glu can exhibit buffering capacity.

2.4 Electrochemistry of Asp/Glu Solutions

To probe if amino acids can influence HER kinetics, cyclic voltammetry (CV) measurements were carried out using Asp and Glu solutions at 5, 10, 20, and 30 mM on platinum rotating disk electrodes (Pt-RDE). The CVs of Asp (Fig. 2.7a) showcase two reduction regions: an initial cathodic reduction at low overpotential (0 to -0.4 V vs RHE) followed by a plateau, and a second cathodic reduction at higher overpotential (~-1 V vs RHE). The shape of the cathodic scan is reminiscent of HER curves recorded on Pt at $\text{pH} \geq 2$, with the first reduction wave ascribed to proton reduction, leading to a plateau where proton diffusion is limiting, followed by the second reduction wave corresponding to water reduction, which requires greater overpotential. [155], [157] The similarity in the shape of the CV recorded with Asp to that of slightly acidic solutions reveals that the Asp solutions are undergoing the same HER process. Thus, we ascribe the different reduction waves for the amino acid solutions to the respective waves observed for HER in $\text{pH} \geq 2$ solutions. The first cathodic wave, attributed to proton reduction, linearly increases with increasing Asp concentration as seen in Fig. 2.7a, where a large increase in current density is observed (-5 to -30 mA cm^{-2}) when the concentration is increased from 5 mM to 30 mM. When examining the CVs for Glu solutions (Fig. 2.7b), an identical trend is observed. Combining this observation with previous demonstrations that the cathodic plateau is related to proton reduction, we show that amino acids can act as a proton source for HER and can increase the proton reduction wave with increasing concentration without a change in pH between the different concentrations. [155] At greater overpotential, i.e. cathodic potentials below -1 V vs. RHE, water reduction appears to be unchanged with concentration for both Asp and Glu solutions. To determine if there are any structural changes to the amino acids after the HER, NMR measurements are carried out before and after electrochemistry. The NMR spectra shown in (Fig A2.1) showcases two signals, one at 2.9 ppm assigned to the protons bound to the methylene carbon and the second at 4.1 ppm assigned to

proton bound to the amine-bearing carbon. The NMR spectra are unchanged before and after cycling indicating that the structure of the amino acid is unaffected during HER.

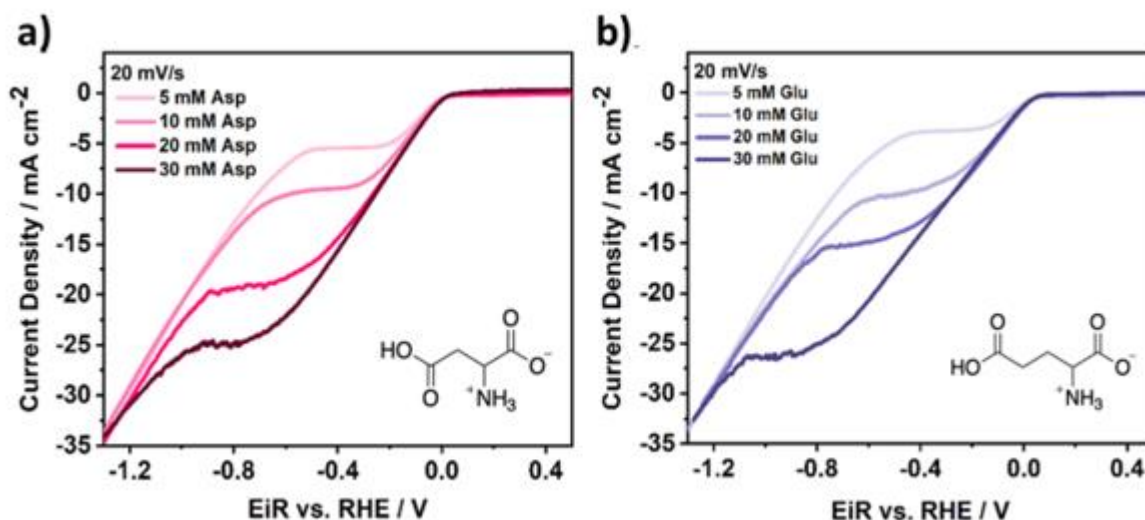


Fig. 2.7 - a) Cyclic voltammograms for 30 mM Asp with 100 mM Li_2SO_4 supporting salt and b) 30 mM Glu with 100 mM Li_2SO_4 supporting salt, all recorded at 20 mV/s on polycrystalline Pt rotating disk electrode (rotation speed of 2000 RPM).

As the increase in amino acid concentration leads to an increase in cathodic current associated with proton reduction, quantification is important for understanding the role of Asp and Glu as proton donors. The Koutecky-Levich equation, Eq. 2.3, where i_L is the limiting current density, D the diffusion coefficient of protons, ω the rotation speed and ν the kinematic viscosity, can be applied to determine the concentration of protons participating to the HER.[155], [157]

$$i_L = 2F(0.62) \times D^{\frac{2}{3}} \times \omega^{\frac{1}{2}} \times \nu^{-\frac{1}{6}} \times C \quad (\text{Eq. 2.3})$$

First, the cathodic current density was estimated from the start, middle, and end of the plateau to account for any deviation from linearity. The Koutecky-Levich equation was applied to each of these values to calculate the concentration of protons reduced, and the error bars were calculated from three separate measurements (Fig A2.2 & A2.3). The concentration of protons corresponding to the cathodic current across the plateau increases linearly with amino acid concentration, as seen in Fig. 2.8. Extrapolating from Fig. 2.8, 30 mM of Asp and Glu acid corresponds to 9 mM of H_3O^+ which is equivalent to a pH of 2.3. Meanwhile, a pH 3 and 3.3 solutions have proton

concentration of 0.9 and 1.8 mM, respectively. Thus, 30 mM Asp and Glu solutions have 4.5x and 10x more proton reduction capability than a standard acidic solution.

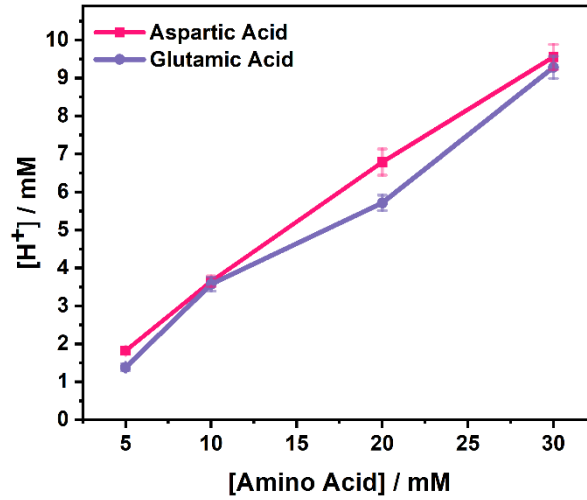


Fig. 2.8 - Concentration of protons reduced $[H^+]$ as calculated from the Koutecky-Levich equation vs. the concentration of amino acid $[Amino\ Acid]$ in the solution.

This increase in proton reduction is tied to the buffering capability of the amino acid, which occurs when the pH is equal to the pKa of any of the ionisable groups. The bulk pH of the solution will be the pI of the amino acid, in the case of Asp, pH 3. Once the HER starts, protons are consumed increasing the pH. As the pH increases towards the pKaR (3.9 for Asp) a buffering effect kicks in and maintains the pH by preventing the depletion of the remaining protons through a fast acid/base equilibrium, thus extending the proton reduction wave. The same rationale applies to Glu, except with slightly different pI and pKaR values. This effect of extending the proton reduction wave has been previously demonstrated with acetate buffers. As with the acetate buffer, the increase in current density in the plateau region can be rationalised through Eq. 2.4 derived from Auinger et al. [158] Following this equation, as the concentration of the buffer increases, in our case Asp or Glu, there is a linear increase in current density, which is demonstrated through our experimental data.

$$j_{Total} = j_{H^+/OH^-} + \frac{c_{z-Asp}^0 F}{\delta_{eff}} \left(\frac{D_{z-Asp} c_{H^+}^{Surface} - D_{z-Asp}^- K_S}{K_S + c_{H^+}^{Surface}} - \frac{D_{z-Asp} c_{H^+}^{Solution} - D_{z-Asp}^- K_S}{K_S + c_{H^+}^{Solution}} \right) \quad (\text{Eq. 2.4})$$

As the Asp and Glu solutions have pH values of 3 and 3.3, respectively, comparing these amino acid solutions to conventional unbuffered acidic solutions with

the same pH can demonstrate the gain through the buffering effect. Comparing the 30 mM Asp to a pH 3 solution (1.8 mM H₂SO₄) (Fig. 2.9a), a similar shape is showcased with the same HER onset. However, the current density measured for the cathodic wave corresponding to proton reduction is found to be much greater for Asp than for an H₂SO₄ solution at pH 3. A similar observation is made when comparing the cathodic scan recorded for the Glu solution to that of a pH 3.3 (0.9 mM H₂SO₄) solution (Fig. 2.9b). The facile depletion of protons for the unbuffered solution shortens the proton reduction wave compared to the amino acid solutions. As calculated, the cathodic current at the plateau recorded for Glu and Asp corresponds to roughly 9 mM of protons. Comparing 30 mM Asp/Glu to a solution with 9 mM H₂SO₄ (pH 2.3) displays very similar current density and onset potential. However, the sharper slope for pH 2.3 would indicate different kinetics (Fig. 2.9a and 2.9b). To determine if the buffering effect of amino acids has any change on the kinetics, Tafel slopes for the amino acid solutions were compared with those of the unbuffered solutions. For the pH 3 H₂SO₄ solution and the 30 mM Asp solution (Fig. 2.9c), slopes of 120 and 110 mV dec⁻¹ are obtained, respectively, indicating a HER mechanism with the Volmer step acting as the rate-determining step (RDS). A similar result is observed for 30 mM Glu and pH 3.3 H₂SO₄ solutions (Fig. 2.9d), with slopes of 140 mV dec⁻¹ and 110 mV dec⁻¹, respectively. These values indicate that the buffering effect does not drastically alter HER kinetics, regardless of the increase in proton reduction compared to the unbuffered solutions. Meanwhile, the pH 2.3 H₂SO₄ solution has a Tafel slope of 60 mV dec⁻¹, indicating faster kinetics and a different mechanism (Fig. 2.9c and 2.9d). The inability of the amino acids to affect the kinetics can be tentatively explained by the neutrality of the zwitterion. Indeed, zwitterions, being net neutral, have zero charge and thus no ionic strength, as previously shown. [166] Thus, one can hypothesise that the addition of amino acids does not influence the electrical double layer, which shows similarly poor ion dynamics, unlike more acidic solutions i.e. the pH 2.3 solution. This result suggests that irrespective of the concentration of protons contributing to the HER, whether they are freely available in the pH 2.3 solution or resulting from a fast acid/base equilibrium with the amino acid, the pH primarily determines the HER kinetics. Following the explanations provided by Koper and co-workers, a lower pH results in a more flexible EDL due to a smaller difference between the applied potential and the potential of zero charge for Pt, hence allowing for more facile kinetics for H⁺ exchange. [153] That being said, the Tafel slopes for both 30 mM Asp and Glu solutions

are found to be similar, whereas the slopes for the unbuffered pH 3.3 and pH 3 H_2SO_4 solutions are not. Meaning, the nature of the proton donor could also be a potential influence on the HER kinetics. Through using Asp and Glu, we have demonstrated that amino acids can not only be used as a proton source, but they also exhibit a buffering effect with a sufficiently fast acid/base equilibrium to extend the proton reduction wave by preventing the depletion of protons at the interface. Furthermore, we also showcase that HER kinetics depend on both pH and the nature of the proton source.

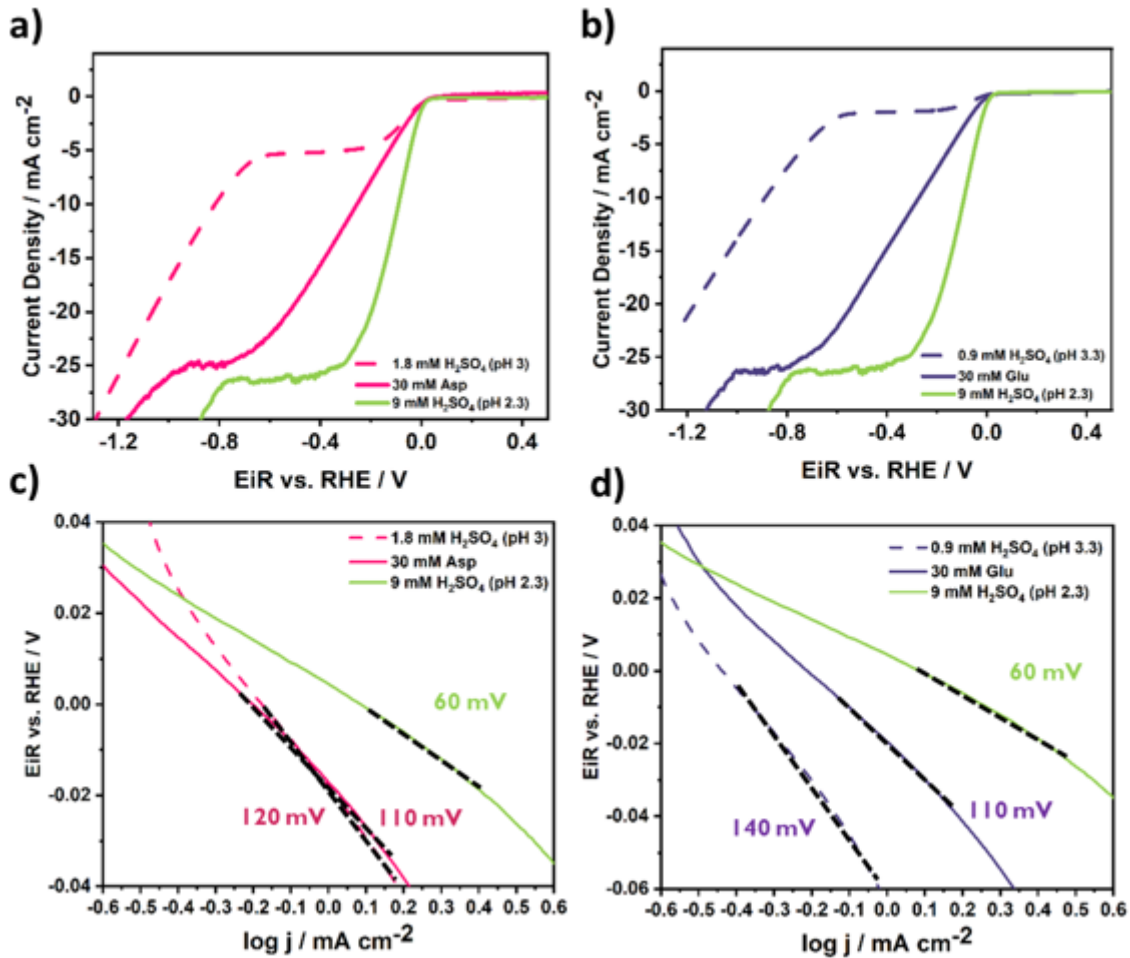


Fig. 2.9 - a) Cyclic voltammograms for 30 mM Asp, 1.8 mM (pH 3) and 9 mM (pH 2.3) H_2SO_4 solutions, b) for 30 mM Glu, 0.9 mM (pH 3.3) and 9 mM (pH 2.3) H_2SO_4 solutions, all recorded at 20 mV/s on polycrystalline Pt rotating disk electrode (rotation speed of 2000 RPM), c) Tafel slopes for 30 mM Asp, 1.8 mM (pH 3) and 9 mM (pH 2.3) H_2SO_4 solutions and d) Tafel slopes for 30 mM Glu, 0.9 mM (pH 3.3) and 9 mM and (pH 2.3) H_2SO_4 solutions. All solutions contain 100 mM Li_2SO_4 supporting salt

2.5 The Electrochemistry of SER/HIS

Ser is an amino acid with a less acidic pI of 5.70, dictated by the carboxyl group with $pK_a^1 = 2.20$ and the amino group with $pK_a^2 = 9.20$, as seen in Fig. 2.10a. Ser does contain an -OH side chain, however this will not contribute to the acid/base chemistry as the pK_a value is ~ 15 . His is a more basic amino acid with a near neutral pI of 7.65, dictated by the imidazole group with $pK_a^1 = 6.10$, and the amino group with $pK_a^2 = 9.20$ as seen in Fig. 2.10b. The CV data, Fig. 2.10c, for Ser displays an onset potential of ~ -0.2 V vs RHE and one reduction regime. A similar curve is obtained for His (Fig. 2.10d). This single reduction regime is similar to that found for $pH \geq 4$ solutions, whereby H_2O is the primary source of protons for the HER. [154], [157] When only considering the pI of 5.7 for Ser and 7.65 for His, this result is expected. However, when factoring in the buffering capability of amino acids, one could expect two cathodic regimes, for H_3O^+ and H_2O reduction. Why do we not see the same effect for Ser and His as we do for Asp and Glu? The more basic pI for Ser and His, 5.7 and 7.6, results in a much lower proton concentration in solution which already favours a switch in reactant to H_2O compared to solutions of Asp and Glu. Furthermore, the pK_a 's for Ser and His are relatively far away from the pI's, hence the already tiny proton concentration cannot be maintained. As a consequence, both Ser and His only display one reduction event corresponding to H_2O reduction. This result would suggest that other amino acids unexplored in this work, which generally have similar pI and pK_a values to Ser, will function in the same way.

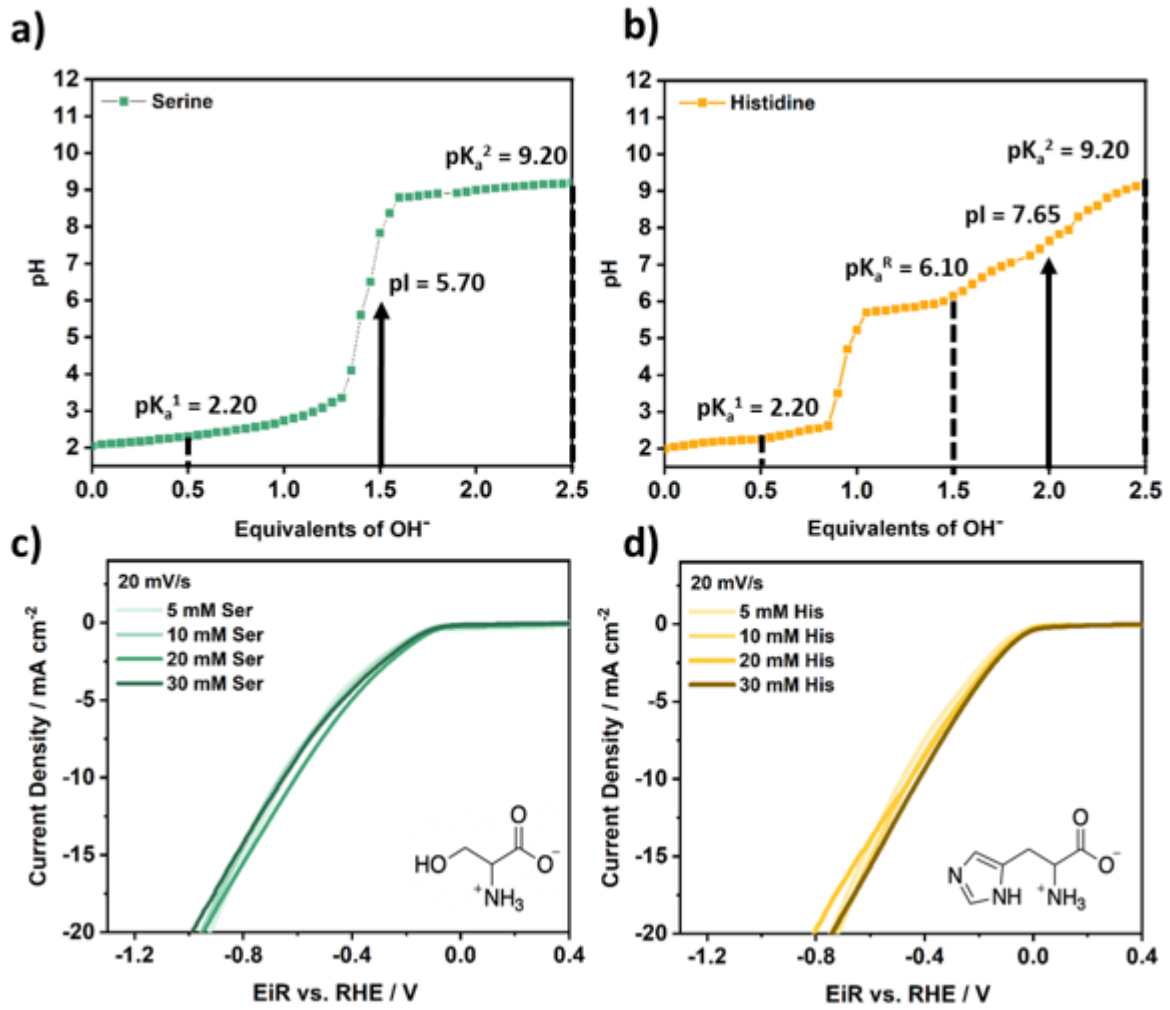


Fig. 2.10 - a) Titration of Serine (Ser), b) titration of Histidine (His), c) cyclic voltammograms for Ser and d) cyclic voltammograms for His recorded on polycrystalline Pt rotating disk electrode (rotation speed 2000 RPM). All solutions contain 100 mM Li_2SO_4 supporting salt.

Conclusions to Chapter 2

While having the initial goal of utilising amino acids to boost the performance of ALIBs, through mitigating reactions like the HER, we instead showcased that the HER kinetics can be manipulated through the use of amino acids. We show that these amino acids can not only serve as a proton source for the HER but also act as a buffer for the reaction. By comparing various amino acids, we identify that the key attribute for effective buffering and sustained proton reduction at high current densities is the close proximity of the isoelectric point (pI) to the buffering pKa values. Asp and Glu, the most acidic amino acids, best illustrate these effects due to their high acidity and the close alignment of their isoelectric point (pI) and pKa values. Although this study did not achieve its initial goal of mitigating the HER, it highlights the dual nature of working on the electrochemistry of aqueous media. On one hand, preventing HER/OER is crucial for batteries. On the other hand, promoting HER/OER has valuable applications, such as in electrolyzers. This thesis focuses on aqueous electrolytes for batteries, with the primary goal of finding practical methods to enhance these systems through electrolyte engineering. Therefore, the remainder of the thesis will return to exploring battery technologies.

Chapter 3: A Guanidium Salt as a Chaotropic Agent for Aqueous Battery Electrolytes

This chapter is primarily based on the following publication:

- **J. Brown**, J. Forero-Saboya, B. Baptiste, M. Karlsmo, G. Rousse & A. Grimaud, 'A guanidium salt as a chaotropic agent for aqueous battery electrolytes' *Chem. Commun.*, vol. 59, pp. 12266-12269, Sep. 2023, DOI: 10.1039/D3CC03769J

3.1 Introduction

As discussed in Chapter 1.5.3, the use of chaotropic agents has been demonstrated to reduce water reactivity, thereby increasing the ESW of the electrolyte. Previous studies have predominantly focused on the effects of chaotropic anions, such as ClO_4^- and CF_3SO_3^- , which enable a wider temperature cycling range. [61], [62], [167] However, the role of kosmotropic and chaotropic cations has been less studied. There has been some work on understanding the insertion properties of different cations into redox active organic materials, and how these properties change depending on the kosmo/chaotropic nature of the cation. [168], [169] However, the impact of cations on water structuring and reactivity, with regards to the ESW, has received little-to-no attention. Interestingly, the Hofmeister series characterises Li^+ as a kosmotropic cation, meaning it will strengthen the HBN of water. On the other hand, TFSI^- has been demonstrated to have chaotropic-like properties. [144] Thus, an interesting prospect would be to combine TFSI^- with a chaotropic cation to create a chaotropic agent that could work similarly to urea. While the true effects of chaotropic ions on HBN and the consequences of such interactions are still unclear within the field of macro-molecular science, this chapter aims to demonstrate that chaotropy plays a role in the reactivity of aqueous electrolytes.

3.2 Guanidium bis(trifluoromethanesulfonyl)imide (GdmTFSI)

A chaotropic cation of particular interest is guanidinium (Gdm^+) (Fig. 3.1 left). Gdm-derived salts have been studied with a wide range of different anions, including TFSI, for the design of ionic liquids. [170], [171], [172] However, the non-functionalised GdmTFSI (Fig. 3.1 right) has, to the best of our knowledge, only been reported twice. [173], [174] While partially characterised, its structure was not resolved and

properties as a salt in aqueous electrolytes were not studied. Herein, we report a synthesis procedure for GdmTFSI, solve its crystal structure, and provide chemical and electrochemical characterisation of the salt for potential use as co-salt for aqueous batteries.

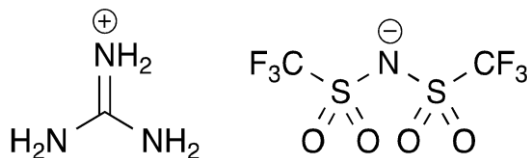


Fig. 3.1 – Guanidium [Gdm]⁺ cation (left), bis(trifluoromethanesulfonyl)imide [TFSI]⁻ anion (right).

3.3 Synthesis and Material Characterisation

The salt was prepared via a cation exchange reaction, using LiTFSI and guanidium sulphate (Gdm₂SO₄) as precursors. In a typical batch, equimolar amounts of LiTFSI and Gdm₂SO₄ were dissolved separately in the minimum volume of water. The Gdm₂SO₄ solution was added dropwise to the LiTFSI solution, with the immediate formation of a crystalline solid. The solution was dried, obtaining a crude solid containing a mixture of GdmTFSI and Li₂SO₄. The mixture was extracted twice with dry acetone, the filtrate was collected, and pure GdmTFSI is obtained after removing the solvent under vacuum, with a yield of 97%. To confirm if the synthesis procedure was successful and the final product was absent of any impurities, inductively coupled plasma mass spectrometry (ICP-MS) was used to probe any residual lithium content, where only 3.7 μgLi.mg⁻¹ was detected (Fig. 3.2a). To confirm that the salt is absent of any residual SO₄²⁻, a simple sulphate test was carried out using BaCl₂. If SO₄²⁻ is present, the insoluble BaSO₄ would precipitate out in aqueous solutions. [175] Dilute equimolar solutions of GdmTFSI and BaCl₂ were mixed and the solution remained clear indicating that no detectable SO₄²⁻ is present in the final product.

Thermogravimetric analysis (TGA) as seen in Fig. 3.2b (grey), showcases that GdmTFSI is free of moisture and has a decomposition temperature of 350 °C indicating the salt has high thermal stability. Differential scanning calorimetry (DSC) seen in Fig. 3.2b (red) which highlights the phase transition at 96 °C from solid to a liquid, consistent with the previously reported melting point of the compound (98 °C). [173], [174] This

would technically denote the GdmTFSI salt as an ionic liquid ($< 100^{\circ}\text{C}$), however there is no real application for an ionic liquid at these high temperatures.

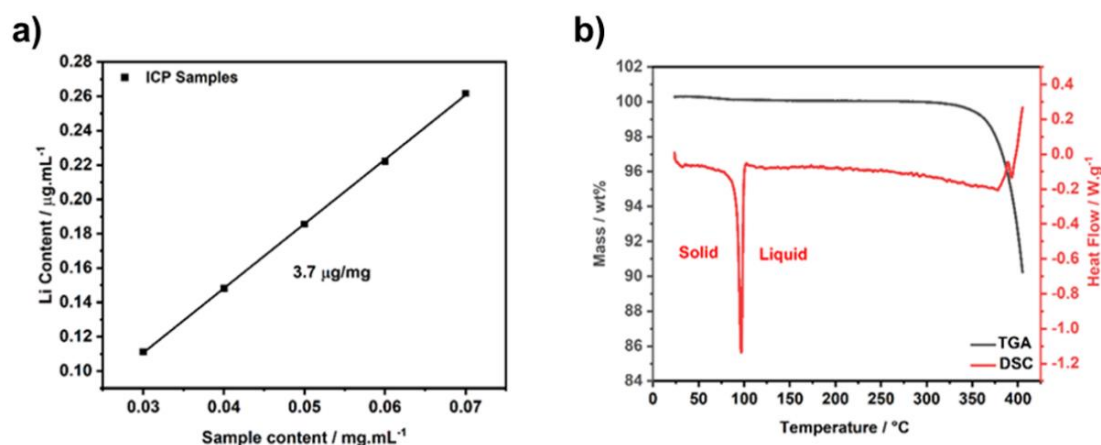


Fig. 3.2 - a) Residual lithium content probed using inductively coupled plasma mass spectrometry (ICP-MS) and b) Thermogravimetric analysis (TGA) in grey and differential scanning calorimetry (DSC) in red.

Single-crystal X-ray diffraction was used to solve the crystal structure of the salt. Suitable crystals were obtained by slow evaporation of a GdmTFSI solution in water. GdmTFSI crystallizes in a triclinic P-1 space group with cell parameters: $a = 15.9721(9)$ Å, $b = 18.6173(9)$ Å, and $c = 25.1641(5)$ Å; and angles $\alpha = 89.960(3)^{\circ}$, $\beta = 85.636(3)^{\circ}$, and $\gamma = 87.428(4)^{\circ}$. The crystals are composed of Gdm-TFSI layers held together by a hydrogen bonding network (HBN) between the $-\text{NH}_2$ groups of the Gdm^+ and the $-\text{SO}_2$ and $-\text{N}-$ atoms of the TFSI^- (Fig. 3.3a). The TFSI^- alternates between cis and trans conformation along the a axis of the cell in cis-trans-cis configuration (Fig. 3.3b). Crystallographic parameters and data refinement results are given in Table 3.1.

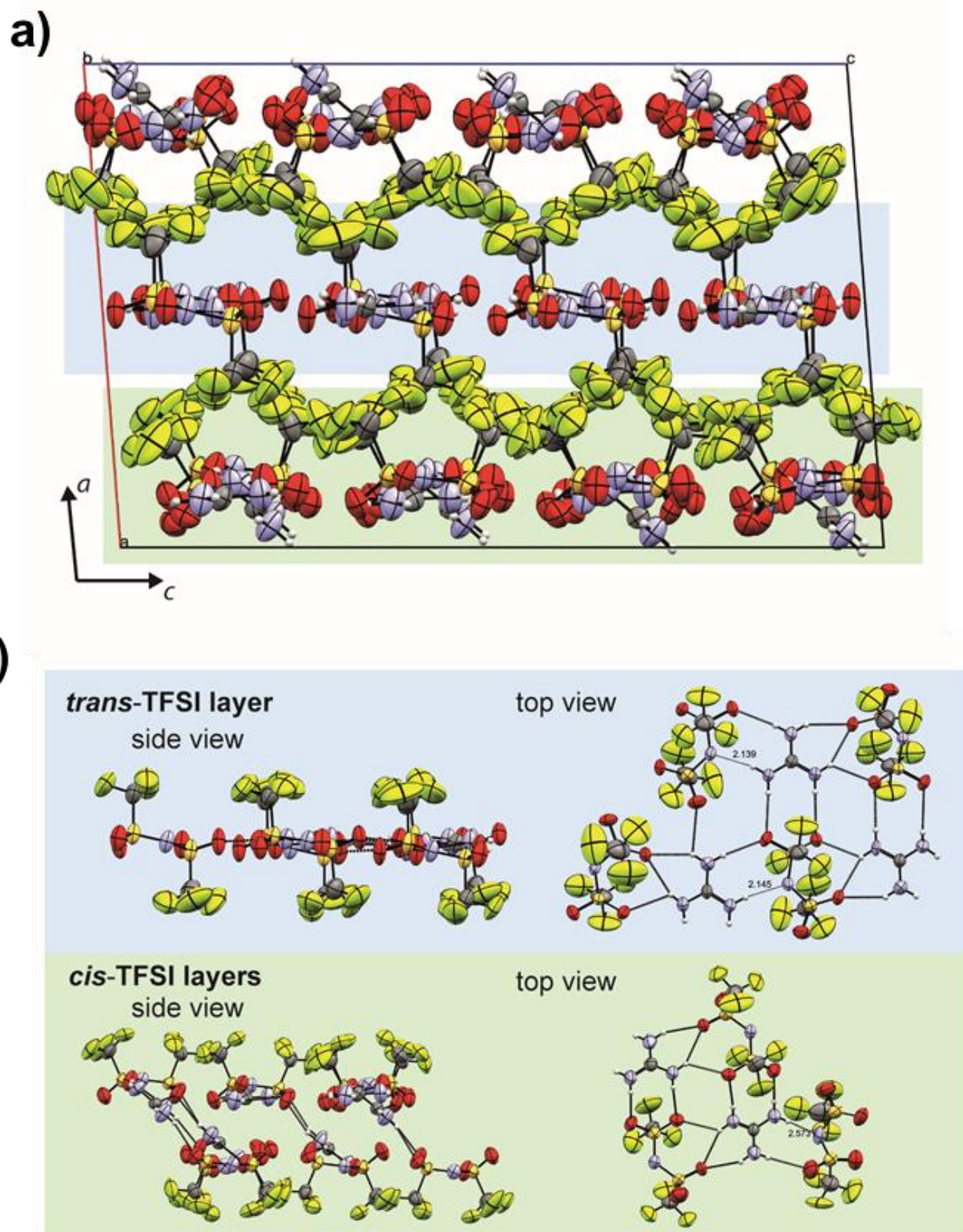


Fig. 3.3 - a) Crystal packing of GdmTFSI and b) *trans*-TFSI layer with side & top view (top) & *cis*-TFSI layer with side & top view(bottom).

Identification code	Gua_ (CCDC number 2284950)
Empirical formula	C ₃ H ₆ F ₆ N ₄ O ₄ S ₂
Formula weight	340.24
Temperature/K	293
Crystal system	triclinic
Space group	P-1
a/Å	15.9721(9)
b/Å	18.6173(9)
c/Å	25.1641(5)
α/°	89.960(3)
β/°	85.636(3)
γ/°	87.428(4)
Volume/Å ³	7453.5(6)
Z	24
ρ _{calc} /cm ³	1.819
μ/mm ⁻¹	0.522
F(000)	4080
Crystal size/mm ³	0.1 × 0.05 × 0.01
Radiation	Mo Kα (λ = 0.71073)
2θ range for data collection/°	3.294 to 46.512
Index ranges	-17 ≤ h ≤ 17, -20 ≤ k ≤ 20, -27 ≤ l ≤ 27
Reflections collected	40087
Independent reflections	20251 [R _{int} = 0.0602, R _{sigma} = 0.0756]
Data/restraints/parameters	20251/306/2452
Goodness-of-fit on F ²	1.038
Final R indexes [I ≥ 2σ (I)]	R ₁ = 0.1025, wR ₂ = 0.2707
Final R indexes [all data]	R ₁ = 0.1390, wR ₂ = 0.3005
Largest diff. peak/hole / e Å ⁻³	1.10/-0.50

Table 3.1 - Crystal data and structure refinement for GdmTFSI.

Further materials characterisation of the salt was carried out using FT-IR. Fig. 3.4a showcases the full FT-IR spectra of the GdmTFSI salt, which displays the presence of both the Gdm⁺ and the TFSI⁻ as the expected bands are visible: $\nu_{\max}/\text{cm}^{-1}$: 3500 – 3200 (ν_{NH}), 1650 (ν_{CN}), 1187 (ν_{aCF_3}), 1122 (ν_{sSO_2}), 1051 (ν_{sSNS}), 791 (ν_{aSNS}), 740 (ν_{sCS}). The different coordination environment of the TFSI between the precursor LiTFSI salt and the obtained GdmTFSI salt can be observed when comparing the respective IR spectras. Fig. 3.4b displays the region between 700 – 850 cm^{-1} , where peaks around 740 cm^{-1} and 800 cm^{-1} correspond to the symmetric and

asymmetric C-S and SNS stretching vibrations (denoted $\nu_s\text{C-S}$ and $\nu_a\text{SNS}$) of the TFSI⁻, respectively. A redshift of these bands is observed for GdmTFSI, indicating that, in the crystal, the TFSI⁻ is more loosely bound compared to LiTFSI. [176] The weaker cation-anion interaction can be explained by the larger size and higher charge delocalization of Gdm⁺ compared to Li⁺ and can be used to explain the lower melting point of 96 °C (GdmTFSI) compared to 234 °C (LiTFSI). [177] The bands in the 3000–3600 cm⁻¹ region corresponds to the -NH stretching vibrations of Gdm⁺, which are influenced by hydrogen bonding interactions between Gdm⁺ and TFSI⁻. Fig. 3.4c illustrates a shift to higher wavenumbers for N-H stretching vibrations in GdmTFSI salt compared to Gdm₂SO₄ salt. This shift can be attributed to the lower charge density of TFSI⁻ compared to SO₄²⁻, resulting in weaker hydrogen bonding with Gdm⁺. Consequently, the N-H bond of Gdm⁺ is strengthened, causing a blueshift of the bands.

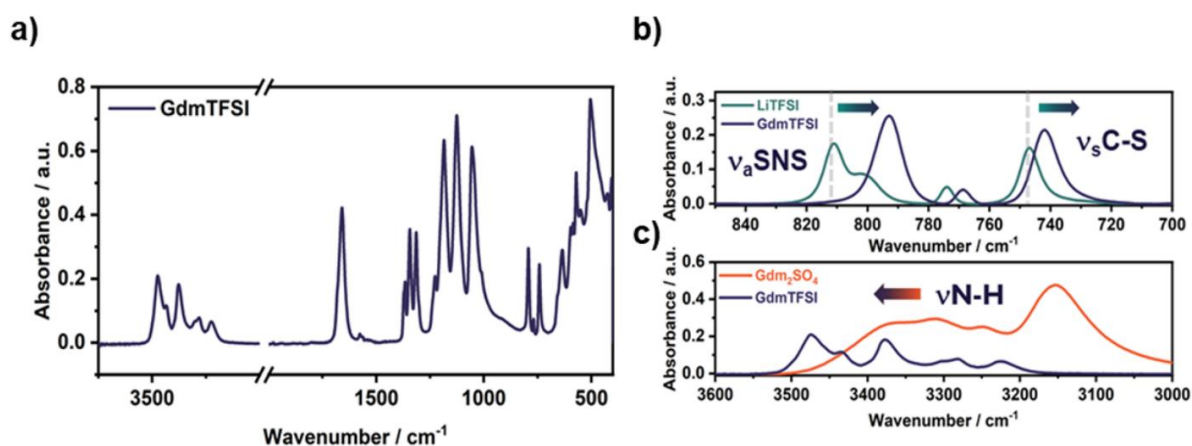


Fig. 3.4 - a) Full IR spectra of GdmTFSI salt, b) 700 – 850 cm⁻¹ IR region of LiTFSI and GdmTFSI salts and c) 3000 – 3600 cm⁻¹ IR region of Gdm₂SO₄ and GdmTFSI salts.

3.4 GdmTFSI in Aqueous Solutions

To probe the characteristics of GdmTFSI in aqueous solutions, electrolytes were prepared up to the saturation limit of 8 m. The FT-IR region at 1000 - 1250 cm⁻¹ which corresponds to vibrations modes from TFSI⁻ of 1, 2, 4 and 8 m are seen in Fig. 3.5a. The region at 700-850 cm⁻¹ studied above for dry salt could not be examined in solution as the peaks are obscured by a broad water band. As the concentration increases, peaks for asymmetric CF₃ and symmetric SNS (denoted $\nu_a\text{CF}_3$ and $\nu_s\text{SNS}$) are shifted to lower wavenumbers, indicating the TFSI⁻ environment changes with

concentration (Fig. 3.5a). Furthermore, the broad band between 1100 and 1150 cm^{-1} , which corresponds to symmetric SO_2 stretching vibration ($\nu_s\text{SO}_2$), appears to be composed of two contributions which vary in intensity as the concentration increases. [178] The low frequency band, centred around 1125 cm^{-1} , becomes predominant for concentrations >4 m. As this band matches the one observed for the GdmTFSI solid, we assign this band to the vibration of TFSI⁻ linked directly to Gdm⁺, i.e. ion pairs, while the high frequency band, centred around 1145 cm^{-1} is assigned to free TFSI⁻ in solution. Hence, as the concentration is increased beyond 4 m, the fraction of ion pairs increases, which is expected to affect the ionic conductivity of the GdmTFSI solutions. Indeed, as the concentration of GdmTFSI is increased from 1 m to 4 m, there is an increase in ionic conductivity, peaking at 48 $\text{mS}\cdot\text{cm}^{-1}$ at 4 m (Fig. 3.5b). However, beyond this point, there is a drop in ionic conductivity until the saturation limit of 8 m. This drop in conductivity beyond 4 m can be attributed to the aforementioned increased ion pairing, observed in the IR spectra, which results in reduced ion mobility. Of course, as the concentration is increased an increase in viscosity is also expected, which also contributes to the decreased ionic conductivity. [179]

Fig. 3.5c showcases the IR region at 2800–4000 cm^{-1} , which includes the -OH stretching vibration modes of water as well as the -NH stretching of Gdm⁺. The water clusters between 2800–4000 cm^{-1} reduce in intensity as the concentration of GdmTFSI increases. This reduction gives way to the presence of -NH stretching frequencies associated with Gdm⁺. The lower wavenumber -OH stretching bands (~ 3200 cm^{-1}), which correspond to strongly H-bonded -OH groups, exhibit a clear decrease in intensity, suggesting a weakening of the HBN of water. [180] This phenomenon could potentially be attributed to the chaotropic effect induced by the salt, which can be further investigated via electrochemistry. We wish to note that for the 8 m GdmTFSI aqueous solution, the salt crystallises out of solution at room temperature during CV measurements, hence measurements were carried out at 30 °C. Glassy carbon tends to have reduced electrocatalytic properties for HER and OER and thus show large overpotentials, producing an elevated ESW compared to a more practical set-up. [181] Nevertheless, these measurements are used for comparative purposes to determine the effect of GdmTFSI salt concentration on the HER/OER kinetics. Defining the current density limit at which water splitting occurs varies from study to study, in our

case we treat a current of $0.25 \text{ mA}\cdot\text{cm}^{-2}$ to be the reductive/oxidative limit of the electrolyte. Probing the ESW (Fig. 3.5d) reveals that as the concentration is increased, there is an expansion of the ESW, from 3.06 V for 1 m GdmTFSI_(aq) to 3.59 V for 8 m GdmTFSI_(aq), showcases an expansion of the reductive limits by 0.21 V and oxidative limits by 0.32 V.

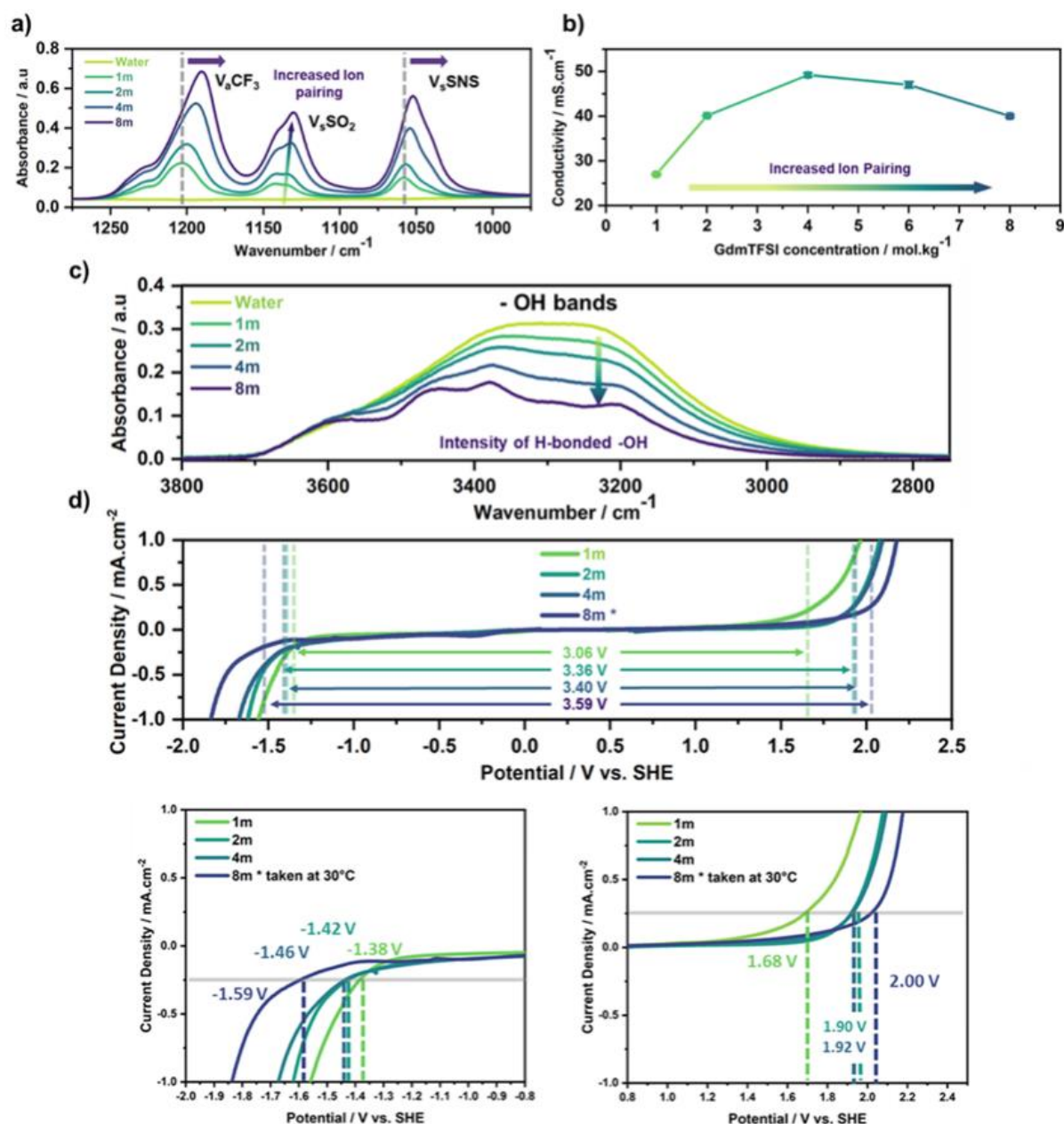


Fig. 3.5 - a) 950-1300 cm^{-1} IR region of GdmTFSI_(aq), b) ionic conductivity of GdmTFSI_(aq), c) 2800-4000 cm^{-1} IR region of GdmTFSI_(aq) and d) ESW from CV data for GdmTFSI_(aq) on glassy carbon taken at 5 mV/s *8m GdmTFSI taken at 30°C.

To ascertain if the formation of a solid electrolyte interphase (SEI) occurs through some sort of decomposition process, as seen with 21 m LiTFSI_(aq), the 8 m GdmTFSI_(aq) electrolyte was tested following the protocol previous utilised by Droguet et al. [11] Fig. 3.6a & 3.6b showcases that the GdmTFSI_(aq) electrolyte did not show evidence of passivation on the GC electrode after 5 cycles with no significant decrease in catalytic current and a lack of a passivation peak, in contrast to 21 m LiTFSI_(aq). The lower saturation limit of GdmTFSI_(aq) may be unable to prevent the dissolution of any decomposition products that result in the formation of a passivating layer. Meanwhile, measurements in ACN as seen in Fig. 3.6c, reveals the salt's stability which is beyond the ESW of ACN (~5 V) [182], indicating that the salt is unable to decompose to form an SEI.

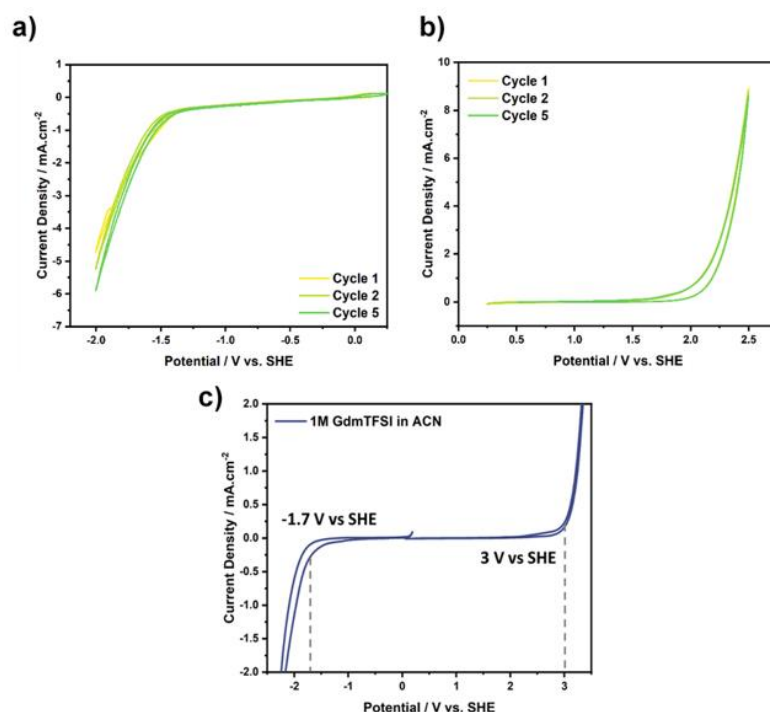


Fig. 3.6 – Passivation test with 8m GdmTFSI_(aq) on glassy carbon taken at 5 mV/s a) in reduction, b) in oxidation and c) Salt decomposition test with 1M GdmTFSI in ACN on glassy carbon taken at 5 mV/s.

3.5 Chaotropic Nature of Gdm⁺

A common way to assess effect of individual ions i.e. chao/kosmo-tropic effects on water structure is to measure the viscosity of dilute solutions (0.0625 – 1 mol/l) and to determine the B-coefficient from the Jones-Dole equation (Eq. 3.1), where positive B-coefficient values = kosmotropic and negative values = chaotropic.

$$\left(\frac{\eta}{\eta_{water}}\right) - 1 = Ac^{\frac{1}{2}} + Bc \text{ (Eq. 3.1)}$$

(η = density, A and B = coefficients and c = concentration)

By comparing the results for GdmTFSI with those obtained for LiTFSI from our previous study, we can calculate the effect of the Gdm cation. [183] Fig. 3.7 provides the slope obtained GdmTFSI solutions at concentrations between 0.0625 – 1 mol/l when fitted linearly with the Jones-Dole equation. GdmTFSI is calculated to have a B-coefficient of +0.46, while LiTFSI was revealed to have a B-coefficient of +0.77 where, Li^+ accounts for +0.18 and TFSI^- +0.59. The positive B-coefficient for TFSI^- , which is unexpected due to the anion being typically characterised as chaotropic, has been explained by the large size and hydrophobic character of the anion. Nevertheless, when using these values, we determine that the Gdm^+ has a B-coefficient of -0.13, indicating the cation is acting as a chaotrope relative to the Li^+ , producing an overall less kosmotropic salt compared to LiTFSI. [183], [184]

A-coefficient	A standard error	B-coefficient	B standard error	R value
-0.068	0.026	0.441	0.035	0.975

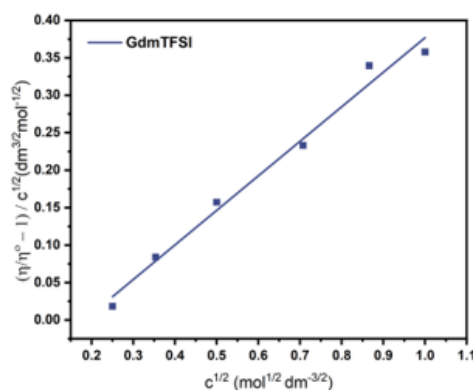


Fig. 3.7 - Viscosity measurements for low concentrations (0.0625 to 1 mol L⁻¹) GdmTFSI(aq) where straight line represents a linear fitting with the Jones-Dole equation.

3.6 Binary Mixture of GdmTFSI + LiTFSI

When comparing GdmTFSI to LiTFSI at the same concentrations, we see an expansion of the ESW by 0.25 V at 1 m and 0.1 V at 8 m, confirming the chaotropic effect of the Gdm^+ (Fig. 3.8a). However, we do take caution in correlating these findings to more quantitative kinetics interpretation. Indeed, when analysing higher concentrations, mass transport factors, such as viscosity, may also contribute to the

reduction of water reactivity. Yet, we hypothesise that the expansion of the ESW is primarily caused by the chaotropic effects of the Gdm^+ . To ascertain the potential application of GdmTFSI as a co-salt, 4 m GdmTFSI is added to 1 m LiTFSI . Doing so, we found the ESW to expand by 0.33 V (Fig. 3.8b). Binary mixtures of salts have recently seen use in so-called “high entropy” electrolytes. [185], [186] While we believe chaotropicity is the main function of GdmTFSI , studying Li^+ dynamics in the bulk and at interfaces in the $\text{GdmTFSI} + \text{LiTFSI}$ mixtures could provide insights into any entropic effects and is worth studying moving forward.

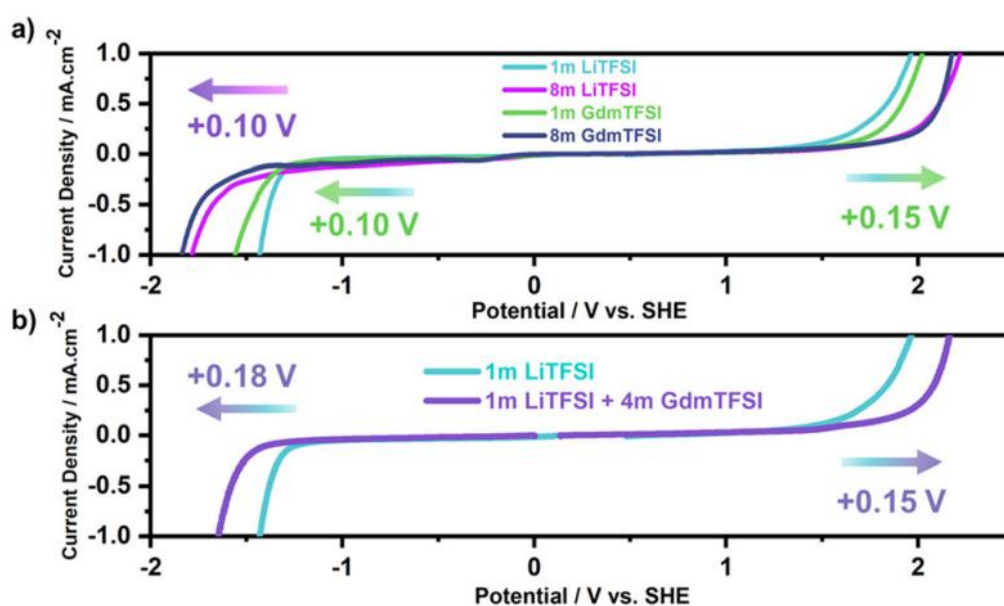


Fig. 3.8 a) ESW from CV data for $\text{GdmTFSI}_{(aq)}$ vs $\text{LiTFSI}_{(aq)}$ on glassy carbon taken at 5 mV/s and b) ESW from CV data for 1 m LiTFSI vs 1 m $\text{LiTFSI} + 4$ m GdmTFSI on glassy carbon taken at 5 mV/s.

Conclusions to Chapter 3

In summary, we have successfully prepared GdmTFSI and confirmed its identity and purity. Probing the FT-IR spectra and viscosity of aqueous GdmTFSI solutions reveals that the salt, particularly the Gdm^+ , which is chaotropic in nature as defined by the Hofmeister series, can disrupt the hydrogen-bonding network of water, reducing water reactivity and expanding the ESW. However, a limitation is the limited solubility in water of GdmTFSI , which prevents water-in-salt regimes that can trigger SEI

formation to further expand the ESW. We envision the potential use of Gdm/Gdm-derived TFSI salts as a co-salt and/or additive with alkaline-metal-based salts.

While no firm application for the salt within a typical two-electrode system was carried out during this study, the idea of using a Gdm-based salt within an aqueous electrolyte was explored for an AZMB within another study carried out in the group. As mentioned in Chapter 1.12, Zn || MnO₂ rechargeable batteries have numerous issues on the anode and cathode side with dendrites and electro-dissolution of MnO₂, respectively. Water reactivity plays a crucial role in these aspects and thus the chaotropic effects of the Gdm cations can be harnessed to mitigate the electro-dissolution of MnO₂ while aiding in preventing dendrites. Fig. 3.9a showcases the results obtained for a Zn || MnO₂ battery utilising 2 M ZnSO₄ as electrolyte, composition classically used in the field. This battery demonstrates high capacity fading with only 69% capacity retention after 50 cycles. Meanwhile, the 2 M ZnSO₄ + 2 M Gdm₂SO₄ has a much-improved capacity retention with 90% of the initial capacity retained after 100 cycles. The cycling curve highlights the reversibility of the system with > 99% CE (Fig. 3.9b). While a more in-depth analysis of this work was not carried out in the context of this thesis, it does highlight a potential practical application of the chaotropic effects of the Gdm⁺.

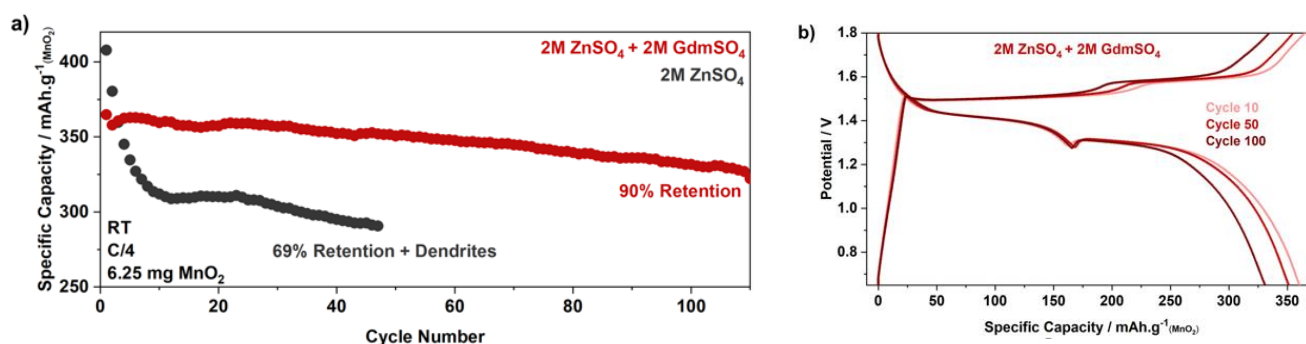


Fig. 3.9 – a) Galvanostatic cycling of Zn || MnO₂ full cell with 2 M ZnSO_{4(aq)} and 2 M ZnSO₄ + 2 M Gdm₂SO_{4(aq)} and b) cycling curve of 2 M ZnSO₄ + 2 M Gdm₂SO_{4(aq)} at cycle 10, 50 and 100.

Chapter 4: Zinc-Oligoether Salts as Electrolyte Additives for Aqueous Zn-Metal Batteries

This chapter is primarily based on two filled patents and a manuscript in preparation:

- **J. Brown**, I. Aguilar, J. M. Tarascon, Novel Oligoether Salts as Additive for Zinc-metal Batteries, (Patent Filled – June 2024)
- I. Aguilar, **J. Brown**, J. M. Tarascon, New Electrolyte Mixture for Stable Zn/MnO₂ Batteries Across Wide Temperature Range, (Patent Filled – June 2024)

4.1 Introduction

Building on the work described in the conclusions of Chapter 3 on AZMBs, we aimed to design novel salts that can potentially improve performance by mitigating dendrite growth. Simultaneously, we wished to build on the principles described in Chapters 1.5.1 and 1.5.5, which relate to molecular crowding and playing on the salt-to-water content. With this in mind, we identified alkali metal oligoether carboxylates as being of particular interest. Specifically, our attention turned to the (2-[2-(2-methoxyethoxy)ethoxy]acetate)₂ (MEEA) (*also denoted as 2,5,8,11-tetraoxatridecan-13-oate - abbreviated to TOTO*) as described by Kunz et al. [187] The anion contains a glyme-like ether chain with one terminal group containing a carboxyl function (Fig. 4.1). Kunz and co-workers synthesised the Li, Na, and K variants of the salt. They focused their efforts on the fact that NaMEEA and LiMEEA were ionic liquids at room temperature. The viscosity and conductivity were only reported for NaMEEA as a pure salt, with 167000 mPa.s⁻¹ and 3.37x10⁻⁴ mS.cm⁻¹, at room temperature, respectively. These values make these salts highly impractical for use as pure ionic liquids, especially when comparing to the commonly used EmimTFSI, which has a viscosity and conductivity of 35 mPa.s⁻¹ and 8 ms.cm⁻¹. [188], [189] They tested the ESW for both Li- and Na-salt by dissolving them in ACN, revealing a fairly wide ESW with 4.7 V reported for NaMEEA and 6.7 V for LiMEEA. However, the exact conditions and cut-off potentials are not reported so these values must be taken with caution. The alkali metal variants of the salts would see little attention after this initial work, and the group would later branch out to organic cations such as quaternary ammonium and choline which resulted in much lower viscosities leading to broader applications outside of batteries. [190] We find these oligoether carboxylates interesting because the anion

can be adapted in length, potentially leading to different characteristics. Given the structural similarities to glymes, ethers, and even polymers—substances extensively used for both aqueous and non-aqueous battery electrolytes—we wanted to revisit these salts, particularly the Zn variants, as these have not previously been reported. However, instead of focusing on their properties as ionic liquids, we aim to use them as primary salts, co-salts, or additives for aqueous electrolytes. [31], [49]

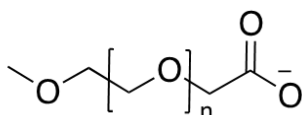


Fig 4.1 – base formula for oligoether chains.

4.2 Zinc Oligoethers

To synthesise $\text{Zn}(\text{MEEA})_2$, the procedure from Kunz et al [187] was used with slight modifications. Using the $\text{Zn}(\text{MEEA})_2$ as an example, the synthesis starts by first synthesising 2-[2-(2-methoxyethoxy)ethoxy]acetic acid. This is done by first dissolving lithium metal in an excess of (2-(2-(2-Methoxyethoxy)ethoxy)ethanol) (TEGDME), after which chloroacetic acid dissolved in TEGME is added dropwise into the solution and is reacted for 16 hours. Excess TEGME is removed via distillation after which the solution is treated with an aqueous solution of orthophosphoric acid. Dichloromethane (DMC) was added to the solution, resulting in the formation of two immiscible phases. The aqueous phase was further washed with DMC, and the organic phase was separated and dried using magnesium sulphate. This solution is then distilled under vacuum to yield the 2-[2-(2-methoxyethoxy)ethoxy]acetic acid (HMEEA). The $\text{Zn}(\text{MEEA})_2$ was prepared via cation exchange reaction in water using zinc carbonate basic ($\text{Zn}_5(\text{CO}_3)_2(\text{OH})_6$). The resulting solution was distilled under vacuum to yield the $\text{Zn}(\text{MEEA})_2$. To synthesize the smaller chains, zinc (2-methoxyethyl carbonate)₂ ($\text{Zn}(\text{MEC})_2$) and zinc (2-(2-methoxyethoxy)acetate)₂ ($\text{Zn}(\text{MEA})_2$), the acid precursors, i.e., HMEC and HMEA, were obtained from suppliers, and the acid neutralisation with zinc carbonate basic was performed. A full description of the synthesis procedure can be found in the materials and methods in the ANNEX for Chapter 4. $\text{Zn}(\text{MEC})_2$ and $\text{Zn}(\text{MEA})_2$ yielded white powders, while $\text{Zn}(\text{MEEA})_2$ formed a slightly yellow and highly viscous liquid.

To confirm the synthesis was successful, ^1H and ^{13}C NMR spectroscopy was used to characterise the salts. The NMR spectra for $\text{Zn}(\text{MEC})_2$ (Fig. 4.2) is in agreement with the expected spectra with three proton environments and four carbon environments detected, albeit with some impurities denoted with * in the spectra. The Elemental Analysis (EA) (*found below the NMR*) for $\text{Zn}(\text{MEC})_2$ revealed the C and H % were within 1.5% for C and 0.3 % for H of the calculated ratios. Meanwhile, Electrospray Ionisation Mass Spectrometry (ESI-MS) for $\text{Zn}(\text{MEC})_2$ detects the full protonated salt and a mass which is in-line with $\text{Zn}(\text{MEC})$. The full mass spectra can be found in Fig. A4.1.

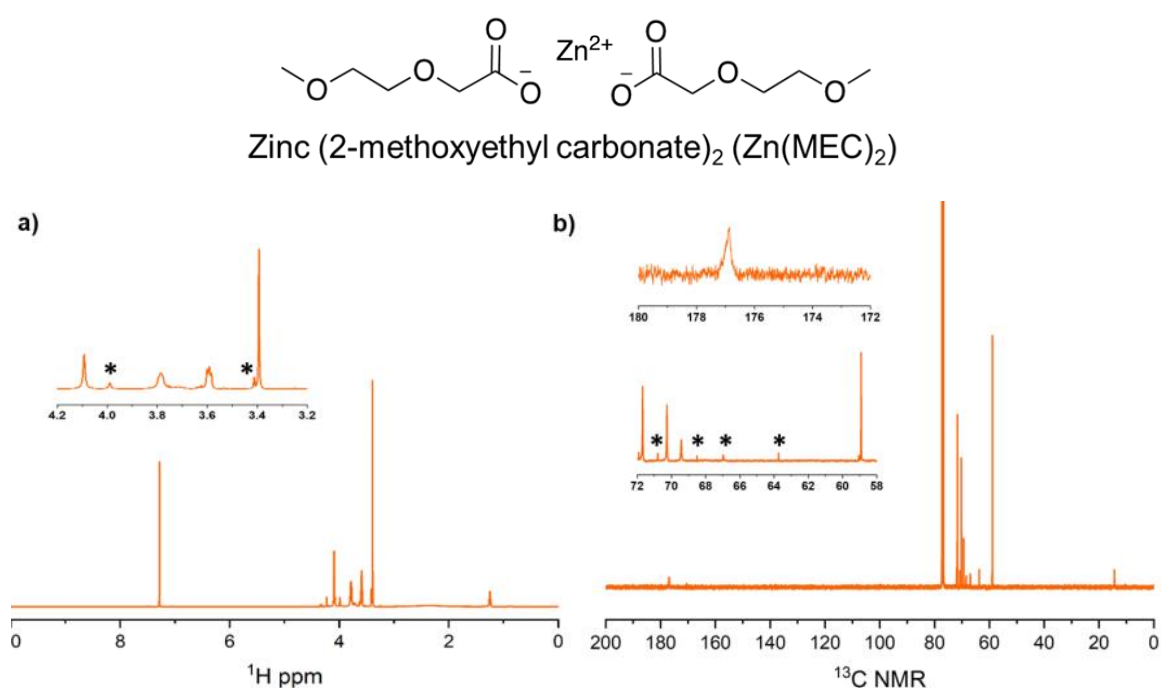


Fig. 4.2 - a) ^1H NMR of $\text{Zn}(\text{MEC})_2$ * denotes impurities, most likely HMEC precursor b) ^{13}C NMR of $\text{Zn}(\text{MEC})_2$ * denotes impurities, most likely HMEC precursor.

^1H -NMR (300 MHz, CDCl_3 , TMS): ^dH : 3.4 (s, 6 H, CH_3), 3.55-3.81 (m, 8 H, CH_2), 4.11 (s, 4 H, CH_2COO^-)

^{13}C -NMR (300 MHz, CDCl_3 , TMS): ^dC : 58.91 (2 C, CH_3), 69.42 (2 C, CH_2COO^-), 68.61 (2 C, CH_2OCH_3), 68.61 (2 C, $\text{CH}_2\text{OCH}_2\text{COO}^-$), 176.81 (2 C, COO^-)

Elemental analysis: calculated: 36.22% C, 5.78% H; found: 34.88% C, 5.47% H

ESI-MS (DCM-MeOH, NH_4Ac): m/z (+): 196.98 (20%, $\text{Zn}(\text{MEC})\text{H}^+$), 331.04 (75%, $\text{Zn}(\text{MEC})\text{H}^+$)

The NMR spectra for $\text{Zn}(\text{MEA})_2$ (Fig. 4.3) is in agreement with the expected spectra with three proton environments and five carbon environments detected. There are some slight impurities, denoted with * in the spectra. The EA for $\text{Zn}(\text{MEA})_2$ revealed the C and H % were within 1 % for C and 0.2 % for H of the calculated ratios. Meanwhile, ESI-MS for $\text{Zn}(\text{MEA})_2$ detects the full protonated salt and a mass which is in-line with $\text{Zn}(\text{MEA})$. The full mass spectra can be found in Fig. A4.2.

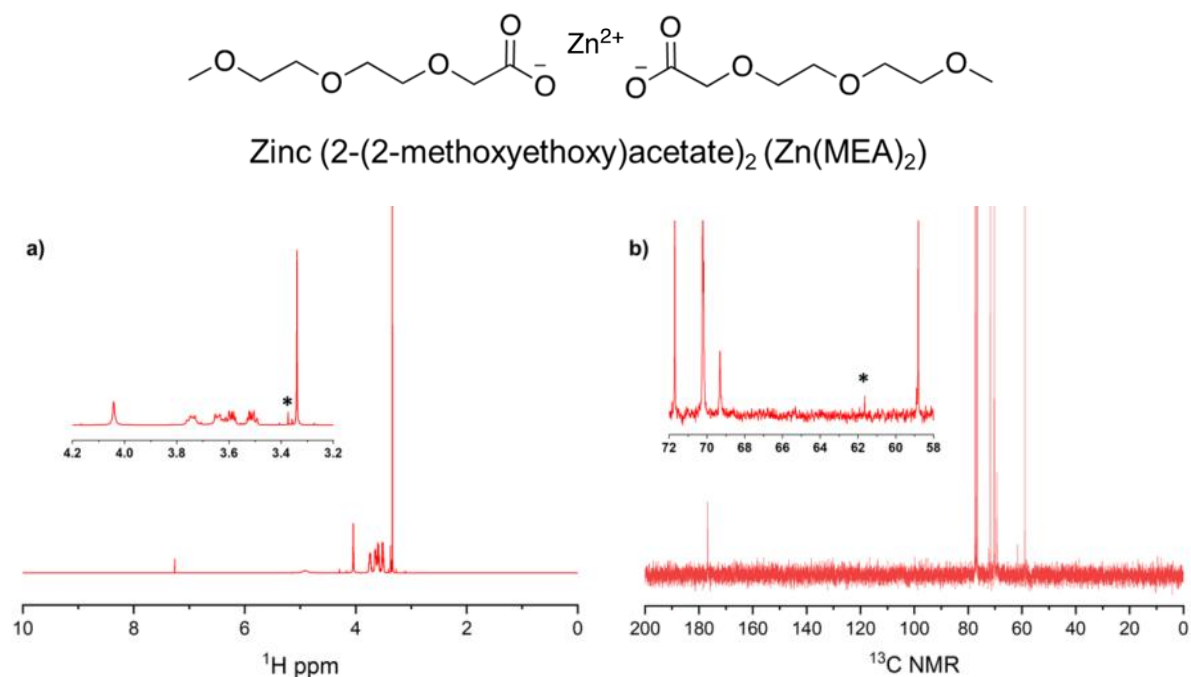


Fig. 4.3 - a) ^1H NMR of $\text{Zn}(\text{MEA})_2$ * denotes impurities, most likely HMEA precursor b) ^{13}C NMR of $\text{Zn}(\text{MEA})_2$ * denotes impurities, most likely HMEC precursor.

^1H -NMR (300 MHz, CDCl_3 , TMS): ^1H : 3.33 (s, 6 H, CH_3), 3.47-3.77 (m, 16 H, CH_2), 4.04 (s, 4 H, CH_2COOH)

^{13}C -NMR (300 MHz, CDCl_3 , TMS): ^{13}C : 58.86 (2 C, CH_3), 68.61 (2 C, CH_2COO^-), 70.21 (6 C, CH_2), 71.72 (2 C, CH_2OCH_3), 176.10 (2 C, COO^-)

Elemental analysis: calculated: 40.06 % C, 6.24% H; found: 39.125% C, 6.546% H

ESI-MS (DCM-MeOH, NH_4Ac): m/z (+p): 241.01 (100%, $\text{Zn}(\text{MEA})\text{H}^+$), 419.09 (100%, $\text{Zn}(\text{MEA})_2\text{H}^+$)

The NMR spectra for $\text{Zn}(\text{MEEA})_2$ (Fig. 4.4) is in agreement with the expected spectra with three proton environments and six carbon environments detected. The EA (found for $\text{Zn}(\text{MEA})_2$ revealed the C and H % were within 1 % for C and 0.8 % for H of the calculated ratios. Meanwhile, ESI-MS for $\text{Zn}(\text{MEEA})_2$ detects the full protonated salt and a mass which is in-line with $\text{Zn}(\text{MEEA})$. The full mass spectra can be found in Fig. A4.3.

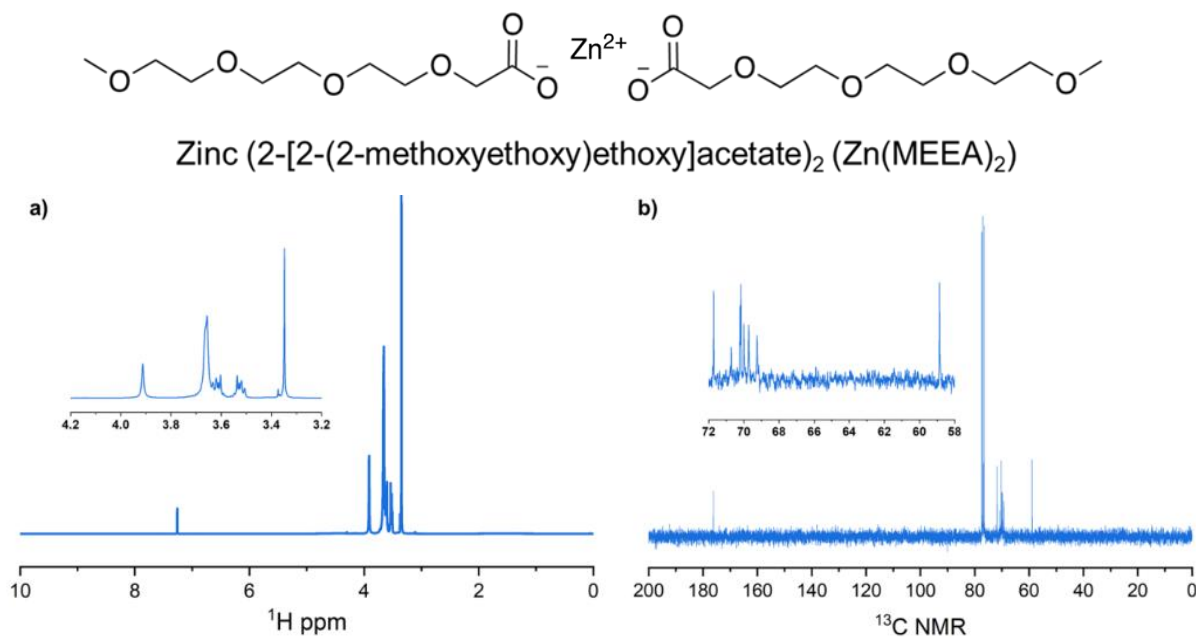


Fig. 4.4 - a) ^1H NMR of $\text{Zn}(\text{MEEA})_2$ b) ^{13}C NMR of $\text{Zn}(\text{MEEA})_2$.

^1H -NMR (300 MHz, CDCl_3 , TMS): δH : 3.30 (s, 6 H, CH_3), 3.48-3.68 (m, 24 H, CH_2), 3.91 (s, 4 H, CH_2COO^-)

^{13}C -NMR (300 MHz, CDCl_3 , TMS): δC : 58.86 (CH_3), 68.61 (CH_2COO^-), 69.95 –70.50 (8 C, CH_2), 71.14 ($\text{CH}_2\text{OCH}_2\text{COO}^-$), 71.77 (CH_3OCH_2), 176.10 (COO^-)

Elemental analysis: calculated: 42.57% C, 6.75% H; found: 43.52% C, 7.56% H

ESI-MS (DCM-MeOH, NH_4Ac): m/z (+p): 285.03 (100%, $\text{Zn}(\text{MEEA})\text{H}^+$), 477.13 (100%, $\text{Zn}(\text{MEEA})_2\text{-CH}_2\text{O}$) 507.14 (75%, $\text{Zn}(\text{MEEA})_2\text{H}^+$)

Based on the NMR, EA and MS data we are confident that the salts were all successfully synthesised. To further characterise the salts, differential scanning calorimetry (DSC) was used and revealed that melting and glass transition temperatures decrease with longer chains. $\text{Zn}(\text{MEC})_2$ has a glass transition temperature of 145 °C (Fig. 4.5a), whereas $\text{Zn}(\text{MEA})_2$ is technically an ionic liquid with a glass transition temperature of 97 °C (Fig. 4.5b). $\text{Zn}(\text{MEEA})_2$ has no discernible glass transition temperature (Fig. 4.5c), indicating that $\text{Zn}(\text{MEEA})_2$ is a room temperature ionic liquid. However, low temperature DSC is needed to confirm this hypothesis and will be carried out in the near future. Thermogravimetric analysis (TGA) demonstrated high thermal stability, with decomposition temperatures around 300°C for all three salts.

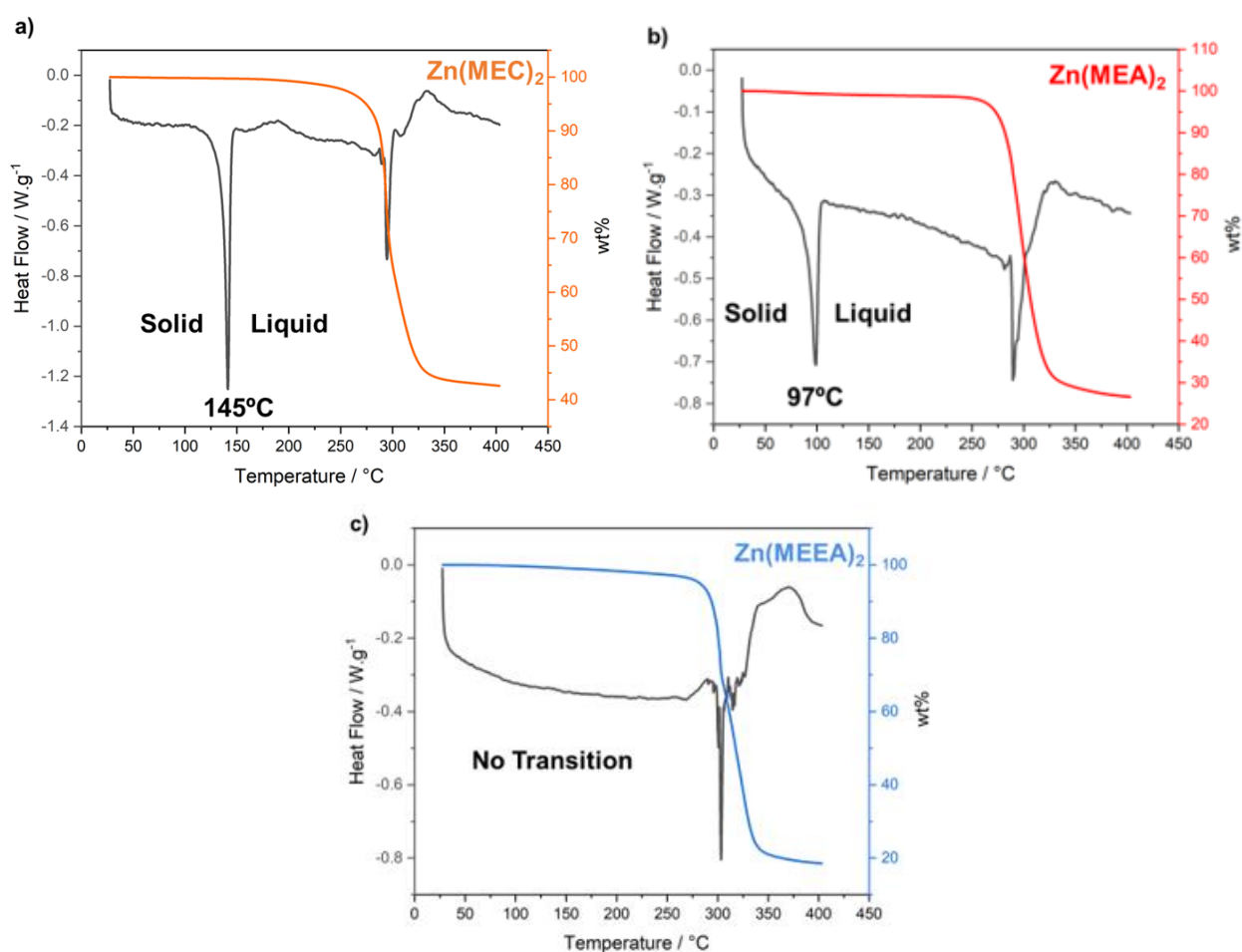


Fig 4.5 – a) Differential scanning calorimetry (DSC) in grey and thermogravimetric analysis (TGA) in orange for $\text{Zn}(\text{MEC})_2$, b) DSC (grey) and TGA (red) for $\text{Zn}(\text{MEC})_2$ and c) DSC (grey) and TGA (red) for $\text{Zn}(\text{MEEA})_2$.

$\text{Zn}(\text{MEC})_2$, $\text{Zn}(\text{MEA})_2$, and $\text{Zn}(\text{MEEA})_2$ were then tested as primary salts in aqueous solutions at a concentration of 1 mol.L^{-1} . The conductivity of the salts is 8.0, 6.1, and 3.4 mS.cm^{-1} , for $\text{Zn}(\text{MEC})_2$, $\text{Zn}(\text{MEA})_2$, and $\text{Zn}(\text{MEEA})_2$, respectively (Fig. 4.8a). This is much lower when compared to 48 mS.cm^{-1} obtained for 2 M ZnSO_4 electrolyte, commonly employed in AZMBs. The drastically reduced conductivity compared to the ZnSO_4 is likely down to the large anion chains which could inhibit ion mobility in solution. $\text{Zn} \parallel \text{Zn}$ symmetric cells were tested at 1 mA.cm^{-2} for 1 mAh.cm^{-2} . The cells using $1 \text{ M Zn}(\text{MEC})_2$ and $\text{Zn}(\text{MEA})_2$ could cycle for up to 100 hours, while using $\text{Zn}(\text{MEEA})_2$ lasted around 50 hours (Fig. 4.6b). As discussed in Chapter 1.7.2, poor conductivity can lead to over-potential, causing changes to the electric field, which results in Zn^{2+} accumulation at the anode–electrolyte interface and promotes dendrite formation. This likely explains the early presence of dendrites in the $1 \text{ M Zn}(\text{MEEA})_2$ solution. Therefore, we believe that any practical application of these salts as primary salts or at high concentrations is unlikely.

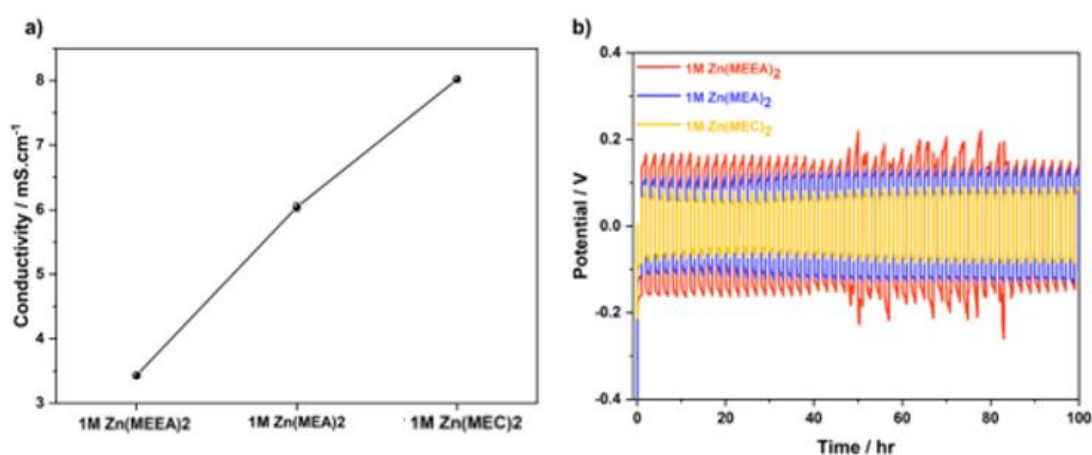


Fig 4.6 – a) Ionic conductivity for $\text{Zn}(\text{MEC})_2$, $\text{Zn}(\text{MEA})_2$ and $\text{Zn}(\text{MEEA})_2$ and b) $\text{Zn} \parallel \text{Zn}$ symmetric cells for $1 \text{ M Zn}(\text{MEC})_2$ (orange), $1 \text{ M Zn}(\text{MEA})_2$ (blue) and $1 \text{ M Zn}(\text{MEEA})_2$ (red).

4.3 Use of $\text{Zn}(\text{MEC})_2$, $\text{Zn}(\text{MEA})_2$ and $\text{Zn}(\text{MEEA})_2$ as Additives

As the conductivity of these novel salts in aqueous media is drastically lower compared to conventional Zn-based aqueous electrolytes, using these salts as additives was tested next. To benchmark this, 2 M ZnSO_4 was used as the base electrolyte, and 5 wt% of $\text{Zn}(\text{MEC})_2$, $\text{Zn}(\text{MEA})_2$, and $\text{Zn}(\text{MEEA})_2$ were added. FT-IR and NMR spectroscopy revealed no drastic changes upon the addition of the salts to 2 M ZnSO_4 that would indicate a change in the solvation or bulk water properties (Fig. 4.7a). NMR did show the presence of the salts within the electrolyte, but no major shifts in peaks, indicating a different chemical environment, were observed (Fig. 4.7b-e).

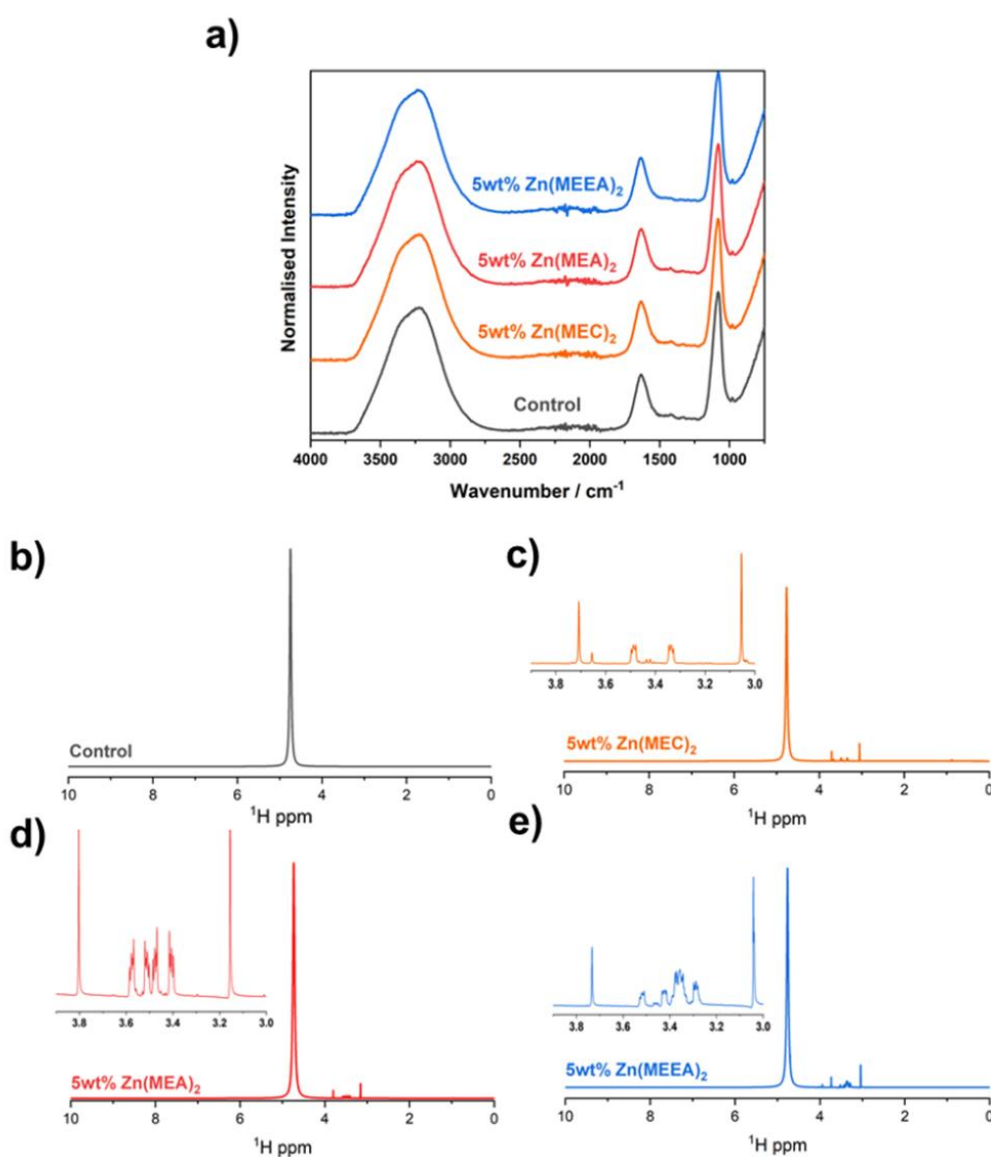


Fig 4.7 – a) FT-IR of 2 M ZnSO_4 (grey), 2 M ZnSO_4 + 5wt% $\text{Zn}(\text{MEC})_2$ (orange), 2 M ZnSO_4 + 5wt% $\text{Zn}(\text{MEA})_2$ (red) and 2 M ZnSO_4 + 5wt% $\text{Zn}(\text{MEEA})_2$ (blue), b) ¹H NMR for 2 M ZnSO_4 , c) ¹H NMR 2 M ZnSO_4 + 5wt% $\text{Zn}(\text{MEC})_2$, d) ¹H NMR 2 M ZnSO_4 + 5wt% $\text{Zn}(\text{MEA})_2$ and e) ¹H NMR 2 M ZnSO_4 + 5wt% $\text{Zn}(\text{MEEA})_2$.

The addition of 5 wt% of the salts decreases the conductivity from $48 \text{ mS}\cdot\text{cm}^{-1}$ to approximately $40 \text{ mS}\cdot\text{cm}^{-1}$ (Fig. 4.8a). Cyclic voltammetry (CV) on glassy carbon was used to investigate the stripping/plating process (Fig. 4.8b). This analysis revealed that the addition of the salts causes a slight increase in polarisation with chain length. Specifically, adding 5 wt% of $\text{Zn}(\text{MEEA})_2$ shifts the onset of Zn nucleation to 40 mV lower in potential compared to the 2 M ZnSO_4 control. This reduced nucleation potential is hypothesised to result in Zn deposits with a smaller nucleation radius and grain size, leading to a more uniform Zn deposition compared to the 2 M ZnSO_4 control (Fig. 4.8c). [138] Aside from the increased polarisation, no drastic changes were observed in the stripping/plating process on glassy carbon.

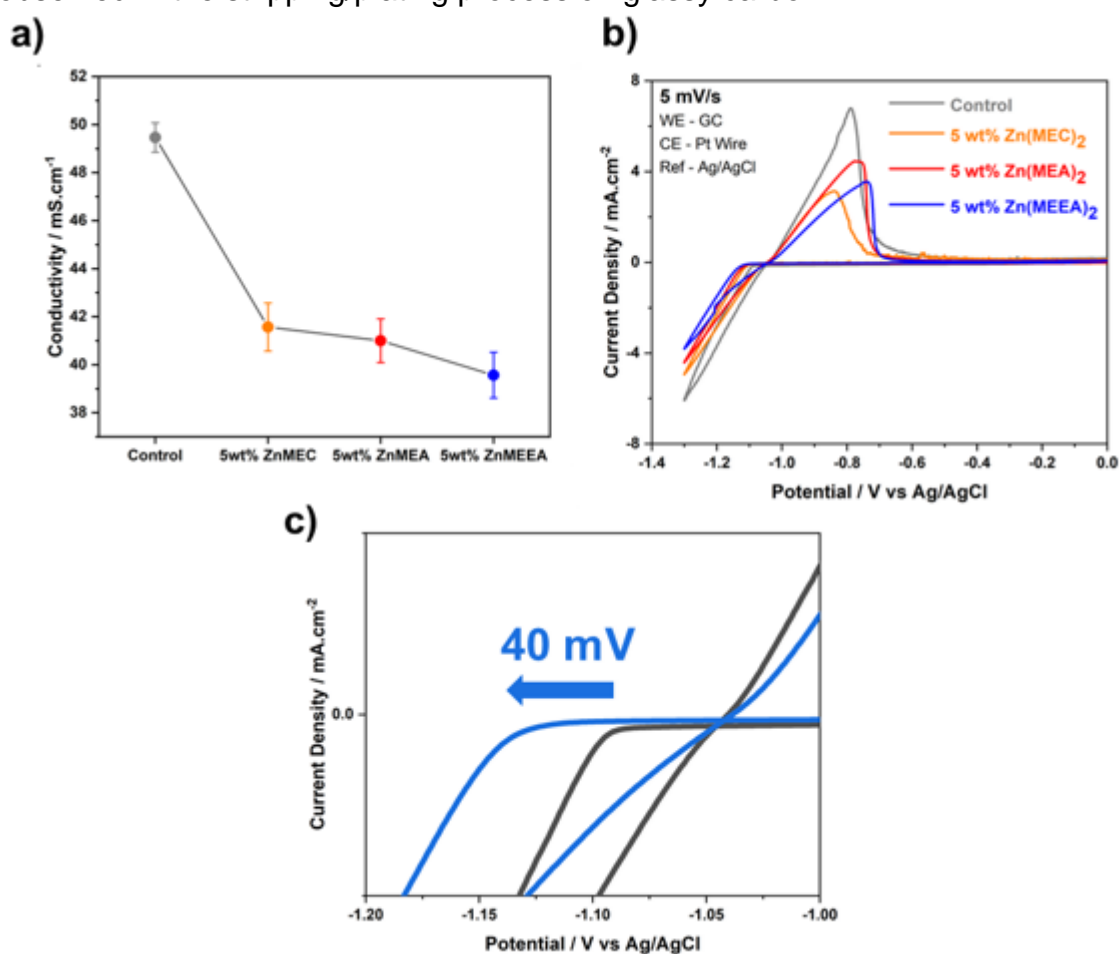


Fig 4.8 – a) Ionic conductivity for 2 M ZnSO_4 (grey), 2 M ZnSO_4 + 5wt% $\text{Zn}(\text{MEC})_2$ (orange), 2 M ZnSO_4 + 5wt% $\text{Zn}(\text{MEA})_2$ (red) and 2 M ZnSO_4 + 5wt% $\text{Zn}(\text{MEEA})_2$ (blue) b) cyclic voltammetry of electrolytes at 5 mV/s on glassy carbon (WE), Pt wire (CE) and Ag/AgCl leakless electrode (REF) and c) zoomed on Zn plating step for 2 M ZnSO_4 (grey) 2 M ZnSO_4 + 5wt% $\text{Zn}(\text{MEEA})_2$ (blue).

To test the long-term stability of these electrolytes, galvanostatic cycling of Zn || Zn symmetric cells were conducted. A capacity of $2.5 \text{ mAh}\cdot\text{cm}^{-2}$ at a current density of $0.624 \text{ mA}\cdot\text{cm}^{-2}$, equivalent to a C-rate of C/4, was used. The control electrolyte, containing only 2 M ZnSO_4 , cycled for 200 hours before dendrite formation occurred, consistent with previous reports in the literature. [133], [138], [139] Meanwhile, all electrolytes containing the zinc oligoether salts demonstrated over 1000 hours of stable cycling. $\text{Zn}(\text{MEEA})_2$ showed a slight increase in polarisation compared to $\text{Zn}(\text{MEC})_2$ and $\text{Zn}(\text{MEA})_2$, which had comparable overpotentials. Figure 4.9 illustrates that the cycling curves for electrolytes with 5 wt% $\text{Zn}(\text{MEC})_2$, $\text{Zn}(\text{MEA})_2$, and $\text{Zn}(\text{MEEA})_2$ reveal no significant differences between cycling at 200 hours and 900 hours, with no soft shorts occurring.

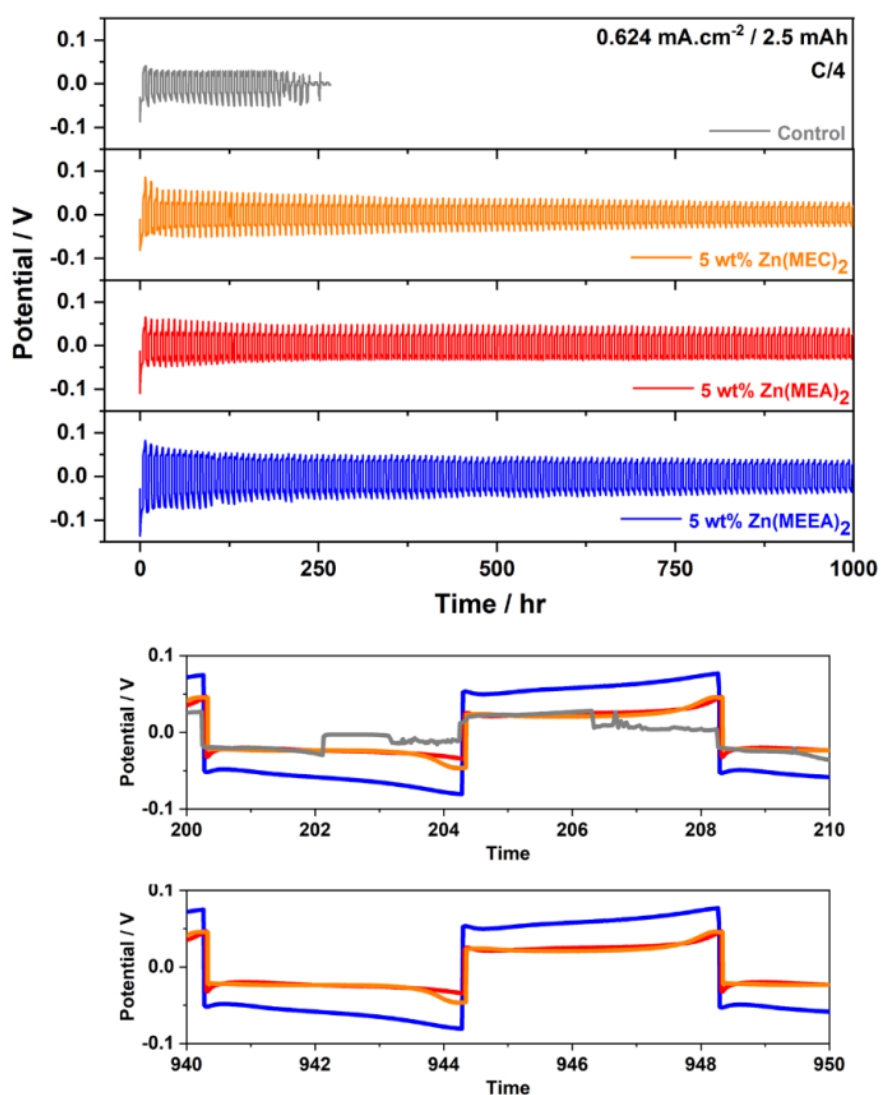


Fig 4.9 – Zn || Zn symmetric cells for 2 M ZnSO_4 (grey), $2 \text{ M ZnSO}_4 + 5\text{wt}\% \text{ Zn}(\text{MEC})_2$ (orange), $2 \text{ M ZnSO}_4 + 5\text{wt}\% \text{ Zn}(\text{MEA})_2$ (red) and $2 \text{ M ZnSO}_4 + 5\text{wt}\% \text{ Zn}(\text{MEEA})_2$ (blue).

Upon visual observation of Zn anodes recovered after cycling, a clear improvement in morphology is evident when using the additives compared to the control (Fig. 4.10 top). To investigate the morphology of the cycled Zn anodes, scanning electron microscopy (SEM) was employed on Zn anodes after 20 cycles at C/4. SEM images reveal mossy zinc growth and general inhomogeneity in the Zn anode cycled with the control 2 M ZnSO₄ electrolyte (Fig. 4.10a). The SEM images of the 5 wt% Zn(MEC)₂ anodes show similar mossy Zn growth and inhomogeneity, though with fewer voids, which could indicate less dead zinc (Fig. 4.10b). In contrast, the Zn anodes cycled with 5 wt% Zn(MEA)₂ (Fig. 4.10c) and Zn(MEEA)₂ (Fig. 4.10d) exhibit a markedly different morphology with vastly improved homogeneity. Zn(MEEA)₂ displays the most homogeneous surface, with what appears to be a predominantly horizontal array of Zn crystals, along with some random orientations and defects. It has been reported that horizontal crystal growth, Zn(002) plane, offers higher chemical stability for Zn electrodeposition due to its lower surface energy compared to other planes.[191] Conversely, the Zn(100) plane, which signifies vertical crystal growth, has a higher surface energy, leading to a higher self-diffusion barrier for Zn. This results in a higher likelihood of dendrite growth due to the increased number of nucleation sites. It is believed that increasing the proportion of Zn(002) relative to Zn(100) during electrodeposition promotes greater cyclic reversibility.[191], [192], [193] The (002) and (100) crystal orientations can be identified using X-ray diffraction (XRD) patterns (Fig. 4.10 bottom). By examining the ratio between (002) and (100), we can determine if one orientation is preferred over the other upon the addition of Zn(MEEA)₂. The (002)/(100) ratios are 1.28 for 2 M ZnSO₄ and 1.60 for 2 M ZnSO₄ + 5 wt% Zn(MEEA)₂. This indicates that the addition of Zn(MEEA)₂ promotes the growth of (002) crystals, resulting in more favourable electrodeposition.

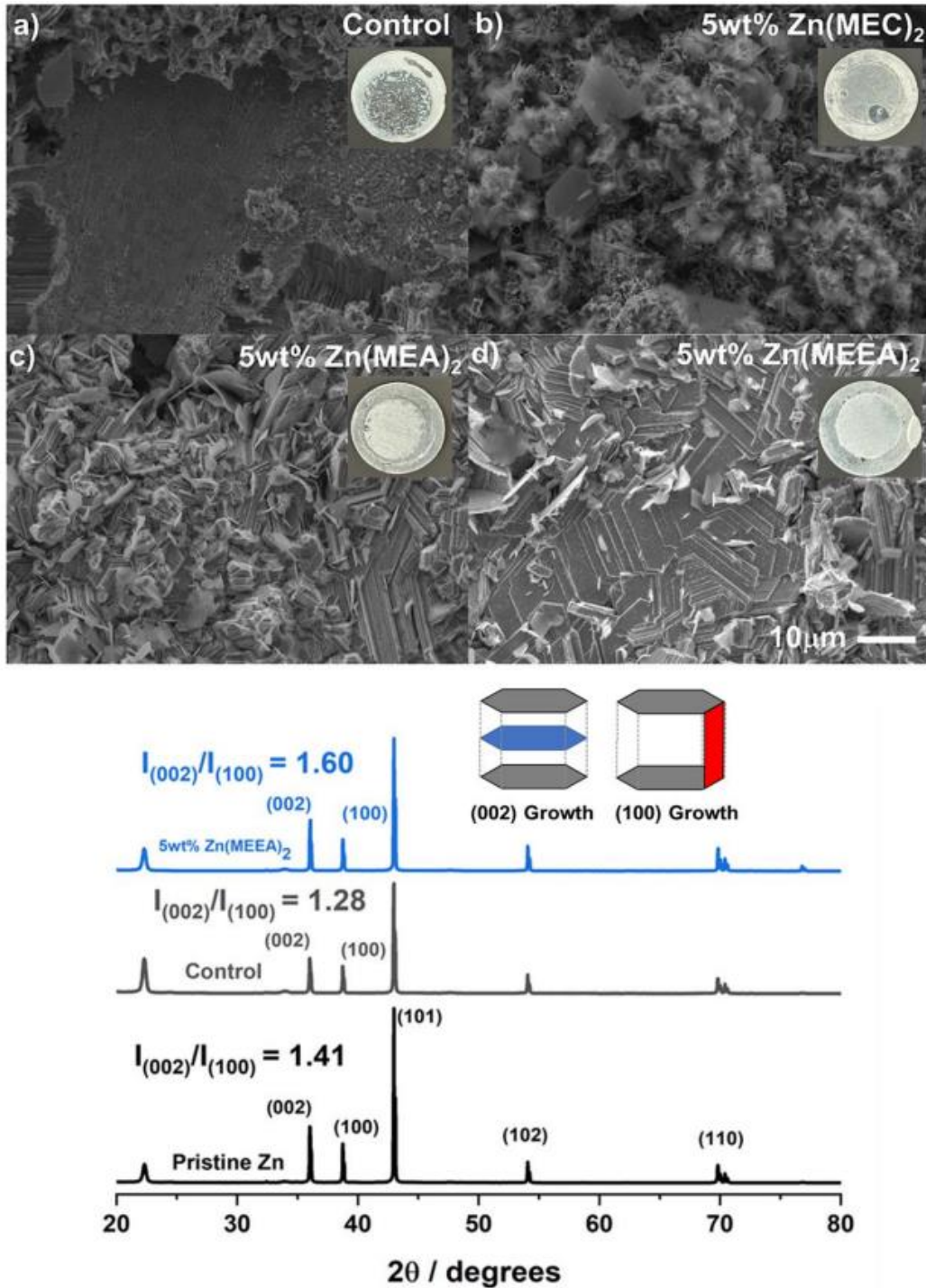


Fig 4.10 – (top) a) SEM for Zn anode cycled in 2 M ZnSO₄ taken after 20 cycles, b) 2 M ZnSO₄ + 5wt% Zn(MEC)₂, c) 2 M ZnSO₄ + 5wt% Zn(MEA)₂ and d) 2 M ZnSO₄ + 5wt% Zn(MEEA)₂ with picture of cycled Zn anodes and (bottom) XRD patterns for pristine Zn anode (black), 2 M ZnSO₄ (grey) and 2 M ZnSO₄ + 5wt% Zn(MEEA)₂ (blue) with diagram of (002) vs (100) growth.

To further investigate the reversibility of the Zn anode, Zn || Cu asymmetric cells were tested to obtain the coulombic efficiency (CE%) utilising method described by Xu *et al.* [194] After a precondition step, where 4 mAh.cm⁻² was plated on the Cu to form a reservoir, 50 cycles at 1 mAh.cm⁻² and 1 mA.cm⁻² were carried out, after which a full stripping step took place. The equation to determine the CE% is: $CE = \frac{50Q_c + Q_s}{50Q_c + Q_r}$. The control was unable to reach 50 cycles before dendrite formation led to a short circuit (Fig. 4.11a). In contrast, with the addition of all three additives, the Zn || Cu cell was able to complete the procedure. The Coulombic efficiencies (CE) obtained for the 5 wt% Zn(MEC)₂, Zn(MEA)₂, and Zn(MEEA)₂ additives were 83.4%, 98.2%, and 99%, respectively, with the latter two in particular demonstrating high reversibility (Fig. 4.11b). [194] - [200]

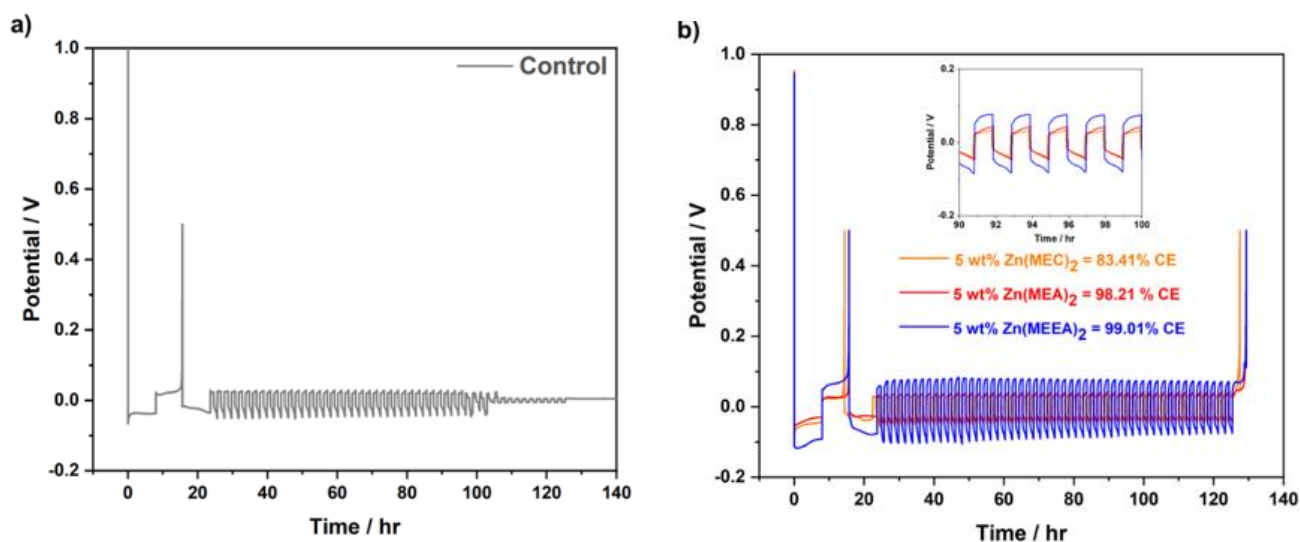


Fig 4.11 – a) Zn || Cu cell cycled with 2 M ZnSO₄ using CE% method following Xu *et al.* which failed and b) Zn || Cu cell with 2 M ZnSO₄ + 5wt% Zn(MEC)₂ (orange), 2 M ZnSO₄ + 5wt% Zn(MEA)₂ (red) and 2 M ZnSO₄ + 5wt% Zn(MEEA)₂ (blue).

Despite all three salts demonstrating high stability in Zn || Zn symmetric cells, Zn(MEEA)₂ appears to be the best-performing additive based on the Zn || Cu asymmetric cells. To probe performance further, Zn || Cu asymmetric cells containing 5 wt% Zn(MEEA)₂ were cycled at a capacity of 2.5 mAh.cm⁻² and a current density of 2.5 mA.cm⁻² and were found to cycle for 750 hours (Fig. 4.12a). Additionally, when tested at higher current rates for Zn || Zn cells, 2.5 mA.cm⁻² for a capacity of 2.5 mAh.cm⁻², the 5 wt% Zn(MEEA)₂ demonstrated stable cycling over 750 hours (Fig. 4.12b).

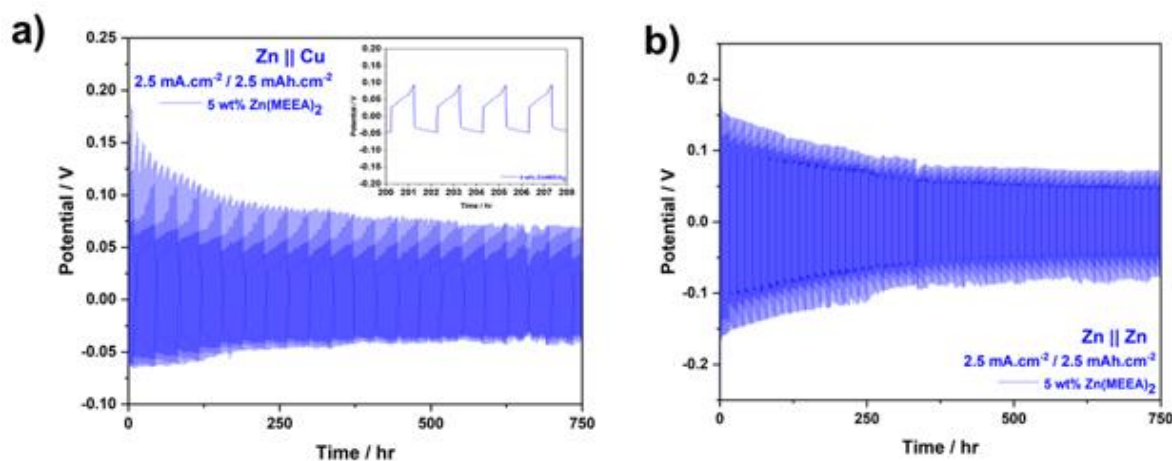


Fig 4.12 – a) Zn || Cu cell cycled with 2 M ZnSO₄ + 5wt% Zn(MEEA)₂, b) Zn || Zn cell with 2 M ZnSO₄ + 5wt% Zn(MEEA)₂ cycled at 1C.

4.4 SEI Formation

To understand the reason behind the significant improvement in performance, X-ray photoelectron spectroscopy (XPS) was used to investigate the presence of a solid electrolyte interphase (SEI). The comparison was made between 2 M ZnSO₄ + 5 wt% Zn(MEEA)₂ and a control of 2 M ZnSO₄. Zn anodes measured were cycled in a Zn || Zn symmetric cell, continuously discharged (i.e., plated) at 2.5 mA·cm⁻² until the Zn was either completely stripped from one side or dendrites formed. XPS analysis (Fig. 4.13) of Zn electrodes was conducted at depths of 0, ~50, and ~100 nm using Ar⁺ ion beam. These ion beam depths, estimated using TaSO₅ from the Advantage XPS software, may differ from the actual values. The S 2p spectrum for 2 M ZnSO₄ + 5 wt% Zn(MEEA)₂ shows peaks at 169.1 eV for ZnSO₄, 166.5 eV for ZnSO₃, and 161.8 eV for ZnS on the Zn electrode surface. The ZnSO₄ is likely due to precipitation from the electrolyte, while ZnS formation is probably the result of the reduction of SO₄²⁻ and/or SO₃²⁻ to ZnS. ZnSO₄ and ZnS are also detected in the 2 M ZnSO₄ control, but in negligible amounts compared to the 2 M ZnSO₄ + 5 wt% Zn(MEEA)₂. ZnS is observed up to a depth of 100 nm in the 2 M ZnSO₄ + 5 wt% Zn(MEEA)₂ sample, indicating a significant presence of ZnS. In contrast, ZnS is not detected beyond 100 nm in the 2 M ZnSO₄ control. We hypothesise that Zn(MEEA)₂ facilitates the precipitation of ZnSO₄, which allows SO₄²⁻ to be reduced to form ZnS. A ZnS-based SEI has been shown to contribute to a highly stable Zn anode. [138], [139]

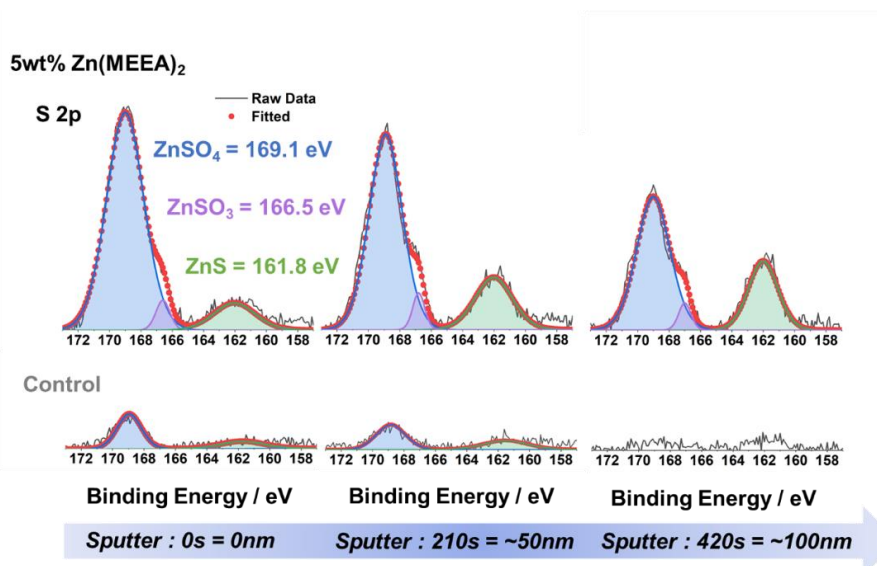


Fig 4.13 – S 2p XPS spectra for Zn anodes cycled in 2 M ZnSO_4 + 5wt% Zn(MEEA)_2 (top) and 2 M ZnSO_4 (bottom) with Ag^+ ion beam up to a depth of ~ 100 nm.

The C 2s XPS spectra are inconclusive regarding the presence of organic components in the SEI. Both spectra (Fig. 4.14) show a peak for adventitious carbon at 284.8 eV, which, surprisingly, remains even after extensive ion beam. The control spectra exhibit a lower intensity of this peak compared to the 2 M ZnSO_4 + 5 wt% Zn(MEEA)_2 sample, suggesting a higher concentration of carbon-containing species on the surface of the latter. Indeed, the XPS spectra for the Zn anodes cycled with 2 M ZnSO_4 + 5 wt% Zn(MEEA)_2 show the presence of C-O at 286.5 eV, not present in the control spectra, which could potentially arise from the reduction of the C-O-C ether chains of MEEA^- . Additionally, C=O species were observed, which could be attributed to the carboxyl group of MEEA^- . However, since the C=O peak at 289.6 eV is also present in the control spectra, it is likely that this signal is either a contaminant or the result of a reaction with CO_2 . Analysing C 2s XPS spectra can be challenging due to the presence of adventitious carbon and hydrocarbons, which should be considered when interpreting organic-based SEIs. While we expect that most contaminants are removed during Ag^+ ion beam, we are also aware that the ion beam process itself may affect the spectra.

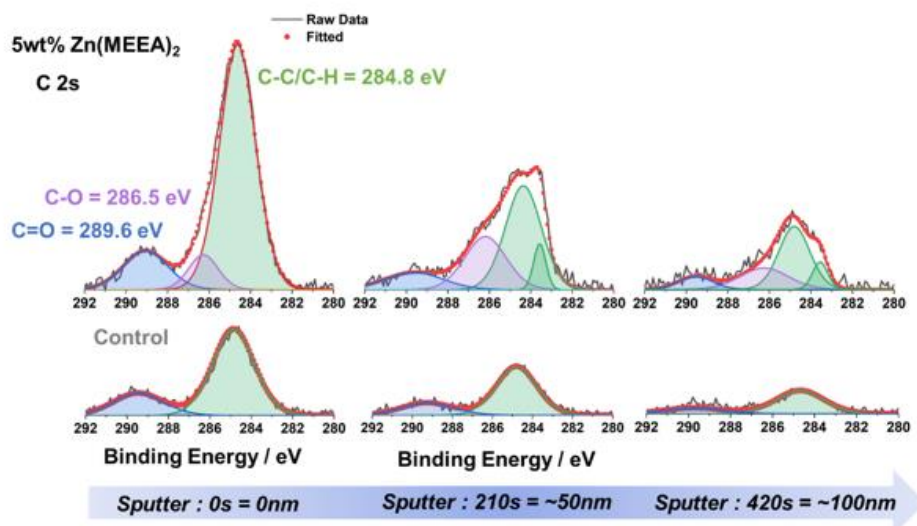


Fig 4.14 – C 2s XPS spectra for Zn anodes cycled in 2 M ZnSO₄ + 5wt% Zn(MEEA)₂ (top) and 2 M ZnSO₄ (bottom) with Ag⁺ ion beam up to a depth of ~100 nm.

The Zn 2p spectra for 2 M ZnSO₄ + 5 wt% Zn(MEEA)₂ (Fig. 4.15a) further indicate the presence of an SEI. During ion beam, there is a decrease in the intensity of the Zn²⁺ peak ($2p_{1/2} = 1044.4$ eV and $2p_{3/2} = 1021.9$ eV) and an increase in the intensity of the metallic Zn peak ($2p_{1/2} = 1043.8$ eV and $2p_{3/2} = 1021$ eV). Overall, the XPS analysis suggests that the Zn anodes cycled with 2 M ZnSO₄ + 5 wt% Zn(MEEA)₂ have an SEI comprising of a rich inorganic ZnS layer and potentially an organic layer. The presence of Zn(MEEA)₂ enhances the ZnS layer, while any organic layer originates from the carbon chains in the oligoether, containing C=O and C-O-C groups. The mechanism by which Zn(MEEA)₂ facilitates ZnS SEI formation requires further investigation to elucidate the decomposition pathway. The significance of ZnS as an SEI component was confirmed using an electrolyte with 1.5 M Zn(Ac)₂ + 5 wt% Zn(MEEA)₂. This cell lasted only 280 hours before dendrite formation occurred, indicating that Zn(MEEA)₂ alone is insufficient to prevent dendrites and must work in conjunction with specific salts (Fig. 4.15b). As mentioned in Chapter 1.7.2, HTFSI has recently been used to promote the formation of a ZnS layer though aiding in the decomposition process of the ZnSO₄ and we believe a similar principle can be applied here. [139] Further experiments are underway to determine the role Zn(MEEA) plays.

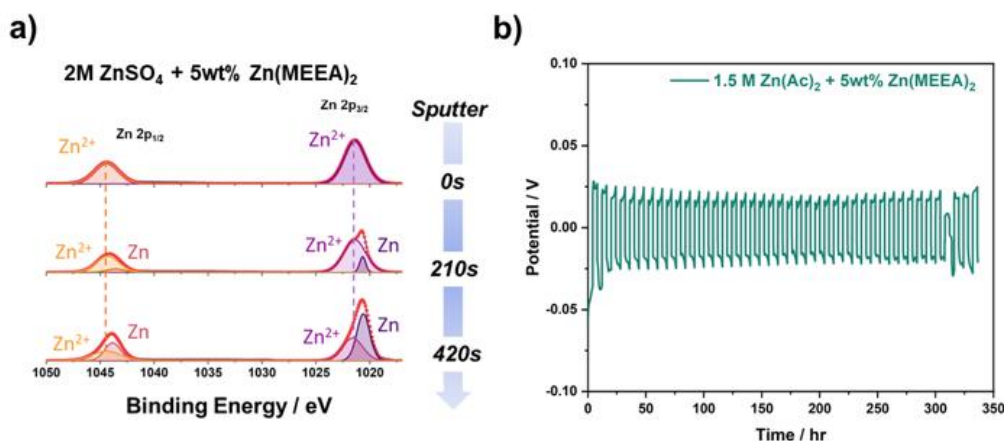


Fig 4.15 – a) Zn 2p XPS spectra for Zn anodes cycled 2 M ZnSO₄ + 5wt% Zn(MEEA)₂ with Ag⁺ ion beam up to a depth of ~100 nm and b) 1.5 M Zn(Ac)₂ + 5wt% Zn(MEEA)₂ cycled at C/4.

4.5 Full Cell – Zn || MnO₂

Previously, the group has worked on the development of the rechargeable Zn || MnO₂. [93] In addition to the Gdm-based electrolyte discussed in Chapter 3, another electrolyte developed in the lab is 2 M ZnSO₄ + 10 M urea. Although the work on this electrolyte falls outside the scope of this thesis, a brief overview is appropriate. As detailed in Chapter 1.5.4, urea disrupts the hydrogen bonding network of water, which helps suppress Mn electro-dissolution and promotes stable cycling. Without urea, a 2 M ZnSO₄ electrolyte would experience significant cycling decay due to high levels of irreversible Mn electro-dissolution.[93], [201], [202] When comparing the urea-based electrolyte to the Gdm-based one, a key advantage of the urea-based electrolyte is its broader temperature range. It functions effectively from -15 to 55°C, whereas the Gdm-based electrolyte performs well only at room temperature. However, while this electrolyte has improved performance on the cathode side, gains on the anode side have been limited, with dendrite formation still present. The current question is whether adding Zn(MEEA)₂ could address the ongoing issues with Zn dendrites. Zn || Zn symmetric cells containing 2 M ZnSO₄ + 10 M Urea + 5wt% Zn(MEEA)₂ are compared to a control (2 M ZnSO₄ + 10 M Urea) (Fig. 4.16 top). The control lasts a similar duration to the 2 M ZnSO₄ at around 200 hours before dendrites and an eventual short circuit, indicating that urea has a minimal effect on the Zn electrodeposition process. Meanwhile the electrolyte containing 5 wt% Zn(MEEA)₂ showcases a similar drastic

improvement to the cycle life, with over 2000 hours of cycling obtained with 2.5 mAh.cm^{-1} at 0.624 mA.cm^{-1} . Temperature fluctuations in the room during hours 800 to 1200 lead to some changes to the electrochemistry, however, this did not affect the cycling curves (Fig. 4.16 bottom).

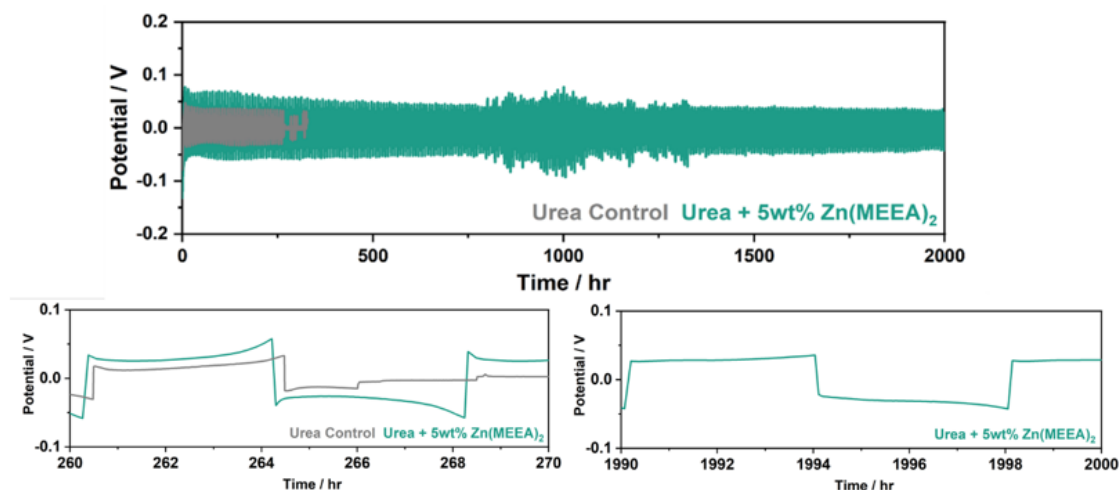


Fig 4.16 – Zn || Zn cell cycled with $2 \text{ M ZnSO}_4 + 10 \text{ M Urea}$ (Grey) and $2 \text{ M ZnSO}_4 + 10 \text{ M Urea} + 5\text{wt}\% \text{ Zn(MEEA)}_2$ (Green) cycled at $C/4$ (top) and cycling curves at 260 – 270 hr and 1990 – 2000 hr (bottom).

The XPS data (Fig. 4.16) for Zn anodes cycled in $2 \text{ M ZnSO}_4 + 10 \text{ M urea} + 5 \text{ wt}\% \text{ Zn(MEEA)}_2$ is very similar to the data obtained for $5 \text{ wt}\% \text{ Zn(MEEA)}_2$ without urea. The S 2p spectra (Fig. 4.17a) show the same peaks for ZnSO_4 , ZnSO_3 , and ZnS at 169.1, 166.5, and 161.8 eV, respectively. These peaks gradually decrease in intensity with increasing ion beam depth. Similarly, the C 2s XPS spectra (Fig. 4.17b) are comparable to those for $5 \text{ wt}\% \text{ Zn(MEEA)}_2$ without urea, with C=O at 289 eV and C-O-C at 286.5 eV detected. However, carbon is completely removed by $\sim 100 \text{ nm}$, indicating a reduced depth of carbon compared to the electrolyte without urea. The Zn $2p_{1/2}$ and $2p_{3/2}$ spectra (Fig. 4.17c) also match those for the electrolyte without urea. This suggests that the presence of Zn(MEEA)_2 results in the formation of the SEI, whereas urea has little influence.

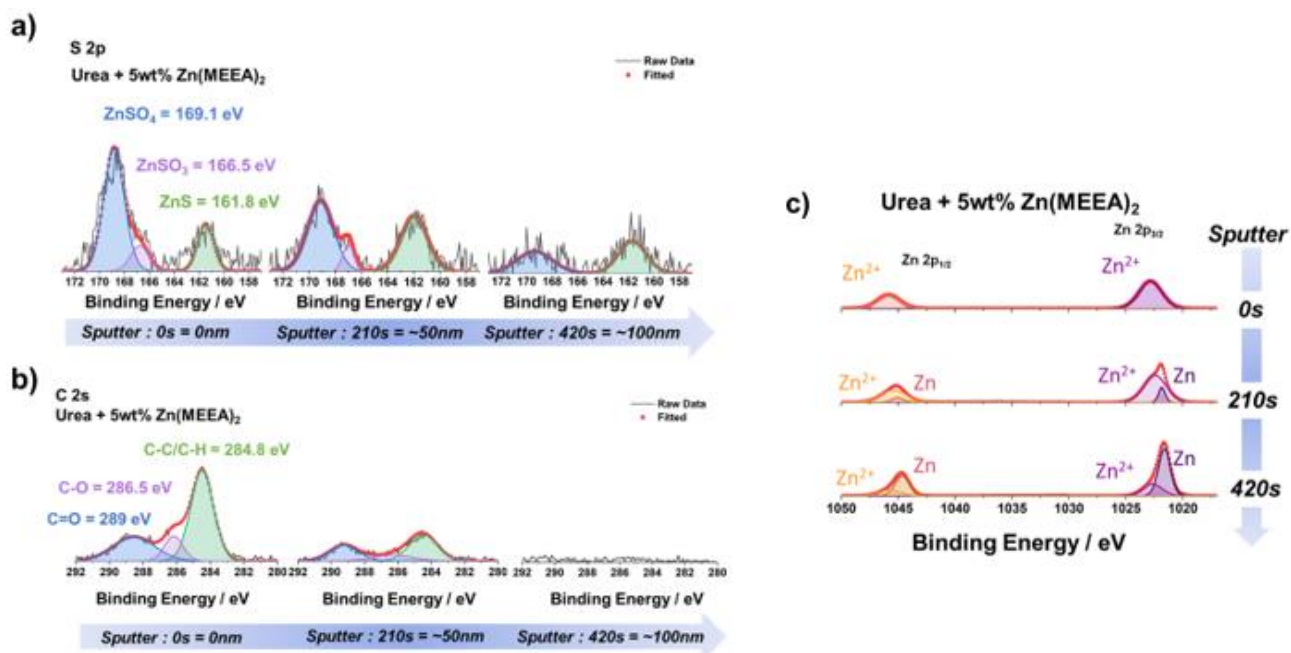


Fig 4.17 – a) S 2p XPS spectra for Zn anodes cycled in 2 M ZnSO₄ + 10 M Urea + 5wt% Zn(MEEA)₂, b) C 2s XPS spectra and c) Zn 2p XPS spectra, all with Ag⁺ ion beam up to a depth of 100 nm.

After establishing that Zn(MEEA)₂ enhances the performance of the 2 M ZnSO₄ + 10 M urea electrolyte in Zn || Zn cells, attention shifted to the Zn || MnO₂ full cell. While the 2 M ZnSO₄ + 10 M urea control electrolyte shows stable cycling, dendrites form after 30 cycles at 2.5 mA·h·cm⁻² and 0.624 mA·cm⁻² (C/4). This test uses a low C-rate and a relatively high mass loading of 12.5 mg (6.25 mg of MnO₂) for the cathode composite to provide a more practical evaluation of the Zn || MnO₂ system, as high C-rates (>5C) or low mass loadings can mask potential issues. Upon adding 5 wt% Zn(MEEA)₂ to the electrolyte, the cell cycles beyond 200 cycles (Fig. 4.18a). This improved cycle life is attributed to dendrite prevention enabled by the addition of Zn(MEEA)₂. Importantly, Zn(MEEA)₂ does not interfere with urea's ability to stabilise the cathode side. There were significant temperature fluctuations from cycles 90 to 150 that affected capacity. However, the electrochemical curves remained consistent with the expected Zn || MnO₂ behaviour, showing only a slight increase in polarisation over cycling (Fig. 4.18b). Although more extensive cycling tests are needed to fully assess the performance of the electrolyte, these initial results are very promising. Another advantage of adding Zn(MEEA)₂ is the extended temperature range of the electrolyte. Preliminary tests were carried out -25°C, however, showed rapid capacity fading after

only 10 cycles (Fig. 4.18c). The reduced C-rate to C/8 was necessary due to the likely significant drop in conductivity caused by increased viscosity. We suspect that $\text{Zn}(\text{MEEA})_2$ lowers the freezing point of the electrolyte, a property commonly achieved by adding salts and glymes.[203], [204], [205] Further studies, including low-temperature DSC measurements, are needed to determine the exact effects.

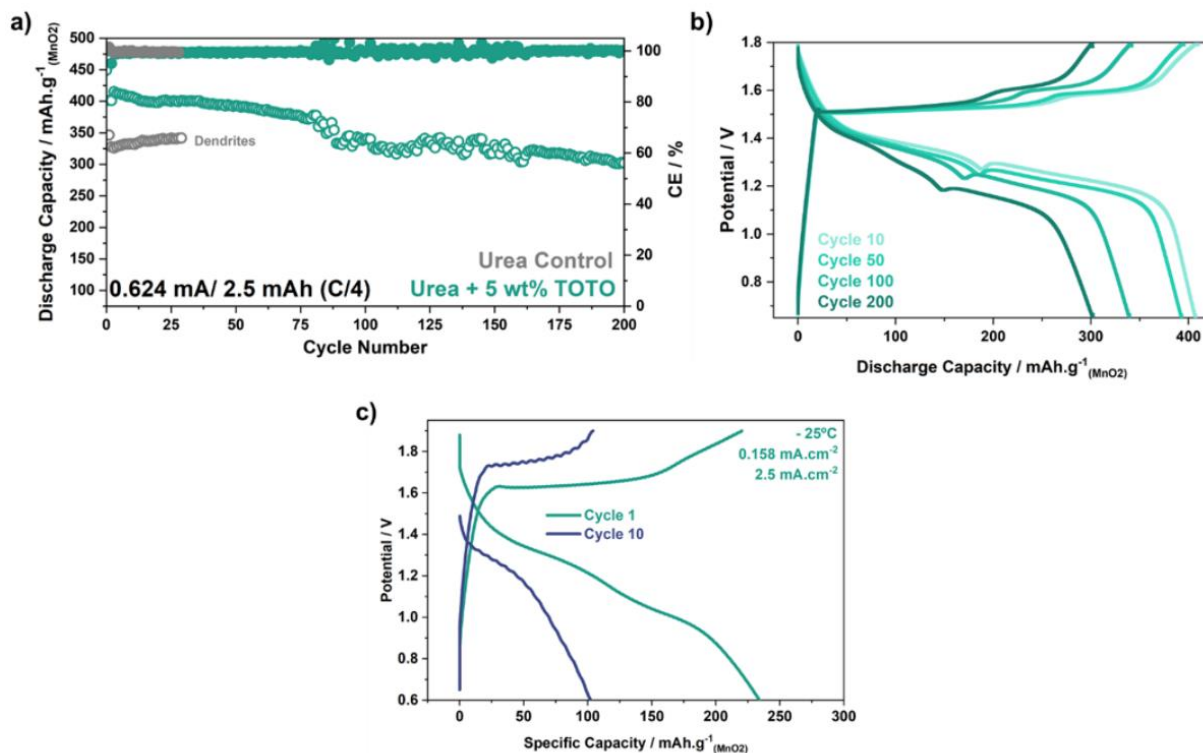


Fig 4.18 – a) Zn || MnO₂ cell cycled with 2 M ZnSO₄ + 10 M Urea (Grey) and 2 M ZnSO₄ + 10 M Urea + 5wt% Zn(MEEA)₂ (Green) at C/4, b) cycling curves for 2 M ZnSO₄ + 10 M Urea + 5wt% Zn(MEEA)₂ showcasing no change to the electrochemistry despite the temperature fluctuations and c) cycling curves for 2 M ZnSO₄ + 10 M Urea + 5wt% Zn(MEEA)₂ at -25°C at C/8.

4.6 LiMEEA + LiTFSI in Water

Moving back towards ALIBs, we wanted to revisit the Li variant of the salts as no testing of these salts in aqueous electrolytes was ever carried out. LiMEEA was synthesised according to methods described by Kunz et al. and purity was confirmed via ^1H and ^{13}C NMR spectroscopy (Fig. A4.4). The resultant product was a slightly yellow and highly viscous liquid. LiMEEA appeared to be completely miscible in water, enabling super concentrations to be probed. An initial cycling test with $\text{Mo}_6\text{S}_8 \parallel \text{LFP}$ was carried out using 20 m LiMEEA (Fig. 4.19). The cycling revealed a high polarisation, even at C/2, with a prolonged oxidation indicating the electrolyte decomposition during the first cycle. Subsequent cycles indicate the high irreversibility which is likely the result of a lack of SEI, required to stabilise the Mo_6S_8 . [206]

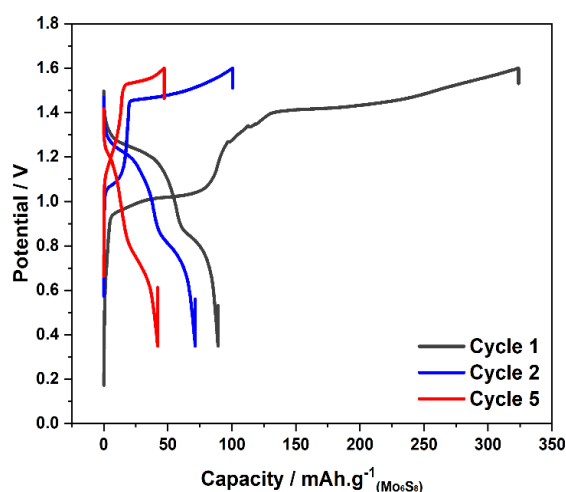


Fig. 4.19 - Galvanostatic cycling of $\text{Mo}_6\text{S}_8 \parallel \text{LFP}$ full cell at C/2 with 20 m LiMEEA.

Realising that LiTFSI is most likely required to enable the formation of an SEI, mixtures of LiTFSI, LiMEEA and H_2O were probed. From the ternary plot we found that LiTFSI was soluble in LiMEEA with no water needed, where a $\text{LiTFSI}_{(0.6)}\text{LiMEEA}_{(0.4)}$ mixture could be obtained. Nevertheless, the mixture was highly viscous and difficult to handle. This finding is reminiscent of PEO/LiTFSI binary mixture which have been utilised in polymer electrolytes. [207] Chemically PEO and LiMEEA share some similarities and it's possible that LiMEEA is able to create a polymer-like network. While this is not the focus of this work, it would certainly be an interesting avenue to explore moving forward.

As the LiTFSI can dissolve in LiMEEA, ternary mixtures with water were able to reach very high concentrations, with 30 m LiTFSI + 30 m LiMEEA the highest obtained, beyond the saturation limit of LiTFSI in water (21 m). As the range of concentrations possible was rather wide, concentrations up to 20 m LiTFSI + 20 m LiMEEA were probed (Fig. 4.20a). When comparing the FTIR (Fig. 4.20b) of a 20 m LiTFSI solution vs a 20 m LiMEEA solution, there is a distinct difference in the water region between 3000–3700 cm^{-1} where LiTFSI has a sharper band between 3400–3700 cm^{-1} , whereas 20 m LiMEEA has a broader band which is shifted to lower wavenumbers between 3000–3600 cm^{-1} . The lower wavenumbers are indicative of water molecules forming strong HBN in solution, meaning LiMEEA has a weaker interaction with water, compared to LiTFSI. The peaks observed at 2700 cm^{-1} are attributed to the C-H stretching of the LiMEEA and are similar to what has previously been observed with LiTFSI/PEG/H₂O “molecular crowding” electrolyte (Fig. 4.20b).[31] As the concentration of LiTFSI is gradually increased, a shift of the water region to higher wavenumbers is observed, indicating the reduction of free water concentration. Indeed, the addition of LiTFSI disrupts the HBN of water, through chaotropic/hydrootropic effects, leading to a blue shift in the oscillation of the H-O covalent bond as previously observed with WISE (Fig. 4.20b). [40] Upon probing the cycling of 20 m LiTFSI + 20 m LiMEEA, we see more stable cycling (C/2) compared to the 20 m LiMEEA, likely due to the formation of an SEI (Fig. 4.20c). The curve is slightly polarised when compared to WISE [11], [39], however, this is expected as the conductivity of 20 m LiTFSI + 20 m LiMEEA is 0.45 $\text{mS}\cdot\text{cm}^{-1}$ compared to the 12.5 $\text{mS}\cdot\text{cm}^{-1}$ for 20 m LiTFSI. Further work is necessary to test these electrolytes more thoroughly, especially at lower concentrations of LiTFSI, and determine if the SEI formation is maintained. The diverse compositions could have positive implications for ALIBs, as well as for polymer-like electrolytes. Moreover, altering the length of the anion chain in the salt could introduce greater chemical diversity. Despite the limited literature on alkali-metal oligoether salts for battery use, there is certainly potential for the lithium variant of these salts.

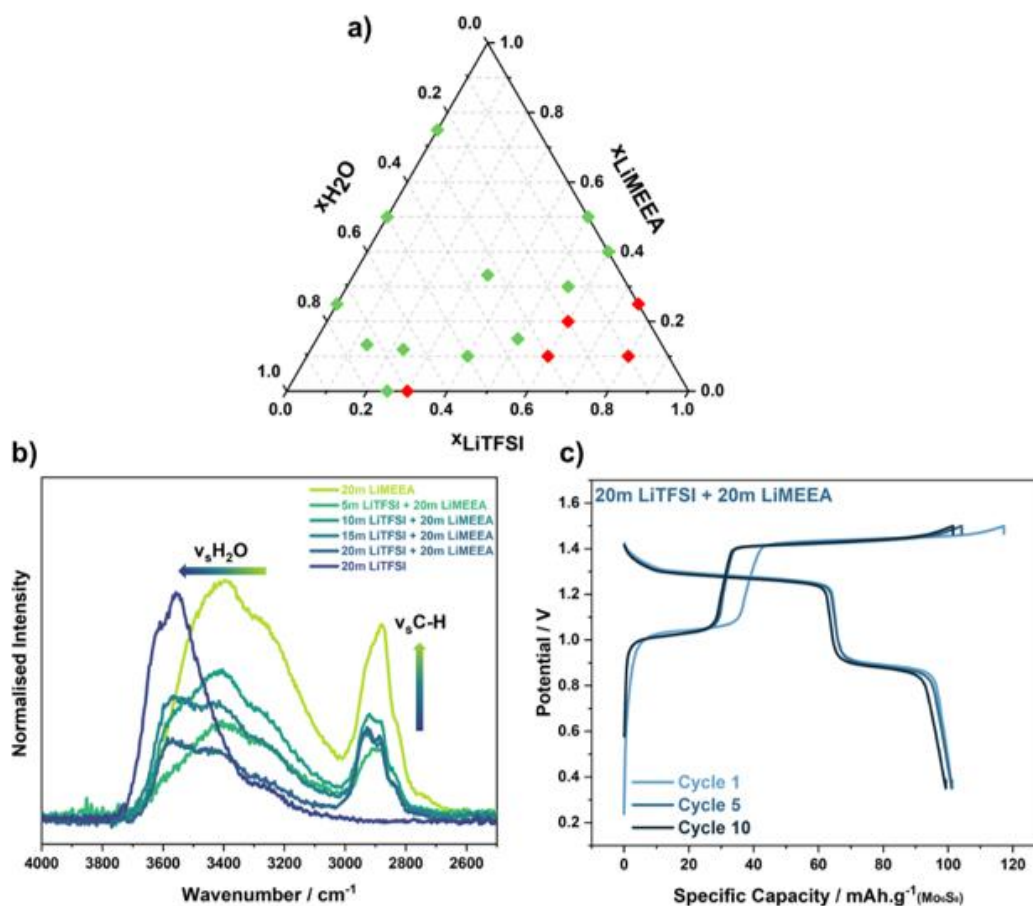


Fig. 4.20 - a) Ternary diagram for LiTFSI, LiMEEA and water (green denotes liquid & red denotes solid), b) 2500 – 4000 cm^{-1} FTIR region of electrolytes and c) galvanostatic cycling of $\text{Mo}_6\text{S}_8 \parallel \text{LFP}$ full cell with 20m LiTFSI + 20m LiMEEA at C/2.

Conclusions to Chapter 4

The oligoether salts exhibit significant potential across various chemistries, leveraging different effects. Although using these salts as primary salts in both Li and Zn systems is not effective, they show intriguing characteristics that could benefit both ALIBs and AZMBs. Research into ALIBs with LiMEEA has revealed that this salt can exhibit polymer-like effects when combined with another salt, such as LiTFSI, although the cycling performance is limited due to low conductivity. Experimenting with different compositions and primary salts remains a valuable endeavour, particularly from a fundamental research perspective.

For zinc-based systems, the zinc variants of these salts can significantly enhance the cycle life of ZMBs by facilitating a stable Zn electrodeposition process that

prevents dendrite growth. Among these, $\text{Zn}(\text{MEEA})_2$, with its longer chain, improves the performance of $\text{Zn} \parallel \text{MnO}_2$ full cells when added to a pre-existing in-house developed urea-based electrolyte. However, there is still a lack of fundamental understanding of why these novel salts improve Zn electrodeposition morphology. Early XPS data suggest the formation of a stable SEI that protects the Zn surface, but further investigation is necessary. We hypothesise that oligoethers might influence the double layer similarly to polymers and amino acids. Electrochemical capacitance measurements could help determine this, while EQCM-R could probe both the double layer and SEI formation. Additionally, operando IR has been effectively used in our group to understand and elucidate SEI formation mechanisms. [208]

Chapter 5: Exploring the Electrochemistry of PTCDI for Aqueous Lithium-ion Batteries

This chapter is primarily based on the following publication:

- **J.Brown**, M. Karlsmo, E. Bendadesse, P. Johansson & A.Grimaud, 'Exploring the electrochemistry of PTCDI for aqueous lithium-ion batteries', *Energy Storage Materials*, vol. 66, pp. 103218, Jan. 2024, DOI: 10.1016/j.ensm.2024.103218.

5.1 Introduction

As highlighted in previous chapters, although we've achieved progress in other areas, our attempts to engineer an electrolyte for ALIBs have not been entirely successful. Thus, investigating new materials to maximise the performance of existing electrolytes offers another valuable direction for research. As discussed throughout the thesis, the primary goal of developing rechargeable aqueous batteries is to create low-cost, environmentally friendly, and safe energy storage solutions. The integration of redox-active organic materials (ROMs) with aqueous electrolytes makes this even more compelling, as ROMs are derived from abundant elements, offering renewability and environmental friendliness consistent with the green principles of aqueous electrolytes. N-type ROMs containing carbonyls are the most interesting owing to their wide potential range and chemical diversity. Of further interest are perylene-type ROMs, specifically perylene-3,4,9,10-tetracarboxylic acid di-imide (PTCDI) which has been successfully implemented in aqueous sodium-ion, potassium-ion, and magnesium batteries (SIBs, PIBs, MgBs). [83] - [86] However, PTCDI's use in ALIBs remains unexplored. A common theme of these aqueous PTCDI-based batteries has been to apply high C-rates and/or high salt concentrations. The former, however, could hide potential frailties of the material and pose a potential challenge for practical implementation when more realistic discharge times are relevant. Therefore, we set out to assess how well PTCDI performs in low-to-moderately concentrated electrolytes, while avoiding high c-rates.

5.2 Reversibility with Aqueous Electrolytes

To assess the feasibility of using PTCDI under non-WISE conditions, 1.0 m LiTFSI_(aq) was probed and the first cycle of the CV reveals a single reduction peak at 2.0 V (vs. Li/Li⁺) and two oxidation peaks at 2.10 V and 2.6 V (Fig. 5.1a). In the subsequent cycles, two reduction peaks emerge at 2.25 V and 2 V, while the oxidation peaks remain the same, pointing towards an activation step occurring on the first cycle, which is also present for PTCDI with organic electrolytes (Fig. 5.1b). This activation step is also present during galvanostatic cycling with a large irreversible capacity after the first charge (Fig. 5.1c). The presence of an activation cycle has been previously observed with saturated NaTFSI_(aq) electrolyte for PTCDI. [209] While the aqueous and organic electrolytes share an activation step, they display different redox behaviour where a single broad redox between ~2 V - 2.4 on reduction and ~2.4 - 2.8 V on oxidation is observed for a 1.0 m LiTFSI_(EC:PC). The difference between aqueous and non-aqueous was not observed for sodium and potassium-based electrolytes and raises the question of whether the redox mechanism for PTCDI remains the same in aqueous conditions. [83], [210], [211] There could be structural changes, different coordination pathways unique to aqueous electrolytes and/or alternative charge carriers present, such as H⁺.

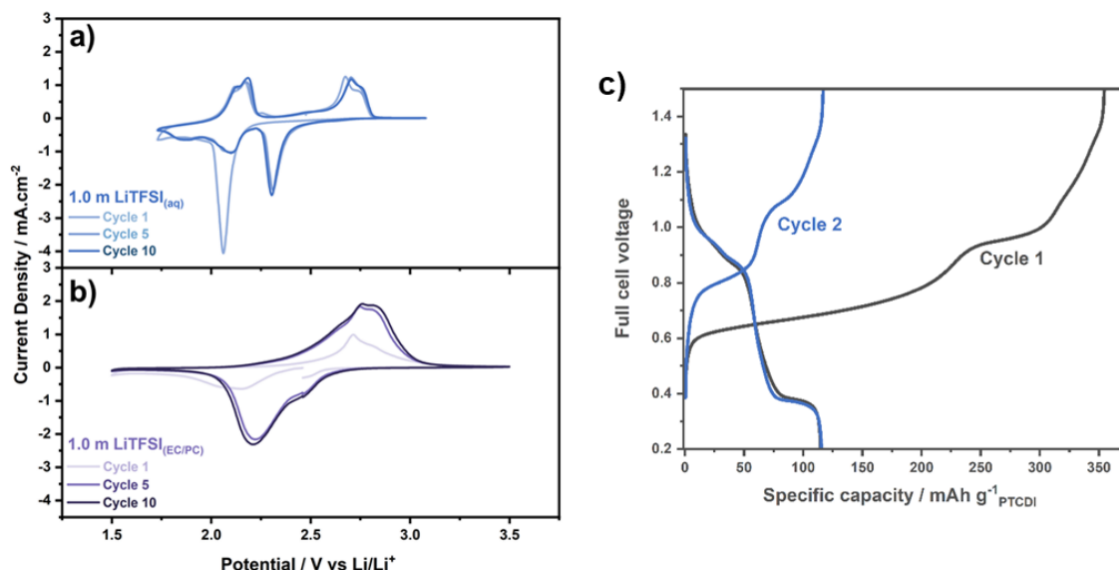


Fig. 5.1 - a) Cyclic voltammogram of the PTCDI electrode using a 1.0 m LiTFSI_(aq) electrolyte in a 3-electrode Swagelok cell, b) CV of the PTCDI electrode using 1.0 m LiTFSI_(EC/PC) in coin cell and c) GC charge/discharge curves of a PTCDI vs. LFP (coin cell, pseudo half-cell) cell with 1.0 m LiTFSI_(aq).

To ascertain whether the variations in cycling behaviour are related to structural changes, FT-IR spectroscopy was taken at charged and discharged states with 1.0 M LiTFSI_(aq). Both pure PTCDI and pristine electrodes were shown to display characteristic absorption bands at 1277 cm⁻¹, 1363 cm⁻¹, 1685 cm⁻¹, and 3154 cm⁻¹, corresponding to the C-N, C=O, and N-H stretching vibrations of the imide groups, respectively (Fig. 5.2a). Additionally, they show stretching vibrations of the perylene ring and aromatic C-H at 1589 cm⁻¹, 2857 cm⁻¹, and 3041 cm⁻¹, respectively (Fig. 5.2a). Upon the first charge, *i.e.*, reduction of PTCDI, significant shifts and/or intensity changes are observed for all peaks, suggesting a significant transformation in the local environment. The significant reduction in the C=O and aromatic C-H bands accompanied by a downward shift of the perylene ring band indicates a decreased π -electron delocalization, which is consistent with enolization of the C=O group by cation coordination, following the reaction $C=O \rightarrow C-O-Li$ via delocalisation of the conjugated ring, as previously demonstrated for both aqueous and organic electrolytes. [212] During the following discharge, *i.e.*, oxidation of PTCDI, most bands recover their original intensities and positions, indicating de-enolization and thus a reversible redox mechanism. The merging of the 1685 cm⁻¹ C=O vibration from a double to a single peak is similar to with organic electrolytes [213], and the new 1065 cm⁻¹ peak which remains during discharge has previously been associated with a C-O bond (Fig. 5.2b). Meanwhile, the decrease in intensity of the 875 cm⁻¹ C=C vibration indicates a potential change to the delocalisation of the structure (Fig. 5.2b). [214] The observed IR changes between the pristine and discharged states, together with the irreversible capacity from the first cycle, suggest that residual Li⁺ remains in the PTCDI structure after the initial charge. This residual Li⁺ could be the cause of the activation step seen in the earlier electrochemistry.

The X-ray diffractograms of the pure PTCDI, both in powder and electrode forms, match the expected crystal structure with the P12₁/n1 space group in a monoclinic phase (Fig. 5.2c). [215] Upon charging the (12 $\bar{1}$), (11 $\bar{2}$) and (12 $\bar{2}$) peaks undergo shifts to lower 2 θ angles, accompanied with an overall loss in crystallinity, but again this is reversible: upon discharge, the crystallinity returns and the aforementioned peaks shift back. The discharged pattern does, however, change slightly from the pristine state, with peak shifts and reduced crystallinity, indicating a potential alteration in the crystal structure; yet it remains uncertain whether this is due

to structural activation or to the pre-measurement cleaning process. The loss and return of crystallinity upon charge/discharge occurs for cycles 5 and 10, indicating the reversibility of the material. In addition, the SEM seen in Fig. 5.2d supports the reversibility of the process where a reversible change in morphology is observed across cycling. It is worth noting that an unexplained deposition or surface formation occurs on the PTCDI electrode in the early charged states that reversibly disappears during discharge. Moreover, a continuous merging of the elongated PTCDI crystals is observed upon cycling and this could very well be related to the structural activation and explain the differences in the XRD patterns between the pristine and cycled electrodes.

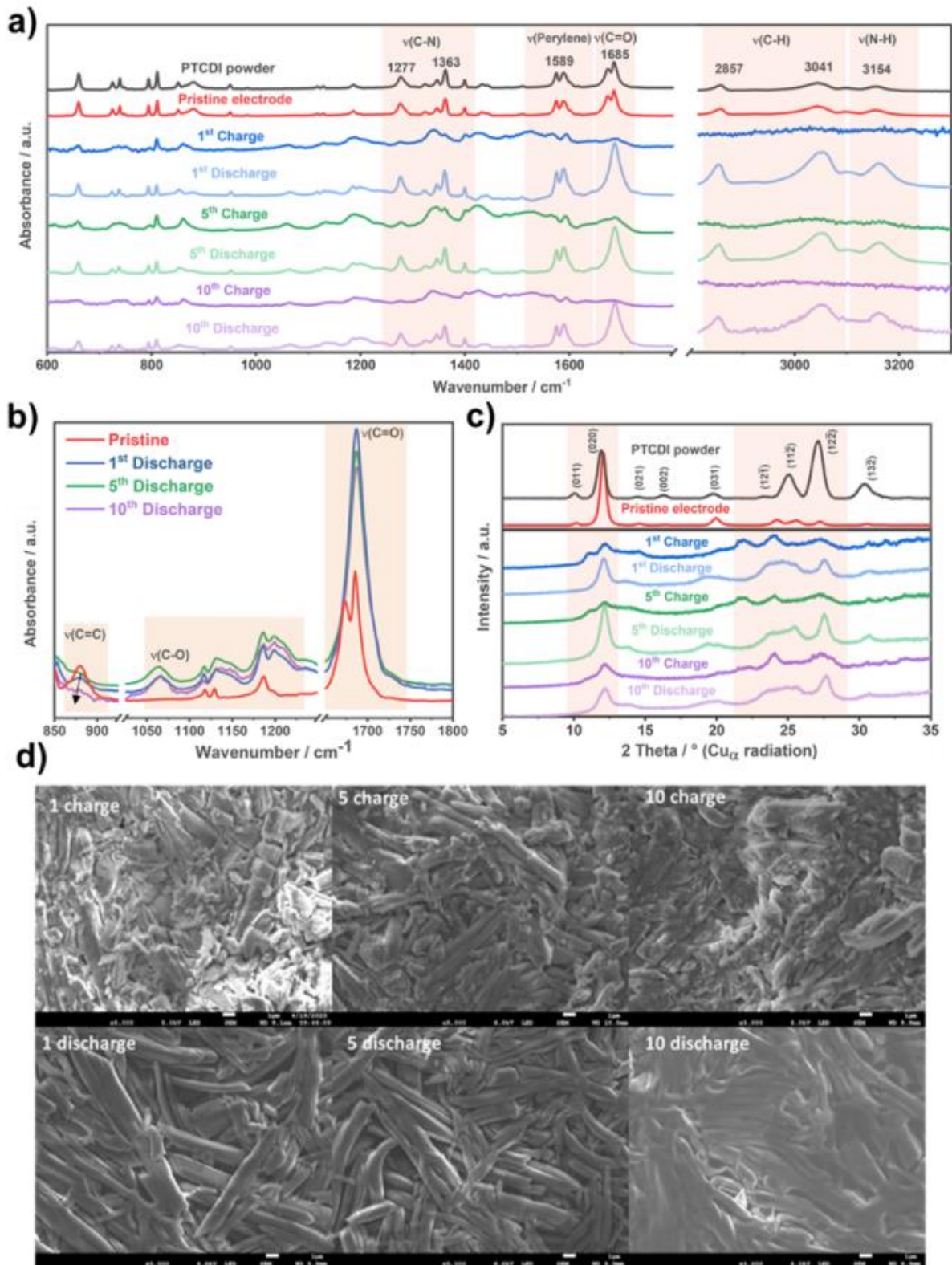


Fig. 5.2 - Ex situ a) full FTIR spectra and b) FTIR spectra focusing on the 600 – 1800 cm^{-1} region, c) X-ray diffractograms of free-standing PTCDI electrodes cycled with 1.0 m $\text{LiTFSI}_{(\text{aq})}$ and d) Ex situ SEM of PTCDI electrodes cycled with 1.0 m $\text{LiTFSI}_{(\text{aq})}$ at different charging state and different cycles.

5.3 Active Charge Carrier(s)

From the structural analysis, it appears the charge storage mechanism occurs via enolization of the C=O bond, but further investigations are required to identify the charge carrier(s). 1.0 m $\text{Li}_2\text{SO}_{4(\text{aq})}$ was also tested alongside 1.0 m $\text{LiTFSI}_{(\text{aq})}$ to determine if anion plays a role to the charge compensation. Through in situ Electrochemical Quartz Crystal Microbalance-Resistance Monitoring (EQCM-R), which enables simultaneous measurement of motional resistance and frequency fluctuations, significant mass increases are observed during reduction for both electrolytes (Fig. 5.3a & 5.3b). This can be attributed to electrode swelling through the uptake of solvated ions (Fig. 5.3c), such as Li^+ . [216] Indeed, upon oxidation the frequency does not fully recover, suggesting an irreversible process during the first cycle, which could explain the structural activation of PTCDI. This behaviour is also observed when using non-aqueous 1.0 m $\text{LiTFSI}_{(\text{EC:PC})}$ electrolyte, suggesting that this phenomenon is not exclusive to aqueous electrolytes and matches with the observations via CVs (Fig. A5.1). The first cycle for both $\text{Li}_2\text{SO}_{4(\text{aq})}$ and $\text{LiTFSI}_{(\text{aq})}$ displays high motional resistance (R_m) at $\Delta 200 \Omega$ and $\Delta 1000 \Omega$ respectively (Fig. A5.2). R_m can depend on many factors such as: film roughness, electrolyte properties, mass changes, and electrode characteristics, and hence a high ΔR_m could be an indicator of structural changes which would occur upon solvated ion uptake. Unfortunately, a large ΔR_m relative to Δf disrupts the mass-frequency linearity, nullifying the use of the Sauerbrey equation (Eq. 5.1) which is used to quantify the frequency fluctuations via EQCM. We treat $\Delta f/\Delta R_m > 25 \text{ Hz}/\Omega$ as our limit for applying the Sauerbrey equation, otherwise a qualitative analysis of the EQCM data is carried out. [217], [218]

$$\Delta m = -\frac{A\sqrt{\rho_q\mu_q}}{2f_0^2}\Delta f = -C_f\Delta f \text{ (Eq. 5.1)}$$

A = piezoelectrically active area (0.196 cm²), ρ_q = density of quartz (2.648 g cm⁻³), and μ_q = shear modulus of the quartz crystal (2.947 × 10¹¹ g cm⁻¹ s⁻²), C_f = sensitivity coefficient/calibration constant, which is 1.23 ± 0.03 ng Hz⁻¹ and determined by Ag electrodeposition detailed in a previous study.

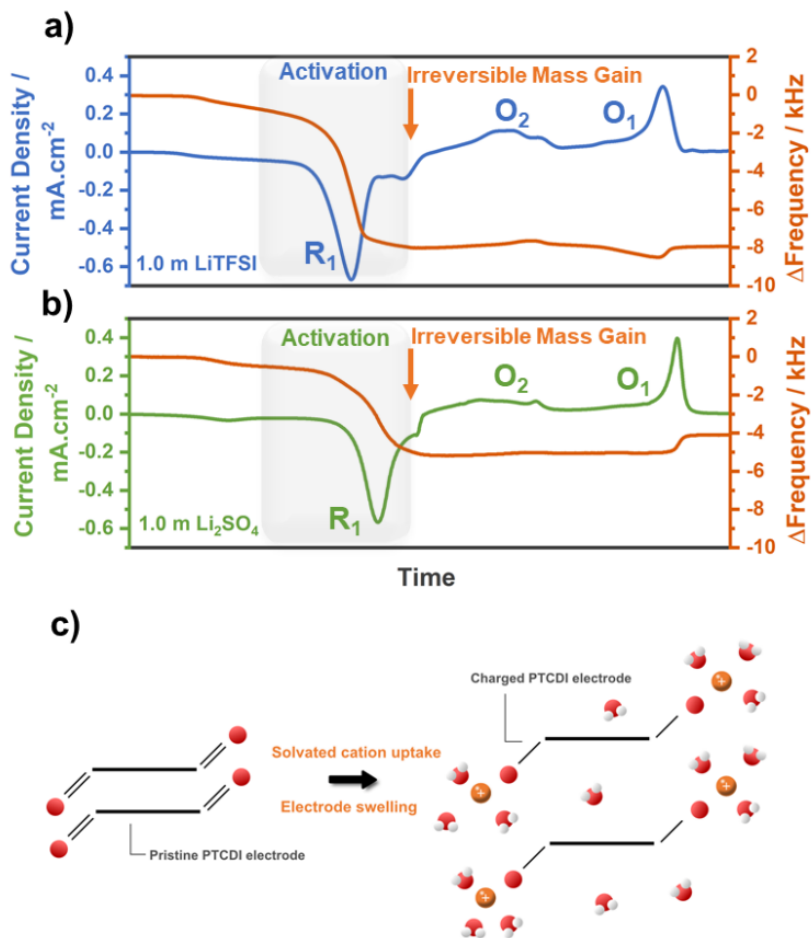


Fig. 5.3 - EQCM response during Cycle 1 of PTCDI using a) 1.0 m LiTFSI_(aq), b) 1.0 m Li₂SO_{4(aq)} electrolytes, respectively, where R₁ = first reduction peak and O_{1,2} = first and second oxidation peaks and c) Activation schematic of solvated Li⁺ uptake.

In the 5th cycle, the 1.0 m LiTFSI_(aq) the EQCM response deviates from convention with a f gain/mass loss before R₁, f loss/mass gain before O₁, pointing towards a redox process opposed to a pure cation de(intercalation)/coordination (Fig. 5.4a). However, the second redox feature (R₂/O₂) matches with cation (de)intercalation/coordination. The frequency fluctuations observed during R₁ and O₁ are not present in non-aqueous as the response for the 1.0 m LiTFSI_(EC:PC) electrolyte matches a typical one step cation (de)intercalation/coordination process albeit with a slight irreversibility (Fig. A5.3). Meanwhile, the 5th cycle for 1.0 m Li₂SO_{4(aq)} showcases the expected cation (de)intercalation/coordination response, with a Δf decrease for R₁ and R₂, and a Δf increase for O₁ and O₂, although there is an irreversible mass gain between O₁ and O₂ (Fig. 5.4b). During reduction for Li₂SO_{4(aq)}, $\Delta f/\Delta R_m$ is >25 Hz/ Ω (Fig. A5.4), allowing the use of the Sauberey equation. The calculated “molecular

weights” were 71 g mol^{-1} for R_1 and 75 g mol^{-1} for R_2 , which points to solvated Li^+ with 3.6 and 3.8 water molecules on average, respectively (Fig. 5.4c). We do wish to be transparent and say that on oxidation, the $\Delta f/\Delta R_m$ is $<25 \text{ Hz}/\Omega$ thus we could not apply the Sauerbrey equation, which does cast a cloud on the earlier calculation. Nevertheless, even from a qualitative standpoint the differing responses between $\text{LiTFSI}_{(\text{aq})}$ and $\text{Li}_2\text{SO}_{4(\text{aq})}$ is intriguing. Recent studies have indicated that kosmo/chaotropic effects could play a role. Indeed, a recent study of very structurally similar PTCDA in dilute aqueous Na-based electrolytes, observed that hydrophobic/chaotropic anions exhibited an enhanced presence near the electrode surface, whereas kosmotropic anions showed a diminished presence near the electrode surface.[168] In our case, TFSI^- is hydrophobic and chaotropic, while SO_4^{2-} is kosmotropic and hydrophilic. As a result, TFSI^- may accumulate near the surface, leading to electrostatic interactions with PTCDI and influencing the frequency responses observed in cycle 5 for LiTFSI . Conversely, SO_4^{2-} does not accumulate near the surface, which explains why such frequency responses are absent for Li_2SO_4 . We tentatively attribute these observations to the water-structuring effects of kosmotropic and chaotropic anions. Further studies are certainly required to understand the effects of kosmo/chaotropic anions on the chemistry at the electrode/electrolyte interface.

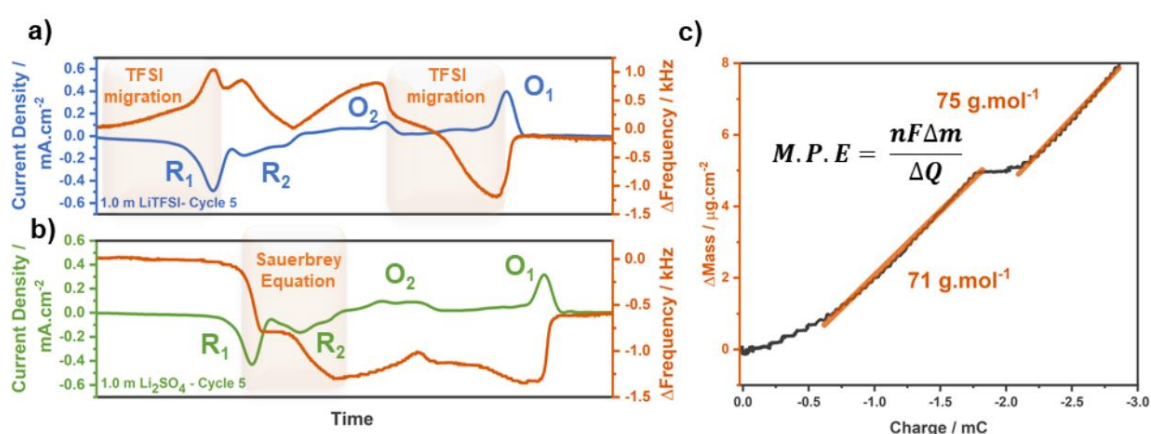


Fig. 5.4 - a) EQCM response from the 5th cycle with 1.0 m $\text{LiTFSI}_{(\text{aq})}$, b) 1.0 m $\text{Li}_2\text{SO}_{4(\text{aq})}$, and c) Δm vs. ΔQ with linear fits to calculate the “molecular weights” for 1.0 m $\text{Li}_2\text{SO}_{4(\text{aq})}$.

Interestingly, by the 50th cycle, the differences between the Δf fluctuations of 1.0 m $\text{LiTFSI}_{(\text{aq})}$ and $\text{Li}_2\text{SO}_{4(\text{aq})}$ dissipate and both observe a conventional response for a two-step cation (de)intercalation/coordination process (Fig. 5.5) indicating that

differences between electrolytes are only present during initial cycles. However, the low $\Delta f/\Delta R_m$ ratios persist, even for the Li_2SO_4 based electrolyte preventing quantification (Fig. A5.5). To fully decipher the early cycle Δf fluctuations, further studies using EQCM-D, which has the added function of measuring dissipation, rather than EQCM-R, can provide insights into electrode viscoelastic properties and explain the electrolyte differences.

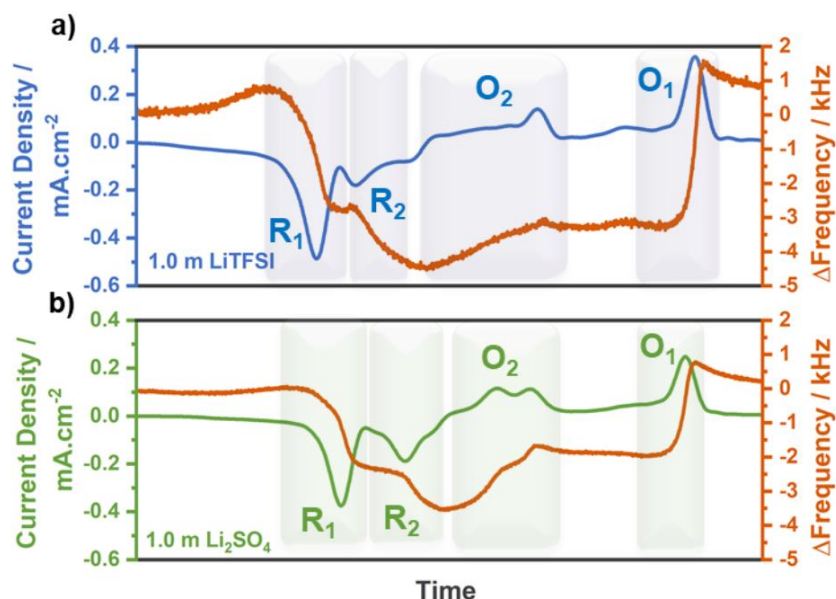


Fig. 5.5 - EQCM responses from the 50th cycle using the a) 1.0 m $\text{LiTFSI}_{(\text{aq})}$ and b) 1.0 m $\text{Li}_2\text{SO}_{4(\text{aq})}$ electrolytes.

We observe that whenever there is an unusual Δf response, it is typically accompanied by a significant variation in ΔR_m . As noted earlier, a high ΔR_m can be attributed to several factors, with dissolution or precipitation—common in ROMs—being a potential cause. UV-Vis spectroscopy was used to analyse cycled electrolytes because PTCDI, being a pigment, would make any dissolution into the electrolyte easily detectable. A dissolution test with 1.0 M $\text{LiTFSI}_{(\text{aq})}$ was carried out and compared to a 1.0 M $\text{LiTFSI}_{(\text{DMSO})}$ electrolyte, as PTCDI is known to be soluble in DMSO from previous studies. [219] 1.0 m $\text{LiTFSI}_{(\text{DMSO})}$ electrolytes display strong absorption bands, indicating PTCDI dissolution into the electrolyte. Whereas no UV-Vis bands are present in either the charged or discharged state for the 1.0 m $\text{LiTFSI}_{(\text{aq})}$ electrolytes, indicating that PTCDI is insoluble in this electrolyte (Fig. 5.6).

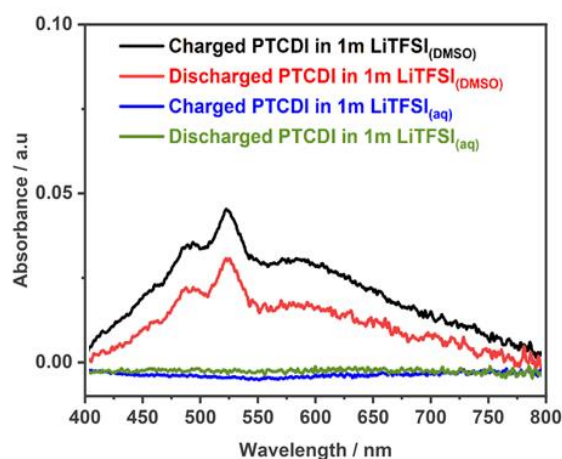


Fig. 5.6 - UV-Vis solubility test of PTCDI (dis)charged with 1.0 m LiTFSI_(DMSO) and 1.0 m LiTFSI_(aq).

While the EQCM study hints towards Li⁺ as the main charge carrier, the “co-insertion” of water could result in other charge carriers being active, such as H⁺. Indeed, a recent study on PTCDA in dilute neutral aqueous electrolytes attributes their EQCM response, which has similarities to ours, to H⁺ uptake. [220] They claim their Δf responses are the result of H⁺ intercalation through water absorption and subsequent OH⁻ dissociation, hence resulting in an overall frequency gain/mass loss during reduction. To determine if this happens with PTCDI, we monitored the pH during cycling in a beaker cell using a drop of phenol red, a pH indicator effective between pH 5 and 9. However, no visible colour change was observed across the charge and discharge cycles (Fig. 5.7). We also used UV-Vis spectroscopy to detect any subtle colour changes in the phenol red-containing electrolyte, but no shifts were found (Fig. 5.7). This leads us to conclude that there was no release of OH⁻, casting doubt on the occurrence of the previously mentioned mechanism for PTCDI.

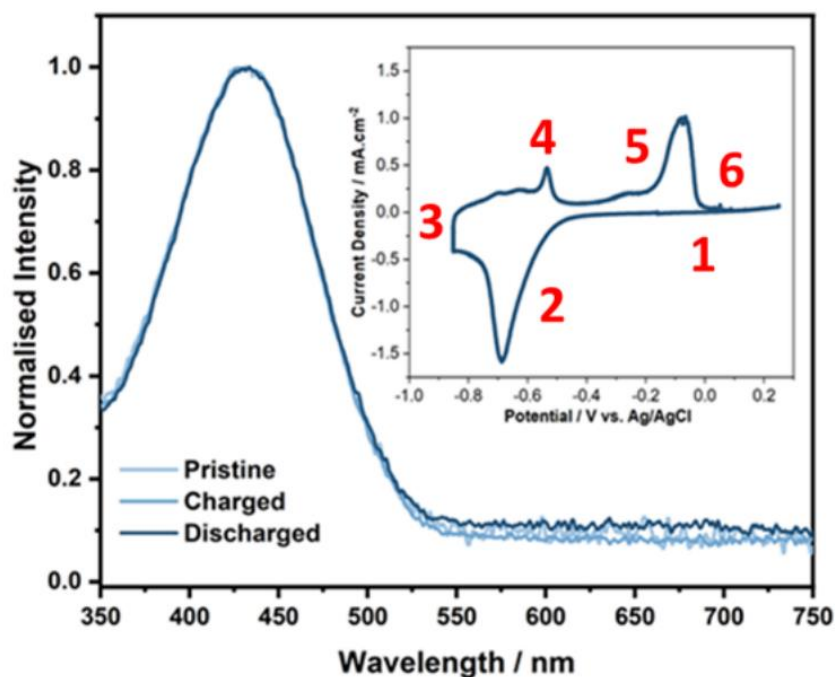


Fig. 5.7 - (top) UV-Vis of 1.0 m LiTFSI_(aq) containing phenol red pH indicator, taken from pristine, charged and discharged states and (bottom) picture of cell taken across cycling.

Moreover, if H⁺ intercalation was to occur via an alternative mechanism to the study proposed above, a Nernstian shift (+59 mV/decade) in the redox potentials should be present as the pH is changed. However, a change in pH from pH 5 to 7 (two-order magnitude [H⁺] change i.e. a shift of 118 mV) does not affect the redox potential (Fig. 5.8a). Conversely, changing the [Li⁺] from 1.0 to 3.0 m LiTFSI_(aq) resulted in a redox shift of +16 mV for R₁ and +30 mV for O₁ and O₂ which is in line with the expected +12 mV and +23 mV Nernstian shift calculated through the Nernst equation (Cal. 1 – 5 & Fig. 5.8b). A shift in redox of +5 mV for R₁ and +30 mV for O₁ and O₂ is observed when switching from 1.0 to 3.0 m for Li₂SO_{4(aq)}, and while R₁ is slightly lower than the expected +13 mV, O₁ and O₂ is very close to the expected +26 mV shifts (Fig. 5.8c). Altogether, these findings strongly suggest that solvated Li⁺ is the primary charge carrier, following the mechanism illustrated in Fig. 5.8d. To the best of our knowledge, no alternative charge carriers are present.

$$\begin{aligned}\Delta E &= -\frac{0.0591}{2} \log \left(\frac{[M_{Li}]}{[LiTFSI]} \right) - \log \left(\frac{[LiTFSI]}{[M_{Li}]} \right) \\ \Delta E &= -\frac{0.0591}{2} \log \left(\frac{[LiTFSI]}{[LiTFSI]} \right) \\ \Delta E &= -\frac{0.0591}{2} \log \left(\frac{[0.85]}{[2.1]} \right) \\ \Delta E &= +11.5 \text{ mV}\end{aligned}$$

Calculation. 1 – Nernst equation and working for LiTFSI for a concentration shift of 1.0 m (0.85 M) – 3.0 m (2.1 M) for R_1 based on the chemical equation $\Rightarrow 2 Li^+ + 2 e^- \Rightarrow 2 M_{Li}$

$$\begin{aligned}\Delta E &= -\frac{0.0591}{1} \log \left(\frac{[M_{Li}]}{[LiTFSI]} \right) - \log \left(\frac{[LiTFSI]}{[M_{Li}]} \right) \\ \Delta E &= -\frac{0.0591}{1} \log \left(\frac{[LiTFSI]}{[LiTFSI]} \right) \\ \Delta E &= -\frac{0.0591}{1} \log \left(\frac{[0.85]}{[2.1]} \right) \\ \Delta E &= +23 \text{ mV}\end{aligned}$$

Calculation. 2 – Nernst equation and working for LiTFSI for a concentration shift of 1.0 m (0.85 M) – 3.0 m (2.1 M) for O_1 and O_2 based on the chemical equation $\Rightarrow Li^+ + e^- \Rightarrow M_{Li}$

$$\begin{aligned}\Delta E &= -\frac{0.0591}{n} \log \left(\frac{[M_{Li}]}{[Li_2SO_4]^2} \right) - \log \left(\frac{[Li_2SO_4]^2}{[M_{Li}]} \right) \\ \Delta E &= -\frac{0.0591}{2} \log \left(\frac{[Li_2SO_4]}{[Li_2SO_4]} \right) \\ \Delta E &= -\frac{0.0591}{2} \log \left(\frac{[0.95]}{[2.6]} \right) \\ \Delta E &= +13 \text{ mV}\end{aligned}$$

Calculation. 3 – Nernst equation and working for Li_2SO_4 for a concentration shift of 1.0 m (0.95 M) – 3.0 m (2.6 M) for R_1 based on the chemical equation $\Rightarrow 2 Li^+ + 2 e^- \Rightarrow 2 M_{Li}$

$$\begin{aligned}\Delta E &= -\frac{0.0591}{n} \log \left(\frac{[M_{Li}]}{[Li_2SO_4]^2} \right) - \log \left(\frac{[Li_2SO_4]^2}{[M_{Li}]} \right) \\ \Delta E &= -\frac{0.0591}{1} \log \left(\frac{[Li_2SO_4]}{[Li_2SO_4]} \right) \\ \Delta E &= -\frac{0.0591}{1} \log \left(\frac{[0.95]}{[2.6]} \right) \\ \Delta E &= +26 \text{ mV}\end{aligned}$$

Calculation. 4 – Nernst equation and working for Li_2SO_4 for a concentration shift of 1.0 m (0.95 M) – 3.0 m (2.6 M) for O_1 and O_2 based on the chemical equation $\Rightarrow Li^+ + e^- \Rightarrow M_{Li}$

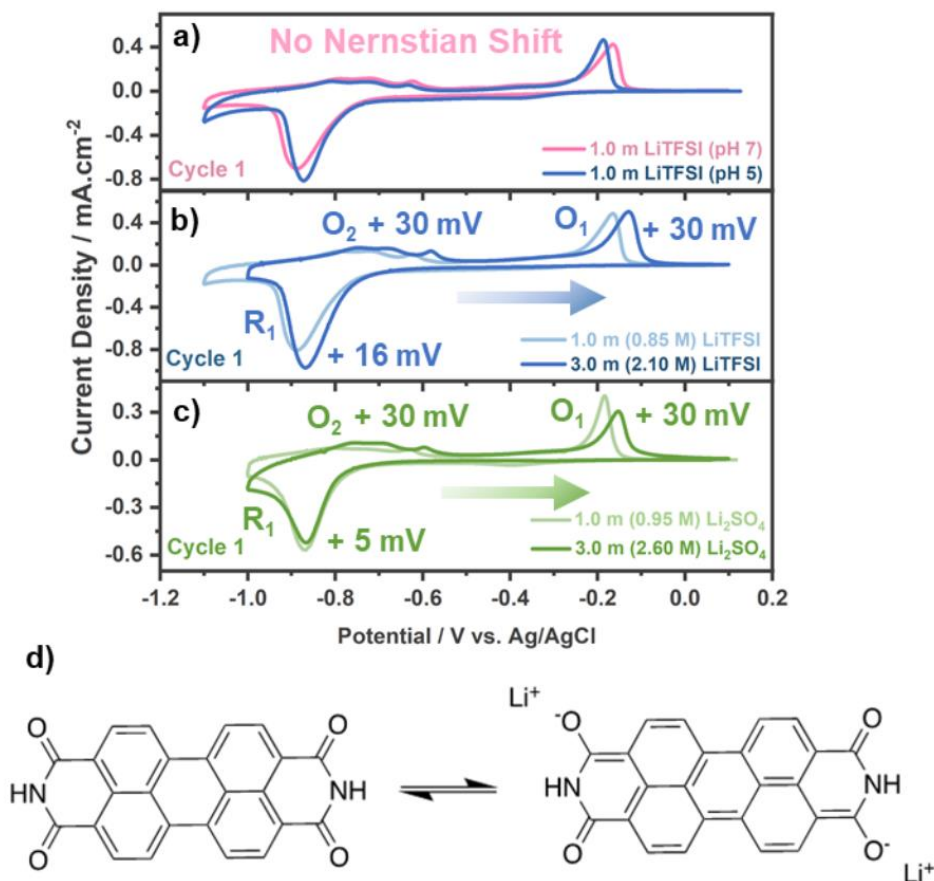


Fig. 5.8 - 1st CV cycle of PTCDI with different a) pH, b) [LiTFSI_(aq)], c) [Li₂SO_{4(aq)}], and d) the proposed charge storage mechanism.

5.4 Electrochemical Performance

To study the cycling performance of the PTCDI electrode, we start by cycling electrodes versus an oversized LFP cathode with 1.0 m LiTFSI_(aq). The PTCDI || LFP pseudo half-cell manages to deliver ca. 117 mAh g⁻¹ in the 2nd cycle, close to the theoretical 137 mAh g⁻¹ based on the uptake of 2 Li⁺ (Fig. 5.9a). The cells exhibit excellent capacity retention with LiTFSI_(aq) at 1C with 90% retained after 1000 cycles and 75% after 600 cycles at 0.2C (Fig. 5.9a & 5.9b). In contrast, cells with Li₂SO_{4(aq)} display severe capacity fading after 200 cycles at 1C, exemplifying the superior stability LiTFSI compared to Li₂SO₄ (Fig. 5.9c). This performance could very well be related to the cause of those differences in EQCM response, potentially down to kosmo/chaotropic anion effects, as observed for PTCDI.[168] Compared with previous aqueous PTCDI studies, applying PTCDI with LiTFSI_(aq) offers one of the best capacity retentions reported so far (Table. 5.1). This was achieved without resorting to

extreme WISE salt concentrations and at comparably low rates. To assess the self-discharge of PTCDI, we conducted a 20-hour OCV step after charging, following a few cycles to ensure activation (Fig. 5.9d). A minimal discharge capacity loss of $2 \text{ mAh}\cdot\text{g}^{-1}$ was observed. Although this represents a slight decrease in Coulombic efficiency (99.9% to 98.3%) compared to continuous cycling, the self-discharge remains low, highlighting the material's stability.

Electrolyte	C-rate	Capacity Retention
1.0 M NaNO_3 (2:1 Glycerol: H_2O) [221]	0.1 A g^{-1} (~0.73C)	75%@100
1.0 M $(\text{NH}_4)_2\text{SO}_4$ [222]	10C	90%@400
22.0 m KOTf [83]	20C	77%@1000
22.0 m KOTf + 0.2 m FeOTf [85]	1 A g^{-1} (~7.3C)	80@200
$\text{K}(\text{FSA})_{0.6}(\text{OTf})_{0.4}\cdot 1.0\text{H}_2\text{O}$ [223]	1 A g^{-1} (~7.3C)	100%@200
5.0 m MgCl_2 + 2.0 m TBMACl [224]	0.05 A g^{-1} (~0.365C)	64%@100
0.5 M $\text{Mg}(\text{NO}_3)_2$ [86]	0.5 A g^{-1} (~3.65C)	87%@10000
1.0 m LiTFSI	0.137 A g^{-1} (1C) 0.027 A g^{-1} (0.2C)	90%@1000 75%@600

Table. 5.1 - Comparison of aqueous PTCDI half-cells.
C-rates are calculated relative to the theoretical capacity of PTCDI (137 mAh g^{-1}).

To gain a deeper understanding of the charge storage mechanism — whether capacitive or diffusion-limited — a methodology previously developed by Dunn and co-workers is employed. [225] The b -values extracted from this methodology demonstrate a mixture of faradaic ($b = 0.5$) and non-faradaic ($b = 1$) reaction mechanisms, with the first reduction peak (R_1) and the first oxidation peak (O_1) displaying a mixture of both mechanisms with $b = 0.75$ and 0.65 , respectively, while the second peaks (R_2 , O_2' , and O_2'') are more non-faradaic, or pseudocapacitive with $b = 0.8$ and 1 (Fig. 5.9e). This is in line with previous studies of PTCDI using aqueous Na and Zn-based electrolytes. [226], [227] A more capacitive controlled reaction mechanism should enable the PTCDI electrode to exhibit strong rate performance. Rate capability tests demonstrate this strong performance, with 75% of the capacity retained at 5C, with > 98 CE% obtained for all cycle rates (Fig. 5.9f). The rate retention is comparable with previous studies using PTCDI with aqueous electrolytes, although we note few other studies apply rates <1C.

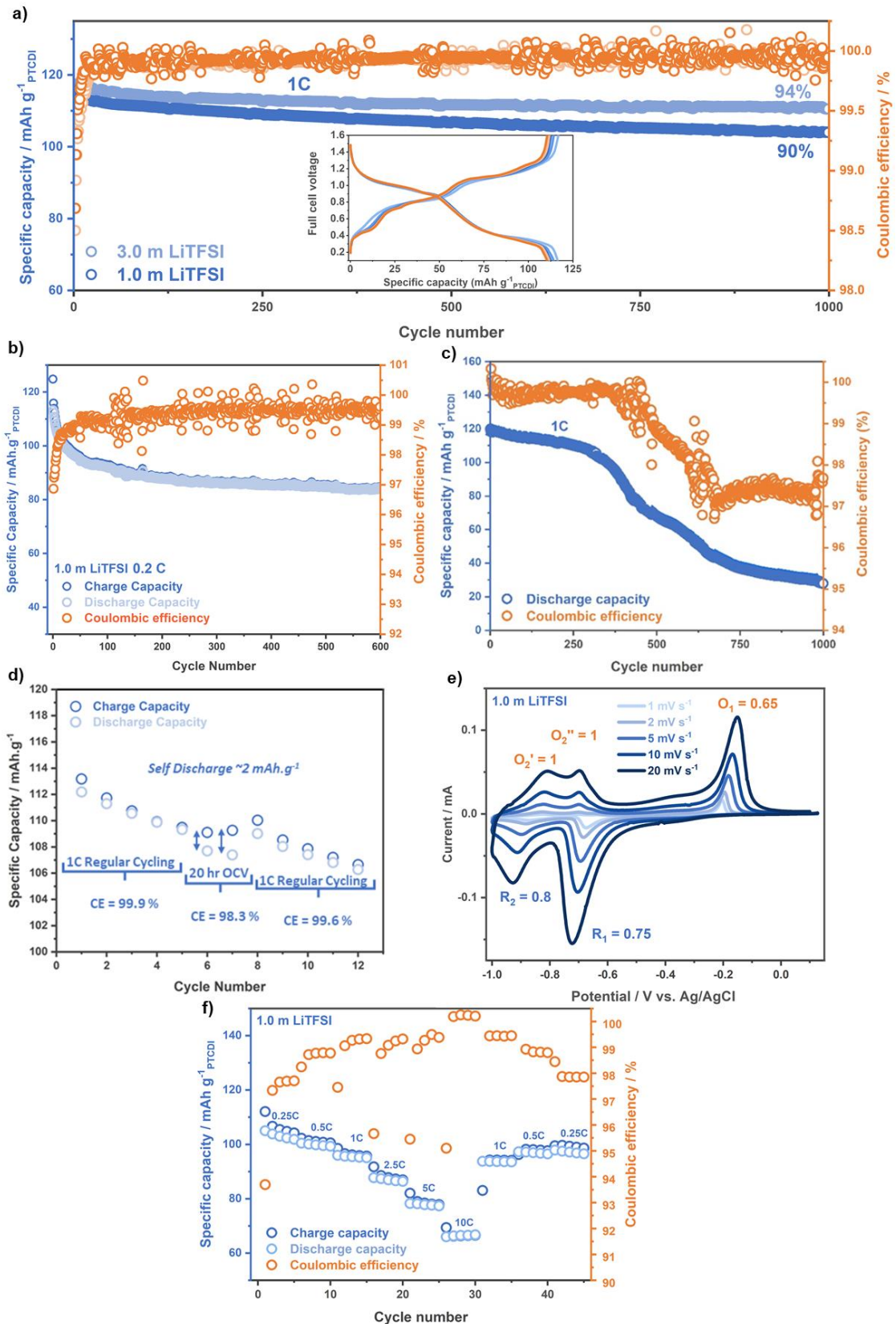


Fig. 5.9. - a) long term cycling vs. LFP (coin cell, pseudo half-cell), b) long-term cycling vs. LFP (Coin cell, 0.2C) c) long-term cycling with 3.0 m Li₂SO₄(aq), d) Self-discharge test with 1.0 m LiTFSI(aq) at 1C followed by charge with 20 h OCV for 2 cycles and then back to regular 1C cycling, e) CV and b-values from PTCDI vs. LFP (EQCM Cell, 3-electrode half-cell) and f) rate capability cycled vs. LFP (coin cell, pseudo half-cell).

Finally, PTCDI || LMO full cells with 1.0, 3.0, and 5.0 m LiTFSI_(aq) electrolytes (Fig. 5.10a) were employed to test a higher energy density system. A poor capacity retention is observed for the 1.0 and 3.0 m electrolytes, attributed to the instability of LMO with aqueous electrolytes, while the 5.0 m electrolyte performs much better with: a nominal voltage of 1.47 V, an energy density of 71 Wh kg⁻¹_(PTCDI+LMO, 10th cycle), and a capacity retention of 74%@500 (Fig. 5.10b). While the salt concentration is rather high, diluents and additives can be employed to not only reduce the salt concentration, but also to mitigate the dissolution of LMO. We also acknowledge that Mn is a critical raw material (albeit in the lowest “very low” risk group) [228], but stress that these cells serve as a proof-of-concept to demonstrate a practical implementation of PTCDI for less expensive and more sustainable ALIBs as compared to WISE based batteries.

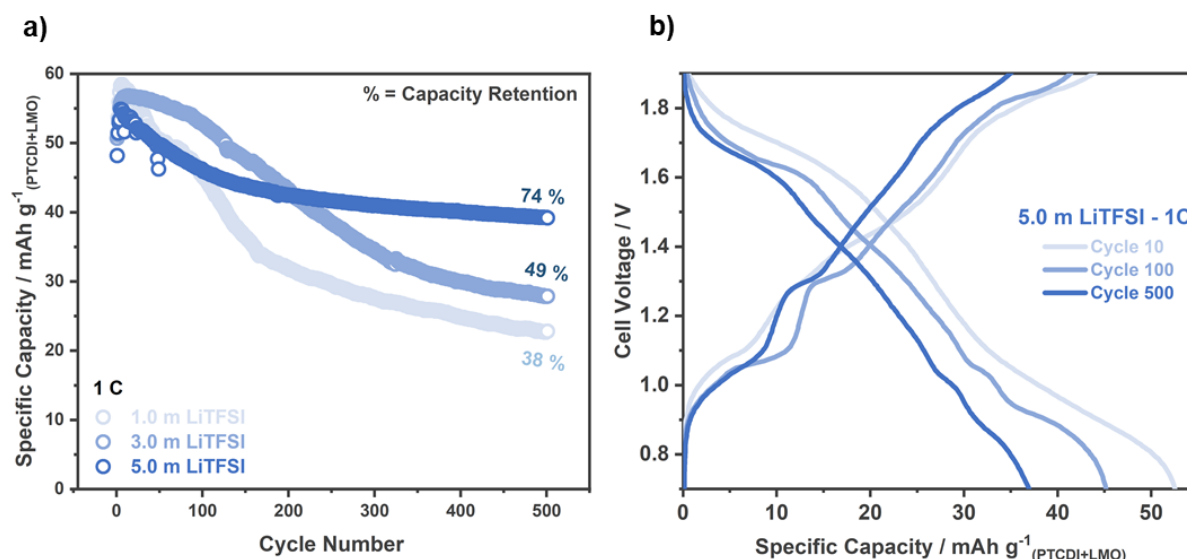


Fig. 5.10 - a) Long-term cycling of balanced PTCDI || LMO full cells (coin cells) and b) the corresponding potential curves for 5.0 m LiTFSI_(aq).

Conclusions to Chapter 5

The electrochemical behaviour and performance of PTCDI was studied for the first time applied for ALIBs. Despite the different redox responses using organic and aqueous electrolytes, we can conclude Li^+ to be the primary charge carrier, albeit likely involving solvated Li^+ in the aqueous electrolyte. From EQCM-R data it would appear the anion choice, kosmo/chao-tropic, appears to have consequences to the electrochemistry, however, further studies involving EQCM-D or even molecular dynamics (MD) simulations are required to fully comprehend these effects. The anion choice also influences the long-term cycling stability, with 1.0 m $\text{LiTFSI}_{(\text{aq})}$ vastly more stable than 3.0 m $\text{Li}_2\text{SO}_{4(\text{aq})}$. Indeed, the electrochemical performance of PTCDI in half-cells with 1.0 m $\text{LiTFSI}_{(\text{aq})}$ and proof-of-concept full cells with 5.0 m $\text{LiTFSI}_{(\text{aq})}$ showcase the high stability of the material in non-WISE conditions while cycling at much lower C-rates compared to the previous examples. While the PTCDI itself is certainly a viable option for use as an anode for ALIBs, there are plenty of untested ROMs for ALIBs. Altogether, this study aims to broaden the scope of ALIBs by implementing non-typical materials and electrolytes, leading to more sustainable and safe electrochemical energy storage.

Conclusion and Perspectives

The initial goals of this thesis were to utilise electrolyte engineering to improve ALIBs by building on the principles of super-concentrated electrolytes and their diluent variants. While addressing these issues, we often found ourselves taking different paths that led us to study fundamentals of water splitting, ROMs, and AZMBs. This journey has provided many interesting insights that can certainly be built upon, both from a fundamental perspective and potentially from an industrial one.

Upon setting out to explore alternative methods for modulating solvation properties, the use of amino acids came to mind due to their chemical structure and broad range of functionalities. These characteristics offer numerous ways to engineer and tailor our electrolytes. Our initial attempts with citrulline, which we hypothesised would provide functionalities similar to urea, were unsuccessful. However, it is worth noting that there are hundreds of amino acids, and as we demonstrated with citrulline, they exhibit interesting physico-chemical interactions with LiTFSI and water. The potential of using amino acids to deepen our understanding of PCET reactions is certainly promising. Our study demonstrates that amino acids can leverage their buffering effects to influence the HER. Although our findings suggest that only Asp and Glu will be effective for this reaction, targeting other amino acids by adjusting the starting pH of their solutions to the pKa values where buffering occurs could be a viable approach for other PCET reactions, such as the OER, CO₂ and N₂ reduction. However, exploring these reactions was beyond the scope of this thesis, which primarily focused on enhancing aqueous electrolytes for batteries.

Returning to aqueous electrolytes for batteries, we focused on novel salts. We leveraged the principles of the Hofmeister series, which has long been used to characterise various properties of ions in solution, including salting-in and salting-out effects. Crucially, the Hofmeister series also provides insights into hydrogen bond breaking and formation of water, which was the target of our next study. In LiTFSI, Li⁺ is kosmotropic and reinforces the HBN of water. To counteract this, we sought a chaotropic cation that could break down the HBN. We identified guanidinium (Gdm⁺) as a suitable candidate and, for the first time, reported the novel GdmTFSI salt. We

characterised the salt and determined its crystal structure before testing it in aqueous solutions. The results confirmed our hypothesis that changing the cation from kosmotropic to chaotropic influences the HBN of water and thus broadens the ESW. However, the salt's solubility limit of 8 m restricted the formation of a stable SEI, limiting its practical use. A potential solution could involve adapting the Gdm^+ to create a slightly more disordered crystal structure that promotes water solubility. While this could reduce the chaotropic effect, a balance between solubility and chaotropy could be achieved. Despite this, Gdm-based salts hold promise for AZMBs, a topic that the CSE lab is actively exploring. For instance, the addition of 2 M GdmSO_4 as a co-salt to 2 M ZnSO_4 significantly improved the cycle life of a $\text{Zn} \parallel \text{MnO}_2$ battery under our testing conditions, surpassing previous benchmarks. While this thesis did not investigate the exact mechanism by which Gdm^+ functions, it suggests that Gdm-based salts can positively impact aqueous electrolytes. Zn-based technologies are notably more sustainable than Li due to Zn's abundance, low cost, and availability. It would be intriguing to explore how GdmTFSI combined with Zn(TFSI)_2 performs in AZMBs. Additionally, investigating other sustainable chemistries, such as Na, K, or Mg-ion systems with Gdm-based salts, could be a promising direction for future research.

To advance our work with AZMBs, we sought additional salts that could enhance cycling performance. This investigation led us to explore oligoether salts, which had been previously reported for Li, Na, and K, but not for Zn. Although Zn(MEC)_2 , Zn(MEA)_2 , and Zn(MEEA)_2 salts performed poorly as primary salts, their use as additives at 5 wt% in conjunction with 2 M ZnSO_4 and 2 M ZnSO_4 + 10 M urea significantly improved the Zn electrodeposition process. This enhancement enabled long-term cycling of $\text{Zn} \parallel \text{Zn}$, $\text{Zn} \parallel \text{Cu}$, and $\text{Zn} \parallel \text{MnO}_2$ cells. The performance boost appears to be due to the formation of a stable ZnS-based SEI. However, a complete understanding of the underlying mechanism is required. Ongoing research aims to elucidate the science behind these salts, with EQCM-R, double-layer capacitance measurements, and impedance spectroscopy as high priorities moving forward. Beyond the fundamental science, our work with these salts has led to two patents, which is significant given our lab's active exploration of a $\text{Zn} \parallel \text{MnO}_2$ within the context of a start-up. Meanwhile, it is certainly worth revisiting the Li-based oligoethers. Preliminary experiments suggest that highly concentrated electrolytes can be achieved

by forming binary mixtures of LiTFSI and LiMEEA. Moreover, the chemical similarities between these salts and glymes or polymers may reveal properties that could enhance the performance of ALIBs and LIBs.

Finally, shifting focus from electrolyte engineering to utilising materials that function within the ESW of non-super concentrated electrolytes, we examined PTCDI. We explored its fundamental chemistry to identify the primary charge carrier and the mechanism of lithium uptake through various measurements. From a performance standpoint, PTCDI demonstrates exceptional stability in low-to-moderately concentrated electrolytes, achieving 1000 cycles at lower C-rates when used with LFP in 1 m LiTFSI. The performance appears to be influenced by the nature of the anion, and investigating this further will be a focus moving forward. To fully utilise the ESW of our electrolyte, we employed LMO, which has a redox potential near the upper limits of water splitting concerning the OER. The dissolution of Mn leads to significant capacity fading at lower concentrations, prompting us to use 5 m LiTFSI. This thesis explores various strategies for electrolyte engineering that could address this issue. For instance, employing GdmTFSI + LiTFSI or LiTFSI + LiMEEA could help reduce the concentration of LiTFSI while leveraging additional properties such as chaotropicity.

Moving forward we feel a transition away from super-concentration may be in order. Although super-concentration is interesting and effective in harnessing the potential of ALIBs, even the most effective systems pale in comparison to non-aqueous LIBs regarding performance. Additionally, the key aspects of aqueous batteries, namely sustainability and low cost, are compromised with these electrolytes. Instead, we propose finding ways to maximise what can be achieved with dilute electrolytes, which can be done through ROMs such as PTCDI which also elevate the sustainability of the battery. Transitioning completely from lithium-ion batteries (LIBs) to greener and cleaner, albeit "weaker," battery technologies could be a forward-looking approach. While LIBs are widely used across various applications, stationary energy storage for wind and solar power could avoid using LIBs, as it does not require high energy density. AZMBs are one of many alternatives we could consider for such applications. We demonstrated the effectiveness of electrolyte engineering in advancing this technology through our work on designing novel, task-specific salts. The flexibility and myriad possibilities in salt design make it a valuable approach for developing

innovative electrolytes. Regardless of the specific technology, there is no doubt that electrolyte engineering remains a critical factor in advancing any battery domain. Aqueous electrolytes, with their potential benefits, undoubtedly have a significant role to play in diversifying our energy storage systems. As society continues to confront the ongoing challenges of climate change and global warming, embracing innovative approaches in electrolyte engineering will be essential for achieving a sustainable energy future.

ANNEX

Chapter 2

Materials and Methods

Electrochemical measurements

All chemicals were purchased from commercial suppliers without any further purification. Ultrapure Mili-Q water (18.2 M Ω cm) was used for all experiments. Electrolytes based on lithium bis(trifluoromethanesulfonyl)imide (LiTFSI) (99.9%, Solvionic) and citrulline (99.9%, abcr) were mixed at different compositions to create the ternary plot. For the full cells test using Mo₆S₈ and LFP, composite self-standing electrodes were fabricated using Bellcore technique. Both active materials were mixed with carbon super P (Csp, Timcal), and poly(vinylidene fluoride)-co-hexafluoropropylene (PVdF-HFP) (Solvay) in the ration of 73 wt% of AM, 8 wt% of Csp, and 19 wt% of PVdF-HFP and mixed in acetone to form a slurry Dibutylphtalate (DBP, 99% Sigma-Aldrich) was added to use as plasticizer. Then, the as-prepared slurry was casted by doctor blade technique and left to dry overnight. Electrodes were punched with a 0.5 in. diameter and loading of around 7 mg cm⁻² (Mo₆S₈) and 21 mg cm⁻² (LFP) of active material were obtained. Finally, electrodes were washed three times in diethyl ether (99% min, Alfa Aesar) and dried at 60 °C under vacuum. Coin cells were assembled in an Ar-filled glovebox (MBRAUN). Electrolytes were saturated with argon prior to any experiment. Two Whatman glass fibers used as separators were soaked with the electrolyte. Mo₆S₈/LFP (1:3) full cells were assembled using stainless steel as current collectors. Galvanostatic cycling were performed in a temperature-controlled oven using a MPG2 multichannel potentiostat (Bio-Logic).

Glassware was rinsed twice with ultrapure water, followed by being boiled in ultrapure water and was further rinsed before use. Cyclic voltammetry measurements were performed in an electrochemical glass cell. SEI stability was performed using a PTFE embedded glassy carbon disc (3 mm diameter, Pine Research Instrumentation) as working electrode, Pt wire as counter electrode and standard calomel electrode (SCE) as the reference.

Pt electrodes (Pine Research) were polished with 0.6 μm and 0.05 μm ultrafine alumina slurry, after which the electrode was sonicated in a 50/50 mix of acetone/water for 2 mins. Amino acid solutions with concentrations of 5, 10, 20 and 30 mM were prepared using L-aspartic acid (99%, Alfa-Aesar), L-glutamic acid (99%, Sigma-Aldrich), L-serine (99%, Alfa-Aesar) and L-histidine (98% +, Alfa-Aesar) in Li_2SO_4 (99%, monohydrate, Alfa-Aesar) 100 mM solutions to minimise the ohmic drop. pH 2.3, 3 and 3.3 were prepared using H_2SO_4 (96%, Sigma-Aldrich) in 100 mM Li_2SO_4 . All electrolytes were degassed using Ar (Linde, purity 5) for 10 mins prior to any electrochemical measurements to remove O_2 and CO_2 . The pH of each electrolyte was determined through measuring the potential between a reference hydrogen electrode and a standard calomel electrode, for which the potential was 0.248 V; the pH is then calculated using the Nernst equation, $\text{pH} = (E - 0.248 \text{ V})/0.059 \text{ V}$. All cyclic voltammetry measurements have a scan rate of 20 mV s^{-1} with the use of a rotating disk electrode (Pine Research) at a rotation speed of 2000 rpm.

Conductivity and IR Spectroscopy

The ion conductivities (σ) were measured using a Mettler-Toledo SevenCompact S230 conductivity meter with a 12 mm InLab® 710 Cond probe with 4 Pt poles conductivity cell ($\pm 0.5\%$).

Fourier-transform infrared (FTIR) vibrational spectra were obtained using a Bruker Alpha attenuated total reflection (ATR-FTIR) spectrometer and a Ge crystal, for the same electrodes as for the *ex situ* XRD. The spectra were recorded with 2 cm^{-1} resolution and 512 scans.

Amino Acid Titrations

The procedure was derived from [229] using 30 mM of amino acid for all four utilised in this study. The amino acid solutions were brought down to pH 2 using HCl (37%, Carlo Erba) 50 mM solution, then 1 mL aliquots of NaOH (>98% pellets, Sigma Aldrich) 60 mM solution was added gradually.

NMR measurements

The amino acid structure before and after electrochemistry was evaluated by ^1H liquid-state NMR spectra, recorded in a Bruker 7.046 T (300 MHz for ^1H) Advance III NMR spectrometer mounted with a 5 mm HX(F) probe head. 30 mM Aspartic acid solutions were made in D_2O (99.9%, Sigma Aldrich) with 100 mM Li_2SO_4 . The samples were measured in a 5 mm glass tube. The spectra were recorded with a 90° acquisition sequence, over 32 scans (10 s acquisition time each), and were referenced with the residual signal of water.

Supplementary Figures

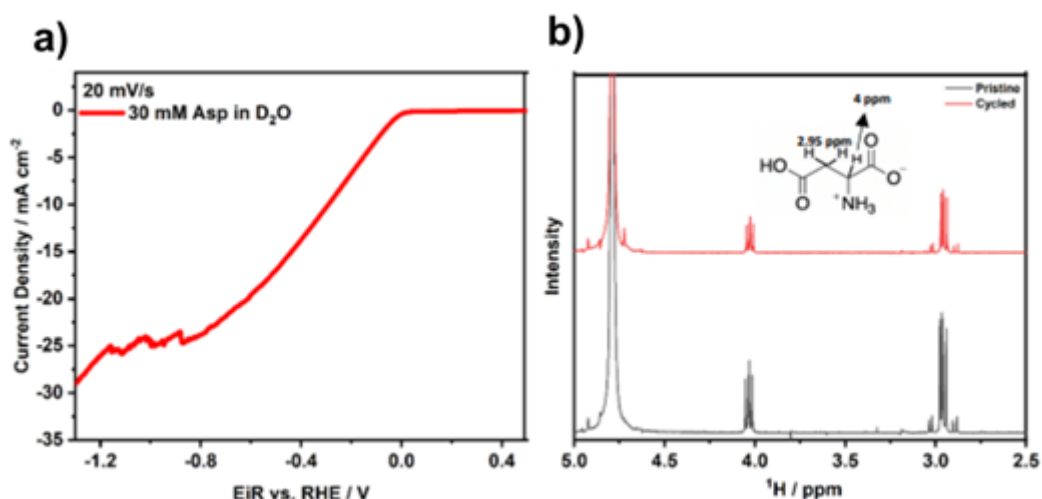


Fig. A2.1 – a) Cyclic voltammograms measurement for 30 mM Aspartic Acid in D_2O with 100 mM Li_2SO_4 supporting salt recorded at 20 mV/s on polycrystalline Pt rotating disk electrode (rotation speed of 2000 RPM) and b) NMR data for pristine and cycled measurement for 30 mM Aspartic Acid in D_2O with 100 mM Li_2SO_4 supporting salt: δH (300 MHz; D_2O) 2.95 (2 H, m) and 4.05 (1 H, dd), 4.75 (s, H_2O).

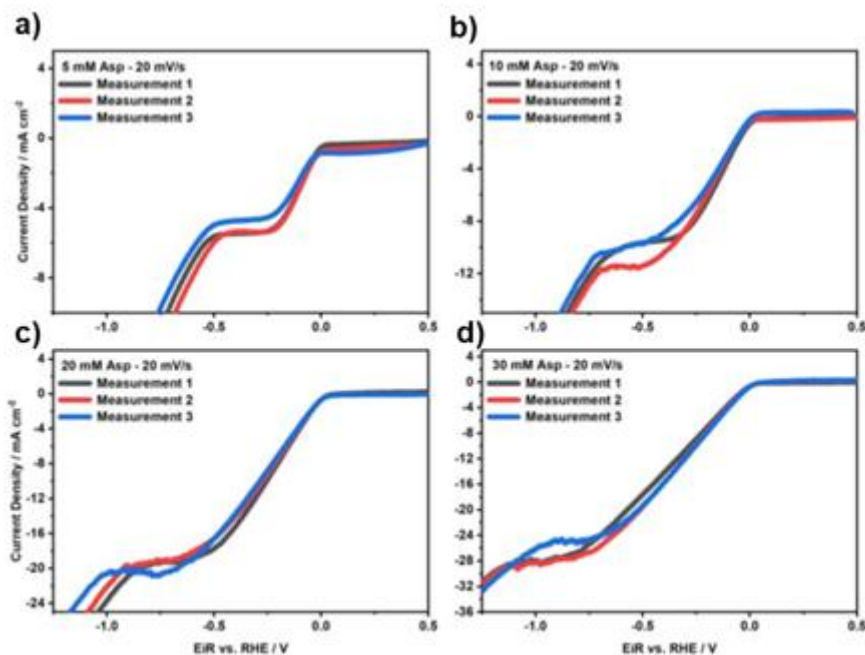


Fig A2.2 - Three separate cyclic voltammograms measurements for a) 5 mM Aspartic Acid (Asp), b) 10 mM Asp, c) 20 mM Asp and d) 30 mM Asp with 100 mM Li_2SO_4 supporting salt recorded at 20 mV/s on polycrystalline Pt rotating disk electrode (rotation speed of 2000 RPM).

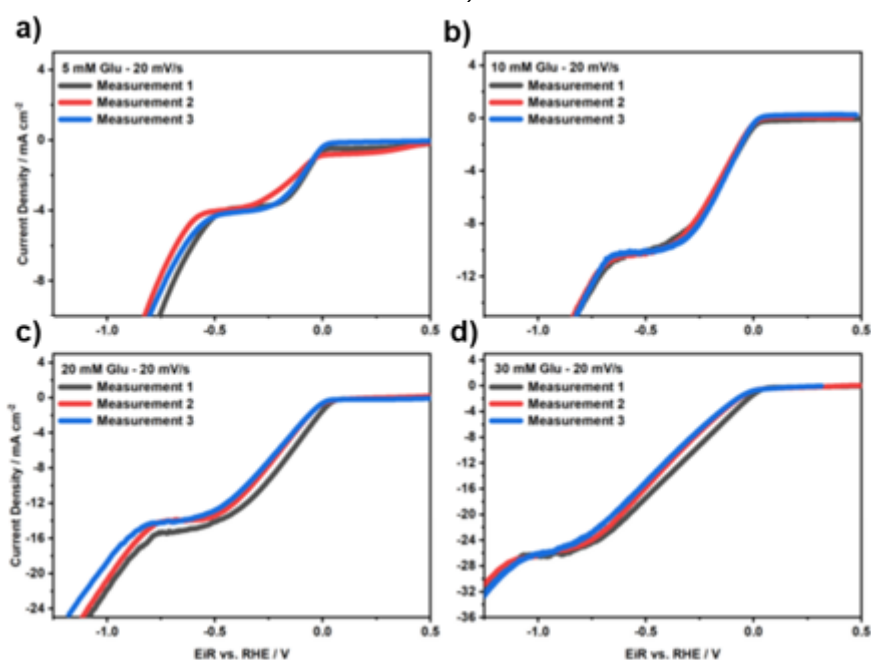


Fig A2.3 - Three separate cyclic voltammograms measurements for a) 5 mM Glutamic Acid (Glu), b) 10 mM Glu, c) 20 mM Glu and d) 30 mM Glu with 100 mM Li_2SO_4 supporting salt recorded at 20 mV/s on polycrystalline Pt rotating disk electrode (rotation speed of 2000 RPM).

Chapter 3

Materials and Methods

Synthesis Procedure for GdmTFSI

To synthesis the material, 0.0104 mol of LiTFSI (99.9% extra dry, Solvionic) and 0.0052 mol of Guanidium Sulphate (99%, Sigma Aldrich) was dissolved in the minimum volume of water, after which the LiTFSI solution is added dropwise under stirring into the Gdm₂SO₄ forming a cloudy solution. This solution is dried, forming a white precipitate containing a mixture of GdmTFSI and Li₂SO₄. Acetone (10 mL, extra dry, Alfa Aesar) is added to the mixture and stirred for 1 h, after which this mixture is filtered. The filtrate, containing the GdmTFSI, is rotary evaporated under vacuum to form a cloudy ionic liquid which, once cooled, crystallises to form the desired final product that is dried under vacuum overnight with a yield of 97%.

Single Crystal XRD

The X-ray diffraction experiment was performed in the XRD platform of the IMPMC (Paris). A transparent platy crystal (100x50x10µm³) was selected and mounted on a MiteGen micro-loop within silicon oil. The data was collected at 293K using a Rigaku MM007HF Mo rotating anode diffractometer equipped with a RAXIS4++ IP detector, Osmic confocal multilayers optics. A 180° omega scan (1 min and 1° width/frame) was carried out and 40087 reflections were collected (20251 independent). Our “homemade” goniometer only allows for omega scans, and this explains the relatively limited completeness (94.6% at the maximum crystallographic resolution). The crystal quality was good however, low thickness limited the diffraction to $d_{min}=0.9 \text{ \AA}$. The unit cell parameters determination, refinement and data reduction were carried out with CrysAlisPro RED.1 The measured reflections were scaled and merged with the same program. Then, using Olex2 suite, the structure was solved in the P-1 space group with the SHELXT structure solution program (Intrinsic Phasing method) and refined with the SHELXL refinement package using least squares minimisation methods. The asymmetric unit contains 12 [Gdm]⁺ and 12 [TFSI]⁻. All non-H atoms were refined with anisotropic displacement parameters, RIGU and a few geometrical restraints were

applied to some atoms of the 4 disordered [TFSI]⁻. The data can be obtained free of charge from The Cambridge Crystallographic Data Centre via www.ccdc.cam.ac.uk/structures (CCDC deposition number # 2284950).

IR spectroscopy

FTIR spectra were acquired in ATR mode on a Nicolet™ iSTM 5 FTIR spectrometer (Thermo Fisher Scientific) in the range of ~500 to 4000 cm⁻¹.

Thermogravimetric Analysis/Difference Scanning Calorimeter

The thermal stability was analysed by TGA/DSC using a Mettler Toledo TGA/DSC3+LF/1100. Around ~10 mg of the sample was put in an aluminium crucible and heated at a rate of 5°C/min from ambient temperature to 400°C under air.

Inductively Coupled Plasma Mass Spectroscopy

The residual Li content was quantified using inductively coupled plasma mass spectroscopy (ICP-MS, Nexion 2000, Perkin Elmer). Solution used was dilute nitric acid solution (Sigma-Aldrich). To factor in any residual Li content within the stock solution. Five different concentrations of GdmTFSI in this solution were probed and the gradient of these values is used as the Li content of the GdmTFSI powder.

Aqueous solution preparation

GdmTFSI_(aq) solutions were created with ultra-pure water (Millipore® Direct-Q® Purification, 18.2 MΩ·cm at 25°C) in magnet stirred vials at ~ 25°C.

Ionic conductivity measurements

The ion conductivities (σ) were measured using a Mettler-Toledo SevenCompact S230 conductivity meter with a 12 mm InLab® 710 Cond probe with 4 Pt poles conductivity cell ($\pm 0.5\%$).

Electrochemical Measurements

ESW measurements were performed using a PTFE embedded glassy carbon disc (3 mm diameter, Pine Research Instrumentation) as working electrode, Pt wire as counter electrode and saturated calomel electrode (SCE) was used as a reference. ~5 mL of electrolyte was used for each measurement. Temperature for 8m GdmTFSI was controlled by flowing water controlled via a chiller into a mantle around the electrochemical glass cell. Cyclic voltammetry experiments were all performed on a VMP3 potentiostat (Bio-Logic) at a $5 \text{ mV}\cdot\text{s}^{-1}$ scan rate determination with potentials converted Standard Hydrogen Electrode (SHE) from SCE (+0.248 V). Separate scans were taken to determine the cathodic and anodic limits. For measurements in acetonitrile, a leak-less Ag/AgCl reference electrode was used and these measurements were carried out in an Ar-filled glovebox (Braun)

Viscosity Measurements

The viscosities of the electrolytes were measured at 25°C using a Lovis 2000 ME rolling ball viscometer, coupled with an Anton Paar DMA 4500 M oscillation U-tube densitometer

Chapter 4

Materials and Methods

Synthesis of Zn(MEC)₂

Zn(MEC)₂ was prepared by dissolving 2-(2-methoxyethoxy)acetic acid (TCI) in water to which Zn₅(CO₃)₂(OH)₆ (Sigma Aldrich) was added until the pH of the solution reached 7. The resulting solution was distilled under vacuum to obtain the zinc (2-methoxyethyl carbonate)₂.

Synthesis of Zn(MEA)₂

Zn(MEA)₂ was prepared by dissolving 2-[2-(2-methoxyethoxy)ethoxy]acetic acid (TCI) in water to which Zn₅(CO₃)₂(OH)₆ (Sigma Aldrich) was added until the pH of the solution reached 7. The resulting solution was distilled under vacuum to obtain the zinc (2-(2-methoxyethoxy)acetate)₂.

Synthesis of Zn(MEEA)₂

2-[2-(2-methoxyethoxy)ethoxy]acetic acid (HMEEA) is prepared in a Ar-filled glovebox by dissolving lithium metal (0.132 mol) in excess TEGME (TCI) (2-(2-(2-Methoxyethoxy)ethoxy)ethanol) (50 mL), after which chloroacetic acid (Sigma Aldrich) (0.067 mol) dissolved in TEGME (10mL) is added dropwise into the solution and is reacted for 16 hours. Excess TEGME is removed via distillation after which the solution is treated with an aqueous solution of orthophosphoric acid (0.098 mol). Dichloromethane (DMC) (VWR, 99%) was added to the solution resulting in two phases. The aqueous phase was washed further with DMC and the organic phases were combined and dried using magnesium sulphate. This solution is then distilled under vacuum to yield the 2-[2-(2-methoxyethoxy)ethoxy]acetic acid. The Zn(MEEA)₂ was prepared via cation exchange reaction in water using Zinc carbonate basic (Zn₅(CO₃)₂(OH)₆) (Sigma Aldrich, 99%). 2-[2-(2-methoxyethoxy)ethoxy]acetic acid was dissolved in water to which Zn₅(CO₃)₂(OH)₆ was added until the pH of the solution

reached 7. The resulting solution was distilled under vacuum to yield the zinc (2-[2-(2-methoxyethoxy)ethoxy]acetate)₂.

Synthesis of LiMEEA

2-[2-(2-methoxyethoxy)ethoxy]acetic acid (MEEA) is prepared in a Ar-filled glovebox by dissolving lithium metal (Sigma Aldrich) (0.132 mol) in excess 2-(2-(2-Methoxyethoxy)ethoxy)ethanol (TEGME) (TCI) (50 mL), after which chloroacetic acid (99%, Sigma Aldrich) (0.067 mol) dissolved in TEGME (10mL) is added dropwise into the solution and is reacted for 16 hours. Excess TEGME is removed via distillation after which the solution is treated with an aqueous solution of orthophosphoric acid (0.098 mol). Dichloromethane (DMC) (VWR, 99%) was added to the solution resulting in two phases. The aqueous phase was washed further with DMC and the organic phases were combined and dried using magnesium sulphate (Sigma Aldrich, 99%). This solution is then distilled under vacuum to yield the 2-[2-(2-methoxyethoxy)ethoxy]acetic acid. The LiMEEA was prepared via cation exchange reaction in water using lithium carbonate (Sigma Aldrich, 99%). The resulting solution was distilled under vacuum to yield the LiMEEA.

NMR measurements

To confirm a successful synthesis of the salts ¹H and ¹³C liquid-state NMR spectra was carried out recorded in a Bruker 7.046 T (300 MHz for ¹H) Advance III NMR spectrometer mounted with a 5 mm HX(F) probe head, using CDCl₃ (Sigma Aldrich) as the solvent.

Electrospray Ionisation Mass Spectrometry (ESI-MS)

MS analysis was done by infusing the sample in the electrospray source of a Synapt G2-S (Waters, SN: UEB205) mass spectrometer operating in positive or negative mode. Capillary and cone voltage were respectively 3000V and 30V. Source and desolvation temperatures were respectively 250°C and 100°C. Mass spectra are acquired over a range of 50-1500 Da.

Elemental Analysis

15 mg of the sample was placed in a tin capsule and was transferred into an inert gas chamber (zero blank) under Helium flow. After which the catalytic combustion of the capsule and sample at a temperature of 1150°C was carried out. Followed by a reduction of the combustion gases over hot copper in a second furnace at 850°C. The gases formed for analysis N₂, CO₂, H₂O, and SO₂ remain in a Helium carrier gas stream. Separation of the gas mixture in a TPD column (Elementar patent) "temperature-programmed desorption column". Signal detection by a TCD katharometer "thermal conductivity detector" for C, H, and N nuclei.

Thermogravimetric Analysis/Difference Scanning Calorimeter

The thermal stability was analysed by TGA/DSC using a Mettler Toledo TGA/DSC3+LF/1100. Around ~10 mg of the sample was put in an aluminium crucible and heated at a rate of 5°C/min from ambient temperature to 400°C under air.

Electrolyte Preparation for zinc oligoethers

For electrolytes using the oligoethers as a primary salt, 1 M of Zn(MEC)₂, Zn(MEA)₂ and Zn(MEEA)₂ was dissolved into Milli-Q ultrapure water. For electrolytes using the oligoethers as an additive, 2 M ZnSO₄ was prepared by dissolving ZnSO₄ (Alfa Aesar, 99%) salt into Milli-Q ultrapure water. The mixtures were stirred for 5 minutes. The desired amount of the additive of 2.5wt%, 5wt% or 10wt%, was added to a 2 M ZnSO₄ blank electrolyte and the solution was vortexed for 1 min. For the electrolytes containing urea, 10 M of urea (99.9% Sigma Aldrich) was dissolved in Milli-Q ultrapure water, to which 2 M ZnSO₄ was added. Zn(MEEA)₂ was then added at 5wt% to the solution.

Ionic conductivity measurements

The ion conductivities (σ) were measured using a Mettler-Toledo SevenCompact S230 conductivity meter with a 12 mm InLab® 710 Cond probe with 4 Pt poles conductivity cell ($\pm 0.5\%$).

IR spectroscopy

FTIR spectra were acquired in ATR mode on a Nicolet™ iSTM 5 FTIR spectrometer (Thermo Fisher Scientific) in the range of ~ 500 to 4000 cm^{-1} .

Electrochemical Measurements using zinc oligoethers

Initial zinc stripping/plating measurements was performed in an electrochemical glass cell using a PTFE embedded glassy carbon disc (3 mm diameter, Pine Research Instrumentation) as working electrode, Pt wire as counter electrode and Ag/AgCl leakless electrode was used as a reference. $\sim 5\text{ mL}$ of electrolyte was used for each measurement.

Zn symmetric cells using a PFA Hardware Swagelok cell were assembled with two zinc metal electrodes (Zn disk 1 cm \varnothing) which were untreated before use. Two Whatman glass fiber separators (GF/D, 1.27 cm \varnothing) were added between the two electrodes along with 100 μL of electrolyte, carefully incorporated using a micropipette. The Swagelok cells were sealed with parafilm® to ensure a tight seal. The cycling rate of the cells were 0.624 and 2.5 $\text{mA}\cdot\text{cm}^{-2}$ with a capacity of 2.5 $\text{mAh}\cdot\text{cm}^{-2}$, which correlates to C/4 and 1C. Zn || Cu coin cells were prepared using copper metal foil electrodes (99.99 %, Cu disk 1 cm \varnothing) and zinc metal electrodes (Zn disk 1 cm \varnothing) which both were untreated before use. Two Whatman glass fiber separators (GF/D, 1.27 cm \varnothing) were added between the two electrodes along with 100 μL of electrolyte. The cycling conditions used were described by Xu et al. [194] CMD- γ - MnO_2 was synthesised according to [93] and MnO_2 was mixed and grinded with super-p carbon in a ratio of 1:1.

Zn || MnO_2 full cells were prepared using a PFA Hardware Swagelok cell. 12.5mg (6.25 mg of MnO_2) of powder was added with a zinc metal electrode (Zn disk 1 cm \varnothing),

between Two Whatman glass fiber separators (GF/D, 1.27 cm Ø) soaked with 100 µL of electrolyte. The Swagelok cells were sealed with parafilm© to ensure a tight seal. The cycling rate of the cells were 0.624 and 2.5 mA.cm⁻² with a capacity of 2.5 mAh.cm⁻²

Scanning electron microscopy

The scanning electron microscopy (SEM) images were taken with a JEOL 7800F Prime at an acceleration voltage of 6.0 kV and 10 mm working distance.

X-ray photoelectron spectroscopy

X-ray photoelectron spectroscopy (XPS) measurements were conducted on Thermo Fisher Scientific K-alpha instrument with an Al X-ray source. Pristine and ex situ powder samples were pressed into a copper holder and mounted in a vacuum transfer chamber in an argon-filled glovebox to avoid exposure to air and moisture. Data fitting and analysis was performed using Avantage software.

Electrolyte Preparation for LiMEEA

Electrolytes based on lithium bis(trifluoromethanesulfonyl)imide (LiTFSI) (99.9%, Solvionic) and LiMEEA were mixed at different compositions to create the ternary plot.

Electrochemical Measurements using LiMEEA

For the full cells test using Mo₆S₈ and LFP, methods described in ANNEX for chapter 2 were utilised. Galvanostatic cycling was performed in a temperature-controlled oven using a MPG2 multichannel potentiostat (Bio-Logic).

Cyclic voltammetry measurements were performed in an electrochemical glass cell. SEI stability was performed using a PTFE embedded glassy carbon disc (3 mm diameter, Pine Research Instrumentation) as working electrode, Pt wire as counter electrode and standard calomel electrode (SCE) as the reference.

Supplementary Figures

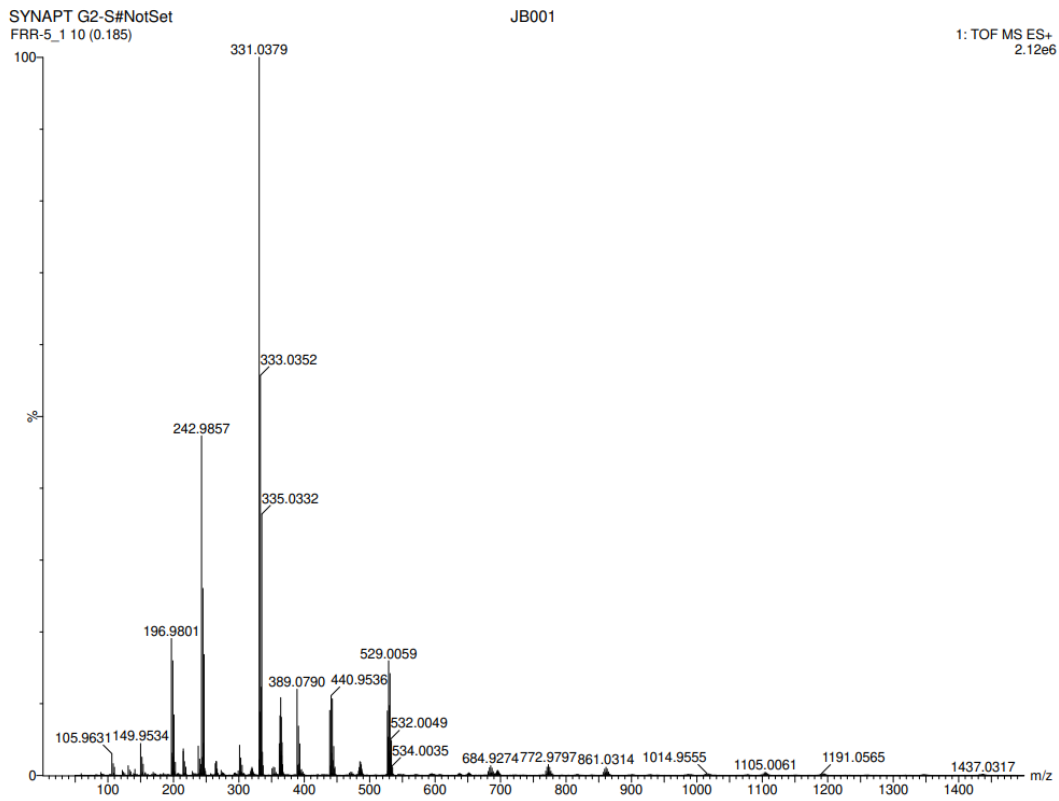


Fig. A4.1 – Mass spectra for Zn(MEC)₂.

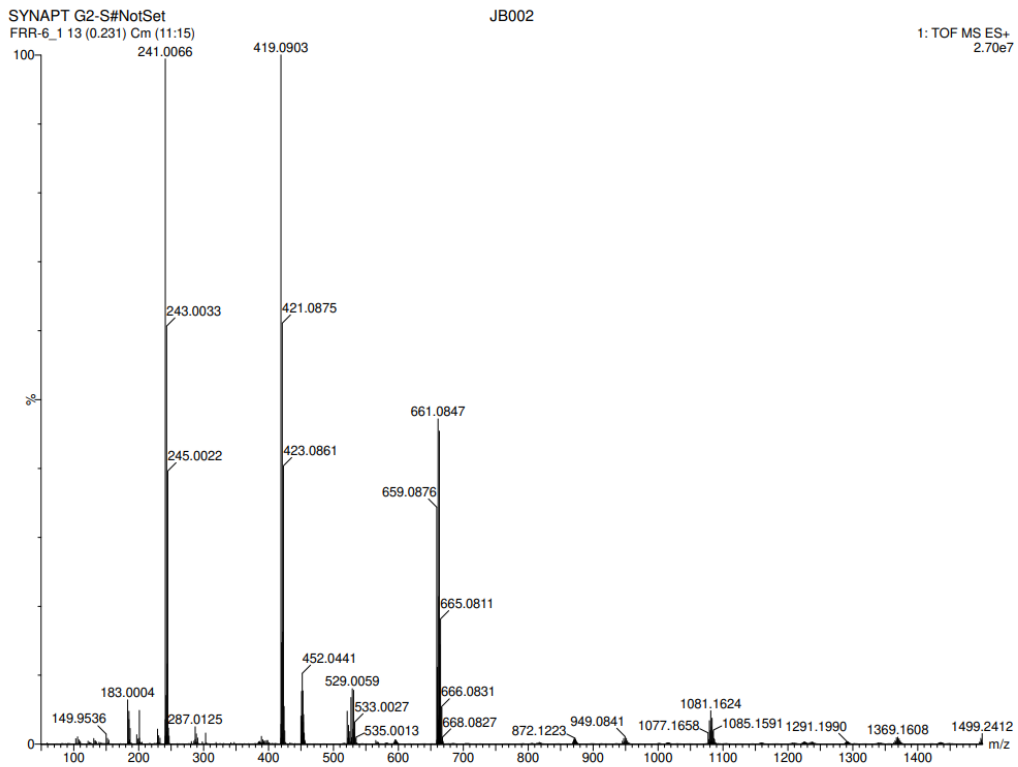


Fig. A4.2 – Mass spectra for Zn(MEA)₂.

Annex

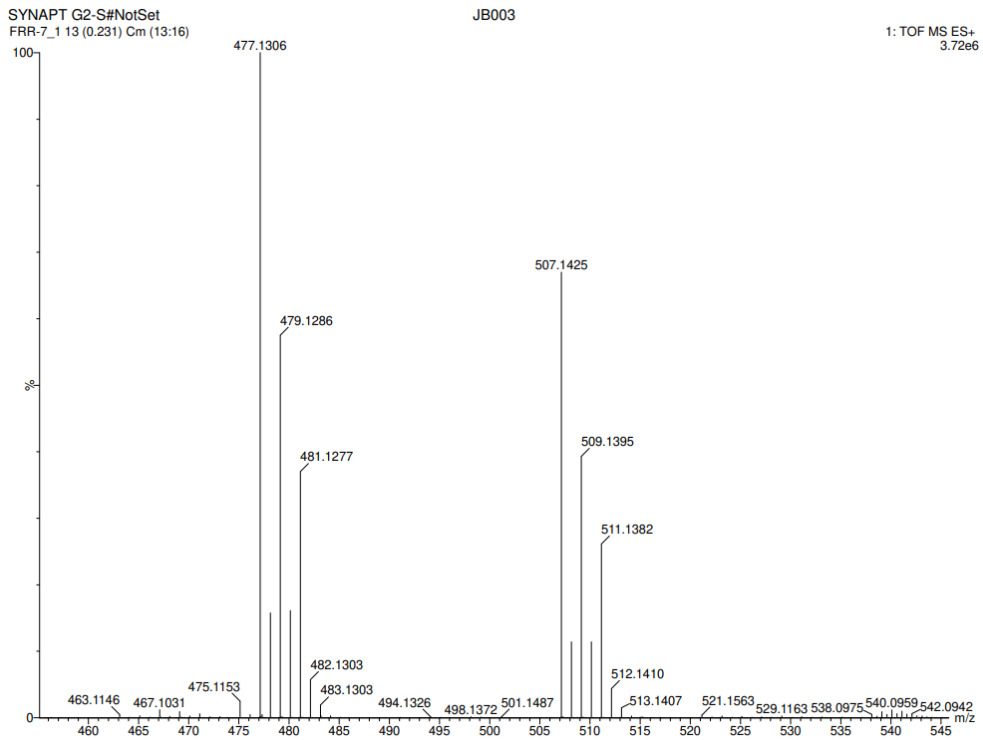
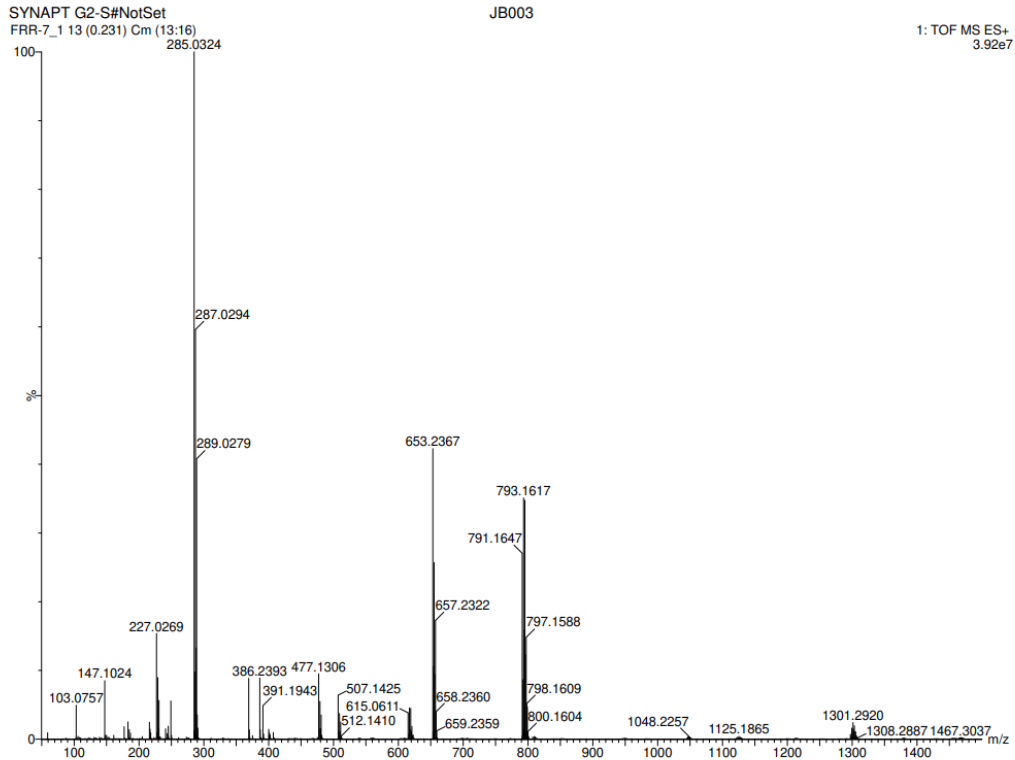


Fig. A4.3 – Mass spectra for Zn(MEEA)₂.

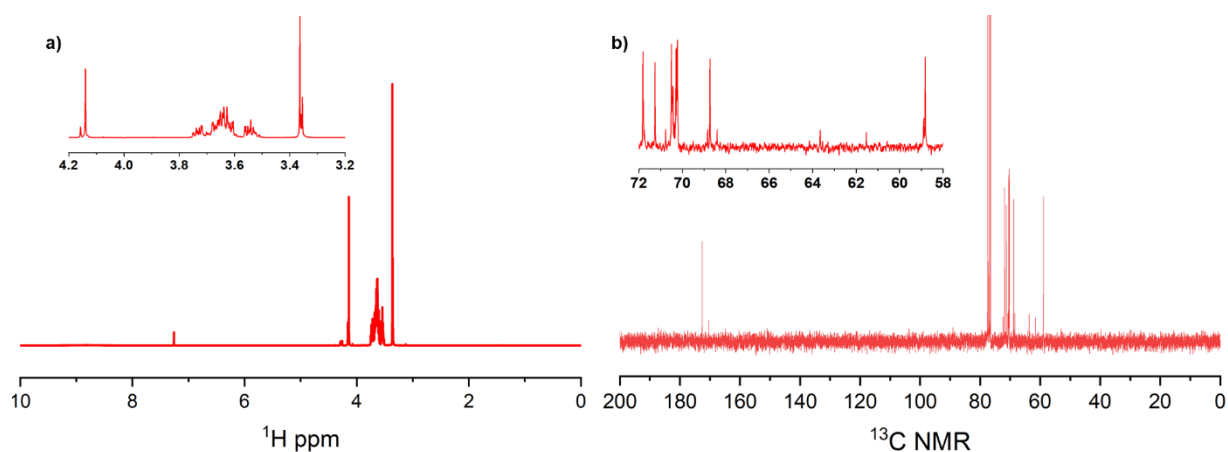


Fig. A4.4 - a) ^1H NMR of LiMEEA b) ^{13}C NMR of LiMEEA.

^1H -NMR (300 MHz, CDCl_3 , TMS): δH : 3.36 (s, 3 H, CH_3), 3.50-3.70 (m, 12 H, CH_2), 4.14 (s, 2 H, CH_2COO^-)

^{13}C -NMR (300 MHz, CDCl_3 , TMS): δC : 58.86 (CH_3), 68.73 ($\text{CH}_2\text{OCH}_2\text{COO}^-$), 70.02 – 70.64 (4 C, CH_2), 71.26 (CH_2COO^-), 71.83 (CH_3OCH_2), 172.54 (COO^-)

Chapter 5

Materials and Methods

LiMn₂O₄ synthesis

LiMn₂O₄ (LMO) active material (AM) powder was prepared by heating at 800°C a stoichiometric mixture of Li₂CO₃ (5% excess) and MnO₂ in air for 24 h, followed by two successive grinding and identical annealing sequences. The samples were cooled at a rate of 2°C min⁻¹ until 300°C to ensure the proper oxygen stoichiometry.

Electrode fabrication

The PTCDI AM (≥94%, Thermo Fisher Scientific) based electrodes were made by first preparing a 3 wt% carboxymethyl cellulose (CMC) (Sigma-Aldrich) solution in ultra-pure water (Millipore® Direct-Q® Purification, 18.2 MΩ·cm at 25°C) until complete dissolution in magnet stirred vials. PTCDI and carbon black (CB) (Super-P, Alfa Aesar) were thereafter manually mixed with a mortar and added to the CMC solution for 12 h. The slurry was casted on graphite foil (SGL Carbon) using a Doctor Blade followed by 12 h vacuum drying at 80°C. The electrode weight ratio PTCDI:CB:CMC was 75:15:10 with a final thickness of 30-50 μm and an active material loading of 2-3 mg cm⁻².

The freestanding PTCDI, LiFePO₄ (LFP, Umicore) and LMO electrodes were prepared using the Bellcore method as described in Annex for chapter 2. Resulting loadings varied depending on the purpose of the electrodes, but generally PTCDI = 4-6 mg cm⁻², LFP = ~20 mg cm⁻² and LMO = 4-6 mg cm⁻².

Electrolyte preparation

Electrolytes based on lithium bis(trifluoromethanesulfonyl)imide (LiTFSI) (99.9%, Solvionic) and lithium sulfate (Li₂SO₄) (anhydrous, 99.5%, Sigma-Aldrich) were created with ultra-pure water (Millipore® Direct-Q® Purification, 18.2 MΩ·cm at 25°C) in magnet stirred vials at ca. 50°C. The pH of the electrolytes was adjusted using

bis(trifluoromethanesulfonyl)imide acid (HTFSI) (99.9%, Solvionic) and sulfuric acid (H₂SO₄) (99.999%, Sigma-Aldrich), respectively.

Electrochemical and battery assessments

For cycling of the PTCDI with LFP, coin cells with carbon foil supported PTCDI working electrodes (WEs) (10 mm Ø), freestanding oversized LFP CEs (10-14 mm Ø), and two Whatman cellulose filter separators (16 mm Ø) between 0.2 and 1.6 V at 0.25-10C.

PTCDI||LMO full cells were assembled with 10 mm Ø and the PTCDI : LMO is balanced in a weight ratio of 1:1.1. The specific capacity Q (mAh g⁻¹) of the full cells were calculated as:

$$Q = \frac{It}{m}, \quad (\text{Eq. A5.1})$$

where I (mA) is the discharge current, t (h) the discharge time, and m (g) is the mass of AM in the electrode.

The AM level specific energy density E (Wh kg⁻¹) was then calculated as:

$$E = \frac{\int IV(t)dt}{3.6m}, \quad (\text{Eq. A5.2})$$

where, I (A) is the applied current, V (V) is the voltage of the cell, t (s) is the corresponding discharge time, and m (g) is the sum of the weight of AM in both electrodes. 40 µl of electrolyte was used for all cells, Swagelok and coin cells.

Cycling voltammetry measurements were carried out using a 3-electrode Swagelok cell assembled with a PTCDI WE, a free-standing LFP CE, both 10 mm Ø, and an Ag/AgCl reference electrode (RE) (5 mm Ø, 0.127 mm silver foil, Alfa Aesar/AgCl ink, ALS Japan) together with the same separators between -1.0 V and 0.15 V vs. Ag/AgCl at 0.2 mV s⁻¹. 40 µl of electrolyte was used for all cells, Swagelok and coin cells.

For the dissolution measurements, a beaker cell utilising self-standing PTCDI, LFP and Ag/AgCl reference electrode was used for phenol red (Sigma Aldrich) measurements, one drop of phenol red was added to 10 mL of electrolyte, the cell was purged with Ar

gas and a magnetic stirrer was added to ensure the electrolyte was mixed during the measurement.

All of the above electrochemical studies were carried out Biologic VMP4 multichannel potentiostat/galvanostat or a Scribner Associates Incorporated 580

EQCM-R Measurements

For the electrochemical quartz crystal microbalance (EQCM-R) measurements, a diluted slurry (73:18:9 PTCDI:Csp:PVDF wt%) using NMP as a solvent was prepared and sonicated to ensure homogenous particle dispersion. This solution was subsequently sprayed onto 9 MHz QCM resonators (Bio-Logic) made from gold that were heated to 150°C during the spraying process to evaporate the solvent upon contact and then heated to 200°C for 30 min to melt the binder to ensure good film cohesion. The resonators modified with the PTCDI thin films were mounted in an airtight EQCM cell developed previously. For the aqueous electrolytes the PTCDI coated EQCM electrode acted as WE, a Pt-rod coated with self-standing Bellcore LFP as CE, and Ag/AgCl (saturated K₂SO₄) as RE. For the measurements using organic electrolytes, Li metal was used as CE and RE. Each measurement used 2 mL of electrolyte. The EQCM measurements were performed using a S2 Biologic SP200 workstation coupled with a commercial SEIKO QCM922A microbalance, which permitted the resonance frequency (f) to be monitored during electrochemical cycling. The scan rates used for aqueous electrolytes was 5 mV s⁻¹ between -1.0 V and 0.15 V vs. Ag/AgCl. For the CV utilised to determine b -values, the scan rate was taken between 1-20 mV s⁻¹. For the organic cell, the scan rate was 0.2 mV s⁻¹ between a voltage range of 1.5 to 3.5 V vs. Li.

The logarithm of the peak current (i_p) was plotted vs. the sweep rate (v), and the b parameter from:

$$\log i = b \cdot \log v + \log a, \quad (\text{Eq. A5.3})$$

was taken as the slope of the linearization and used to determine if the current originates from Faradaic redox reactions or non-Faradaic capacitive behaviour as the former would generate $b \approx 0.5$, and the latter $b \approx 1.0$.

Materials characterisation

Free-standing PTCDI electrodes (5 mm Ø) were pre-cycled to charged and discharged states by galvanostatic cycling (GC) in 2-electrode coin cells (CR2032) with freestanding oversized LFP counter electrodes (CE) (10 mm Ø), and two Whatman cellulose filter separators (Grade 44, Sigma-Aldrich) (14 mm Ø). Post cycling, the electrodes were recovered, washed with 1 ml ultra-pure water and dried at 60°C for 12 h.

Ex situ X-ray diffraction (XRD)

was performed on electrodes put on top of Si single crystal low background sample holders and for the PTCDI powder in a standard sample holder levelled with the surface, using a Bruker D8 Discovery in the range 5-35° 2 Theta. Cu K α radiation was used with a Ni filter to cut Cu K β contributions, with two 2.5° soller slits to improve peak shapes. The incidence slit was set to Fixed Sample Illumination mode with 5 mm illumination, and an anti-scatter shield was placed 2.5 mm above the samples. The samples were measured with 0.02° increments and 2 s per step, summing up to 3150 s per scan, while rotated at 10 rpm.

Ex-situ FT-IR spectroscopy

FT-IR was obtained using a Bruker Alpha attenuated total reflection (ATR-FTIR) spectrometer and a Ge crystal, for the same electrodes as for the *ex situ* XRD. The spectra were recorded with 2 cm⁻¹ resolution and 512 scans.

The scanning electron microscopy (SEM)

SEM images were taken with a JEOL 7800F Prime at an acceleration voltage of 6.0 kV and 10 mm working distance.

UV-Vis spectroscopy

UV-Vis spectra were recorded on a Mettler Toledo UV5bio spectrometer using an absorption quartz cell across a wavelength range of 200 – 800 nm (Hellma analytics, Quartz Glass High Performance 200 – 2500 nm, 1 mm optical path length).

Supplementary Figures

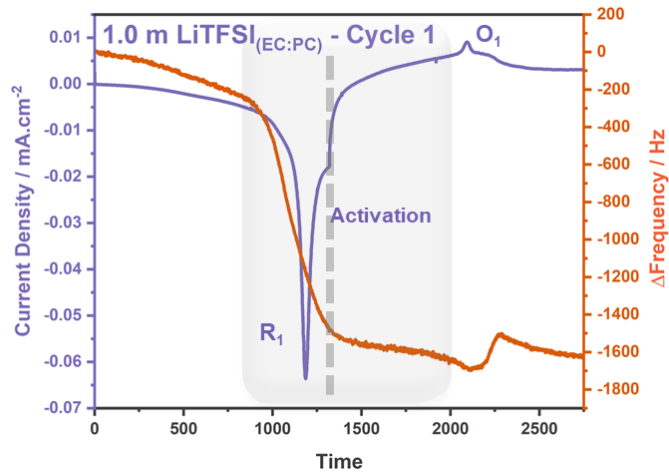


Fig. A5.1 - Electrochemical and EQCM response of 1.0 m LiTFSI_(EC:PC).

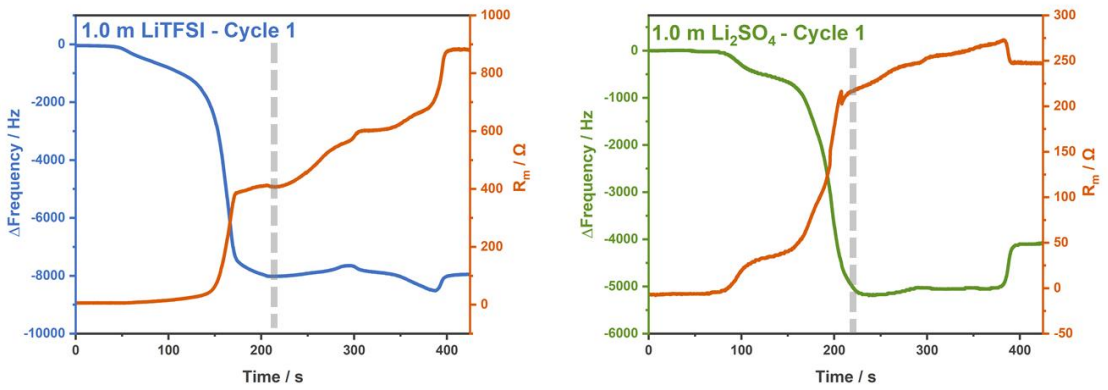


Fig. A5.2 – Frequency response and motional resistance of 1.0 m LiTFSI_(aq) (left) and 1.0 m Li₂SO_{4(aq)} (right) at cycle 1.

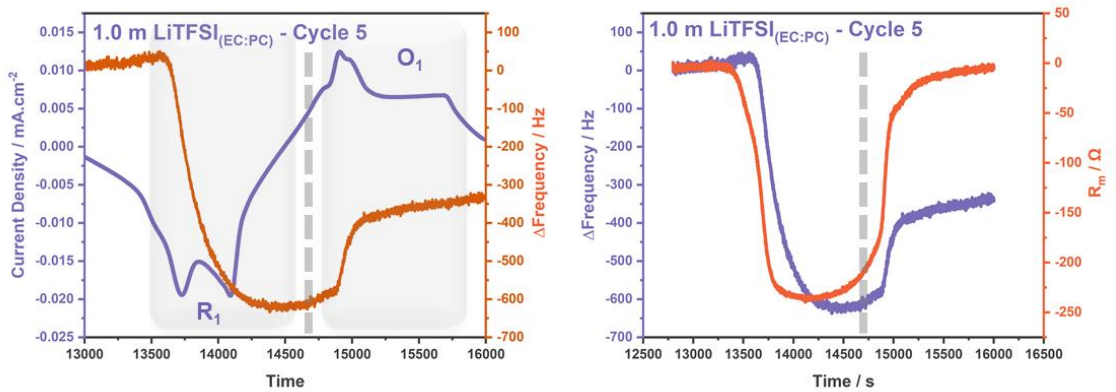


Fig. A5.3 - Electrochemistry and frequency response for 1.0 m LiTFSI_(EC:PC) (left) and frequency response and motional resistance (right) at cycle 5.

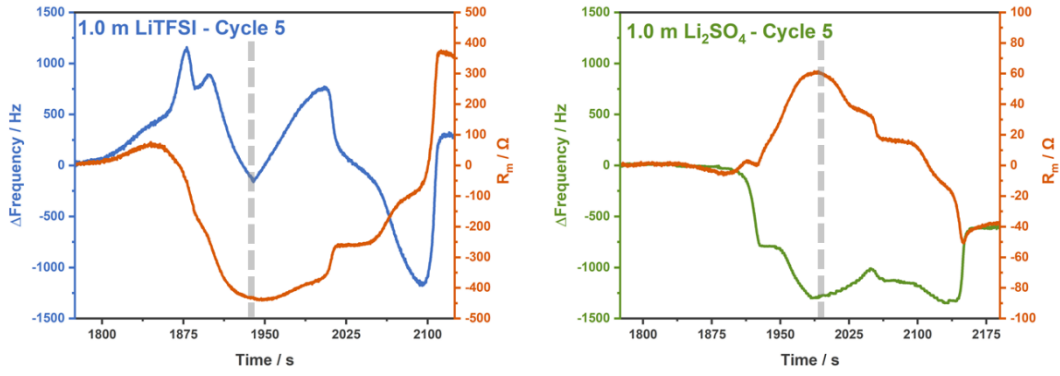


Fig. A5.4 - Frequency response and motional resistance of 1.0 m LiTFSI_(aq) (left) and 1.0 m Li₂SO_{4(aq)} (right) at cycle 5.

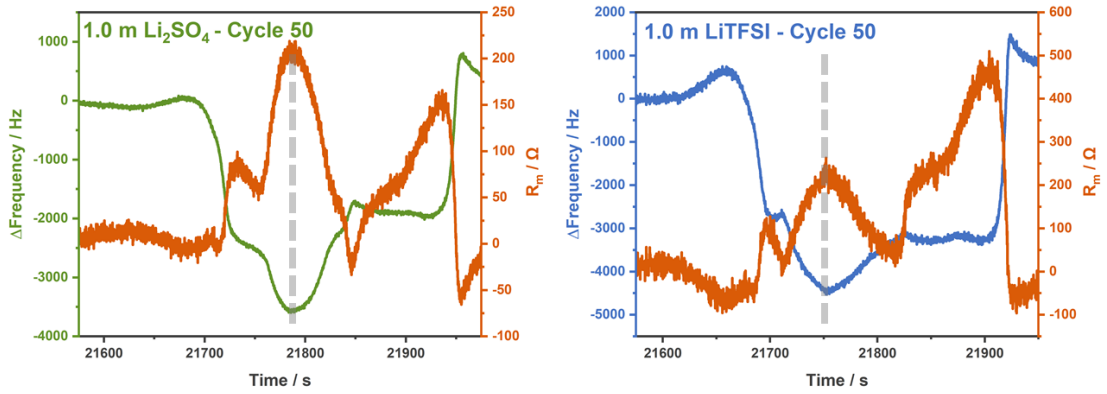


Fig. A5.5 - Frequency response and motional resistance of 1.0 m LiTFSI_(aq) (left) and 1.0 m Li₂SO_{4(aq)} (right) at cycle 50.

References

- [1] ‘Net Zero by 2050 : A Roadmap for the Global Energy Sector’, 2021.
- [2] ‘French ministry of ecological transition, “Energy Outlook”, 2023’, 2023. Accessed: Jul. 07, 2024. [Online]. Available: Bilan énergétique de la France | Chiffres clés de l’énergie - Édition 2023 (developpement-durable.gouv.fr)
- [3] ‘INTERNATIONAL ENERGY OUTLOOK 2023’, 2023. Accessed: Jul. 07, 2024. [Online]. Available: <https://www.eia.gov/outlooks/ieo/>
- [4] D. Larcher and J.-M. Tarascon, ‘Towards greener and more sustainable batteries for electrical energy storage’, *Nat Chem*, vol. 7, no. 1, pp. 19–29, 2015, doi: 10.1038/nchem.2085.
- [5] C. P. Grey and D. S. Hall, ‘Prospects for lithium-ion batteries and beyond—a 2030 vision’, *Nat Commun*, vol. 11, no. 1, p. 6279, 2020, doi: 10.1038/s41467-020-19991-4.
- [6] H. Ahn, D. Kim, M. Lee, and K. W. Nam, ‘Challenges and possibilities for aqueous battery systems’, *Commun Mater*, vol. 4, no. 1, p. 37, 2023, doi: 10.1038/s43246-023-00367-2.
- [7] T. Reddy & D. Linden, *Linden’s Handbook of Batteries (4th Edition)*. New York, USA: McGraw Hill Professional Publishing, 2010.
- [8] G. J. May, A. Davidson, and B. Monahov, ‘Lead batteries for utility energy storage: A review’, Feb. 01, 2018, *Elsevier Ltd*. doi: 10.1016/j.est.2017.11.008.
- [9] Z. P. Cano *et al.*, ‘Batteries and fuel cells for emerging electric vehicle markets’, Apr. 01, 2018, *Nature Publishing Group*. doi: 10.1038/s41560-018-0108-1.
- [10] ‘Avicenne Energy Report: EU Battery Demand and Supply (2019-2030) in a Global Context.’, 2019.
- [11] L. Droguet, A. Grimaud, O. Fontaine, and J. M. Tarascon, ‘Water-in-Salt Electrolyte (WiSE) for Aqueous Batteries: A Long Way to Practicality’, *Adv Energy Mater*, vol. 10, no. 43, Nov. 2020, doi: 10.1002/aenm.202002440.
- [12] P. J. McHugh, A. D. Stergiou, and M. D. Symes, ‘Decoupled Electrochemical Water Splitting: From Fundamentals to Applications’, Nov. 01, 2020, *Wiley-VCH Verlag*. doi: 10.1002/aenm.202002453.
- [13] S. M. Whittingham, ‘CHALCOGENIDE BATTERY’, US4009052A, 1977
- [14] S. M. Whittingham, ‘science.192.4244.1126’, *Science (1979)*, vol. 192, no. 4244, pp. 1126–1127, 1976.
- [15] S. M. Whittingham, ‘Intercalation Chemistry and Energy Storage’, *J Solid State Chem*, vol. 29, pp. 303–310, 1979.
- [16] D. Lin, Y. Liu, and Y. Cui, ‘Reviving the lithium metal anode for high-energy batteries’, *Nat Nanotechnol*, vol. 12, no. 3, pp. 194–206, 2017, doi: 10.1038/nnano.2017.16.
- [17] N. Yabuuchi and T. Ohzuku, ‘Novel lithium insertion material of LiCo_{1/3}Ni_{1/3}Mn_{1/3}O₂ for advanced lithium-ion batteries’, in *Journal of Power Sources*, Jun. 2003, pp. 171–174. doi: 10.1016/S0378-7753(03)00173-3.
- [18] P. Kalyani and N. Kalaiselvi, ‘Various aspects of LiNiO₂ chemistry: A review’, *Sci Technol Adv Mater*, vol. 6, no. 6, p. 689, 2005, doi: 10.1016/j.stam.2005.06.001.
- [19] A. Yoshino, ‘The birth of the lithium-ion battery’, Jun. 11, 2012. doi: 10.1002/anie.201105006.
- [20] ‘The Nobel Prize in Chemistry 2019’. Accessed: Jul. 07, 2024. [Online]. Available: <https://www.nobelprize.org/prizes/chemistry/2019/summary/>
- [21] S.-J. An, J. Li, C. Daniel, D. Mohanty, S. C. Nagpure, and D. L. Wood, ‘The state of understanding of the lithium-ion-battery graphite solid electrolyte interphase (SEI) and

References

- its relationship to formation cycling’, *Carbon N Y*, vol. 105, pp. 52–76, 2016, [Online]. Available: <https://api.semanticscholar.org/CorpusID:101440819>
- [22] R. Schmich, R. Wagner, G. Hörpel, T. Placke, and M. Winter, ‘Performance and cost of materials for lithium-based rechargeable automotive batteries’, *Nat Energy*, vol. 3, no. 4, pp. 267–278, 2018, doi: 10.1038/s41560-018-0107-2.
- [23] A. Manthiram, ‘A reflection on lithium-ion battery cathode chemistry’, *Nat Commun*, vol. 11, no. 1, p. 1550, 2020, doi: 10.1038/s41467-020-15355-0.
- [24] S. Hess, M. Wohlfahrt-Mehrens, and M. Wachtler, ‘Flammability of Li-Ion Battery Electrolytes: Flash Point and Self-Extinguishing Time Measurements’, *J Electrochem Soc*, vol. 162, no. 2, p. A3084, Jan. 2015, doi: 10.1149/2.0121502jes.
- [25] C. Arbizzani, G. Gabrielli, and M. Mastragostino, ‘Thermal stability and flammability of electrolytes for lithium-ion batteries’, *J Power Sources*, vol. 196, no. 10, pp. 4801–4805, 2011, doi: <https://doi.org/10.1016/j.jpowsour.2011.01.068>.
- [26] F. Duffner, N. Kronemeyer, J. Tübke, J. Leker, M. Winter, and R. Schmich, ‘Post-lithium-ion battery cell production and its compatibility with lithium-ion cell production infrastructure’, *Nat Energy*, vol. 6, no. 2, pp. 123–134, 2021, doi: 10.1038/s41560-020-00748-8.
- [27] S. Ahmed, P. A. Nelson, and D. W. Dees, ‘Study of a dry room in a battery manufacturing plant using a process model’, *J Power Sources*, vol. 326, pp. 490–497, 2016, doi: <https://doi.org/10.1016/j.jpowsour.2016.06.107>.
- [28] Y. Yokoyama, T. Fukutsuka, K. Miyazaki, and T. Abe, ‘Origin of the Electrochemical Stability of Aqueous Concentrated Electrolyte Solutions’, *J Electrochem Soc*, vol. 165, no. 14, p. A3299, Oct. 2018, doi: 10.1149/2.0491814jes.
- [29] J. Y. Luo and Y. Y. Xia, ‘Aqueous lithium-ion battery $\text{LiTi}_2(\text{PO}_4)_3/\text{LiMn}_2\text{O}_4$ with high power and energy densities as well as superior cycling stability’, *Adv Funct Mater*, vol. 17, no. 18, pp. 3877–3884, Dec. 2007, doi: 10.1002/adfm.200700638.
- [30] W. Li, J. R. Dahn, and D. S. Wainwright, ‘Rechargeable Lithium Batteries with Aqueous Electrolytes’, *Science (1979)*, vol. 264, no. 5162, pp. 1115–1118, 1994, doi: 10.1126/science.264.5162.1115.
- [31] J. Xie, Z. Liang, and Y. C. Lu, ‘Molecular crowding electrolytes for high-voltage aqueous batteries’, *Nat Mater*, vol. 19, no. 9, pp. 1006–1011, Sep. 2020, doi: 10.1038/s41563-020-0667-y.
- [32] O. Borodin, J. Self, K. A. Persson, C. Wang, and K. Xu, ‘Uncharted Waters: Super-Concentrated Electrolytes’, Jan. 15, 2020, *Cell Press*. doi: 10.1016/j.joule.2019.12.007.
- [33] K. Ueno, K. Yoshida, M. Tsuchiya, N. Tachikawa, K. Dokko, and M. Watanabe, ‘Glyme-lithium salt equimolar molten mixtures: Concentrated solutions or solvate ionic liquids?’, *Journal of Physical Chemistry B*, vol. 116, no. 36, pp. 11323–11331, Sep. 2012, doi: 10.1021/jp307378j.
- [34] Y. Yamada *et al.*, ‘Unusual Stability of Acetonitrile-Based Superconcentrated Electrolytes for Fast-Charging Lithium-Ion Batteries’, *J Am Chem Soc*, vol. 136, no. 13, pp. 5039–5046, Apr. 2014, doi: 10.1021/ja412807w.
- [35] L. Suo, Y.-S. Hu, H. Li, M. Armand, and L. Chen, ‘A new class of Solvent-in-Salt electrolyte for high-energy rechargeable metallic lithium batteries’, *Nat Commun*, vol. 4, no. 1, p. 1481, 2013, doi: 10.1038/ncomms2513.
- [36] Y. Yamada *et al.*, ‘Unusual stability of acetonitrile-based superconcentrated electrolytes for fast-charging lithium-ion batteries’, *J Am Chem Soc*, vol. 136, no. 13, pp. 5039–5046, Apr. 2014, doi: 10.1021/ja412807w.
- [37] L. Suo, Y. S. Hu, H. Li, M. Armand, and L. Chen, ‘A new class of Solvent-in-Salt electrolyte for high-energy rechargeable metallic lithium batteries’, *Nat Commun*, vol. 4, 2013, doi: 10.1038/ncomms2513.

References

- [38] J. Wang, Y. Yamada, K. Sodeyama, C. H. Chiang, Y. Tateyama, and A. Yamada, ‘Superconcentrated electrolytes for a high-voltage lithium-ion battery’, *Nat Commun*, vol. 7, no. 1, p. 12032, 2016, doi: 10.1038/ncomms12032.
- [39] L. Suo *et al.*, ‘“Water-in-salt” electrolyte enables high-voltage aqueous lithium-ion chemistries’, *Science (1979)*, vol. 350, no. 6263, pp. 938–943, 2015, doi: 10.1126/science.aab1595.
- [40] T. Tsurumura, Y. Hashimoto, M. Morita, Y. Umebayashi, and K. Fujii, ‘Anion Coordination Characteristics of Ion-pair Complexes in Highly Concentrated Aqueous Lithium Bis(trifluoromethane- sulfonyl)amide Electrolytes’, *Analytical Sciences*, vol. 35, no. 3, pp. 289–294, 2019, doi: 10.2116/analsci.18P407.
- [41] N. Dubouis, P. Lemaire, B. Mirvaux, E. Salager, M. Deschamps, and A. Grimaud, ‘The role of the hydrogen evolution reaction in the solid-electrolyte interphase formation mechanism for “: Water-in-Salt ” electrolytes’, *Energy Environ Sci*, vol. 11, no. 12, pp. 3491–3499, Dec. 2018, doi: 10.1039/c8ee02456a.
- [42] R. Jommongkol, S. Deebansok, J. Deng, Y. Zhu, R. Bouchal, and O. Fontaine, ‘Unveiling LiTFSI Precipitation as a Key Factor in Solid Electrolyte Interphase Formation in Li-Based Water-in-Salt Electrolytes’, *Small*, vol. 20, no. 4, Jan. 2024, doi: 10.1002/smll.202303945.
- [43] J. Vatamanu and O. Borodin, ‘Ramifications of Water-in-Salt Interfacial Structure at Charged Electrodes for Electrolyte Electrochemical Stability’, *Journal of Physical Chemistry Letters*, vol. 8, no. 18, pp. 4362–4367, Sep. 2017, doi: 10.1021/acs.jpcclett.7b01879.
- [44] Y. Yamada, K. Usui, K. Sodeyama, S. Ko, Y. Tateyama, and A. Yamada, ‘Hydrate-melt electrolytes for high-energy-density aqueous batteries’, *Nat Energy*, vol. 1, no. 10, Oct. 2016, doi: 10.1038/nenergy.2016.129.
- [45] L. Chen *et al.*, ‘A 63 m Superconcentrated Aqueous Electrolyte for High-Energy Li-Ion Batteries’, *ACS Energy Lett*, vol. 5, no. 3, pp. 968–974, Mar. 2020, doi: 10.1021/acseenergylett.0c00348.
- [46] L. Suo *et al.*, ‘“Water-in-salt” electrolyte enables high-voltage aqueous lithium-ion chemistries’. [Online]. Available: <https://www.science.org>
- [47] S. I. Nakano, D. Miyoshi, and N. Sugimoto, ‘Effects of molecular crowding on the structures, interactions, and functions of nucleic acids’, Mar. 12, 2014, *American Chemical Society*. doi: 10.1021/cr400113m.
- [48] L. A. Ferreira, V. N. Uversky, and B. Y. Zaslavsky, ‘Role of solvent properties of water in crowding effects induced by macromolecular agents and osmolytes’, *Mol Biosyst*, vol. 13, no. 12, pp. 2551–2563, 2017, doi: 10.1039/c7mb00436b.
- [49] D. Dong, J. Xie, Z. Liang, and Y. C. Lu, ‘Tuning Intermolecular Interactions of Molecular Crowding Electrolyte for High-Performance Aqueous Batteries’, *ACS Energy Lett*, vol. 7, no. 1, pp. 123–130, Jan. 2022, doi: 10.1021/acseenergylett.1c02064.
- [50] P. Jaumaux *et al.*, ‘Localized Water-In-Salt Electrolyte for Aqueous Lithium-Ion Batteries’, *Angewandte Chemie - International Edition*, vol. 60, no. 36, pp. 19965–19973, Sep. 2021, doi: 10.1002/anie.202107389.
- [51] Y. Wang *et al.*, ‘Enabling high-energy-density aqueous batteries with hydrogen bond-anchored electrolytes’, *Matter*, vol. 5, no. 1, pp. 162–179, Jan. 2022, doi: 10.1016/j.matt.2021.10.021.
- [52] V. K. H. Brown, L. W. Ferrigan, and D. E. Stevenson, ‘Acute Toxicity and Skin Irritant Properties of Sulfolane’, *Br J Ind Med*, vol. 23, no. 4, p. 302, Oct. 1966, doi: 10.1136/oem.23.4.302.

References

- [53] A. K. Soper, E. W. Castner, and A. Luzar, 'Impact of urea on water structure: a clue to its properties as a denaturant?', *Biophys Chem*, vol. 105, pp. 649–666, 2003, doi: 10.1016/S0301-4622(03)00095-4.
- [54] J. Xu *et al.*, 'Aqueous electrolyte design for super-stable 2.5 V LiMn₂O₄ || Li₄Ti₅O₁₂ pouch cells', *Nat Energy*, vol. 7, no. 2, pp. 186–193, Feb. 2022, doi: 10.1038/s41560-021-00977-5.
- [55] Y. Cui, 'Hydrotropic Solubilization by Urea Derivatives: A Molecular Dynamics Simulation Study', *J Pharm (Cairo)*, vol. 2013, pp. 1–15, Feb. 2013, doi: 10.1155/2013/791370.
- [56] A. R. Sá Couto, A. Ryzhakov, and T. Loftsson, 'Disruption of α - and γ -cyclodextrin aggregates promoted by chaotropic agent (urea)', *J Drug Deliv Sci Technol*, vol. 48, pp. 209–214, Dec. 2018, doi: 10.1016/j.jddst.2018.09.015.
- [57] F. Hofmeister, 'Zur Lehre von der Wirkung der Salze', *Archiv für experimentelle Pathologie und Pharmakologie*, vol. 24, no. 4, pp. 247–260, 1888, doi: 10.1007/BF01918191.
- [58] Y. Marcus, 'Effect of ions on the structure of water: Structure making and breaking', Mar. 11, 2009. doi: 10.1021/cr8003828.
- [59] A. S. Thomas and A. H. Elcock, 'Molecular dynamics simulations of hydrophobic associations in aqueous salt solutions indicate a connection between water hydrogen bonding and the hofmeister effect', *J Am Chem Soc*, vol. 129, no. 48, pp. 14887–14898, Dec. 2007, doi: 10.1021/ja073097z.
- [60] M. G. Cacace, E. M. Landau, and J. J. Ramsden, 'The Hofmeister series: Salt and solvent effects on interfacial phenomena', 1997. doi: 10.1017/S0033583597003363.
- [61] G. Yang *et al.*, 'An aqueous zinc-ion battery working at -50°C enabled by low-concentration perchlorate-based chaotropic salt electrolyte', *EcoMat*, vol. 4, no. 2, p. e12165, Mar. 2022, doi: <https://doi.org/10.1002/eom2.12165>.
- [62] Q. Zhang *et al.*, 'Chaotropic Anion and Fast-Kinetics Cathode Enabling Low-Temperature Aqueous Zn Batteries', *ACS Energy Lett*, vol. 6, no. 8, pp. 2704–2712, Aug. 2021, doi: 10.1021/acsenenergylett.1c01054.
- [63] J. Kim, Y. Kim, J. Yoo, G. Kwon, Y. Ko, and K. Kang, 'Organic batteries for a greener rechargeable world', *Nat Rev Mater*, vol. 8, no. 1, pp. 54–70, 2023, doi: 10.1038/s41578-022-00478-1.
- [64] G. Kwon, Y. Ko, Y. Kim, K. Kim, and K. Kang, 'Versatile Redox-Active Organic Materials for Rechargeable Energy Storage', *Acc Chem Res*, vol. 54, no. 23, pp. 4423–4433, Dec. 2021, doi: 10.1021/acs.accounts.1c00590.
- [65] M. Miroshnikov *et al.*, 'Power from nature: designing green battery materials from electroactive quinone derivatives and organic polymers', *J Mater Chem A Mater*, vol. 4, no. 32, pp. 12370–12386, 2016, doi: 10.1039/C6TA03166H.
- [66] Y. Lu and J. Chen, 'Prospects of organic electrode materials for practical lithium batteries', *Nat Rev Chem*, vol. 4, no. 3, pp. 127–142, 2020, doi: 10.1038/s41570-020-0160-9.
- [67] N. Ravet, C. Michot, and M. Armand, 'Novel cathode materials based on organic couples for lithium batteries', in *Materials Research Society Symposium - Proceedings*, 1998, pp. 263–273. [Online]. Available: <https://www.scopus.com/inward/record.uri?eid=2-s2.0-0031628024&partnerID=40&md5=1339be2401da2b4c785169e0456861f9>
- [68] M. Armand, C. Michot, and N. Ravet, 'Novel Electrode Materials Derived From Polyquinoid Ionic Compounds And Their Uses In Electrochemical Generators', 1998. [Online]. Available: <http://v3.espacenet.com/textdoc?DB=EPODOC&IDX=WO9928984>

References

- [69] C. Munivenkatappa, V. R. Shetty, and S. G. Shivappa, 'Chalcone as Anode Material for Aqueous Rechargeable Lithium-Ion Batteries', *Russian Journal of Electrochemistry*, vol. 57, no. 4, pp. 419–433, 2021, doi: 10.1134/S1023193520120162.
- [70] M. Karlsmo, R. Bouchal, and P. Johansson, 'High-Performant All-Organic Aqueous Sodium-Ion Batteries Enabled by PTCDA Electrodes and a Hybrid Na/Mg Electrolyte', *Angewandte Chemie International Edition*, vol. 60, no. 46, pp. 24709–24715, Nov. 2021, doi: <https://doi.org/10.1002/anie.202111620>.
- [71] R. Cang *et al.*, 'A new perylene-based tetracarboxylate as anode and LiMn2O4 as cathode in aqueous Mg-Li batteries with excellent capacity', *Chemical Engineering Journal*, vol. 405, p. 126783, 2021, doi: <https://doi.org/10.1016/j.cej.2020.126783>.
- [72] L. Chen *et al.*, 'Aqueous Lithium-Ion Batteries Using O₂ Self-Elimination Polyimides Electrodes', *J Electrochem Soc*, vol. 162, no. 10, p. A1972, Jul. 2015, doi: 10.1149/2.0101510jes.
- [73] A. L. Lubis, F. Baskoro, T.-H. Lin, H. Q. Wong, G.-S. Liou, and H.-J. Yen, 'Redox-Active High-Performance Polyimides as Versatile Electrode Materials for Organic Lithium- and Sodium-Ion Batteries', *ACS Appl Mater Interfaces*, Dec. 2023, doi: 10.1021/acsami.3c10722.
- [74] T. Ma, A. D. Easley, R. M. Thakur, K. T. Mohanty, C. Wang, and J. L. Lutkenhaus, 'Nonconjugated Redox-Active Polymers: Electron Transfer Mechanisms, Energy Storage, and Chemical Versatility', *Annu Rev Chem Biomol Eng*, vol. 14, no. Volume 14, 2023, pp. 187–216, 2023, doi: <https://doi.org/10.1146/annurev-chembioeng-092220-111121>.
- [75] R. Cang *et al.*, 'A new perylene-based tetracarboxylate as anode and LiMn2O4 as cathode in aqueous Mg-Li batteries with excellent capacity', *Chemical Engineering Journal*, vol. 405, p. 126783, 2021, doi: <https://doi.org/10.1016/j.cej.2020.126783>.
- [76] J. Wang *et al.*, 'Anhydride-Based Compound with Tunable Redox Properties as Advanced Organic Cathodes for High-Performance Aqueous Zinc-Ion Batteries', *ACS Appl Mater Interfaces*, vol. 15, no. 42, pp. 49447–49457, Oct. 2023, doi: 10.1021/acsami.3c12163.
- [77] T. Ma, A. D. Easley, R. M. Thakur, K. T. Mohanty, C. Wang, and J. L. Lutkenhaus, 'Nonconjugated Redox-Active Polymers: Electron Transfer Mechanisms, Energy Storage, and Chemical Versatility', *Annu Rev Chem Biomol Eng*, vol. 14, no. Volume 14, 2023, pp. 187–216, 2023, doi: <https://doi.org/10.1146/annurev-chembioeng-092220-111121>.
- [78] Z. Zhang and K. Awaga, 'Redox-active metal–organic frameworks as electrode materials for batteries', *MRS Bull*, vol. 41, no. 11, pp. 883–889, 2016, doi: DOI: 10.1557/mrs.2016.245.
- [79] A. Jouhara, N. Dupré, A.-C. Gaillot, D. Guyomard, F. Dolhem, and P. Poizot, 'Raising the redox potential in carboxyphenolate-based positive organic materials via cation substitution', *Nat Commun*, vol. 9, no. 1, p. 4401, 2018, doi: 10.1038/s41467-018-06708-x.
- [80] H. Qin, Z. P. Song, H. Zhan, and Y. H. Zhou, 'Aqueous rechargeable alkali-ion batteries with polyimide anode', *J Power Sources*, vol. 249, pp. 367–372, 2014, doi: <https://doi.org/10.1016/j.jpowsour.2013.10.091>.
- [81] W. Luo, M. Allen, V. Raju, and X. Ji, 'An Organic Pigment as a High-Performance Cathode for Sodium-Ion Batteries', *Adv Energy Mater*, vol. 4, no. 15, p. 1400554, Oct. 2014, doi: <https://doi.org/10.1002/aenm.201400554>.

References

- [82] X. Han, C. Chang, L. Yuan, T. Sun, and J. Sun, 'Aromatic Carbonyl Derivative Polymers as High-Performance Li-Ion Storage Materials', *Advanced Materials*, vol. 19, no. 12, pp. 1616–1621, Jun. 2007, doi: <https://doi.org/10.1002/adma.200602584>.
- [83] L. Jiang *et al.*, 'Building aqueous K-ion batteries for energy storage', *Nat Energy*, vol. 4, no. 6, pp. 495–503, 2019, doi: [10.1038/s41560-019-0388-0](https://doi.org/10.1038/s41560-019-0388-0).
- [84] Z. Huang *et al.*, 'Small-Dipole-Molecule-Containing Electrolytes for High-Voltage Aqueous Rechargeable Batteries', *Advanced Materials*, vol. 34, no. 4, p. 2106180, Jan. 2022, doi: <https://doi.org/10.1002/adma.202106180>.
- [85] J. Ge, L. Fan, A. M. Rao, J. Zhou, and B. Lu, 'Surface-substituted Prussian blue analogue cathode for sustainable potassium-ion batteries', *Nat Sustain*, vol. 5, no. 3, pp. 225–234, 2022, doi: [10.1038/s41893-021-00810-7](https://doi.org/10.1038/s41893-021-00810-7).
- [86] B. Wen *et al.*, 'Water-induced 3D MgMn₂O₄ assisted by unique nanofluidic effect for energy-dense and durable aqueous magnesium-ion batteries', *Chemical Engineering Journal*, vol. 435, p. 134997, 2022, doi: <https://doi.org/10.1016/j.cej.2022.134997>.
- [87] M. L. Vera, W. R. Torres, C. I. Galli, A. Chagnes, and V. Flexer, 'Environmental impact of direct lithium extraction from brines', *Nat Rev Earth Environ*, vol. 4, no. 3, pp. 149–165, 2023, doi: [10.1038/s43017-022-00387-5](https://doi.org/10.1038/s43017-022-00387-5).
- [88] R. B. Kaunda, 'Potential environmental impacts of lithium mining', *Journal of Energy & Natural Resources Law*, vol. 38, no. 3, pp. 237–244, Jul. 2020, doi: [10.1080/02646811.2020.1754596](https://doi.org/10.1080/02646811.2020.1754596).
- [89] A. A. Yaroshevsky, 'Abundances of chemical elements in the Earth's crust', *Geochemistry International*, vol. 44, no. 1, pp. 48–55, 2006, doi: [10.1134/S001670290601006X](https://doi.org/10.1134/S001670290601006X).
- [90] A. Innocenti, D. Bresser, J. Garche, and S. Passerini, 'A critical discussion of the current availability of lithium and zinc for use in batteries', *Nat Commun*, vol. 15, no. 1, p. 4068, 2024, doi: [10.1038/s41467-024-48368-0](https://doi.org/10.1038/s41467-024-48368-0).
- [91] D. Dong, T. Wang, Y. Sun, J. Fan, and Y.-C. Lu, 'Hydrotropic solubilization of zinc acetates for sustainable aqueous battery electrolytes', *Nat Sustain*, vol. 6, no. 11, pp. 1474–1484, 2023, doi: [10.1038/s41893-023-01172-y](https://doi.org/10.1038/s41893-023-01172-y).
- [92] W. J. Wruck, B. Reichman, K. R. Bullock, and W. -H. Kao, 'Rechargeable Zn - MnO₂ Alkaline Batteries', *J Electrochem Soc*, vol. 138, no. 12, p. 3560, Dec. 1991, doi: [10.1149/1.2085459](https://doi.org/10.1149/1.2085459).
- [93] I. Aguilar *et al.*, 'Identifying interfacial mechanisms limitations within aqueous Zn-MnO₂ batteries and means to cure them with additives', *Energy Storage Mater*, vol. 53, pp. 238–253, 2022, doi: <https://doi.org/10.1016/j.ensm.2022.08.043>.
- [94] T. Yamamoto and T. Shoji, 'Rechargeable Zn|ZnSO₄|MnO₂-type cells', *Inorganica Chim Acta*, vol. 117, no. 2, pp. L27–L28, 1986, doi: [https://doi.org/10.1016/S0020-1693\(00\)82175-1](https://doi.org/10.1016/S0020-1693(00)82175-1).
- [95] Z. Yi, G. Chen, F. Hou, L. Wang, and J. Liang, 'Strategies for the Stabilization of Zn Metal Anodes for Zn-Ion Batteries', *Adv Energy Mater*, vol. 11, no. 1, p. 2003065, 2021, doi: <https://doi.org/10.1002/aenm.202003065>.
- [96] T. Wang, Y. Zhang, J. You, and F. Hu, 'Recent Progress in Aqueous Zinc-Ion Batteries: From Fundamental Science to Structure Design', *The Chemical Record*, vol. 23, no. 5, p. e202200309, 2023, doi: <https://doi.org/10.1002/tcr.202200309>.
- [97] T. Xiong *et al.*, 'Defect Engineering of Oxygen-Deficient Manganese Oxide to Achieve High-Performing Aqueous Zinc Ion Battery', *Adv Energy Mater*, vol. 9, no. 14, p. 1803815, 2019, doi: <https://doi.org/10.1002/aenm.201803815>.
- [98] K. W. Nam, H. Kim, J. H. Choi, and J. W. Choi, 'Crystal water for high performance layered manganese oxide cathodes in aqueous rechargeable zinc batteries', *Energy Environ. Sci.*, vol. 12, no. 6, pp. 1999–2009, 2019, doi: [10.1039/C9EE00718K](https://doi.org/10.1039/C9EE00718K).

References

- [99] C. Xu, B. Li, H. Du, and F. Kang, 'Energetic Zinc Ion Chemistry: The Rechargeable Zinc Ion Battery', *Angewandte Chemie International Edition*, vol. 51, no. 4, pp. 933–935, 2012, doi: <https://doi.org/10.1002/anie.201106307>.
- [100] P. Oberholzer, E. Tervoort, A. Bouzid, A. Pasquarello, and D. Kundu, 'Oxide versus Nonoxide Cathode Materials for Aqueous Zn Batteries: An Insight into the Charge Storage Mechanism and Consequences Thereof', *ACS Appl Mater Interfaces*, vol. 11, no. 1, pp. 674–682, Jan. 2019, doi: 10.1021/acsami.8b16284.
- [101] G. Fang *et al.*, 'Suppressing Manganese Dissolution in Potassium Manganate with Rich Oxygen Defects Engaged High-Energy-Density and Durable Aqueous Zinc-Ion Battery', *Adv Funct Mater*, vol. 29, no. 15, p. 1808375, 2019, doi: <https://doi.org/10.1002/adfm.201808375>.
- [102] W. Sun *et al.*, 'Zn/MnO₂ Battery Chemistry With H⁺ and Zn²⁺ Coinsertion', *J Am Chem Soc*, vol. 139, no. 29, pp. 9775–9778, Jul. 2017, doi: 10.1021/jacs.7b04471.
- [103] J. Huang *et al.*, 'Polyaniline-intercalated manganese dioxide nanolayers as a high-performance cathode material for an aqueous zinc-ion battery', *Nat Commun*, vol. 9, no. 1, p. 2906, 2018, doi: 10.1038/s41467-018-04949-4.
- [104] S. J. Kim *et al.*, 'Toward the Understanding of the Reaction Mechanism of Zn/MnO₂ Batteries Using Non-alkaline Aqueous Electrolytes', *Chemistry of Materials*, vol. 33, no. 18, pp. 7283–7289, Sep. 2021, doi: 10.1021/acs.chemmater.1c01542.
- [105] M. Mateos, N. Makivic, Y.-S. Kim, B. Limoges, and V. Balland, 'Accessing the Two-Electron Charge Storage Capacity of MnO₂ in Mild Aqueous Electrolytes', *Adv Energy Mater*, vol. 10, no. 23, p. 2000332, 2020, doi: <https://doi.org/10.1002/aenm.202000332>.
- [106] H. Moon *et al.*, 'Direct Proof of the Reversible Dissolution/Deposition of Mn²⁺/Mn⁴⁺ for Mild-Acid Zn-MnO₂ Batteries with Porous Carbon Interlayers', *Advanced Science*, vol. 8, no. 6, p. 2003714, 2021, doi: <https://doi.org/10.1002/advs.202003714>.
- [107] B. Lee *et al.*, 'Critical Role of pH Evolution of Electrolyte in the Reaction Mechanism for Rechargeable Zinc Batteries', *ChemSusChem*, vol. 9, no. 20, pp. 2948–2956, 2016, doi: <https://doi.org/10.1002/cssc.201600702>.
- [108] T. Otani, M. Nagata, Y. Fukunaka, and T. Homma, 'Morphological evolution of mossy structures during the electrodeposition of zinc from an alkaline zincate solution', *Electrochim Acta*, vol. 206, pp. 366–373, 2016, doi: <https://doi.org/10.1016/j.electacta.2016.04.124>.
- [109] R. Y. Wang, D. W. Kirk, and G. X. Zhang, 'Effects of Deposition Conditions on the Morphology of Zinc Deposits from Alkaline Zincate Solutions', *J Electrochem Soc*, vol. 153, no. 5, p. C357, Mar. 2006, doi: 10.1149/1.2186037.
- [110] Y. Zuo *et al.*, 'Zinc dendrite growth and inhibition strategies', *Mater Today Energy*, vol. 20, p. 100692, 2021, doi: <https://doi.org/10.1016/j.mtener.2021.100692>.
- [111] F. Wang *et al.*, 'Highly reversible zinc metal anode for aqueous batteries', *Nat Mater*, vol. 17, no. 6, pp. 543–549, 2018, doi: 10.1038/s41563-018-0063-z.
- [112] H. Liu, Y. Zhang, C. Wang, J. N. Glazer, Z. Shan, and N. Liu, 'Understanding and Controlling the Nucleation and Growth of Zn Electrodeposits for Aqueous Zinc-Ion Batteries', *ACS Appl Mater Interfaces*, vol. 13, no. 28, pp. 32930–32936, 2021, doi: 10.1021/acsami.1c06131.
- [113] X. Long *et al.*, 'Electric field distribution regulation of a zinc anode toward long cycle life zinc metal batteries', *J. Mater. Chem. A*, vol. 12, no. 22, pp. 13181–13190, 2024, doi: 10.1039/D4TA00629A.
- [114] J. Xu *et al.*, 'Understanding the Electrical Mechanisms in Aqueous Zinc Metal Batteries: From Electrostatic Interactions to Electric Field Regulation', *Advanced*

References

- Materials*, vol. 36, no. 3, p. 2309726, 2024, doi: <https://doi.org/10.1002/adma.202309726>.
- [115] J. Shin, J. Lee, Y. Park, and J. W. Choi, ‘Aqueous zinc ion batteries: focus on zinc metal anodes’, *Chem. Sci.*, vol. 11, no. 8, pp. 2028–2044, 2020, doi: 10.1039/D0SC00022A.
- [116] X. G. Zhang, ‘Corrosion and electrochemistry of zinc’, 1996. [Online]. Available: <https://api.semanticscholar.org/CorpusID:92941180>
- [117] J. Zheng *et al.*, ‘Regulating electrodeposition morphology in high-capacity aluminium and zinc battery anodes using interfacial metal–substrate bonding’, *Nat Energy*, vol. 6, no. 4, pp. 398–406, 2021, doi: 10.1038/s41560-021-00797-7.
- [118] H. He *et al.*, ‘Engineering interfacial layers to enable Zn metal anodes for aqueous zinc-ion batteries’, *Energy Storage Mater*, vol. 43, pp. 317–336, 2021, doi: <https://doi.org/10.1016/j.ensm.2021.09.012>.
- [119] Y. An *et al.*, ‘Highly Reversible Zn Metal Anodes Enabled by Freestanding, Lightweight, and Zincophilic MXene/Nanoporous Oxide Heterostructure Engineered Separator for Flexible Zn-MnO₂ Batteries’, *ACS Nano*, vol. 16, no. 4, pp. 6755–6770, Apr. 2022, doi: 10.1021/acsnano.2c01571.
- [120] X. Xie *et al.*, ‘Manipulating the ion-transfer kinetics and interface stability for high-performance zinc metal anodes’, *Energy Environ. Sci.*, vol. 13, no. 2, pp. 503–510, 2020, doi: 10.1039/C9EE03545A.
- [121] W. Zhou, M. Chen, Q. Tian, J. Chen, X. Xu, and C.-P. Wong, ‘Cotton-derived cellulose film as a dendrite-inhibiting separator to stabilize the zinc metal anode of aqueous zinc ion batteries’, *Energy Storage Mater*, vol. 44, pp. 57–65, 2022, doi: <https://doi.org/10.1016/j.ensm.2021.10.002>.
- [122] H. Qin *et al.*, ‘A Nature-Inspired Separator with Water-Confined and Kinetics-Boosted Effects for Sustainable and High-Utilization Zn Metal Batteries’, *Small*, vol. 19, no. 20, p. 2300130, 2023, doi: <https://doi.org/10.1002/smll.202300130>.
- [123] J. Cao, D. Zhang, X. Zhang, Z. Zeng, J. Qin, and Y. Huang, ‘Strategies of regulating Zn²⁺ solvation structures for dendrite-free and side reaction-suppressed zinc-ion batteries’, *Energy Environ. Sci.*, vol. 15, no. 2, pp. 499–528, 2022, doi: 10.1039/D1EE03377H.
- [124] Z. Zheng *et al.*, ‘Electrolyte additives toward practical aqueous zinc-ion batteries: recent advances and future challenges’, *Next Energy*, vol. 1, no. 4, p. 100073, 2023, doi: <https://doi.org/10.1016/j.nxener.2023.100073>.
- [125] H. Cao *et al.*, ‘Regulating the solvated structure to achieve highly reversible zinc plating/stripping for dendrite-free Zn anode by sulfolane additive’, *Chemical Engineering Journal*, vol. 455, p. 140538, 2023, doi: <https://doi.org/10.1016/j.cej.2022.140538>.
- [126] J. Yang *et al.*, ‘Three Birds with One Stone: Tetramethylurea as Electrolyte Additive for Highly Reversible Zn-Metal Anode’, *Adv Funct Mater*, vol. 32, no. 49, 2022, doi: 10.1002/adfm.202209642.
- [127] Z. Hou, H. Tan, Y. Gao, M. Li, Z. Lu, and B. Zhang, ‘Tailoring desolvation kinetics enables stable zinc metal anodes’, *J. Mater. Chem. A*, vol. 8, no. 37, pp. 19367–19374, 2020, doi: 10.1039/D0TA06622B.
- [128] W. He *et al.*, ‘Decreasing Water Activity Using the Tetrahydrofuran Electrolyte Additive for Highly Reversible Aqueous Zinc Metal Batteries’, *ACS Appl Mater Interfaces*, vol. 15, no. 5, pp. 6647–6656, 2023, doi: 10.1021/acami.2c17714.
- [129] T.-B. Song, Z.-H. Huang, X.-R. Zhang, J.-W. Ni, and H.-M. Xiong, ‘Nitrogen-Doped and Sulfonated Carbon Dots as a Multifunctional Additive to Realize Highly

References

- Reversible Aqueous Zinc-Ion Batteries’, *Small*, vol. 19, no. 31, 2023, doi: 10.1002/sml.202205558.
- [130] K. Zhao *et al.*, ‘Stabilizing Zinc Electrodes with a Vanillin Additive in Mild Aqueous Electrolytes’, *ACS Appl Mater Interfaces*, vol. 13, no. 40, pp. 47650–47658, Oct. 2021, doi: 10.1021/acsami.1c14407.
- [131] Z. Chen *et al.*, ‘Arginine Cations Inhibiting Charge Accumulation of Dendrites and Boosting Zn Metal Reversibility in Aqueous Rechargeable Batteries’, *ACS Sustain Chem Eng*, vol. 9, no. 19, pp. 6855–6863, May 2021, doi: 10.1021/acssuschemeng.1c01609.
- [132] Y. Jin *et al.*, ‘Stabilizing Zinc Anode Reactions by Polyethylene Oxide Polymer in Mild Aqueous Electrolytes’, *Adv Funct Mater*, vol. 30, no. 43, 2020, doi: 10.1002/adfm.202003932.
- [133] M. Yan, C. Xu, Y. Sun, H. Pan, and H. Li, ‘Manipulating Zn anode reactions through salt anion involving hydrogen bonding network in aqueous electrolytes with PEO additive’, *Nano Energy*, vol. 82, p. 105739, 2021, doi: <https://doi.org/10.1016/j.nanoen.2020.105739>.
- [134] C. Lin *et al.*, ‘Regulating the plating process of zinc with highly efficient additive for long-life zinc anode’, *J Power Sources*, vol. 549, p. 232078, 2022, doi: <https://doi.org/10.1016/j.jpowsour.2022.232078>.
- [135] D. Han *et al.*, ‘A Self-Regulated Interface toward Highly Reversible Aqueous Zinc Batteries’, *Adv Energy Mater*, vol. 12, no. 9, 2022, doi: 10.1002/aenm.202102982.
- [136] Y.-X. Song *et al.*, ‘Interfacial chemistry regulation via dibenzenesulfonamide-functionalized additives enables high-performance Zn metal anodes’, *Energy Storage Mater*, vol. 58, pp. 85–93, 2023, doi: <https://doi.org/10.1016/j.ensm.2023.03.005>.
- [137] N. Wang *et al.*, ‘Zincophobic Electrolyte Achieves Highly Reversible Zinc-Ion Batteries’, *Adv Funct Mater*, vol. 33, no. 27, 2023, doi: 10.1002/adfm.202300795.
- [138] C. Huang *et al.*, ‘Stabilizing Zinc Anodes by Regulating the Electrical Double Layer with Saccharin Anions’, *Advanced Materials*, vol. 33, no. 38, 2021, doi: 10.1002/adma.202100445.
- [139] Q. Nian *et al.*, ‘Highly reversible zinc metal anode enabled by strong Brønsted acid and hydrophobic interfacial chemistry’, *Nat Commun*, vol. 15, no. 1, p. 4303, 2024, doi: 10.1038/s41467-024-48444-5.
- [140] X. Ji and L. F. Nazar, ‘Best practices for zinc metal batteries’, *Nat Sustain*, vol. 7, no. 2, pp. 98–99, 2024, doi: 10.1038/s41893-023-01257-8.
- [141] Q. Li, A. Chen, D. Wang, Z. Pei, and C. Zhi, ‘“Soft Shorts” Hidden in Zinc Metal Anode Research’, *Joule*, vol. 6, no. 2, pp. 273–279, 2022, doi: <https://doi.org/10.1016/j.joule.2021.12.009>.
- [142] H.-C. Tseng, C.-Y. Lee, W.-L. Weng, and I.-M. Shiah, ‘Solubilities of amino acids in water at various pH values under 298.15K’, *Fluid Phase Equilib*, vol. 285, no. 1, pp. 90–95, 2009, doi: <https://doi.org/10.1016/j.fluid.2009.07.017>.
- [143] L. A. Ferreira, E. A. Macedo, and S. P. Pinho, ‘KCl effect on the solubility of five different amino acids in water’, *Fluid Phase Equilib*, vol. 255, no. 2, pp. 131–137, 2007, doi: <https://doi.org/10.1016/j.fluid.2007.04.004>.
- [144] D. Reber, R. Grissa, M. Becker, R. S. Kühnel, and C. Battaglia, ‘Anion Selection Criteria for Water-in-Salt Electrolytes’, *Adv Energy Mater*, vol. 11, no. 5, Feb. 2021, doi: 10.1002/aenm.202002913.
- [145] Y. R. Dougassa, J. Jacquemin, L. El Ouatani, C. Tessier, and M. Anouti, ‘Viscosity and Carbon Dioxide Solubility for LiPF₆, LiTFSI, and LiFAP in Alkyl Carbonates: Lithium Salt Nature and Concentration Effect’, *J Phys Chem B*, vol. 118, no. 14, pp. 3973–3980, Apr. 2014, doi: 10.1021/jp500063c.

References

- [146] A. J. Göttle and M. T. M. Koper, 'Proton-coupled electron transfer in the electrocatalysis of CO₂ reduction: prediction of sequential vs. concerted pathways using DFT', *Chem. Sci.*, vol. 8, no. 1, pp. 458–465, 2017, doi: 10.1039/C6SC02984A.
- [147] A. Yamaguchi, R. Inuzuka, T. Takashima, T. Hayashi, K. Hashimoto, and R. Nakamura, 'Regulating proton-coupled electron transfer for efficient water splitting by manganese oxides at neutral pH', *Nat Commun*, vol. 5, no. 1, p. 4256, 2014, doi: 10.1038/ncomms5256.
- [148] J. Durst, A. Siebel, C. Simon, F. Hasché, J. Herranz, and H. A. Gasteiger, 'New insights into the electrochemical hydrogen oxidation and evolution reaction mechanism', *Energy Environ. Sci.*, vol. 7, no. 7, pp. 2255–2260, 2014, doi: 10.1039/C4EE00440J.
- [149] N. Dubouis and A. Grimaud, 'The hydrogen evolution reaction: from material to interfacial descriptors', *Chem. Sci.*, vol. 10, no. 40, pp. 9165–9181, 2019, doi: 10.1039/C9SC03831K.
- [150] A. Yamaguchi, R. Inuzuka, T. Takashima, T. Hayashi, K. Hashimoto, and R. Nakamura, 'Regulating proton-coupled electron transfer for efficient water splitting by manganese oxides at neutral pH', *Nat Commun*, vol. 5, no. 1, p. 4256, 2014, doi: 10.1038/ncomms5256.
- [151] Y. Jiang, J. Huang, B. Mao, T. An, J. Wang, and M. Cao, 'Inside solid-liquid interfaces: Understanding the influence of the electrical double layer on alkaline hydrogen evolution reaction', *Appl Catal B*, vol. 293, p. 120220, 2021, doi: <https://doi.org/10.1016/j.apcatb.2021.120220>.
- [152] M. T. M. Koper, 'Theory of multiple proton–electron transfer reactions and its implications for electrocatalysis', *Chem. Sci.*, vol. 4, no. 7, pp. 2710–2723, 2013, doi: 10.1039/C3SC50205H.
- [153] I. Ledezma-Yanez, W. D. Z. Wallace, P. Sebastián-Pascual, V. Climent, J. M. Feliu, and M. T. M. Koper, 'Interfacial water reorganization as a pH-dependent descriptor of the hydrogen evolution rate on platinum electrodes', *Nat Energy*, vol. 2, no. 4, p. 17031, 2017, doi: 10.1038/nenergy.2017.31.
- [154] N. Mahmood, Y. Yao, J.-W. Zhang, L. Pan, X. Zhang, and J.-J. Zou, 'Electrocatalysts for Hydrogen Evolution in Alkaline Electrolytes: Mechanisms, Challenges, and Prospective Solutions', *Advanced Science*, vol. 5, no. 2, p. 1700464, 2018, doi: <https://doi.org/10.1002/advs.201700464>.
- [155] D. Strmcnik *et al.*, 'Improving the hydrogen oxidation reaction rate by promotion of hydroxyl adsorption', *Nat Chem*, vol. 5, no. 4, pp. 300–306, 2013, doi: 10.1038/nchem.1574.
- [156] T. Shinagawa, A. T. Garcia-Esparza, and K. Takanabe, 'Insight on Tafel slopes from a microkinetic analysis of aqueous electrocatalysis for energy conversion', *Sci Rep*, vol. 5, no. 1, p. 13801, 2015, doi: 10.1038/srep13801.
- [157] N. Dubouis, C. Yang, R. Beer, L. Ries, D. Voiry, and A. Grimaud, 'Interfacial Interactions as an Electrochemical Tool To Understand Mo-Based Catalysts for the Hydrogen Evolution Reaction', *ACS Catal*, vol. 8, no. 2, pp. 828–836, Feb. 2018, doi: 10.1021/acscatal.7b03684.
- [158] M. Auinger *et al.*, 'Near-surface ion distribution and buffer effects during electrochemical reactions', *Phys. Chem. Chem. Phys.*, vol. 13, no. 36, pp. 16384–16394, 2011, doi: 10.1039/C1CP21717H.
- [159] J. L. Alvarez-Hernandez, A. E. Sopchak, and K. L. Bren, 'Buffer pK_a Impacts the Mechanism of Hydrogen Evolution Catalyzed by a Cobalt Porphyrin-Peptide', *Inorg Chem*, vol. 59, no. 12, pp. 8061–8069, 2020, doi: 10.1021/acs.inorgchem.0c00362.

References

- [160] G. Marcandalli, K. Boterman, and M. T. M. Koper, 'Understanding hydrogen evolution reaction in bicarbonate buffer', *J Catal*, vol. 405, pp. 346–354, 2022, doi: <https://doi.org/10.1016/j.jcat.2021.12.012>.
- [161] M. N. Jackson, O. Jung, H. C. Lamotte, and Y. Surendranath, 'Donor-Dependent Promotion of Interfacial Proton-Coupled Electron Transfer in Aqueous Electrocatalysis', *ACS Catal*, vol. 9, no. 4, pp. 3737–3743, Apr. 2019, doi: [10.1021/acscatal.9b00056](https://doi.org/10.1021/acscatal.9b00056).
- [162] Carey F.A, *Organic Chemistry*, 4th ed. New York City: McGraw-Hill, 2000.
- [163] Hardy P.M, *In Chemistry and Biochemistry of the Amino Acids*. London: Chapman and Hall, 1985.
- [164] D. HÄUSSINGER, S. SOBOLL, A. J. MEIJER, W. GEROK, J. M. TAGER, and H. SIES, 'Role of plasma membrane transport in hepatic glutamine metabolism', *Eur J Biochem*, vol. 152, no. 3, pp. 597–603, 1985, doi: <https://doi.org/10.1111/j.1432-1033.1985.tb09237.x>.
- [165] W. J. Ferguson *et al.*, 'Hydrogen ion buffers for biological research', *Anal Biochem*, vol. 104, no. 2, pp. 300–310, 1980, doi: [https://doi.org/10.1016/0003-2697\(80\)90079-2](https://doi.org/10.1016/0003-2697(80)90079-2).
- [166] E. Stellwagen, J. D. Prantner, and N. C. Stellwagen, 'Do zwitterions contribute to the ionic strength of a solution?', *Anal Biochem*, vol. 373, no. 2, pp. 407–409, 2008, doi: <https://doi.org/10.1016/j.ab.2007.10.038>.
- [167] Z. A. Zafar *et al.*, 'Chaotropic anion based "water-in-salt" electrolyte realizes a high voltage Zn-graphite dual-ion battery', *J Mater Chem A Mater*, vol. 10, no. 4, pp. 2064–2074, Jan. 2022, doi: [10.1039/d1ta10122f](https://doi.org/10.1039/d1ta10122f).
- [168] A. Nimkar *et al.*, 'Influences of Cations' Solvation on Charge Storage Performance in Polyimide Anodes for Aqueous Multivalent Ion Batteries', *ACS Energy Lett*, vol. 6, no. 7, pp. 2638–2644, Jul. 2021, doi: [10.1021/acsenenergylett.1c01007](https://doi.org/10.1021/acsenenergylett.1c01007).
- [169] Y. Zhang *et al.*, 'Chaotropic Electrolyte Enabling Wide-Temperature Metal-Free Battery', *ACS Nano*, vol. 17, no. 22, pp. 22656–22667, Nov. 2023, doi: [10.1021/acsnano.3c06948](https://doi.org/10.1021/acsnano.3c06948).
- [170] G. V. S. M. Carrera, R. F. M. Frade, J. Aires-De-Sousa, C. A. M. Afonso, and L. C. Branco, 'Synthesis and properties of new functionalized guanidinium based ionic liquids as non-toxic versatile organic materials', *Tetrahedron*, vol. 66, no. 45, pp. 8785–8794, Nov. 2010, doi: [10.1016/j.tet.2010.08.040](https://doi.org/10.1016/j.tet.2010.08.040).
- [171] P. S. Kulkarni, L. C. Branco, J. G. Crespo, M. C. Nunes, A. Raymundo, and C. A. M. Afonso, 'Comparison of physicochemical properties of new ionic liquids based on imidazolium, quaternary ammonium, and guanidinium cations', *Chemistry - A European Journal*, vol. 13, no. 30, pp. 8478–8488, 2007, doi: [10.1002/chem.200700965](https://doi.org/10.1002/chem.200700965).
- [172] N. Bucher *et al.*, 'A novel ionic liquid for Li ion batteries-uniting the advantages of guanidinium and piperidinium cations', *RSC Adv*, vol. 4, no. 4, pp. 1996–2003, 2014, doi: [10.1039/c3ra46118a](https://doi.org/10.1039/c3ra46118a).
- [173] A. J. Kunov-Kruse, C. C. Weber, R. D. Rogers, and A. S. Myerson, 'The A Priori Design and Selection of Ionic Liquids as Solvents for Active Pharmaceutical Ingredients', *Chemistry - A European Journal*, vol. 23, no. 23, pp. 5498–5508, Apr. 2017, doi: [10.1002/chem.201605704](https://doi.org/10.1002/chem.201605704).
- [174] Z. Zhao, K. Ueno, and C. A. Angell, 'High conductivity, and "dry" proton motion, in guanidinium salt melts and binary solutions', *Journal of Physical Chemistry B*, vol. 115, no. 46, pp. 13467–13472, Nov. 2011, doi: [10.1021/jp206491z](https://doi.org/10.1021/jp206491z).
- [175] E. T. Allen and J. Johnston, 'THE EXACT DETERMINATION OF SULPHUR IN SOLUBLE SULPHATES.', *J Am Chem Soc*, vol. 32, no. 5, pp. 588–617, May 1910, doi: [10.1021/ja01923a002](https://doi.org/10.1021/ja01923a002).

References

- [176] I. Rey, J. C. Lassègues, J. Grondin, and L. Servant, ‘Infrared and Raman study of the PEO-LiTFSI polymer electrolyte’, *Electrochim Acta*, vol. 43, no. 10, pp. 1505–1510, 1998, doi: [https://doi.org/10.1016/S0013-4686\(97\)10092-5](https://doi.org/10.1016/S0013-4686(97)10092-5).
- [177] Y. Hu, H. Li, X. Huang, and L. Chen, ‘Novel room temperature molten salt electrolyte based on LiTFSI and acetamide for lithium batteries’, *Electrochem Commun*, vol. 6, no. 1, pp. 28–32, 2004, doi: [10.1016/j.elecom.2003.10.009](https://doi.org/10.1016/j.elecom.2003.10.009).
- [178] N. H. C. Lewis, Y. Zhang, B. Dereka, E. V. Carino, E. J. Maginn, and A. Tokmakoff, ‘Signatures of Ion Pairing and Aggregation in the Vibrational Spectroscopy of Super-Concentrated Aqueous Lithium Bistriflimide Solutions’, *Journal of Physical Chemistry C*, vol. 124, no. 6, pp. 3470–3481, Feb. 2020, doi: [10.1021/acs.jpcc.9b10477](https://doi.org/10.1021/acs.jpcc.9b10477).
- [179] D. Brouillette, G. Perron, and J. E. Desnoyers, ‘Apparent Molar Volume, Heat Capacity, and Conductance of Lithium Bis(trifluoromethylsulfone)imide in Glymes and Other Aprotic Solvents’, *J Solution Chem*, vol. 27, no. 2, pp. 151–182, 1998, doi: [10.1023/A:1022609407560](https://doi.org/10.1023/A:1022609407560).
- [180] S. Burikov, T. Dolenko, S. Patsaeva, Y. Starokurov, and V. Yuzhakov, ‘Raman and IR spectroscopy research on hydrogen bonding in water-ethanol systems’, *Mol Phys*, vol. 108, no. 18, pp. 2427–2436, Sep. 2010, doi: [10.1080/00268976.2010.516277](https://doi.org/10.1080/00268976.2010.516277).
- [181] R.-S. Kühnel, D. Reber, and C. Battaglia, ‘Perspective—Electrochemical Stability of Water-in-Salt Electrolytes’, *J Electrochem Soc*, vol. 167, no. 7, p. 070544, Jan. 2020, doi: [10.1149/1945-7111/ab7c6f](https://doi.org/10.1149/1945-7111/ab7c6f).
- [182] K. Xu, S. P. Ding, and T. R. Jow, ‘Toward Reliable Values of Electrochemical Stability Limits for Electrolytes’, *J Electrochem Soc*, vol. 146, no. 11, p. 4172, Nov. 1999, doi: [10.1149/1.1392609](https://doi.org/10.1149/1.1392609).
- [183] N. Dubouis *et al.*, ‘Chasing Aqueous Biphasic Systems from Simple Salts by Exploring the LiTFSI/LiCl/H₂O Phase Diagram’, *ACS Cent Sci*, vol. 5, no. 4, pp. 640–643, Apr. 2019, doi: [10.1021/acscentsci.8b00955](https://doi.org/10.1021/acscentsci.8b00955).
- [184] H. D. B. Jenkins and Y. Marcus, ‘Viscosity B-Coefficients of Ions in Solution’, *Chem Rev*, vol. 95, no. 8, pp. 2695–2724, 1995, doi: [10.1021/cr00040a004](https://doi.org/10.1021/cr00040a004).
- [185] C. Yang *et al.*, ‘All-temperature zinc batteries with high-entropy aqueous electrolyte’, *Nat Sustain*, vol. 6, no. 3, pp. 325–335, Mar. 2023, doi: [10.1038/s41893-022-01028-x](https://doi.org/10.1038/s41893-022-01028-x).
- [186] H. Ji *et al.*, ‘High-entropy solvent design enabling a universal electrolyte with a low freezing point for low-temperature aqueous batteries’, *Chem. Commun.*, vol. 59, no. 56, pp. 8715–8718, 2023, doi: [10.1039/D3CC02214E](https://doi.org/10.1039/D3CC02214E).
- [187] O. Zech *et al.*, ‘Alkali Metal Oligoether Carboxylates—A New Class of Ionic Liquids’, *Chemistry – A European Journal*, vol. 15, no. 6, pp. 1341–1345, 2009, doi: <https://doi.org/10.1002/chem.200801806>.
- [188] P. Kubisiak, P. Wróbel, and A. Eilmes, ‘How Temperature, Pressure, and Salt Concentration Affect Correlations in LiTFSI/EMIM-TFSI Electrolytes: A Molecular Dynamics Study’, *J Phys Chem B*, vol. 125, no. 44, pp. 12292–12302, 2021, doi: [10.1021/acs.jpcc.1c07782](https://doi.org/10.1021/acs.jpcc.1c07782).
- [189] M. Gouverneur, F. Schmidt, and M. Schönhoff, ‘Negative effective Li transference numbers in Li salt/ionic liquid mixtures: does Li drift in the “Wrong” direction?’, *Phys. Chem. Chem. Phys.*, vol. 20, no. 11, pp. 7470–7478, 2018, doi: [10.1039/C7CP08580J](https://doi.org/10.1039/C7CP08580J).
- [190] R. Klein, O. Zech, E. Maurer, M. Kellermeier, and W. Kunz, ‘Oligoether Carboxylates: Task-Specific Room-Temperature Ionic Liquids’, *J Phys Chem B*, vol. 115, no. 29, pp. 8961–8969, 2011, doi: [10.1021/jp200624g](https://doi.org/10.1021/jp200624g).
- [191] S. Wu, Z. Hu, P. He, L. Ren, J. Huang, and J. Luo, ‘Crystallographic engineering of Zn anodes for aqueous batteries’, *eScience*, vol. 3, no. 3, p. 100120, 2023, doi: <https://doi.org/10.1016/j.esci.2023.100120>.

References

- [192] J. Wang *et al.*, ‘Stable interphase chemistry of textured Zn anode for rechargeable aqueous batteries’, *Sci Bull (Beijing)*, vol. 67, no. 7, pp. 716–724, 2022, doi: <https://doi.org/10.1016/j.scib.2022.01.010>.
- [193] J. Zheng *et al.*, ‘Reversible epitaxial electrodeposition of metals in battery anodes’, *Science (1979)*, vol. 366, no. 6465, pp. 645–648, 2019, doi: 10.1126/science.aax6873.
- [194] L. Ma *et al.*, ‘Critical Factors Dictating Reversibility of the Zinc Metal Anode’, *Energy & Environmental Materials*, vol. 3, no. 4, pp. 516–521, 2020, doi: <https://doi.org/10.1002/eem2.12077>.
- [195] Z. Wu, Y. Li, and J. Liu, ‘Coulombic Efficiency for Practical Zinc Metal Batteries: Critical Analysis and Perspectives’, *Small Methods*, vol. 8, no. 1, p. 2300660, 2024, doi: <https://doi.org/10.1002/smt.202300660>.
- [196] X. Zhao *et al.*, ‘Advanced Buffering Acidic Aqueous Electrolytes for Ultra-Long Life Aqueous Zinc-Ion Batteries’, *Small*, vol. 18, no. 21, p. 2200742, May 2022, doi: <https://doi.org/10.1002/sml.202200742>.
- [197] N. Patil, C. de la Cruz, D. Ciurduc, A. Mavrandonakis, J. Palma, and R. Marcilla, ‘An Ultrahigh Performance Zinc-Organic Battery using Poly(catechol) Cathode in Zn(TFSI)₂-Based Concentrated Aqueous Electrolytes’, *Adv Energy Mater*, vol. 11, no. 26, p. 2100939, Jul. 2021, doi: <https://doi.org/10.1002/aenm.202100939>.
- [198] C. Wu *et al.*, ‘2-methyl imidazole electrolyte additive enabling ultra-stable Zn anode’, *Chemical Engineering Journal*, vol. 452, p. 139465, 2023, doi: <https://doi.org/10.1016/j.cej.2022.139465>.
- [199] J. Shi *et al.*, ‘Ultrahigh coulombic efficiency and long-life aqueous Zn anodes enabled by electrolyte additive of acetonitrile’, *Electrochim Acta*, vol. 358, p. 136937, 2020, doi: <https://doi.org/10.1016/j.electacta.2020.136937>.
- [200] Q. Zhang *et al.*, ‘Modulating electrolyte structure for ultralow temperature aqueous zinc batteries’, *Nat Commun*, vol. 11, no. 1, p. 4463, 2020, doi: 10.1038/s41467-020-18284-0.
- [201] N. Zhang *et al.*, ‘Rechargeable aqueous zinc-manganese dioxide batteries with high energy and power densities’, *Nat Commun*, vol. 8, no. 1, p. 405, 2017, doi: 10.1038/s41467-017-00467-x.
- [202] H. Pan *et al.*, ‘Reversible aqueous zinc/manganese oxide energy storage from conversion reactions’, *Nat Energy*, vol. 1, no. 5, p. 16039, 2016, doi: 10.1038/nenergy.2016.39.
- [203] X. Lu, E. J. Hansen, G. He, and J. Liu, ‘Eutectic Electrolytes Chemistry for Rechargeable Zn Batteries’, *Small*, vol. 18, no. 21, p. 2200550, 2022, doi: <https://doi.org/10.1002/sml.202200550>.
- [204] X. Li, H. Wang, X. Sun, J. Li, and Y.-N. Liu, ‘Flexible Wide-Temperature Zinc-Ion Battery Enabled by an Ethylene Glycol-Based Organohydrogel Electrolyte’, *ACS Appl Energy Mater*, vol. 4, no. 11, pp. 12718–12727, Nov. 2021, doi: 10.1021/acsaem.1c02433.
- [205] H. Huang, Z. Zhao, P. Li, H. Zhang, and G. Li, ‘Optimizing electrolyte systems for stable and low-temperature zinc-ion batteries via efficient coordinator’, *J Power Sources*, vol. 602, p. 234340, 2024, doi: <https://doi.org/10.1016/j.jpowsour.2024.234340>.
- [206] L. Droguet, ‘Toward aqueous superconcentrated electrolytes for Li-ion battery application’, Sorbonne Université, 2021. [Online]. Available: <https://theses.hal.science/tel-03553001>
- [207] I. Rey, J. C. Lassègues, J. Grondin, and L. Servant, ‘Infrared and Raman study of the PEO-LiTFSI polymer electrolyte’, *Electrochim Acta*, vol. 43, no. 10, pp. 1505–1510, 1998, doi: [https://doi.org/10.1016/S0013-4686\(97\)10092-5](https://doi.org/10.1016/S0013-4686(97)10092-5).

References

- [208] C. Gervillie-Mouravieff *et al.*, ‘Unlocking cell chemistry evolution with operando fibre optic infrared spectroscopy in commercial Na(Li)-ion batteries’, *Nat Energy*, vol. 7, no. 12, pp. 1157–1169, 2022, doi: 10.1038/s41560-022-01141-3.
- [209] Z. Huang *et al.*, ‘Manipulating anion intercalation enables a high-voltage aqueous dual ion battery’, *Nature Communications* 2021 12:1, vol. 12, no. 1, pp. 1–11, May 2021, doi: 10.1038/s41467-021-23369-5.
- [210] M. Xiong, W. Tang, B. Cao, C. Yang, and C. Fan, ‘A small-molecule organic cathode with fast charge–discharge capability for K-ion batteries’, *J. Mater. Chem. A*, vol. 7, no. 35, pp. 20127–20131, 2019, doi: 10.1039/C9TA06376E.
- [211] W. Deng, Y. Shen, J. Qian, Y. Cao, and H. Yang, ‘A Perylene Diimide Crystal with High Capacity and Stable Cyclability for Na-Ion Batteries’, *ACS Appl Mater Interfaces*, vol. 7, no. 38, pp. 21095–21099, Sep. 2015, doi: 10.1021/acsami.5b04325.
- [212] X. Lei, Y. Zheng, F. Zhang, Y. Wang, and Y. Tang, ‘Highly stable magnesium-ion-based dual-ion batteries based on insoluble small-molecule organic anode material’, *Energy Storage Mater*, vol. 30, pp. 34–41, Sep. 2020, doi: 10.1016/J.ENSM.2020.04.025.
- [213] J. Chen *et al.*, ‘Unraveling the Role of Aromatic Ring Size in Tuning the Electrochemical Performance of Small-Molecule Imide Cathodes for Lithium-Ion Batteries’, *ACS Appl Mater Interfaces*, vol. 14, no. 39, pp. 44330–44337, Oct. 2022, doi: <https://doi.org/10.1021/acsami.2c11138>.
- [214] P. Zhao *et al.*, ‘Stable lithium metal anode enabled by high-dimensional lithium deposition through a functional organic substrate’, *Energy Storage Mater*, vol. 33, pp. 158–163, 2020, doi: <https://doi.org/10.1016/j.ensm.2020.08.025>.
- [215] K. Tojo and J. Mizuguchi, ‘Refinement of the crystal structure of 3,4:9,10-perylenebis(dicarboximide), C₂₄H₁₀N₂O₄, at 263 K’, vol. 217, no. 1, pp. 45–46, 2002, doi: 10.1524/ncrs.2002.217.1.45.
- [216] S. Wang, F. Li, A. D. Easley, and J. L. Lutkenhaus, ‘Real-time insight into the doping mechanism of redox-active organic radical polymers’, *Nat Mater*, vol. 18, no. 1, pp. 69–75, 2019, doi: 10.1038/s41563-018-0215-1.
- [217] P. Lemaire, T. Dargon, D. Alves Dalla Corte, O. Sel, H. Perrot, and J.-M. Tarascon, ‘Making Advanced Electrogravimetry as an Affordable Analytical Tool for Battery Interface Characterization’, *Anal Chem*, vol. 92, no. 20, pp. 13803–13812, Oct. 2020, doi: 10.1021/acs.analchem.0c02233.
- [218] E. Bendadesse, A. V Morozov, A. M. Abakumov, H. Perrot, J.-M. Tarascon, and O. Sel, ‘Deciphering the Double-Layer Structure and Dynamics on a Model Li_xMoO₃ Interface by Advanced Electrogravimetric Analysis’, *ACS Nano*, vol. 16, no. 9, pp. 14907–14917, Sep. 2022, doi: 10.1021/acsnano.2c05784.
- [219] M. Esmaelpourfarkhani, K. Abnous, S. M. Taghdisi, and M. Chamsaz, ‘A novel turn-off fluorescent aptasensor for ampicillin detection based on perylenetetra-carboxylic acid diimide and gold nanoparticles’, *Biosens Bioelectron*, vol. 164, p. 112329, 2020, doi: <https://doi.org/10.1016/j.bios.2020.112329>.
- [220] S. Zhang *et al.*, ‘Insights on the proton mechanism in carbonyl-based organic electrode of neutral aqueous battery’, *J Power Sources*, vol. 550, p. 232110, 2022, doi: <https://doi.org/10.1016/j.jpowsour.2022.232110>.
- [221] Y. Sun *et al.*, ‘Dilute Hybrid Electrolyte for Low-Temperature Aqueous Sodium-Ion Batteries’, *ChemSusChem*, vol. 15, no. 23, p. e202201362, 2022, doi: <https://doi.org/10.1002/cssc.202201362>.
- [222] X. Wu, Y. Qi, J. J. Hong, Z. Li, A. S. Hernandez, and X. Ji, ‘Rocking-Chair Ammonium-Ion Battery: A Highly Reversible Aqueous Energy Storage System’,

References

- Angewandte Chemie International Edition*, vol. 56, no. 42, pp. 13026–13030, 2017, doi: <https://doi.org/10.1002/anie.201707473>.
- [223] T. Hosaka *et al.*, ‘Origin of enhanced capacity retention of aqueous potassium-ion batteries using monohydrate-melt electrolyte’, *J Power Sources*, vol. 548, p. 232096, 2022, doi: <https://doi.org/10.1016/j.jpowsour.2022.232096>.
- [224] K. Kim, L. Tang, J. M. Muratli, C. Fang, and X. Ji, ‘A Graphite||PTCDI Aqueous Dual-Ion Battery’, *ChemSusChem*, vol. 15, no. 5, p. e202102394, 2022, doi: <https://doi.org/10.1002/cssc.202102394>.
- [225] J. Wang, J. Polleux, J. Lim, and B. Dunn, ‘Pseudocapacitive Contributions to Electrochemical Energy Storage in TiO₂ (Anatase) Nanoparticles’, *The Journal of Physical Chemistry C*, vol. 111, no. 40, pp. 14925–14931, 2007, doi: [10.1021/jp0744464w](https://doi.org/10.1021/jp0744464w).
- [226] N. Liu *et al.*, ‘Building High Rate Capability and Ultrastable Dendrite-Free Organic Anode for Rechargeable Aqueous Zinc Batteries’, *Advanced Science*, vol. 7, no. 14, p. 2000146, 2020, doi: <https://doi.org/10.1002/advs.202000146>.
- [227] Z. Huang *et al.*, ‘Manipulating anion intercalation enables a high-voltage aqueous dual ion battery’, *Nat Commun*, vol. 12, no. 1, p. 3106, 2021, doi: [10.1038/s41467-021-23369-5](https://doi.org/10.1038/s41467-021-23369-5).
- [228] E. Commission, E. for Internal Market Industry, SMEs, M. Grohol, and C. Veeh, *Study on the critical raw materials for the EU 2023 – Final report*. Publications Office of the European Union, 2023. doi: [doi/10.2873/725585](https://doi.org/10.2873/725585).
- [229] C. M. Dobson and N. S. Winter, ‘The Identification of Amino Acids by Interpretation of Titration Curves: An Undergraduate Experiment for Biochemistry’, *World Journal of Chemical Education*, vol. 2, no. 4, pp. 59–61, 2014, doi: [10.12691/wjce-2-4-3](https://doi.org/10.12691/wjce-2-4-3).

List of Abbreviations

ACN	Acetonitrile
AGG	Ionic Aggregates
AKIB	Aqueous K-ion Battery
ALIBs	Aqueous Li-ion Battery
AMIB	Aqueous Mg-ion Battery
ASIB	Aqueous Na-ion Battery
AZMB	Aqueous Zn-metal Battery
Asp	Aspartic Acid
BQ	Benzoquinone
C	C-rate
CE%	Coulombic Efficiency
CIP	Contact-ion Pairs
CIT	Citrulline
CV	Cyclic Voltammetry
DBP	Dibutylphthalate
DSC	Differential Scanning Calorimetry
EA	Elemental Analysis
EQCM-D	Electrochemical Quartz Crystal Microbalance-Dissipation
EQCM-R	Electrochemical Quartz Crystal Microbalance-Resistance Monitoring
ESI-MS	Electrospray Ionisation Mass Spectrometry
ESW	Electrochemical Stability Window
FT-IR	Fourier-Transform Infrared Spectroscopy
GdmTFSI	Guanidium bis(trifluoromethanesulfonyl)imide
Glu	Glutamic Acid
HBN	Hydrogen Bonding Network
HER	Hydrogen Evolution Reaction
His	Histidine
ICP-MS	Inductively Coupled Plasma Mass Spectrometry
IHP	Inner Helmholtz Plane
KMEEA	Potassium 2-[2-(2-methoxyethoxy)ethoxy]acetate
LCO	LiCoO_2
LFP	LiFePO_4
LiBETI	Lithium bis(pentafluoroethanesulfonyl)imide
LIBs	Li-ion Battery
LiFSI	Lithium bis(fluorosulfonyl)imide
LiMEEA	Lithium 2-[2-(2-methoxyethoxy)ethoxy]acetate
LiTFSI	Lithium bis(trifluoromethanesulfonyl)imide
LMO	LiMn_2O_4
LNMO	$\text{LiNi}_{0.5}\text{Mn}_{1.5}\text{O}_4$
LTP	$\text{LiTi}_2(\text{PO}_4)_3$

List of Abbreviations

MD	Molecular Dynamics
MEEA	2-[2-(2-methoxyethoxy)ethoxy]acetate
NaMEEA	Sodium 2-[2-(2-methoxyethoxy)ethoxy]acetate
Ni-Cd	Nickel-Cadmium
Ni-MH	Nickel-Metal Hydride
NMC	$\text{LiNi}_x\text{Mn}_y\text{Co}_{1-x-y}\text{O}_2$
NMR	Nuclear Magnetic Resonance Spectroscopy
NTCDA	1,4,5,8-naphthalenetetracarboxylic dianhydride
OCV	Open Circuit Voltage
OEMS	Online Electrochemical Mass Spectrometry
OER	Oxygen Evolution Reaction
PCET	Proton-coupled Electron Transfer
PEG	Poly(ethylene) Glycol
PEO	Polyethylene Oxide
PI	Polyimide
pl	Isoelectric Point
PNTCDA	Polyimide-derived 1,4,5,8-naphthalenetetracarboxylic dianhydride
PTCDI	Perylene-3,4,9,10-tetracarboxylic acid diimide
Pt-RDE	Platinum Rotating Disk Electrodes
PVdF-HFP	Poly(vinylidene fluoride)-co-hexafluoropropylene
PVP	Polyvinylpyrrolidone
RDS	Rate-Determining Step
RHE	Reference Hydrogen Electrode
R_m	Motional Resistance
ROMs	Organic Redox-active Materials
SCE	Standard Hydrogen Electrode
SEI	Solid Electrolyte Interphase
SEM	Scanning Electron Microscopy
Ser	Serine
SLI	Vehicle Starting, Lighting, and Ignition
SSIP	Solvent-Separated Ion Pairs
TGA	Thermogravimetric Analysis
THF	Tetrahydrofuran
TOTO	2,5,8,11-tetraoxatridecan-13-olate
UPS	Uninterruptible Power Supplies
UV-Vis	UV-Vis Spectroscopy
XPS	X-ray Photoelectron Spectroscopy
ZHS	$\text{Zn}_4\text{SO}_4(\text{OH})_6 \cdot 5\text{H}_2\text{O}$
$\text{Zn}(\text{MEA})_2$	Zinc (2-(2-methoxyethoxy)acetate) ₂
$\text{Zn}(\text{MEC})_2$	Zinc (2-methoxyethyl carbonate) ₂
$\text{Zn}(\text{MEEA})_2$	Zinc (2-[2-(2-methoxyethoxy)ethoxy]acetate) ₂

Résumé en Français

Les batteries Li-ion sont la principale source d'énergie pour l'électronique portable et les véhicules électriques, car elles offrent une densité énergétique élevée pouvant atteindre 400 Wh kg^{-1} . Cependant, l'utilisation d'électrolytes organiques inflammables et toxiques dans ces batteries pose d'importants problèmes de durabilité. Par conséquent, la recherche se concentre désormais sur le développement de dispositifs de batterie alternatifs utilisant des matériaux abondants en ressources et rentables. Les piles alcalines-métalliques aqueuses et zinc-ion aqueuses semblent être des options plus sûres et plus durables. L'eau, ininflammable et économique, offre plusieurs avantages par rapport aux électrolytes organiques, mais sa nature réactive et sa fenêtre de stabilité électrochimique (ESW) étroite de 1,23 V, causée par les réactions d'évolution de l'hydrogène et de l'oxygène (HER & OER), posent des problèmes. En ce qui concerne les piles au zinc métal, le principal problème est la présence de dendrites, qui finit par provoquer des courts-circuits. L'ingénierie des électrolytes, qui fait appel à des stratégies telles que la superconcentration, la dilution avec des solvants organiques et des additifs, a joué un rôle crucial dans la résolution de ces problèmes. La découverte que le LiTFSI en superconcentration (21 mol/kg (m)) pouvait former une interphase d'électrolyte solide (SEI) a été la percée qui a permis d'améliorer radicalement l'ESW à plus de 3 V, permettant le cyclage d'une cellule $\text{Mo}_6\text{S}_8 \parallel \text{LiFePO}_4$ (LFP) de 2,3 V. Ces travaux ont donné le coup d'envoi à de nouvelles recherches sur la superconcentration et de nombreuses stratégies ont été proposées pour améliorer davantage les performances. Ces stratégies comprennent l'utilisation du sulfolane pour moduler la chimie de solvation des électrolytes, des polymères qui peuvent agir comme des encombrants moléculaires, et de l'urée qui peut exploiter les effets chaotropiques, ce qui permet d'obtenir des batteries encore plus puissantes. Nous nous appuyons sur ces découvertes ainsi que sur le développement de nouveaux sels et additifs à utiliser dans les électrolytes aqueux des batteries.

Tout d'abord, en explorant d'autres moyens de moduler les propriétés de solvation, l'utilisation d'acides aminés s'est révélée être une option intéressante en raison de leur structure chimique et de leur large gamme de fonctionnalités. Ces caractéristiques offrent de nombreuses possibilités d'ingénierie et d'adaptation de nos

électrolytes. Nos premières tentatives avec la citrulline, que nous pensions capable de fournir des fonctionnalités similaires à celles de l'urée, ont été infructueuses. Bien qu'il ait été possible d'obtenir un LiTFSI + citulline + eau intéressante, les performances de cyclage étaient très faibles en raison de l'absence de formation de SEI, ce qui est essentiel pour l'utilisation du Mo_6S_8 . Nous avons découvert que l'utilisation d'acides aminés peut servir à développer une compréhension fondamentale de la dynamique acide/base des HER. Il a été largement démontré que les HER dépendent fortement du pH et de la source de protons, et qu'un avantage cinétique évident apparaît dans les conditions acides par rapport aux conditions neutres et alcalines, en raison du passage du réactif de H_3O^+ à H_2O . En jouant sur la chimie acide/base des systèmes aqueux, on peut éviter les faiblesses cinétiques. Par exemple, les systèmes tampons peuvent être utilisés pour maintenir la concentration en protons à un pH intermédiaire, entraînant la réduction de H_3O^+ au détriment de H_2O . Les acides aminés sont capables d'agir comme des tampons et, à la lumière de cela, nous examinons l'influence des acides aminés sur la cinétique HER sur les surfaces de platine en utilisant des électrodes à disque rotatif. L'acide aspartique (Asp) et l'acide glutamique (Glu) sont les plus acides des acides aminés essentiels et leur point isoélectrique (pI) et leur pKa tampon sont assez proches (pour Asp pI = 3, pKa = 3,5 - 4,5 et pour Glu pI = 3,3, pKa = 3,5 - 4,5). La proximité de ces valeurs permet à l'Asp et au Glu d'agir en tant que donneurs de protons, mais aussi d'avoir une action tampon suffisante pour maintenir la réduction de H_3O^+ même à une densité de courant élevée. En effet, nous sommes en mesure d'augmenter la densité de courant de H_3O^+ cinq fois avec l'Asp par rapport à l'utilisation d'une solution ordinaire non tamponnée au même pH. Nous avons prouvé que la proximité de leur point isoélectrique (pI) et de leur pKa de tamponnage est la clé en testant l'histidine (His) et la sérine (Ser), qui ont des valeurs de pI et de pKa > 5 de différence. Bien qu'il semble que seuls l'Asp et le Glu puissent être utilisés pour les HER, l'ajustement du pH de départ de leurs solutions aux valeurs de pKa où le tamponnage se produit pourrait être ciblé pour d'autres acides aminés en ce qui concerne d'autres réactions de transfert d'électrons couple avec des protons, telles que l'OER, la réduction du CO_2 , etc. Cependant, ce travail aurait dépassé le cadre de cette thèse et, pour rester fidèle à l'objectif des piles aqueuses, nous avons exploré d'autres moyens.

Le travail précédent n'ayant pas permis d'améliorer les performances des ALIB, nous avons choisi d'examiner les sels susceptibles d'exploiter les effets chaotropiques. Pour approfondir cette question, nous nous sommes intéressés la série de Hofmeister, qui organise les ions en fonction de leur effet le plus important (kosmotrope) de salage à l'entrée et de salage à la sortie (chaotrope) sur les protéines. Au fur et à mesure du progrès de la recherche, la série de Hofmeister a également pu être utilisée pour regrouper les ions qui créent des structures kosmotropes et ceux qui brisent des structures chaotropes. Les kosmotropes organisent le réseau de liaison hydrogène (HBN) de l'eau, tandis que les chaotropes désorganisent le HBN de l'eau. Il est intéressant de noter que la série de Hofmeister suggère que les cations Li^+ sont kosmotropes, renforçant ainsi le HBN. Il serait donc pertinent de combiner les TFSI⁻ avec un cation chaotrope pour former un sel qui pourrait bénéficier de la fonctionnalité susmentionnée des TFSI⁻, tout en présentant potentiellement des effets similaires à ceux de l'urée, afin d'être utilisé comme co-sel avec un sel conventionnel à base de métaux alcalins. Nous avons donc examiné l'utilisation du Guanidinium (Gdm^+) qui est considéré comme un cation hautement chaotrope. Pour la première fois, nous avons fait état du nouveau sel GdmTFSI . La synthèse du sel est très simple, avec une réaction d'échange de cations utilisant LiTFSI et GdmSO_4 dans l'eau. Nous avons caractérisé le sel par spectroscopie FT-IR, analyse thermogravimétrique (TGA) et calorimétrie différentielle à balayage (DSC) et résolu sa structure cristalline par diffraction des rayons X en monocristal. Nous avons ensuite testé des solutions aqueuses du sel jusqu'à la limite de saturation de 8 m. Plus la concentration, augmente, plus l'ESW augmente également : de 1 à 8 m, l'ESW passe de 3,06 V à 3,59 V. Grâce à des mesures FT-IR et de viscosité, nous attribuons cette augmentation des performances à l'effet chaotrope qui a réduit la réactivité de l'eau. Cependant, la solubilité du sel à 8 m restreint la formation d'un SEI, ce qui limite son utilisation. Les sels à base de Gdm seraient plutôt utiles pour les ZMB, un sujet que le laboratoire du CSE étudie activement. D'ailleurs, l'ajout de GdmSO_4 comme co-sel à une solution de 2 M ZnSO_4 a prolongé la durée de vie d'une batterie $\text{Zn} \parallel \text{MnO}_2$ dans nos conditions de test, bien au-delà des résultats précédents.

Pour poursuivre notre travail sur les ZMB, nous avons cherché d'autres sels susceptibles d'améliorer les performances cyclistes. Cela nous a conduits à examiner les sels d'oligoéther, qui avaient déjà été signalés dans la littérature pour Li, Na et K.

Cependant, les variantes de Zn n'avaient pas encore été documentées auparavant. La synthèse des sels a été plus compliquée et a nécessité plusieurs étapes, mais nous avons réussi à synthétiser le carbonate de zinc (2-méthoxyéthyle)₂ (Zn(MEC)₂), l'acétate de zinc (2-(2-méthoxyéthoxy)₂ (Zn(MEA)₂) et l'acétate de zinc (2-[2-(2-méthoxyéthoxy)éthoxy])₂ (Zn(MEEA)₂), ce qui a été confirmé par la RMN, la spectroscopie de masse et l'analyse élémentaire. Les trois sels étaient médiocres en tant que sels primaires, mais leur utilisation en tant qu'additifs à 5 wt% avec du 2M ZnSO₄ a considérablement amélioré le processus d'électrodéposition du Zn. Cela a permis des cycles à long terme de Zn || Zn, Zn || Cu, avec plus de 1000 heures contre seulement 200 heures sans le contrôle. Ceci est dû à l'amélioration drastique du processus de dépôt de Zn rendu possible par les sels. Des études préliminaires indiquent que l'augmentation des performances découle d'un SEI stable à base de ZnS. Toutefois, le mécanisme n'a pas encore été parfaitement compris. Le travail en cours vis à comprendre la science qui sous-tend ces sels, l'EQCM, les mesures de capacité de double couche et l'impédance étant des priorités absolues pour l'avenir. Au-delà de la science fondamentale, notre travail sur ces sels a donné lieu à deux brevets, ce qui est important dans le contexte de l'exploration active par notre laboratoire du potentiel d'une start-up Zn || MnO₂. Nous souhaitons également revenir sur les sels de Li et de Na. Nous décrivons brièvement quelques expériences indiquant que des électrolytes très concentrés peuvent être obtenus en formant des mélanges binaires de LiTFSI et LiMEEA. En outre, les similitudes chimiques de ces sels avec les glymes et les polymères pourraient révéler des propriétés intéressantes susceptibles d'améliorer les performances des ALIB.

Enfin, nous avons décidé de nous éloigner de l'ingénierie des électrolytes et de nous concentrer sur l'utilisation de matériaux qui fonctionnent dans l'ESW d'électrolytes non superconcentrés. Nous avons décidé d'étudier le diimide d'acide perylène-3,4,9,10-tétracarboxylique (PTCDI), car ce matériau a fait l'objet d'une grande attention pour d'autres technologies aqueuses, mais pas pour les ALIB. Nous avons approfondi la chimie fondamentale afin de déterminer le porteur de charge primaire et le mécanisme d'absorption du lithium par le biais de diverses mesures telles que la microbalance électrochimique à cristal de quartz (EQCM), le XRD ex-situ et le FT-IR. Du point de vue des performances, le matériau présente une stabilité extrêmement élevée dans les électrolytes faiblement à moyennement concentrés,

avec des cycles bien au-delà de 1000 cycles avec le LFP dans 1-3 m LiTFSI. Pour maximiser l'ESW de notre électrolyte, nous avons utilisé LiMn_2O_4 , dont le potentiel d'oxydoréduction se situe aux limites supérieures de la séparation de l'eau en ce qui concerne l'OER et 0,5 V de plus que le LFP. La dissolution du Mn signifie que des concentrations plus faibles ont une capacité élevée, ce qui nous a conduit à utiliser 5 m LiTFSI. Cette thèse couvre différentes stratégies d'ingénierie de l'électrolyte qui pourraient être utilisées ici pour résoudre ce problème. Par exemple, l'utilisation de GdmTFSI + LiTFSI ou LiTFSI + LiMEEA pourrait nous permettre de réduire la concentration de LiTFSI tout en exploitant d'autres caractéristiques telles que la chaotropie.

Pour l'avenir, nous pensons qu'il est nécessaire de s'éloigner de WISE pour les ALIB. Bien que la superconcentration soit intéressante et efficace pour maximiser le potentiel des ALIB, ses performances sont bien inférieures à celles des LIB non aqueuses. En outre, les aspects clés des batteries aqueuses, à savoir la durabilité et le faible coût, sont compromis avec ces électrolytes. A la place, nous proposons de trouver des moyens de maximiser ce qui peut être accompli avec des électrolytes dilués, ce qui peut être fait grâce à de nouveaux matériaux tels que le PTCDI. Les ROM sont également en accord avec l'esprit écologique et propre des électrolytes aqueux. L'ingénierie des électrolytes reste un aspect important, et pour résoudre les divers problèmes rencontrés avec les électrolytes aqueux, il faut mettre davantage l'accent sur la conception et la synthèse de nouveaux sels. En effet, si l'on considère les technologies de batteries vertes et propres, il est peut-être préférable de s'éloigner complètement du Li-ion, en particulier pour les applications qui ne nécessitent pas de systèmes à forte densité énergétique, comme les batteries stationnaires. Les sels à base de Gdm et les sels à base d'oligoéther de zinc ont ouvert la voie à cette transition. Les concepts et les idées des chapitres 3 et 4 de cette thèse ont donné lieu à des dépôts de brevets pour les ZMB. Bien que la science qui sous-tend les gains de performance nécessite encore de l'attention, le potentiel de commercialisation est là. Alors que notre société continue de s'attaquer aux problèmes sans fin liés au changement climatique, la diversification de nos systèmes de stockage d'énergie devient primordiale, et les électrolytes aqueux ont certainement un rôle à jouer.

Abstract

Li-ion batteries are the go-to solution for electrical energy storage. However, the flammable and toxic organic solvents they require present sustainability challenges. Aqueous batteries have emerged as safer, more sustainable options. The non-flammability and low cost of H₂O are significant advantages, but its electrochemical stability window (ESW) of 1.23 V hinders performance. This thesis utilises electrolyte engineering to explore the fundamentals of water splitting through the use of amino acids. Additionally, novel salts such as guanidium bis(trifluoromethanesulfonyl)imide (GdmTFSI) and a family of zinc oligoether salts are synthesised to enhance the ESW and prevent dendrite growth in aqueous Zn-metal batteries. Finally, in the search for new electrode materials for aqueous Li-ion batteries, perylene-3,4,9,10-tetracarboxylic acid diimide shows promise, exhibiting high stability even at dilute concentrations.

Keywords: *Electrochemistry, Aqueous Electrolytes, Li-ion, Zn-ion, Salts*

Résumé

Les batteries Li-ion sont la solution privilégiée pour le stockage de l'énergie électrique, mais les solvants organiques inflammables et toxiques qu'elles utilisent posent des défis de durabilité. Les batteries aqueuses, plus durables, bénéficient de la non-inflammabilité et du faible coût de l'eau (H₂O), mais la fenêtre de stabilité électrochimique (FSE) de 1,23 V limite leurs performances. L'ingénierie des électrolytes est nécessaire pour surmonter cette FSE étroite et d'autres défis. Cette thèse explore l'ingénierie des électrolytes pour étudier la dissociation de l'eau via des acides aminés et synthétise des sels novateurs comme le GdmTFSI et une famille de sels d'oligoéthers de zinc pour améliorer la FSE et prévenir la croissance des dendrites dans les batteries à base de zinc aqueux. De plus, la recherche de nouveaux matériaux d'électrode pour les batteries Li-ion aqueuses révèle que le perylène-3,4,9,10-tétracarboxylique diimide présente une haute stabilité même à des concentrations diluées.

Mots clés: *Électrochimie, Électrolytes Aqueux, Li-ion, Zn-ion, Sel*